12-2009

NUCLEATION AND GROWTH BEHAVIOR OF TELLURITE-BASED GLASSES SUITABLE FOR MID-INFRARED APPLICATIONS

Jonathan Massera
Clemson University, massera@clemson.edu

NUCLEATION AND GROWTH BEHAVIOR OF TELLURITE-BASED GLASSES SUITABLE FOR MID-INFRARED APPLICATIONS

A Thesis
Presented to
the Graduate School of
Clemson University

In Partial Fulfillment
of the Requirements for the Degree
Doctor of Philosophy
Materials Science and Engineering

---

by
Jonathan Massera
December 2009

Accepted by:
Dr. Kathleen Richardson, Committee Chair
Dr. Stephen Foulger
Dr. John Ballato
Dr. Yaw Obeng
Dr. Mark Davis

ABSTRACT

Optical fibers transmitting in the 2-5 μm mid-infrared (MIR) spectral region are highly desirable for a variety of military and civilian applications including super-continuum generation, infrared countermeasures (IRCM), and MIR laser sources. These new applications in the mid-infrared require novel optical materials that transmit in this window and can be fabricated into fiber. As tellurite glasses are known to have good transparency in the (NIR) region, tellurite-based glasses are the material of choice for this study due to their high linear and nonlinear refractive index, their low glass transition temperature and the ability to form them into optical fiber.

This dissertation summarizes findings on tellurite-based glasses with the composition $(90\text{-}x)TeO_2\text{-}10Bi_2O_3\text{-}xZnO$ with x = 15, 17.5, 20 and 25 that were processed and characterized for their potential application as novel optical fibers. Different techniques were deployed for characterization purposes, which include primarily linear refractive index measurements, structural characterization using Raman spectroscopy, and nucleation and growth behaviors, among others. The viscosity of the glasses was measured using a beam bending and parallel plate viscometers. The kinetics of crystallization of the bulk glasses and fiber with x =20 were studied using a differential scanning analyzer (DTA), a hot stage XRD and an optical microscope.

The influence of compositional variation on the physical, thermal and optical properties of the glasses in the $TeO_2\text{-}Bi_2O_3\text{-}ZnO$ family was established. The parameters

such as the thermal properties, activation energy for crystallization, Johnson-Mehl-Avrami exponent, or nucleation and growth domains and rates were determined and were found to depend on the glass composition. We correlated the composition-dependent variation of these parameters to the structure of the glasses via Raman spectroscopy. Key physical, thermal, structural and optical differences were observed and quantified between bulk glasses and their corresponding core and core-clad fibers. Also reported are the processing and characterization of modified tellurite-based glass in the TeO_2-Bi_2O_3-ZnO glass family and efforts to reduce their absorption loss due to residual hydroxyl (OH) content. We discuss the impact of this OH reduction in the tellurite network on the physical, thermal and structural properties as well as nucleation and growth behavior of bulk glass and fiber.

ACKNOWLEDGMENTS

This thesis would not have been completed without the help and support of many people. First and foremost I owe my sincere gratitude to *Dr. Kathleen Richardson* for her constant support, guidance and enthusiasm throughout the course of the past four years. Thank you for providing me with the unique opportunity to join the GPCL group. Dr. Richardson provided me the freedom to pursue my research interests and to collaborate with other research groups around the globe. Besides sharing her extensive knowledge, she gave me through the years the fantastic opportunity to interact with some amazingly interesting scientists, some of them whom became dear friends, and to go to multiple conferences in different parts of the world.

Kathleen, your experience, vision and leadership will be invaluable assets I will always admire, learn from and refer to in my career. Thank you so much for all your help, your support, and your guidance! For all this, you have my eternal gratitude.

I would also like to express immense gratitude to the rest of my PhD committee members. My thesis (academic and industrial) committee has given me a lot of help to my research work; not only to review this work but also for their support during all these years. *Dr. Mark Davis* from SCHOTT, his industrial eyes and experience helped me taking into account factors I was unaware of. I deeply appreciate his guidance. He gave me directions when I was lost, taught me life principles, and kept giving often without taking. *Dr. John Ballato* at Clemson University, a leader in optical fiber, has guided me

to the optical fiber drawing process. Thank you, *Dr. Stephen Foulger* at Clemson University for giving me many insightful suggestions that have helped me to think deeper into and perfect my research. *Dr. Yaw Obeng* at NIST, his advice has been very helpful in improving not only my thesis work but also my personal life. It is an honor to include all of you on my committee.

I am very fortunate to have worked with the people at COMSET who share the same passion and fascination with optical fibers. I had the great opportunity to draw the fibers with *Dr. Paul Foy and Wade Hawkins* at COMSET and to characterize them with *Dr. Roger Stolen*. I benefited a lot from the fruitful interactions with them dealing with the intriguing scientific problems.

I am also grateful to the staff of the School of Materials Science and Engineering, especially *Shelby Sheriff and Tonya Bledsoe*, for their kindness and efficiency, and the teachers who gave me one of the greatest gifts of all: knowledge. In particular, I thank *Dr. Henry Rack* for many insightful conversations during the development of this thesis.

I enjoyed also my short trip to Alfred University and express my gratitude to *Dr. Scott Misture* for his input regarding the analysis of the XRD patterns.

Another group that did a lot for me is the Laser Plasma Laboratory led by *Dr. Martin Richardson* at CREOL: *Jiyeon Choi and Troy Anderson*. Thank you for your constant support and knowledge in optics.

I am glad to have the opportunity to work with *Dr. Clara Rivero-Baleine* at Lockheed Martin, the “Raman Girl”.

A special “Kiitos” to *Teemu Kokki* at nLight (Finland) for the measurement of the losses in these “weird” non-silica fibers. Thank you for showing me the equipments and for the fruitful discussions on the losses in optical fiber

I also need to thank my current and former “workmates” of the GPCL for dealing with me and my jokes through the years: *Matthew O’Donnell, Scott Gaylord, Adam Haldeman, Ben Tincher, Jessica Jackson, Nathan (Alison and Charlotte) Carlie, Dave (and Jess) Musgraves, Iona Moog, Charmayne Smith, Jean Remond, Pete (Teresa and Alicia) Watchel.* I will miss our BBQ parties and all the fun we had together.

Friends have been made, among the COMSET, CREOL or REU students, without any order of preference, and all those that I forget, and 4 years of a lifetime is not insignificant. I am thankful to all of you for sharing your friendship and making everyday life a constant travel through the World cultures. I will miss you above everything else!

Merci enfin a mes parents, ma «belle belle-maman», mon frère et ma sœur d’être toujours la pour moi. Merci surtout à ma femme, Laeticia sans qui rien n’aurait été possible….

If some of you are looking for me, I will be back in Europe…. in the cold and sunny Finland for a new episode of my life…

TABLE OF CONTENTS

LIST OF FIGURES

LIST OF TABLES

CHAPTER I: INTRODUCTION

Guiding of light by refraction, the principle that makes fiber optics possible, was first demonstrated by Daniel Colladon and Jacques Babinet in Paris in the early 1840's with Irish inventor John Tyndall offering public displays using water-fountains ten years later [Ba,01]. In 1965, Charles K. Kao and George A. Hockham of the British company Standard Telephones and Cables (STC) were the first to promote the idea that the attenuation in optical fibers could be reduced below 20 decibels per kilometer (dB/km), allowing fibers to be a practical medium for communication [He,99]. New applications in the mid-infrared (MIR) region of the spectrum require novel optical materials that not only transmit in this window but possess unique linear and nonlinear optical properties [El,00]. Infrared (IR) transmitting glasses are of interest for applications such as missile domes and windows for infrared spectrometers [K0,78]. Fused silica (amorphous silicon dioxide, SiO_2) is the dominant material (particularly for optical fiber communications, telecom fibers), because it has a number of very favorable properties such as wide wavelength range with good optical transparency, zero dispersion at around 1.3 μm wavelength, high mechanical strength against pulling and bending, and good chemical stability. However, silica-based glasses exhibit high absorption past 3 μm (and low optical nonlinearities for use in the above cited applications) which precludes their use in the 2-5 μm MIR windows.

Tellurite glasses have attracted the attention of many investigators for optical applications [Ki,93] [Wa,94] as they possess high linear and non-linear indices of

refraction, relatively low phonon energy spectra, multiple valence states of tellurium, low-bonding Te–O strength, and good chemical durability which make them promising candidates for fiber laser and optical amplifier applications [Ru,92]. These glasses also exhibit moderate melting points as compared to silicate-based glasses, low glass transition temperatures, and can be engineered with sufficient crystallization stability to be suitable for fiberization [El,92] [Ki,93]. The successful fabrication of a single-mode Nd^{3+}-doped tellurite fiber laser in 1994 [Wa,94] and the demonstration of a broadband Er^{3+}-doped tellurite fiber amplifier by the NTT opto-electronic group in 1997 [Mo,97] has led to extensive research activity in the use of tellurite-based glasses for a range of optical applications [El,00] [Wa,06]. Recently, Jha et al measured a maximum relative amplification gain of 30dB and 15dB in the C- and L- bands, respectively, in short tellurite-fiber (5-10cm). Here, gain is defined as the difference between pumped and no pump conditions [Jh,07].

As ternary tellurite glasses show excellent thermal resistance against crystallization as compared to the binary glasses [Ko,95], the tellurite glass composition of interest in this study is the TeO_2-Bi_2O_3-ZnO family. Although glasses in this system are of great interest, as exemplified by the publication of a new study on the investigation of 2.0 μm emission in Tm^{3+} and Ho^{3+} co-doped TeO_2–ZnO–Bi_2O_3 glasses [Ga,09], no study on the crystallization mechanism of this glass system has been conducted nor a study on the performance of optical fibers in this glass composition.

The aim of this research is focused on identifying glasses suitable for the engineering of novel fibers for mid-IR applications. The goal of the study was to

understand the effect of the glass composition on the physical, thermal, optical and structural properties as well as on the nucleation and growth behavior of tellurite-based glasses to select the best glass candidate to be drawn into fibers. We have investigated the effect of fiber drawing on the optical and structural properties as well as on the nucleation and growth behavior of the glasses. As the presence of OH in the glass network is disadvantageous due not only to the overtone absorption at 1.38 μm, but also its impact on the thermal and physical properties [St,82] [Sh,00], it is crucial for the development of new fibers to engineer glasses with low absorption in the fundamental and overtone (3.3 and 4.4 μm) regions of the MIR spectrum. Thus, we explored various techniques to reduce the water in the glass and in the fiber, and the impact of such moisture content on the resulting glass and fiber processing.

Specifically, this thesis aims to answer the following questions:

1) what is the compositional effect on the variation of physical, thermal, optical and structural properties within the TeO_2-Bi_2O_3-ZnO system?

Objective: show how chemistry and resulting structure impact the physical and optical properties important to device applications

2) What is the effect of the glass composition on the nucleation and growth behavior of glasses within the TeO_2-Bi_2O_3-ZnO system?

Objective: determine the activation energy for crystallization, Johnson-Mehl-Avrami exponent, nucleation and growth domain and rate, to determine which glasses are most suitable for fiber drawing

3) What significant differences, if any, exist between bulk glass and the corresponding fiber?

Objective: quantify structural differences as well as corresponding property variation.

4) How can the water be reduced in the glasses and in the resulting fiber and what is the impact on OH reduction on the physical, thermal, optical and structural properties as well as the nucleation and growth behavior of the glass with x = 20?

Objective: define processing routes to process glass, preform and fiber with low OH content.

The outline of the dissertation is as follows: Chapter I summarizes background information and theory. Chapter II illustrates experimental techniques, which include glass processing, fiber drawing as well as the chemical, physical, and optical characterization tools used. The subsequent chapters discuss the main findings: chapters IV and V list and discuss, respectively, the results obtained on the processing and characterization of tellurite-based glasses, the study of the nucleation and growth behavior as a function of glass composition, novel fiber processing and characterization and lastly, the reduction of water in tellurite-based glasses. In chapter VI, general conclusion and summary of all the findings is given and chapter VII highlights issues for future study.

CHAPTER II: BACKGROUND

In this chapter, basics on glass formation and glass structure are discussed from an enthalpy, thermodynamic and kinetic point of view. The glasses of interest in this research are tellurite-based glasses. These glasses are often compared to silica-based glasses which, despite their similar structure, have important differences. Application of tellurites in partially crystallized glasses, referred to as glass-ceramics, are reviewed. The thermodynamic and kinetic phenomena driving the formation of crystals in glass are discussed in depth in this chapter. Lastly, a literature review of previously published results on glass fiber properties is presented for a wide range of glass composition such as silicate, chalcogenide or heavy metal fluoride glasses. In this last section, the need for new glass materials able to transmit light in the near- and mid-infrared wavelength range is presented.

II.1 Fundamentals of glass formation

II.1.1 Glasses

Since the study of glasses started, many definitions have been given to these uncommon materials. The first definition, having its origin in the process of formation, defines a glass as a supercooled liquid. Although this statement is true, this definition does not serve to differentiate an inorganic glass from a polymeric glass. Furthermore, some glasses can be formed without having ever been in a liquid state. Two alternative definitions could be: “a solid that does not show long range order” or “a liquid that has

lost its ability to flow" [Ca,07]. A glass can thus be defined as an amorphous (non-crystalline) solid lacking of long range order.

The glass transformation behavior, observed in glasses, is often discussed in terms of enthalpy variation during the glass formation. A plot of enthalpy (or volume) as a function of temperature can be drawn as shown in Figure II.1 below:

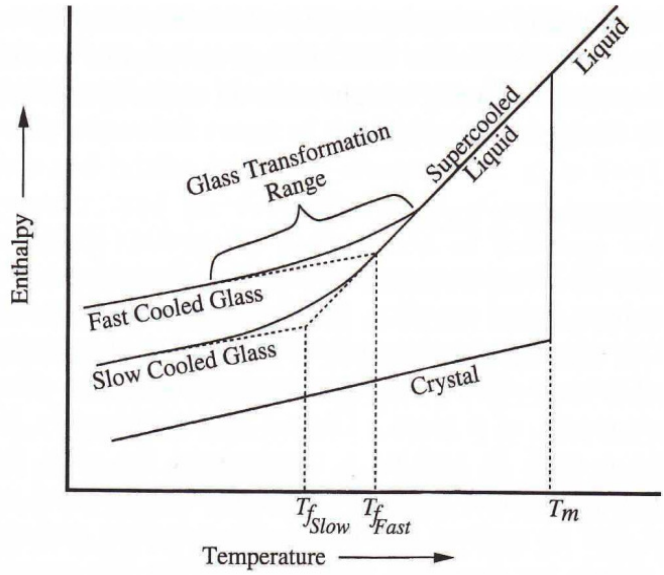

Figure II.1: Effect of temperature on the enthalpy of a glass melt [Sh,05]

One can envision a glass melt mixed at a temperature well above the melting temperature and cooled down at various cooling rates. For melts cooled at a slow rate, the enthalpy decreases linearly with temperature following the "liquid" line and then decreases rapidly without entering the supercooled liquid region. This abrupt change in volume and enthalpy corresponds to the formation of a crystal, giving rise to fully crystallized materials having long range order and periodic atomic arrangement. The change in enthalpy results in a phase change between the liquid state and the solid crystal. This phenomenon typically occurs at the melting temperature, T_m, of the corresponding crystal.

When the cooling rate is fast enough to avoid crystallization, the liquid reaches a state called a *"supercooled liquid"*. The atoms in the liquid will rearrange in a continuous fashion, leading to slow changes in enthalpy, until the viscosity of the liquid reaches a value that inhibits further rearrangement. When the rearrangement of the atoms in the supercooled liquid slows down, the enthalpy starts to deviate from the equilibrium line leading to a decrease in the slope of the graph (see Figure II.1). In other words, the viscosity of the supercooled liquid is such that the atoms can no longer rearrange and this leads to formation of a solid with no long range order. The region in which the slope of the enthalpy/temperature curve changes in the diagram is referred as to *"the transformation range"*, corresponding to the temperature range at which the supercooled liquid becomes a glass. The intercept between the supercooled liquid line and the glass line is commonly referred as to *"the fictive temperature"* T_f [Sh,05]. This temperature is an ideal temperature at which the (solid) glass would possess the exact same structure as that of the supercooled liquid.

Practically, T_f is complicated to measure. From a thermodynamic point of view, if we assume a liquid cooled with an extremely slow cooling rate (i.e. the cooling rate tends to 0), the entropy of the supercooled liquid should have the same value as that of the crystal by extrapolation of the entropy curve. It is impossible to have an amorphous material with an entropy equal to that of the equivalent crystal, and this phenomenon is called the *"Kauzmann's paradox"* [Ka,48]. The only physically reasonable explanation of this phenomenon is, hence, a phase change below T_f. This "region" of glass transformation is called the *"glass transition temperature"*. Through thermal analysis, it is possible to define the glass transition temperature (T_g) corresponding to the

temperature range where bonds between atoms start to break and rearrange. T_g is not a "true" property of the glass since it varies with the heating rate applied to the sample [Sh,05].

II.1.2 Glass-Ceramics

The first glass-ceramic was invented in the 1960s [St,59]. Since this time, the study of partial and controlled crystallization in glasses has been of great interest. Glass-ceramics have been preferred materials in a large variety of applications from aerospace (windows, rings, gamma ray detectors) to biomedical applications (medical tools, dental implants and as substitution for small areas of a bone). Glass-ceramics are also widely used on a day-to-day basis for example in cookware or fireplaces.

i) *For biomedical applications,* a glass or glass-ceramic must be inert and in some cases may need to dissolve after substitution with new tissue. The function of these materials is to develop biologically-active hydroxyl carbonate apatite surface layers that bond with collagen fibrils [He,98]. The main glass-ceramic compositions for biological applications are in the systems: SiO_2-CaO-Na_2O-P_2O_5, SiO_2-CaO-Na_2O-P_2O_5-F or SiO_2-CaO-MgO-Na_2O-K_2O-P_2O_5. Glass-ceramics have been found to have a better failure load, which can vary from 3.52 to 7.44 kg, when compared to a bioglass, which shows a load to failure at around 2.7 kg. Properties such as Vickers hardness, compressive strength and bending strength have been found to be improved by the presence of nanocrystals in the bioglass [Na,85].

ii) For many years, optical materials with a near-zero coefficient of thermal expansion have been explored for use as *precision optics, mirror substrates for*

telescopes, optical elements for comet probes or ring laser gyroscope. Thirty five years ago, ZERODUR® glass-ceramic was developed by Schott; since then, this glass-ceramic has been the leading choice for mirror substrates of earthbound and orbital telescopes, including the Mars Reconnaissance Observer HiRISE (High Resolution Imaging Science Experiment) telescope, and the Keck Telescopes in Hawaii. [Ha,99]. 75% of this glass with the composition SiO_2-Al_2O_3-P_2O_5-Li_2O-MgO-ZnO-K_2O-As_2O_3-TiO_2-ZrO_2 is transformed into the quartz phase, with crystal sizes about 50nm, after thermal treatment. [Ha,99].

iii) MACOR® is a machineable glass-ceramic produced by Corning, and is an efficient insulator and stable up to 1000°C, with a somewhat restrained thermal expansion. This glass-ceramic is often used as *high voltage insulators, spacers, cavities and reflectors in laser assemblies, or windows and doors of NASA's space shuttles.*

iv) One of the most well known glass-ceramics used for *cookware or fireplace windows* is ROBAX® GLASS from Schott. This glass-ceramic has a thermal endurance that far exceeds that of a normal tempered glass. ROBAX® is designed to resist temperatures ranging from -240°C to 750°C [http://www.robaxglass.com/prop.htm].

One of the techniques employed to produce a glass-ceramic consists of heat treating a glassy material at various temperatures. As illustrated in Figure II.2, the first heat treatment forms crystal nucleation sites, while the second heat treatment, occurring at higher temperature, growths the nuclei into crystals with a specific size.

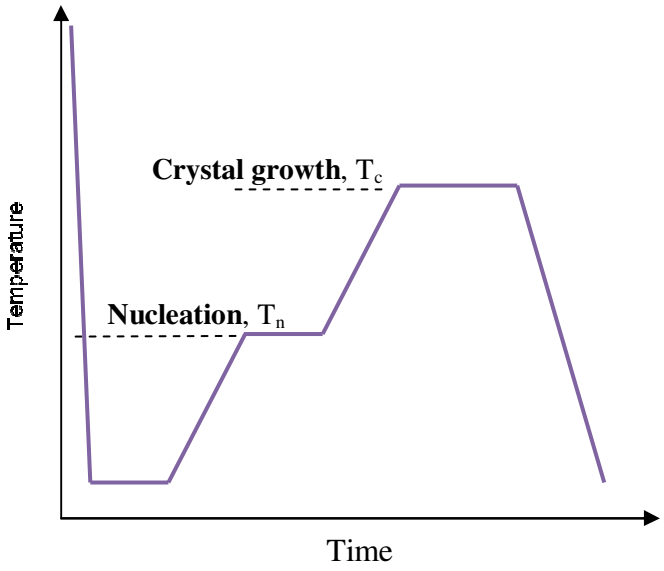

Figure II.2: Schematic illustration of heat treatment cycle conducted to nucleate (at T_N) and growth (T_G) in a glass system [Sh,05]

This technique of glass-ceramic processing allows one to produce crystals in the glass matrix with controlled density, size, and size distribution. The shape of the crystals depends on the kind of growth occurring in the glass system and the chemistry of the crystal. As glass-ceramics are non-porous materials and usually contain a glass-phase, they have a high level of translucency and in some case they can also have good transparency. It is also possible to produce opaque glass-ceramics. The opacity of the glass-ceramic system depends on the chemistry and microstructure of the crystals grown in the glassy matrix and the index match / mismatch between the crystalline and glassy phases [Ho,02]. It has also been demonstrated that not only are the optical properties modified by the presence of crystals but the mechanical properties as well. Indeed, the toughness of a glass-ceramic was found to increase with the presence of a crystalline phase as compared to that of the parent glass alone [Kr,05].

II.1.2.1 Phase separation (spinodal/droplet and nucleation and growth)

The principle of phase separation can be compared to the mixing of water and oil [Sh,05]. When liquid oil and water are mixed together, two distinct phases separate spontaneously. This phenomenon is called *"immiscibility"*. In the case of a glass system which is cooled down rapidly, a glassy solid with droplets of a second glassy phase can be obtained. The size and number of droplets depend mainly on the concentration of the immiscible phase. The glass system is then called *"phase separated"* as a result of liquid-liquid immiscibility [Sh,05]. After glass formation, no further separation can occur unless the glass is re-heated to a temperature high enough to allow viscous flow. As phase separation cannot be seen with the naked eye, electron microscopy must be used to provide evidence of such phenomenon.

The reason for melts to separate into two phases can be explained with thermodynamic principles. Taking into consideration the free energy of mixing, ΔG_m [Ga,03]:

$$\Delta G_m = \Delta H_m - T\Delta S_m \qquad \text{eq. II.1}$$

where ΔH_m is the enthalpy of mixing and ΔS_m is the entropy of mixing, which can be described as follow:

$$\Delta H_m = \alpha X_1 X_2 \qquad \text{eq. II.2}$$

$$\Delta S_m = -R\left[X_1 Ln(X_1) + X_2 Ln(X_2)\right] \qquad \text{eq. II.3}$$

where R is the ideal gas constant, X_1 and X_2 are the mole fraction in phase 1 and 2, respectively and α is a constant defined by the bonding energies of the bonds from the various constituent of the melt.

From eq. II.2 and eq. II.3, the free energy of mixing can be expressed as:

$$\Delta G_m = \alpha X_1 X_2 + TR\left[X_1 Ln(X_1) + X_2 Ln(X_2)\right] \qquad \text{eq. II.4}$$

The sign of ΔG_m is determined by the sign of α.

- If $\alpha < 0$, ΔG_m is negative and the system will not show any phase separation.
- If $\alpha > 0$, the sign of ΔG_m depends on the value of ΔH_m and ΔS_m. At a sufficiently high temperature, ΔG_m is dominated by $T\Delta S_m$ and is negative. The system is homogeneous for any temperature above T_c [Sh,05]. At low temperature (when T approaches 0 K), the entropy term $T\Delta S_m$ goes to 0 and, hence, the free energy will be positive. As a consequence, the mixture separates into the end member components (i.e. compounds 1 and 2 in Figure II.3) if allowed by kinetics [Sh,05]. If T is intermediate (i.e.$0<T<T_c$) the competition between enthalpy and entropy will result in a saddle in the free energy when plotted as a function of composition. Figure II.3 presents the effect of composition for a binary immiscible system [Sh,05]:

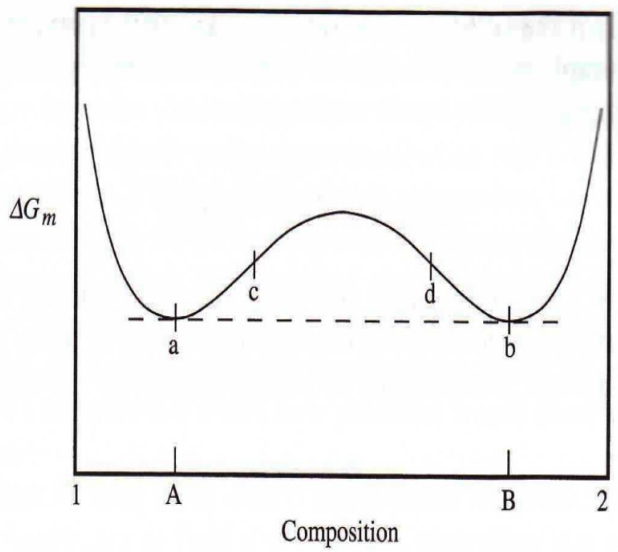

Figure II.3: Effect of composition for a binary immiscible system [Sh,05]

Two domains can be seen on this curve. These two different domains present the two separate paths for phase separation. The first domain is the *"nucleated phase separation"* or the *"nucleation and growth domain"* which is situated in between a-c and d-b. A small change in composition in this region leads to an increase in ΔG_m. The second domain, located in between c and d, is called *"spinodal decomposition"*. A small change in composition in this region leads to a decrease in ΔG_m.

Nucleation and growth and *spinodal decomposition* result in diverse microstructres. Spinodal decomposition leads to a progressive transformation of both phases until an equilibrium state is reached. After completion of this process, the interface between both phases is sharp. Often the second phase is homogeneous in size and shape. On the other hand, during nucleation and growth, nuclei need to form first in order to grow. The composition of the second phase is the one with lesser energy. As opposed to spinodal decomposition, nucleation and growth is often seen as a material with no connectivity between the minor phases. A visual explanation of those two phenomena is shown below [Fa,08]:

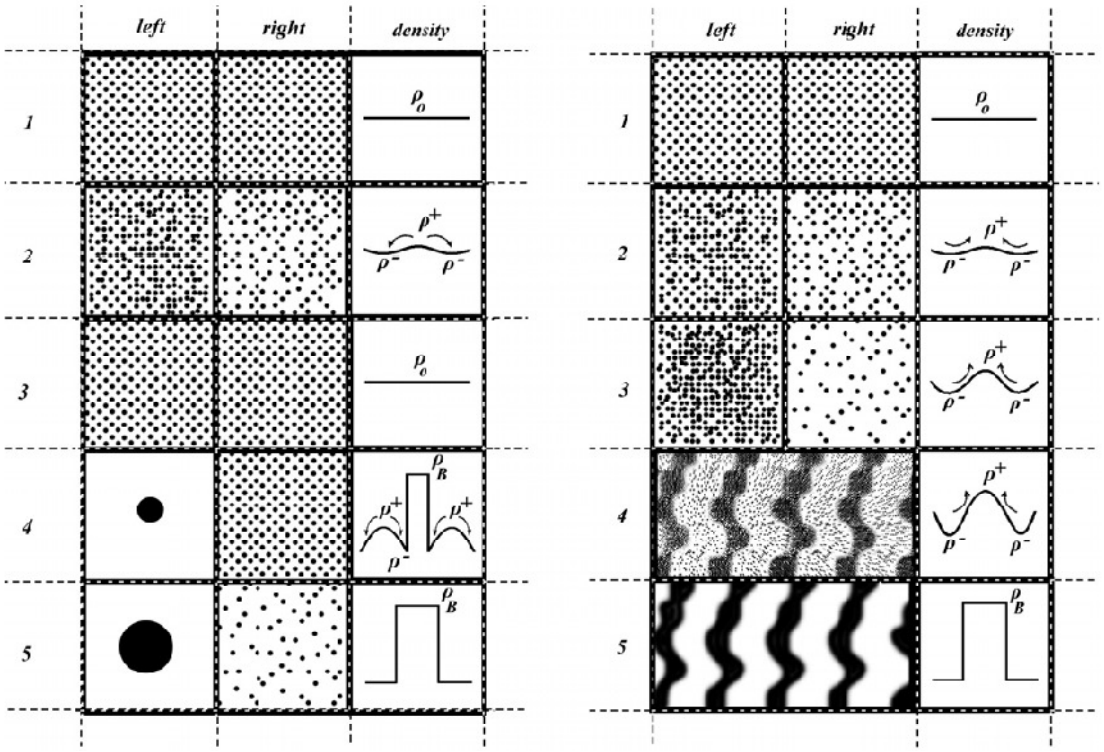

Figure II.4: (a) Nucleation and growth and (b) spinodal decomposition processes [Fa,08]

The two columns named "left" and "right" correspond to two adjacent areas. The column "density" represents the density profile of the system at each step. The black dots represent one of the two components, assuming a binary system. Rows 1 through 3 present the evolution of the system as a function of small energy fluctuations and rows 4 to 5 as a function of large energy fluctuations. In the case of nucleation and growth, small energy diffusion occurs for an infinitesimal fluctuation (row 2 in Figure II.4a). However, after a long heat treatment, if the fluctuation remains constant, the system falls back in its original state, as seen in row 3. For more dramatic energy fluctuations, diffusion occurs leading to formation of nuclei. The growth of the nuclei proceeds with time as shown in rows 4 and 5, respectively [Fa,08]. In the case of spinodal decomposition, Figure II.4b, once a small energy fluctuation is applied, diffusion occurs as seen in the case of

nucleation and growth. If enough time is allowed, diffusion proceeds from left to right (*uphill diffusion*) in order to form areas exclusively formed of the B compounds and A compounds (rows 3 to 5).

II.1.2.2 Nucleation and growth

The nucleation of a crystal is the formation, within the glass, of particles capable of spontaneous growth into larger crystals of a more stable solid phase. These first viable particles are called nuclei and they can form from solid particles (or impurities) already present in the system *(heterogeneous nucleation)*. Nuclei can also be generated spontaneously *(homogeneous nucleation)* [Sh,05].

- **Nucleation process:**

In order to form such nuclei, two distinct barriers must be overcome: the thermodynamic barrier and the kinetic barrier. The steady state nucleation rate (I) can be expressed as follows:

$$I = A\exp\left[-\frac{\left(\Delta G^{*}+\Delta G_{d}\right)}{k_{b}T}\right] \qquad \text{eq II.5}$$

where A is a constant, ΔG^* and ΔG_d are the thermodynamic and kinetic barriers, respectively, k_b is the Boltzmann constant (1.38×10^{-23} m^2 kg s^{-2} K^{-1}) and T is the absolute temperature (K).

- **Thermodynamic barrier:**

The essential driving force in any phase change is the difference in the free energy between the initial phase and the final phase to be formed and this represents the

thermodynamic barrier for crystallization. This energy difference is shown in the Figure below:

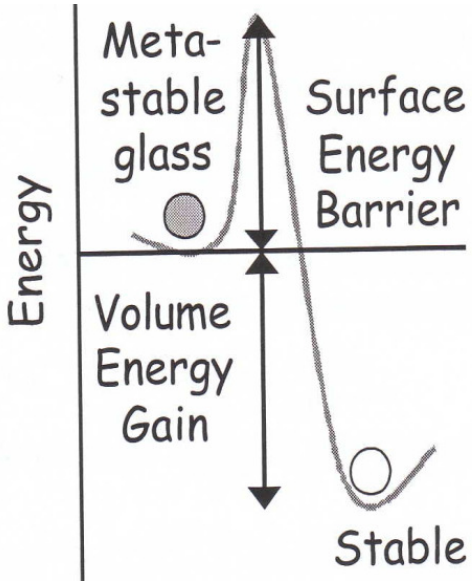

Figure II.5: Energy changes which accompany crystal formation from disordered phases [web.mst.edu/~brow/PDF_nucleation.pdf]

Figure II.5 shows the two different energetic contributions to the nucleation: i) a free energy change which is associated to the transformation of glass to a crystal (volume energy gain) and ii) the formation of a surface energy (surface energy barriers) that inhibits the formation of the crystal. The crystal, having lower energy, is more thermodynamically stable than the glass system, while the glass, with higher energy, is in a metastable form. Hence if the surface energy barrier can be overcome, a crystal forms.

A volume free energy can be assigned to bulk phases, and a surface energy to the interface region. The free energy change can be expressed as follow [Ba,05] [Ch,65]:

$$\Delta G=\Delta G^{bulk}+\Delta G^{interface} \qquad \text{eq II.6}$$

or

$$\Delta G= V\Delta G_v+A\sigma_{ls} \qquad \text{eq. II.7}$$

where ΔG is the change in energy that leads to a phase transformation, ΔG_v is the Gibbs free energy difference between the liquid and the solid state, V and A are the volume and area of the crystals, respectively, and σ_{ls} is the surface tension between the two phases.

In the case of a spherical nucleus forming in a homogeneous manner, equation II.7 can be explicitly written as [Ch,65]:

$$\Delta G = \frac{4\pi r^3}{3}\Delta G_v + 4\pi r^2 \sigma_{ls} \qquad \text{eq. II.8}$$

where r is the radius of the nuclei. Equation II.8 can be plotted as a function of the nuclei radius as illustrated below [Sh,05]:

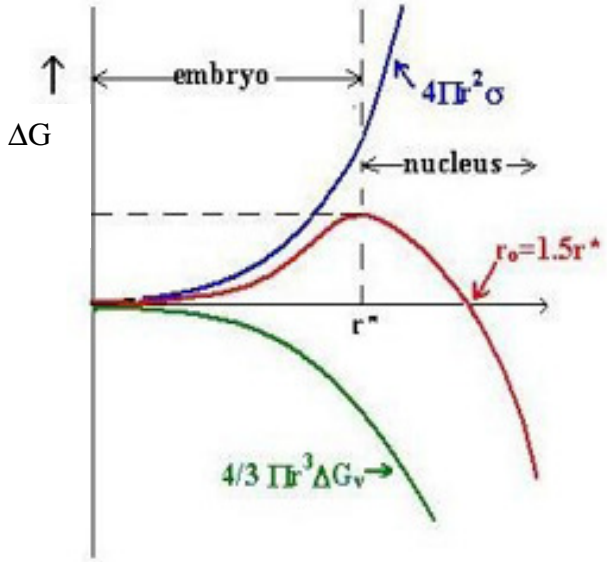

Figure II.6: Nucleation free energy ΔG as a function of the cluster radius, r.

The curve with negative energy (green line) represents the volume term and the curve with positive energy (blue line) represents the surface term. When these two curves are added, the resulting plot (red line) shows a global maximum. This maximum in ΔG corresponds to the minimum energy required to form a nucleus with a stable radius. The radius of this nucleus is commonly called *"critical radius"* and denoted as r*. Nuclei

with radius smaller than the critical radii are unstable and tend to "fall back" to spontaneously re-dissolve into the matrix while nuclei with r greater than r* grow.

The critical radius can be expressed using $\frac{\partial \Delta G}{\partial r} = 0$ as follows:

$$r^* = -\frac{2\sigma_{ls}}{\Delta G_v} \qquad \text{eq. II.9}$$

The energy required to form a nucleus with critical radius can thus be defined as:

$$\Delta G^* = \frac{16\pi\sigma_{ls}^3}{3\Delta G_v^2} \qquad \text{eq. II.10}$$

- **Kinetic barrier:**

The kinetic barrier to crystallization, ΔG_d, is usually discussed in term of viscosity and effective diffusion coefficient "D" which can be written as follows:

$$D = \frac{k_b T \lambda^2}{h} \exp\left(-\frac{\Delta G_d}{k_b T}\right) \qquad \text{eq. II.11}$$

where D is the effective diffusion coefficient, k_b is the Boltzmann constant (1.38×10^{-23} m^2 kg s^{-2} K^{-1}), h is the Planck constant (6.626×10^{-34} m^2 kg s^{-1}), λ is the atomic jump distance and T is the absolute temperature in Kelvin (K).

In order to interpret the effective diffusion as a function of viscosity, the Stokes-Einstein equation can be employed [Sh,05]

$$D = \frac{k_b T}{3\pi\lambda\eta} \qquad \text{eq. II.12}$$

where η is the viscosity at a given temperature T. From Equations II.5, II.10 and II.12, the steady state nucleation rate (I) can be expressed as:

$$I = \frac{Ah}{3\pi\lambda^3\eta} \exp\left(-\frac{16\pi\sigma_{ls}}{3\Delta G_v kT}\right) \qquad \text{eq. II.13}$$

and can be represented as shown below:

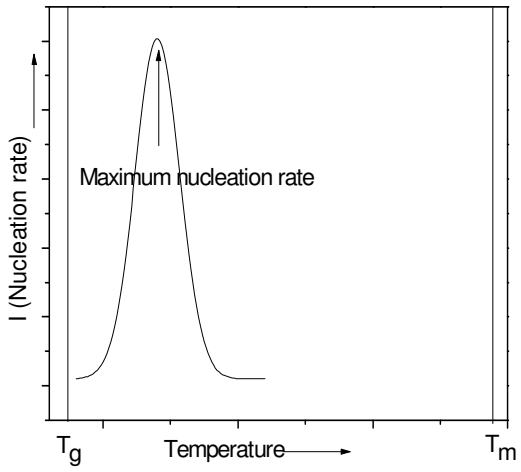

Figure II.7: Effect of temperature on the nucleation rate

At high temperature, or temperatures around the melting temperature T_m, ΔG_v is very small and thus the probability for the nuclei to reach the critical size is low leading to a value of I approaching 0. At those temperatures, it is commonly assumed that the liquid is nuclei free. When the temperature decreases, ΔG_v increases, decreasing the value for r* and hence increasing the value of I. If the system remains long enough in the temperature range where the critical radius is at a size around a few tenths of a nanometer, critical nuclei could form and subsequently lead to crystallization of the glass [Sh,05]. This demonstrates the importance to determine, for each glass system, the minimum cooling rate required to inhibit the formation of nuclei during undercooling.

Note that the above discussion corresponds to steady state nucleation. In the case of steady state nucleation the plot of N_v (number of nuclei formed at a specific nucleation temperature heat treated for specific nucleation time) as a function of the nucleation time is expected to represent a straight line. However, in glasses, a non-linear dependence with

t is often noticed for short nucleation time, as reported by K.F. Kelton, indicating an initially slow nucleation rate that approaches the steady state nucleation for long annealing time [Ke,95]. Transient nucleation is a common phenomenon which has been seen in nucleation of a new crystalline phase within an existing crystalline phase, in a wide variety of glass-forming systems including metallic and silicate-glasses [Ke,95]. Transient effect is not only limited to homogeneous nucleation as heterogeneous transient has also been evidenced [Ke,95].

In the previous paragraph homogeneous nucleation was assumed but it is important to understand that nucleation can also occur heterogeneously. In the case of the heterogeneous nucleation the nuclei will form at preferential sites such as impurities, bubbles or seeds. Because of this foreign surface, the effective surface energy is lowered and thus the free energy barrier is reduced too. In consequence the nucleation is facilitated. The free energy needed for heterogeneous nucleation is equal to the product of homogeneous nucleation and a function of the contact angle [Sh,05]:

$$\Delta G_{heterogeneous} = \Delta G_{homogeneous} * f(\theta) \qquad \text{eq. II.14}$$

where f(θ) is:

$$f(\theta) = \frac{1}{2} + \frac{3}{4}\cos(\theta) - \frac{1}{4}\cos^3(\theta) \qquad \text{eq.II.15}$$

The barrier energy needed for heterogeneous nucleation is then reduced by the presence of the foreign surface. The wetting angle determines the ease of nucleation while the critical radius of the nuclei remains unchanged. However, the volume can be significantly less for heterogeneous nucleation due to the wetting angle affecting the shape of the cluster [Sh,05].

- **Growth process:**

As seen for nucleation two distinct barriers must be overcome for the growth process: the thermodynamic barrier (ΔG_c) and the kinetic barrier (ΔG_a), also called the activation energy. The equation related to crystal growth can be expressed as follows:

$$U = a_0 \nu \exp\left(-\frac{\Delta G_a}{kT}\right)\left[1-\exp\left(-\frac{V\Delta G_c}{kT}\right)\right] \qquad \text{eq.II.16}$$

where ΔG_a and ΔG_c are the kinetic and thermodynamic barriers for crystal growth respectively, a_o is the interatomic separation distance and ν the jump frequency [Py,70]

If a nucleus with critical radius is formed it can, eventually, proceed towards crystal growth under instances where U is non-zero. Crystal growth is the addition of atoms or molecules to the already formed nuclei at a rate which is a function of the thermodynamic and kinetic barriers. The derivation of crystal growth function has been presented by Turnbull for a diffusion-like growth process [Tu,56]. In order for an atom to "leave" the liquid and move across the interface to the crystal, the given atoms (or molecules) must acquire an activation energy ΔG_a. Using the same argument as that shown for nucleation, and hence defining the kinetic barrier using the Stokes-Einstein equation, the growth rate (U) can be formulated as:

$$U = \left(\frac{kT}{3\pi a_0^3 \eta}\right)\left[1-\exp\left(\frac{\Delta G_c}{kT}\right)\right] \qquad \text{eq. II.17}$$

The growth rate (U) can be represented as a function of temperature as shown in Figure II.8:

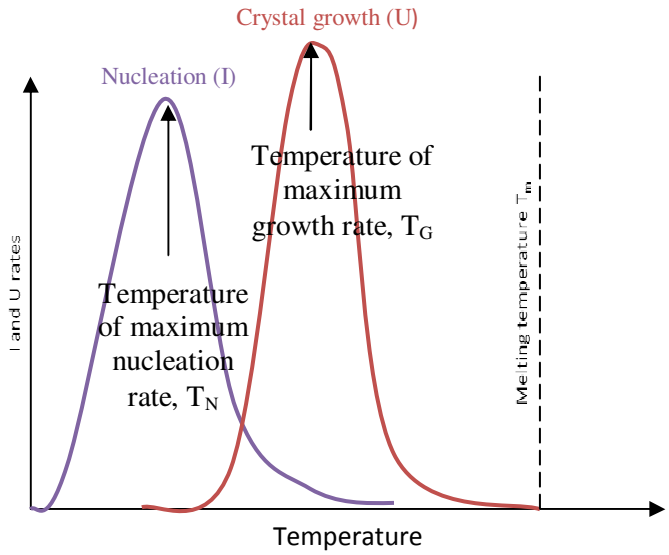

Figure II.8: Nucleation and growth rate as a function of temperature

For high temperatures, the viscosity of the material is expected to be low and hence the crystal growth is limited only by the thermodynamic barrier. However, for lower temperatures the viscosity rapidly increases, inhibiting the growth of crystals by lowering the effective diffusion coefficient. If no nuclei are present in the glass, no growth occurs. When the nucleation and the growth domains overlap, nucleation and growth of crystals occur simultaneously, leading to a broad size distribution in the resulting crystallites observed.

Kirkpatrick et al. summarized in 1981 the idea first theorized by Johnson and Avrami for the description of the overall rate of crystallization with the following assumptions: i) both nucleation and growth occur simultaneously, ii) there is a uniform parent phase that does not contain any crystals and iii) the nucleation occurs randomly, leading to a 3D bulk crystallization (spherical crystal) [Ki,81] [Av,39] [Av,40] [Av,41]. The total extended volume of crystals that form or could form in the materials from the starting of crystallization to any time t can be expressed as:

$$V_{ext} = \frac{4\pi}{3} V \int_{\tau=0}^{\tau=t} I_\tau \left(\int_\tau^t U_t dt \right)^3 d\tau \qquad \text{eq.II.18}$$

where V is the total volume of the system and τ is the time. I and U are the nucleation and growth rates, respectively.

The volume calculated using equation II.18 is known to be larger than the true volume crystallized. This is due to two different phenomena: i) equation II.18 includes the "phantom" nuclei that could have nucleated in the already crystallized volume if it were not a crystal, and ii) this equation does not take into account the volume that has not actually crystallized because two crystals have impinged on each other.

In order to overcome those issues, Kirkpatrick offered a more general definition of the volume crystallized, ϕ [Ki,81]:

$$\phi = 1 - \exp\left[-\frac{4\pi}{3} \int_{\tau=0}^{\tau=t} I_\tau \left(\int_\tau^t U_t \, dt \right)^3 d\tau \right] \qquad \text{eq. II.19}$$

This expression is valid for any variation of the rates of the nucleation and growth with time. In the case of constant nucleation and growth rates, the above equation reduces to give the classic Jonhson-Mehl-Avrami (JMA) equation [Ki,81]:

$$\phi = 1 - \exp\left[-\frac{\pi}{3} I U^3 t^4 \right] \qquad \text{eq. II.20}$$

Although this equation was derived for 3D crystallization, Avrami explained that a more general equation could be used [Av,39] [Av,40] [Av,41]:

$$\phi = 1 - \exp\left(- g I U^m t^n \right) \qquad \text{eq. II.21}$$

where g is a geometric factor, m and n are the Johnson-Mehl-Avrami exponents. The exponent m and n are typically integers or half integers that depend on the kind of growth

occurring in the material (surface crystallization versus 1D, 2D or 3D bulk crystallization). Often the equation is expressed as follows:

$$\phi = 1 - \exp\left(-(kt)^n\right) \qquad \text{eq. II.22}$$

where k is the effective overall reaction rate and is often expressed using the Arrhenian temperature dependence:

$$k = k_0 \exp\left(-\frac{E}{RT}\right) \qquad \text{eq. II.23}$$

where E is the overall activation energy for crystallization, k_0 is the initial reaction rate constant and R the gas constant.

In this dissertation, we have focused our effort on the determination of the crystallization kinetics of the predominant crystalline phase. We have determined i) the Johnson-Mehl-Avrami exponent, ii) the activation energy for crystallization, iii) the nucleation and growth temperature ranges for the ternary glass system and iv) the actual nucleation and growth rates as a function of temperature. From the nucleation and growth rate curves plotted as a function of temperature, it is possible to define the temperature at which the nucleation and growth rate will be maximized and more importantly the extent of overlap between nucleation and growth.

II.2 Determination of nucleation (I) and growth (U) parameter

In this section, we explain in detail how the nucleation and growth rates can be experimentally determined.

II.2.1 Nucleation and growth-like curve

Nucleation and growth-like curves can be determined using the Differential Thermal Analyzer (DTA). When heated up, the glass undergoes transformations which cause the sample to release or gain energy. This change in energy can be seen on the DTA thermogram as an exothermic (release of energy) or an endothermic peak (gain in energy). Figure II.9 shows a typical thermogram of a glass.

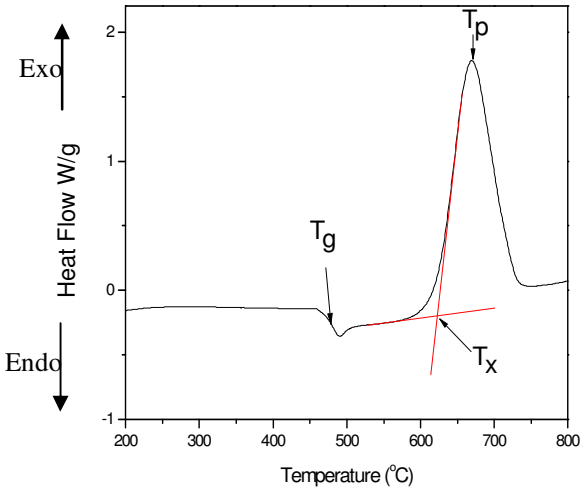

Figure II.9: DTA thermogram of a lithium disilicate glass.

In our experimental work the glass transition temperature (T_g) is taken at the inflection point of the endotherm, as obtained by taking the first derivative of the DTA curve. T_x is plotted by extrapolating the onset of the first crystallization exotherm and the crystallization temperature (T_p) is taken at the maximum of the exothermic peak. The position of the exothermic peaks gives an insight to the temperature of crystallization and the area of the peak to the energy required to fully undergo the crystallization process. The area of the peak (A) can be expressed as follow:

$$A = \int_{T_2}^{T_1} \Delta T dT \qquad \text{eq. II.24}$$

where ΔT is the difference in temperature between the reference and the sample. T_1 and T_2 are the temperatures where the peak starts and ends, respectively [Ra,02].

Nucleation-like curve

The firsts to demonstrate the use of the DTA as evidence of nucleation in glass were Marotta et al. in 1981 [Ma, 81]. The experiment uses a simple method to look for signs of nucleation. A small amount of glass powder (~50mg) is placed in the DTA pan and heated up to T, a temperature believed to be in the vicinity of the maximum nucleation rate, and held for t minutes. The shift of the maxima for the exothermic (crystallization) peak, as compared to the position of the peak measured at a constant heating rate, reflects the variation of the number of nuclei formed in the glass. The nucleation rate (I_o) can be expressed by the equation below:

$$Ln(I_0) = \frac{E_c}{R}\left(\frac{1}{T_p} - \frac{1}{T_p^0}\right) + C \qquad \text{eq. II.25}$$

where E_c is the activation energy for crystal growth, R is the gas constant and C is a constant. T_p and T_p^0 are the maximum of the exothermal peak with and without the nucleation thermal hold, respectively [Ma, 81][Da, 03].

The same experiment is reproduced using isothermal holds at various temperatures near the suspected nucleation maxima. By plotting $\frac{1}{T_p} - \frac{1}{T_p^0}$ as a function of the temperature of nucleation, a "nucleation-like" curve can be obtained. This curve gives an insight on the nucleation temperature range and temperature of maximum nucleation rate, although the real rate cannot be obtained as the constant C is unknown.

Marrotta et al have shown that $T_p^{-1}=f(T)$ can provide useful insight on the crystallization domain [Ma,81][Ra,01].

The method proposed by Ray et al. to ascertain the number of nuclei available for growth, focuses not only on the position of the exotherm peak but also on the height of this exotherm peak. [Ra,97]. Glass particles are heat treated at a temperature which is suspected to lead to a maximum of nucleation and held there until complete crystallization of the glass. The number density of nuclei in a glass N_t can thus be expressed as [Ra,97]:

$$N_t=N_q+N_i+N_h \qquad \text{eq. II.26}$$

where N_q is the concentration of quenched-in nuclei, N_i the number of nuclei formed per unit volume during the isothermal heat treatment and N_h the number of nuclei per unit volume that form during the non-isothermal scan (heating) in the DTA apparatus [Ra,97]. It is important to mention that the heating rate to heat treat the glass must be relatively high (~> 15^{o}C/min) so as to inhibit the formation of nuclei prior to the isothermal hold at the specific temperature and thus leading to the assumption that $N_h\approx 0$. N_q, the concentration of nuclei in the as-quenched glass, should be identical for all samples if they come from the same glass melt. Ray et al. demonstrated that the maximum intensity of the exothermic DTA peak (δT_p) is linearly proportional to the total number of nuclei in the glass [Ra,97]:

$$(\delta T_p)= K(N_q+N_i+N_h)V \qquad \text{eq. II.27}$$

where K in the equation is a proportionality constant, likely to be a temperature-dependent parameter, and V corresponds to the volume of the samples. To simplify the equations, they treated K as a constant [Ra,97].

If the glass partially crystallizes during the nucleation treatment, the volume of the glass, V, must be replaced in the equation IV.6 by the volume of glass that has not yet crystallized [Ra,97]:

$$\frac{\delta T_p}{K} = \left(N_q + N_i\right) exp\left[-\frac{\pi}{3}\left(N_q + N_i\right)(Ut)^3\right] \qquad \text{eq. II.28}$$

where U is the growth rate and t the time allowed for crystal growth.

If K is assumed to be constant, $\frac{\delta T_p}{K}$ as a function of T_n, the nucleation temperature, should mimic the δTp as a function of T_n curve. When I and U are well separated the exponential term tends to 1 and the curve $\frac{\delta T_p}{K}$ as a function of temperature T_n, is thus similar to I as a function of T_n. When I and U partially overlap, the value of $\frac{\delta T_p}{K}$ on the overlapping region is reduced by a factor of $exp\left[-\frac{\pi}{3}\left(N_q + N_i\right)(Ut)^3\right]$. When I=U=0, $\frac{\delta T_p}{K}$ is constant and equal to N_q [Ra,97].

As shown by Marotta et al., T_p^{-1} for glasses prepared from the same melt (i.e. N_q identical for all samples) and nucleated for the same time at various temperatures, is proportional to only N_i and hence to I. Therefore T_p^{-1} and δT_p as a function of T_n are similar to that of I as a function of T_n, independent of any possible overlap between the nucleation and growth domain [Ra,97] [Ma,81].

The area of the DTA peak (A) is proportional to the number of nuclei formed and can be expressed as:

$$A = C(V_g - V_c)(I_N t_N + Nq) \qquad \text{eq. II.29}$$

where C is a proportionality constant, V_c is the volume that crystallizes during the nucleation and growth treatment at T_N and T_G for a time t_N and t_G. V_c, can be expressed as:

$$V_C = V_0 \frac{\pi}{3}\left(I_N t_N + N_q\right)\left(U_G t_G\right)^3 \qquad \text{eq. II.30}$$

where V_0 is the initial volume of the glass sample, N_q is the concentration of nuclei present in the quenched-liquid, I_N and U_G are the steady state nucleation and growth rates at the temperature T_N and T_G, respectively. t_N is the time of nucleation and t_G is the time of growth. $(I_N t_N + N_q)$ is the number of nuclei per unit volume after the nucleation step. The volume that remains untransformed (V_g) can be written as follow:

$$V_g = V_0 - V_c \qquad \text{eq. II.31}$$

As the constant C is unknown, it is possible to compare two DTA runs with two different times for the growth. It is then possible to write equation II.18 as [Ra,00]:

$$\frac{A_1}{A_2} = \frac{M_1\left[1-\frac{\pi}{3}\left(I_N t_N + N_q\right)\left(U_G t_{G1}\right)^3\right]}{M_2\left[1-\frac{\pi}{3}\left(I_N t_N + N_q\right)\left(U_G t_{G2}\right)^3\right]} \qquad \text{eq. II.32}$$

From the above equation the growth rate at a specific temperature needs to be determined separately to determine the quantitative nucleation rate.

Growth "like" curve

The growth like curve can be defined using the technique proposed by Ray et al. [Ra, 01]. A small amount of glass powder (~50mg) is heated in the DTA from room temperature to a potential growth temperature, T, at a high heating rate (larger than 10^oC/min) to avoid nuclei to form during the heating of the sample. After 5 minutes at this temperature, the area of the exothermic peak (A_T) is measured. The same experiment

is reproduced using various growth temperatures and the growth like curve is obtained by plotting $\Delta A=A-A_T$ where A is the exothermic peak area of a glass which was heat treated at any potential growth temperature. While this set of experiments does not give any indication of the absolute growth rate, it allows one to target the approximate temperature range for significant crystal growth.

The crystal growth rate (U_G) can be estimated by heating the glass to a temperature larger than the temperature of maximum nucleation for different durations and by measuring the crystal size as a function of the heat treatment duration [Go, 80]. Once the growth rate (U_G) is known, it is then possible to estimate from equation II.32 the nucleation rate and the concentration of quenched-in nuclei.

II.2.2 Determination of the JMA exponent, n

The value of n can give an insight into the crystal growth behaviour in the system under investigation as summarized in Table II.1, taken from [Ch,65].

Table II.1: Value of n in Kinetic law [Ch,65].

(a) Polymorphic changes, discontinuous precipitation, eutectoid reactions, interface controlled growth, etc.

Conditions	n
Increasing nucleation rate	>4
Constant nucleation rate	4
Decreasing nucleation rate	3–4
Zero nucleation rate (saturation of point sites)	3
Grain edge nucleation after saturation	2
Grain boundary nucleation after saturation	1

(b) Diffusion controlled growth

Conditions	n
All shapes growing from small dimensions, increasing nucleation rate	$>2\frac{1}{2}$
All shapes growing from small dimensions, constant nucleation rate	$2\frac{1}{2}$
All shapes growing from small dimensions, decreasing nucleation rate	$1\frac{1}{2}$–$2\frac{1}{2}$
All shapes growing from small dimensions, zero nucleation rate	$1\frac{1}{2}$
Growth of particles of appreciable initial volume	1–$1\frac{1}{2}$
Needles and plates of finite long dimensions, small in comparison with their separation	1
Thickening of long cylinders (needles) (e.g. after complete end impingement)	1
Thickening of very large plates (e.g. after complete edge impingement)	$\frac{1}{2}$
Precipitation on dislocations (very early stages)	$\sim\frac{2}{3}$

Diverse methods have been proposed to determine n, the JMA exponent, using non-isothermal and isothermal experiments.

Non-isothermal experiments

In a non-isothermal experiment, the JMA exponent can be determined from i) the measurement of the volume fraction of the crystal (ϕ) as a function of temperature for various heating rates or ii) the measurement of the exothermic peak position as a function of the heating rate.

Ozawa demonstrated that the position of the exothermic peak depends on the heating rate used for the measurement, the position of the peak increasing to higher temperatures for faster heating rates [Oz,71]. This variation indicates that the amount of residual glass in the amorphous matrix depends on the heating rate due to the kinetic effect and can be related to the JMA exponent using the following expression:

$$\left|\frac{d\left(Ln\left(-Ln\left(1-\phi\right)\right)\right)}{d\left(Ln\left(q\right)\right)}\right|_T = -n \qquad \text{eq. II.33}$$

where q is the heating rate. This equation suggests that the plot Ln(-Ln(1-ϕ))=f(Ln(q)) yields a straight line, the slope of which is -n.

The activation energy for crystallization (E_c) and glass transition temperature (E_g) can be defined using the Kissinger equation [He,93]:

$$Ln\left(\frac{q}{T_p^2}\right) = -\frac{E_c}{RT_p} + C \qquad \text{eq. II.34}$$

where q is the heating rate and T_p is the maximum of the exothermic peak and C is a constant [Ki, 57]. In order to obtain the activation energy for the glass transition temperature (E_a) T_p should be replaced by T_g.

Equation II.34 can be deceiving in some cases since one of the important assumptions is that the only contribution to crystallization is crystal growth and hence no nucleation occurs during the heating of the glass. In order to take into account nucleation during the heating of the sample, Matusita and Sakka proposed a modification of the Kissinger equation as shown below [Ma,77]:

$$Ln\left(\frac{q^n}{T_p^2}\right) = -\frac{mE}{RT_p} + C \qquad \text{eq. II.35}$$

where m is the second Avrami exponent which is determined from the value of n and the kind of growth in the glass of interest and hence,

$$E = \frac{nE_K}{m} \qquad \text{eq. II.36}$$

where E_K is the activation energy measured using the Kissinger equation.

Note that if the crystallization is a "surface crystallization" then n=m. In the case of bulk crystallization, with no nuclei formed during the heating of the sample, n=m and $E=E_K$. However if crystallization occurs via bulk crystallization with nucleation and crystallization occurring simultaneously, then n=m+1. Once the activation energy for crystallization is calculated, the Avrami parameter, n, can also be determined using the Augis-Bennet equation [Au,78]:

$$n = \frac{2.5RT_p^2}{FWHM * E} \qquad \text{eq. II.37}$$

where FWHM is the full width at half maximum of the crystallization peak.

Isothermal experiments

It is also possible to determine n from an isothermal treatment at a temperature T for a time t. If the duration of the heat treatment is long enough to lead to crystallization of the glass, an exothermic peak appears on the DTA signal. From the time required to induced complete crystallization of samples and from the area of the exothermic peak at each time t it is possible to estimate n using the equations below, derived from Equation II.22

$$Ln(1-\phi) = -(kt^n) \qquad \text{eq. II.38}$$

$$Ln(-Ln(1-\phi) = nLn(k) + nLn(t) \qquad \text{eq. II.39}$$

where Φ is determined as the ratio between the area under the exothermic curve as a function of time and the total area of the crystallization peak.

The slope of the plot of Ln(-Ln(1-ϕ))=f(Ln(t)) gives the value of n. In order to average n and improve the accuracy of the measurement, the experiment should be reproduced using different isothermal temperatures.

II.2.3 Time-Temperature-Transformation (TTT) curve

As explained in the previous paragraph, the crystallization behavior of a glass can be defined using the Avrami equation (eq. II.22). For a given temperature and a specific duration of the heat treatment, it is possible to define the volume of glass crystallized. This gives the so-called TTT curve or literally Time-Temperature-Transformation diagram. Figures II.10 presents an example of a TTT curves for a metallic glass of the composition $Zr_{41.2}$-$Ti_{13.8}$-$Cu_{12.5}$-Ni_{10}-$Be_{22.5}$ [Bu,00].

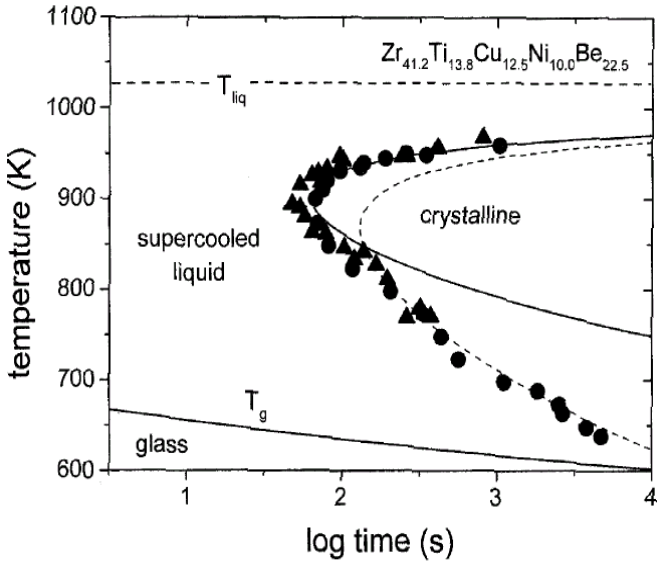

Figure II.10: Time-Temperature-Transformation diagram for the primary crystallization of a $Zr_{41.2}$-$Ti_{13.8}$-$Cu_{12.5}$-Ni_{10}-$Be_{22.5}$ metallic glass [Bu,00].

The glass formation is directly dependent of the position of the TTT curves on the time/temperature axis. If the cooling rate is fast enough to avoid intercepting the TTT diagram, a glass can be formed. It is often said that the average position of the nose of the TTT curves on the temperature can be approximated as $\frac{T_g + T_m}{2}$ where T_g is the glass transition temperature and T_m is the melting temperature [Mi,07].

Many studies have been performed in order to theoretically define the TTT curve of a specific material starting from the works of Turnbull [Tu,69], Uhlmann [Uh,72], and then, Davies [Da,76]. Weinberg et al and Clavaguera et al. further developed the former studies to determine the TTT curves from non-isothermal measurements [We,89] [Cl,93]. However, in order to apply those findings, various parameters of the material of investigation have to be known such as viscosity and heat capacity over a wide range of temperature [Mi,07].

II.3 Effect of crystallization on the optical and mechanical properties of a glass.

One of the main effects of crystal formation on *the optical properties* of glass is increased light scattering. Light scattering induced by particles depends on the size of the crystals, difference in refractive index between crystals and glass, and the wavelength of interest. Light scattering and absorption characteristics of particles that are smaller than the wavelength λ of the incident radiation have been studied with the approximation that the particles can be replaced by one and only one dipole and using the following Rayleigh approximation [Ko,01]: x<<1, $x|m| << 1$

where x=ka is the size parameter with $k = \frac{2\pi}{\lambda}$, a is the size of the scattering center and m is the complex refractive index of particle, relative to that of the medium.

The intensity I of light scattered, by a single particle, from a beam of unpolarized light of wavelength λ and intensity I_0 can be expressed as follows:

$$I = I_0 \frac{1+cos^2(\theta)}{2R^2} \left(\frac{2\pi}{\lambda}\right)^4 \left(\frac{n^2-1}{n^2+1}\right)^2 \left(\frac{d}{2}\right)^6 \qquad \text{eq. II.40}$$

where R is the distance travelled by the light before interacting with the particle, θ is the scattering angle, n is the refractive index of the particle, and d is the diameter of the particle. By integrating this equation over the sphere surrounding the scattering we obtain the Rayleigh scattering cross section:

$$\sigma_s = \frac{2\pi^5}{3} \frac{d^6}{\lambda^4} \left(\frac{n^2-1}{n^2+2}\right)^2 \qquad \text{eq. II.41}$$

The Rayleigh scattering coefficient gor a group of scattering sites is hence the number of particles per unit volume N_v times the cross section. Thus, the Rayleigh scattering does not only depends on teh size of teh scattering sites but also the number of density.

The optical properties of particles with sizes comparable to the wavelength of the incident light can be calculated within the framework of the discrete dipole approximation; a particle, independently of its shape, can be replaced by an array of N point dipoles. In natural media (atmoshpere for example), particles are often much larger than the wavelength of the incident light and hence the Rayleigh and discrete dipole approximation can no longer be applied. In this case, the differential scattering follows the element of the amplitude matrix [Ko,01]. Indeed the geometrical factor is of great importance in this specific situation.

Takebe et al. studied the changes in the optical properties of La_2O_3-Ga_2S_3 glass-ceramics as a function of the heat treatment duration. Figure II.11 presents the IR transmission spectra of the as-prepared and heat treated glasses [Ta,06], taken as an example.

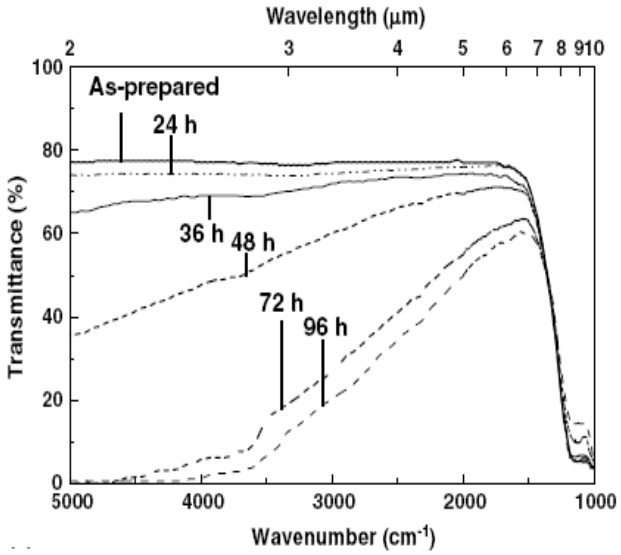

Figure II.11: IR transmission spectra of a La_2O_3-Ga_2S_3 (LG) glass heat treated at 615°C [Ta,06]

As seen above, the IR transmittance decreases with increasing heat treatment time and hence decreases with increasing particle size. Indeed Takebe et al. demonstrated that for heat treatment up to 36h the crystal size remains <1μm while for heat treatment time of 48 to 96h, the crystals reach sizes in the 2-3μm range. After 72hrs of heat treatment, the transmittance reduces to <50% in the 3-5μm wavelength range. The glass-ceramic having particle size of about 1μm shows a transparency over 60%. Takebe et al also explained that the reduction in transparency can also be due to the difference in refractive index between the glass and the crystals.

The mechanical strengthening of a glass is a large field of scientific investigation. There are numerous overviews in the topic including those by Scholze et al and Kerkhoff et al. [Sc,88] [Ke,70] [Kr,05]. The main reviews were reported in the 70‘s and 80’s and are mainly in German, hence difficult to obtain and understand. It was reported that the brittleness, elasticity and the mechanical properties of a glass are not intrinsic properties

of the material but rather depend on i) the surface quality (for example the distribution of surface flaws), ii) the time distribution of the tensile strength, iii) the surrounding medium and iv) the effective surface area under tensile stress [Kr,05]. Because the strength depends on the material and on the fabrication process, strength of the glass is often discussed using the Weibull distribution which gives an indication of the material lifetime. In general, the theoretical strength of a silica glass is ~ 10^4 N/mm^2. However, the strength is often measured to be below 10^2 N/mm^2. This difference in strength has been related to surface flaws [Kr,05]. To improve the strength of the glass, one solution is to create a compressive stress at the surface of the glass. This can be done by chemical strengthening, thermal toughening or surface crystallization [Kr,05]. In the thermal toughening process, the glass or glass-ceramic is heated up at a temperature between the glass transformation temperature and the softening point and then cooled down rapidly. The outside of the glass or glass-ceramic cools down faster than the inside of the bulk creating a compressive stress at the surface and a tensile stress inside of the bulk [Ki,75]. However, often the compressive stress obtained via thermal toughening is too low for most applications in which it is neccesary to guarantee the safety of the users when in service. In order to increase the mechanical properties of a glass, controlled nucleation and growth of crystal in a glassy matrix was found to be efficient. Takebe et al. studied the mechanical properties of undoped- and Nd_2O_3 doped La_2O_3-Ga_2S_3 glass-ceramics as a function of the crystal size [Ta,06]. They focused their study on the variation of the Vickers hardness with respect to heat treatment time. Figure II.12 presents the variations of Vickers hardness H_v as a function of the heat treatment duration for the doped and undoped glass-ceramic:

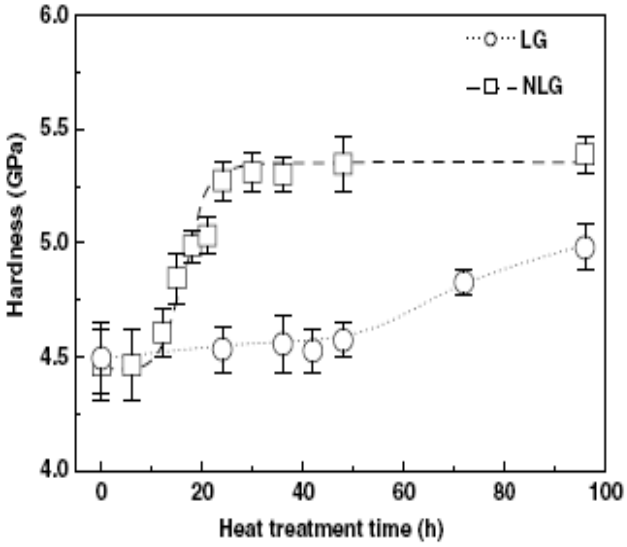

Figure II.12: Variation of Vickers hardness H_v with heat treatment time for La_2O_3-Ga_2S_3 (LG) and Nd_2O_3 doped La_2O_3-Ga_2S_3 (NLG) glasses [Ta,06]

The as-prepared LG and NLG glasses have a H_v value of ~4.5GPa. The Vickers hardness of the undoped glass as a function of the heat treatment duration, and thus as a function of the crystal size, was found to increase to 5GPa when heat treated for 96 hours, while the H_v of the Nd_2O_3 doped glass increases to 5.3GPa after 24 hours of heat treatment but then remains constant within the experimental error for longer heat treatments [Ta,06]. It was clearly shown that not only can the formation of crystals enhance the hardness of a glass, but it can control the fracture mode of the material as well. It is common practice for the ceramic industries to modify the extent of grain boundaries with the aim to control the active fracture modes [Zh,03] [Su,05]. By modifying the coherence of the grain boundaries, it is possible to predict whether the crack propagates in a transgranular or intergranular mode:

- When the propagation of the crack is transgranular, the cracks propagate independently of the orientation of the grain boundaries leading to an increase of the glass strength [Mo,96].

- When the propagation of the crack is intergranular, the cracks debond at the interfaces following the grain boundary directions, increasing the toughness of the material [St,86] [Mo,96].

However, while crack propagation in ceramic materials has been widely studied, few studies have been carried out in the case of glass-ceramics. An increase of the machinable strength of bioactive glass-ceramics can be obtained by promoting the transgranular fracture by controlling the composition and the phase of the crystal formed in the glassy matrix [Ch,07]. Taken as an example, Charitidis et al. studied the influence of crystalline inclusion size on the mechanical properties of a glass-ceramic in the Fe_2O_3-PbO-SiO_2-Na_2O system [Ch,07]. Two different compositions were studied and the main mechanical property studied was the mode of fracture. One glass-ceramic contained granularly shaped crystals while the second possessed needle-like crystalline inclusion randomly oriented as shown below [Ch,07].

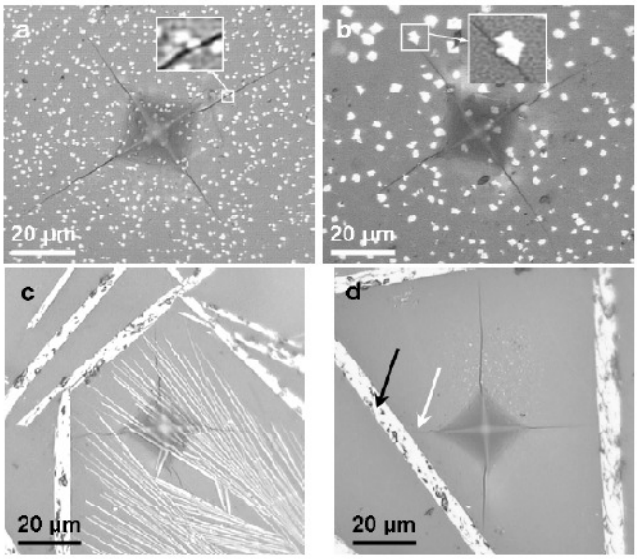

Figure II.13: Optical micrographs of indentation-induced radial cracks from the two different compositions in the Fe_2O_3-PbO-SiO_2-Na_2O composition, indicating ((a) and (c)) transgranular and ((b) and (d)) intergranular propagation. Enlarged photos showing transgranular and intergranular fracture events are shown as insets in figures (a) and (b), respectively [Ch,07].

As seen in Figures II.13a and II.13c , when the crystal size is 0.5µm, the cracks propagate in straight lines independent of the crystal/glass interface position. As a result, the crack propagation is transgranular. When the mean crystal size increases to 3µm, the cracks propagate in curved shapes as shown in the insert Figure II.13b due to the large crystal size. This behavior is thought to inhibit the crack propagation. The crack is hence deflected from the interface, demonstrating an integranular crack mode (Figures II.13b and II.13d) [Ch,07]. Figure II.14 presents the extent of the crack propagation as a function the mean size of the $Pb_8Fe_2O_{11}$ crystals. The extent of the crack was measured as follows: "it is the strength length of the straight line that connects the corner of the Vickers indentation print (from where the crack has emanated) with the crack tip" [Ch,07]. The sample under investigation is the granular crystal containing glass-ceramic.

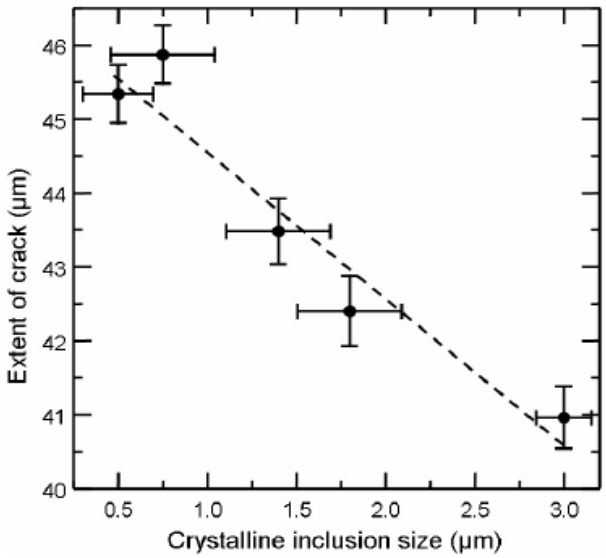

Figure II.14: Extend of crack propagation as a function of mean size of $Pb_8Fe_2O_{11}$ crystalline inclusions for both transgranular and intergranular fractures modes [Ch,07].

The increase of the mean crystal size leads to a decrease of the crack length. Not only is the size of the crystals of great importance, but the volume of glass crystallized can also play an important role on the mechanical properties of the glass-ceramic.

Unfortunately, only a few studies have been focused on the impact of the percent crystallinity on the optical and mechanical properties of the subsequent glass-ceramic. Thompson and Hench demonstrated that when the crystalline phase is produced in a Bioglass matrix, a glass-ceramic with a wide range of glass crystallized volume fraction can be obtained [Th,98]. In [Th,98], a crystal with the composition $Na_2Ca_2Si_3O_9$ was formed in a Bioglass. The strength, the elastic modulus and the fracture toughness changes were studied as a function of volume fraction of the subsequent glass-ceramic. Variation in those mechanical properties induced by crystallization of the glass are presented in Figure II.15 a and b [Th,98].

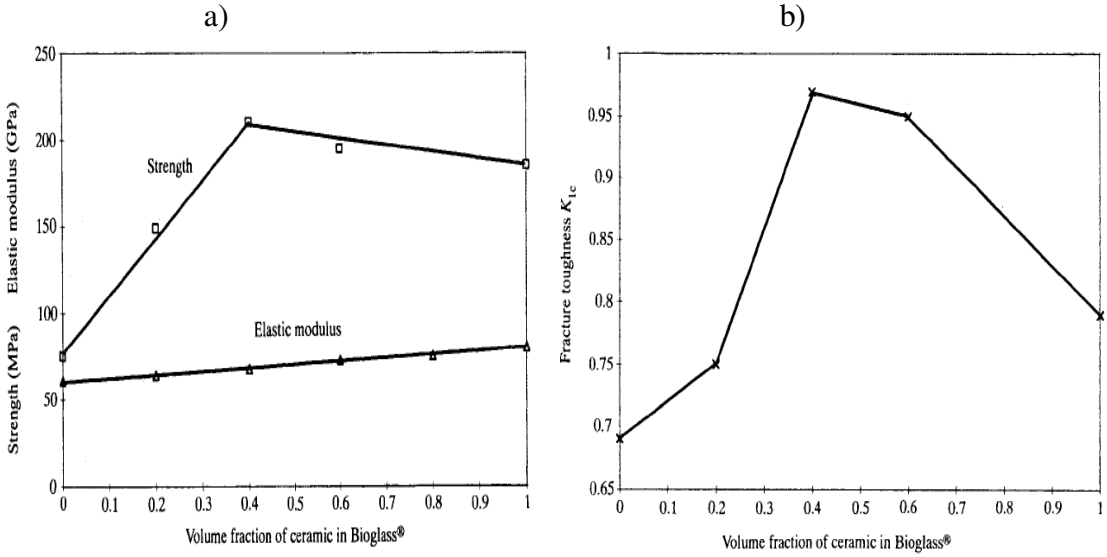

Figure II.15: (a) Strength and elastic modulus and (b) fracture toughness properties of ceramic phased bioactive glass [Th,98].

As seen above, the elastic modulus can be slightly enhanced with crystallization and shows a linear dependence, while the strength and the fracture toughness exhibit a maximum for a volume fraction of ceramic of about 0.4. This study showed that not only is the size of the crystals important, but the volume of crystal in the glassy matrix must be controlled in order to enhance the mechanical properties of the glass system.

II.4 Optical fibers for mid-IR applications

II.4.1 Introduction to optical fibers

In 1952, the physicist Narinder Singh Kapany (father of the optical fiber), based on studies conducted by English physicist John Tyndall that the light could travel in curve inside a material (in Tyndall's experiment this material was water), invented the first optical fiber. In the 1950s and 1960s, the best existing fibers could carry detectable light only on a few meters. [http://www.hardwaresecrets.com/article/154]. A significant breakthrough occurred at Corning Glass in 1970, where researchers adapted chemical vapor deposition techniques for making bulk fused silica to making high-purity silica fibers that had the required physical and chemical characteristics for practical optical transmission. Maturation of the technology occurred in the mid- to late-1980s. The initial focus on reducing sources of light loss in the fibers was broadened to include improvements in the strength and durability of the fibers, and in related technologies, especially fiber coating, splicing, cabling techniques and cable connectors. In 1970, the Corning research team demonstrated the first optical fiber with loss less than 20 dB/km [http://www.sri.com/policy/csted/reports/sandt/techin2/chp3.pdf]. By 1984, attenuation figures had dropped to 0.20 dB/km in mass-produced fibers (0.16 dB/km in the laboratory) due to improved fabrication techniques which reduced impurities. It also stemmed from the development of supporting technologies (e.g., lasers, detectors, and other components) that operated at higher frequencies where intrinsic loss in silica fibers was lowest. [http://www.sri.com/policy/csted/reports/sandt/techin2/chp3.pdf]

In optical fibers, light is used to transfer information. At one end of the cable is the light source, which is often an LED (Light Emitting Diode) or a semiconductor laser. In general the LEDs are used to transfer data up to 300 Mbps but only over short distances. Lasers are more often used to transfer data with a rate of few Gbps in long distance communications. The light used in optical fibers has typically a wavelength of 1.55μm but optical fibers have a wide wavelength range in which the light can be transferred. The table below defines the diverse bands that can be identified as a function of the wavelength applied in the optical fibers.

Table II.2: Spectral bands as a function of wavelength.

Band	Descriptor	Range (nm)
O band	Original	1260 to 1360
E band	Extended	1360 to 1460
S band	Short wavelength	1460 to 1530
C band	Conventional	1530 to 1565
L band	Long wavelength	1565 to 1625
U band	Ultralong wavelength	1625 to 1675

The fundamental principle behind the use of optical fibers is a physical phenomenon called *total internal reflection*. Total internal reflection is an optical phenomenon that occurs when a light wave enters a medium with a refractive n_1 and hits the interface between this medium and the surrounding medium with refractive index n_2 with $n_2<n_1$. The light must enter the core of the fiber with an angle below the critical angle defined as the maximum angle the light can enter the core without going through

the interface. In this case, the light "bounces" off the interface and remains confined in the core material. The critical angle depends on the refractive index n_1 and n_2 as shown by the following equation [Wa,02]:

$$\theta_c = \arcsin\left(\frac{n_2}{n_1}\right) \qquad \text{eq. II.42}$$

An optical fiber typically has two areas, a center region called the core, where the light passes through, and an external region called cladding which covers the core. A schematic of core-clad optical fibers is presented in Figure II.16

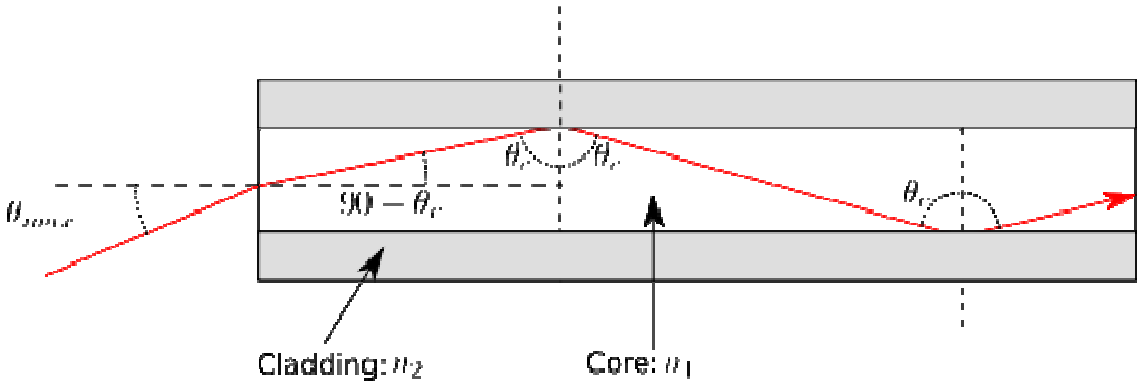

Figure II.16: Anatomy of an optical fiber.

There are two different types of optical fibers, the multimode and the single-mode fiber. *Multimode fibers* rely on the geometric optic. In multimode fibers, the core diameter is typically on the order of ~60 μm, allowing the light to have several propagation modes, i.e. the light goes through the fiber core using several paths. The number of modes that multimode step-index fibers propagate depends on Δn, the difference between n_1 and n_2, and the core radius of the fiber. The number of propagating modes, m, also depends on the wavelength, λ, of the transmitted light and can be estimated using the following equation:

$$m \approx \left(\frac{NA * d}{\lambda} \right)^2 \qquad \text{eq. II.43}$$

where d is the diameter of the core and NA the numerical aperture of the fiber

Multimode fibers can be classified into graded-index and step-index, depending on the refractive index variation between the core and the cladding. The graded-index fibers demonstrate a gradual change between the core and the cladding refractive index. This causes light rays to bend smoothly as they approach the cladding, rather than reflecting abruptly from the core-cladding boundary. The resulting curved paths reduce multi-path dispersion as high-angle rays pass more through the lower-index periphery of the core, rather than the high-index center. In a step-index fiber, this change in index is more abrupt. Step-index fibers can transmit information up to 50 Mbps, while grade-index fibers can transmit data up to 1 Gbps.

Single-mode fibers are used in long-distance cables. The light has only one way (a single mode) of travelling inside the fiber core. The core diameter is between 7 and 10 microns and its cladding diameter is around 125 microns in the case of silica fiber. [http://www.hardwaresecrets.com/article/154].

II.4.2 Losses in optical fibers

Losses in glasses for optical applications can primarily be attributed to absorption, Rayleigh scattering and bending loss [Bu,04].

Losses due to absorption

Any impurities that remain in the glass after the processing can absorb some of the optical energy, leading to an increase in the absorption of the fibers. Among the most

important source of impurities are the hydroxyl group and trace metals. Hydroxyl groups, as characterized by the OH- anion, which, when present in glass, leads to large losses at 1380nm. The fundamental stretching resonance of OH is centered between 2.7 and 3μm, but the position of the OH absorption band depends greatly on the glass composition. The OH vibrational mode is slightly anharmonic, which leads to oscillation components at overtone frequencies. In the case of silicate glasses, loss minima occur at 1.3 and 1.55 μm.

The incorporation of water in the structure of glass decreases the transformation temperature and the transformation range viscosity [Je,88]. In oxide glasses, it is often assumed that OH groups act as alkali or alkaline earth metal ions by terminating the polymeric chains of the glass network [Sh,76]. OH groups exist in the glass network as non-bonded (i.e free OH) and non-bridging oxygens [Ka,99]. It is well known that the physical properties are influenced by the structure of the glass, thus it is crucial to control the OH content of the glass network and consequently the physical and optical properties of the material [Ga,97]. In optical fibers, loss arising from OH is the most difficult extrinsic loss contributor to remove. OH enters the glass through water vapor [Ka,99], the main pathways are thermal diffusion, contamination in the reactant chemicals and contact of the melting batch with the outside environment. In a similar way, traces of metallic or transition metal species can cause absorption of energy at their own particular wavelengths.

Losses due to Rayleigh scattering

The second main source of loss in optical fibers is Rayleigh scattering of light induced by small localized changes in refractive index of the material. The main reasons for the Rayleigh scattering are i) the inevitable slight fluctuation in the glass composition and ii) the different cooling rates in the bulk material when the supercooled liquid cools down to form the glass. In the case of a core-clad fiber, when the light interacts with those areas with different refractive indices, the light is scattered. The light that is now travelling with an angle below the critical angle is lost. The amount of scattering center depends on the size of the discontinuity as compared to the wavelength of the propagated light. The shortest wavelength being propagated, possessing the highest frequency is the most influenced by the scattering centers [Bu,04].

Losses due to bending loss

Bending optical fiber also causes attenuation. Bending loss is classified according to the bend radius of curvature: microbend loss or macrobend loss. *Microbends* are small microscopic bends of the fiber axis that occur mainly when a fiber is cabled whereas m*acrobends* are bends having a large radius of curvature relative to the fiber diameter. Microbend and macrobend losses are very important loss mechanisms. Fiber loss caused by microbending can still occur even if the fiber is cabled correctly. During installation, if fibers are bent too sharply, macrobend losses will occur. Microbend losses are caused by small discontinuities or imperfections in the fiber. Uneven coating applications and improper cabling procedures increase microbend loss. External forces are also a source of microbends. An external force deforms the cabled jacket surrounding the fiber but causes

only a small bend in the fiber. Microbends change the path that propagating modes take. Microbend loss increases attenuation because low-order modes become coupled with high-order modes that are naturally lossy. Macrobend losses are observed when a fiber bend's radius of curvature is large compared to the fiber diameter. These bends become a great source of loss when the radius of curvature is less than several centimeters. Light propagating at the inner side of the bend travels a shorter distance than that on the outer side. To maintain the phase of the light wave, the mode phase velocity must increase. When the fiber bend is less than some critical radius, the mode phase velocity must increase to a speed greater than the speed of light in the material. However, it is impossible to exceed the speed of light. This condition causes some of the light within the fiber to be converted to high-order modes. These high-order modes are then lost or radiated out of the fiber. Fiber sensitivity to bending losses can be reduced. If the refractive index of the core is increased, then fiber sensitivity to bending decreases. Sensitivity also decreases as the diameter of the overall fiber increases. However, increases in the fiber core diameter increase fiber sensitivity. Fibers with larger core size propagate more modes. These additional modes tend to be more lossy.

II.4.3 Fiber processing

Standard optical fibers can be processed by constructing a large-diameter preform, with a carefully controlled refractive index profile which is then pulled to form the long, thin optical fiber. In this section, we list the main techniques used to process a core-clad preform which is then drawn into monomode or multimode fibers.

Preforms via Vapor Deposition

A hollow glass tube approximately 40 cm in length known as a "preform" is placed horizontally and rotated slowly on a lathe, and gases such as silicon tetrachloride ($SiCl_4$) or germanium tetrachloride ($GeCl_4$) are injected with oxygen at the end of the tube. The gases are then heated by means of an external hydrogen burner, bringing the temperature of the gas up to 1900°C, where the tetrachlorides react with oxygen to produce silica or germania (germanium oxide) particles. When the reaction conditions are chosen such that this reaction occurs in the gas phase throughout the tube volume, this technique is called *modified chemical vapor deposition* in contrast to techniques in which the reaction occurs only on the glass surface. The oxide particles then agglomerate to form large particle chains, which are subsequently deposited on the walls of the tube as soot. The torch is then traversed up and down the length of the tube to deposit the material evenly. After the torch has reached the end of the tube, it is then brought back to the beginning of the tube and the deposited particles are then melted to form a solid layer. This process is repeated until a sufficient amount of material has been deposited. For each layer, the composition can be varied by varying the gas composition, resulting in precise control of the finished fiber's optical properties.

In *outside vapor deposition* or vapor axial deposition, the glass is formed by *flame hydrolysis*, a reaction in which silicon tetrachloride and germanium tetrachloride are oxidized by reaction with water (H_2O) in an oxyhydrogen flame. The glass is deposited onto a solid rod, which is removed before further processing.

In vapor axial deposition, a short *seed rod* is used, and a porous preform, whose length is not limited by the size of the source rod, is built up on its end. The porous

preform is consolidated into a transparent, solid preform by heating to about 1800°C. The preform is then placed in a *drawing tower*, where the preform tip is heated and the optic fiber is pulled out as a string. The tension on the fiber can be controlled to maintain the fiber thickness. This manufacturing process is accomplished by numerous optical fiber companies like Corning, Draka, OFS, Sterlite Optical Technologies, Furukawa, Sumitomo, Fujikura and Prysmian.

Preforms via Melting processes

Extrusion

The principle of this process is to press the core melt into the cladding melt. The core glass cylinder is above the clad cylinder in a sleeve. Both are heated until the softening glass temperature and a pressure is applied. A cane with a core-clad structure is extruded by the clad die hole as shown in Figure II.17. The extruded cane is used as a core-clad perform [Le,07].

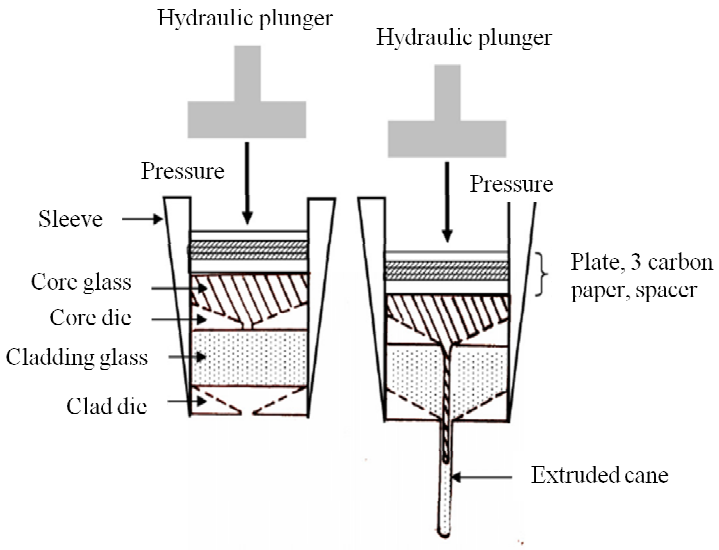

Figure II.17: Extrusion process

Build in casting

This process has been specially developed for fluoride glass fibers. Figure II.18 shows the 3 steps of the process. First, the cladding-glass is quenched in a mold preheated to around the glass transition temperature and immediately turned over. Finally, the coring melt is quenched in the cylindrical hollow in the middle of the mold [Mi,83].

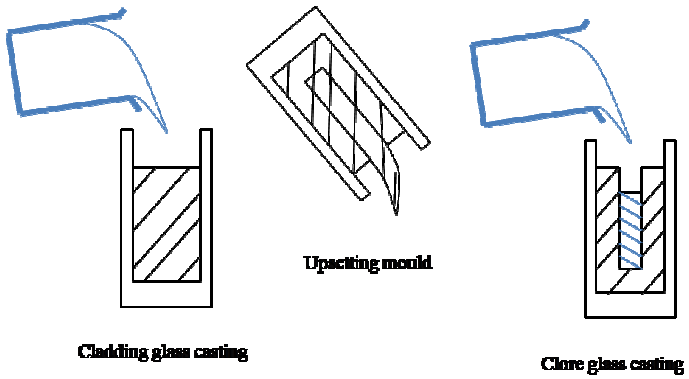

Figure II.18: Sequence of steps required for the build-in casting of preform.

Crucible method

Core raw material powder or bulk glass is inserted in an ampoule sealed at the bottom used as a clad. Figure II.19 shows the ampoule used as a crucible. The sealed ampoule with powder is then heated in a high temperature furnace to get a core-clad preform and finally drawn into a fiber.

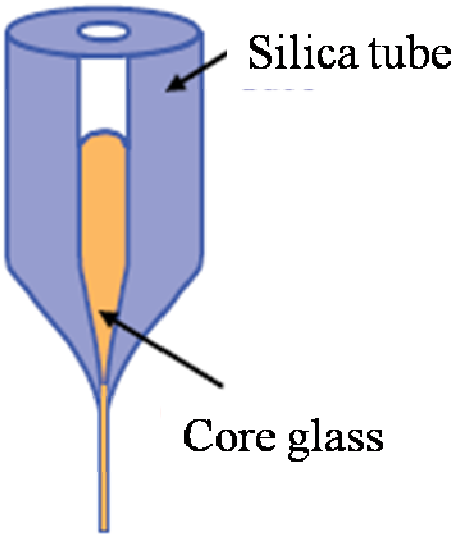

Figure II.19: Crucible method [Go,05].

Rod in tube

The clad is a glass rod drilled through its center. The core is a glass cylinder prepared separately with the same radius as that of the hole in the clad. The first step is to draw a fiber from the two separate core and clad. Then this first fiber is used as new core to draw a new fiber. On this second fiber, the new clad is the same glass than the clad used previously. The modified crucible drawing method is used to draw optical fibers with preforms obtained from this rod in tube technology [Ji,00].

Core suction

This process requires a previously prepared glass tube which will be used as the cladding tube. The core glass raw material powder is melted in a crucible. The molten

core glass is then drawn due to a vacuum pump in the cladding tube to form the core-clad preform as shown in figure II.20.

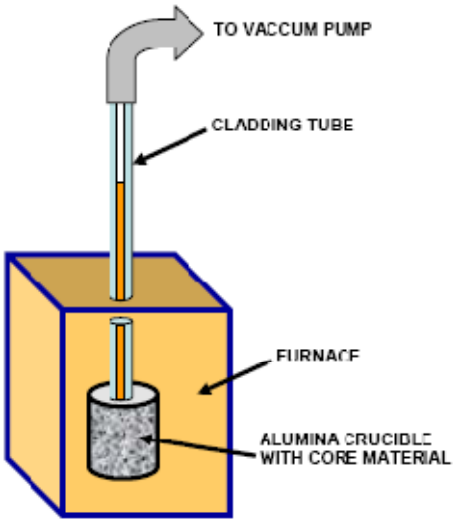

Figure II.20: Core suction method.

Rotational caster

The core-clad preforms processed at Clemson University for this study have been obtained using a rotational caster (Figure II.21).

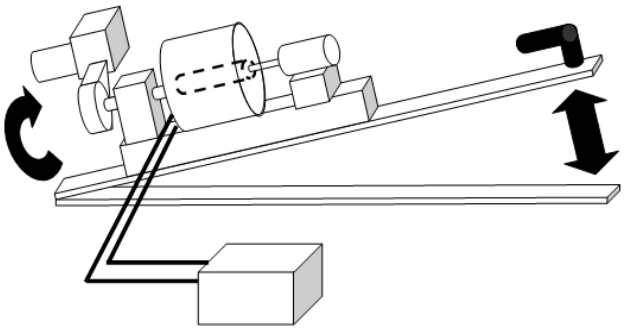

Figure II.21: Rotational Casting Rig

This process is based on individual preparation of both core and cladding composition melts. The first stage consists of preheating the mold in the furnace. When

the cladding melt is ready, the table is lifted up vertically and the glass is cast into the mold. The table is then quickly turned horizontally and the mold is spun for few seconds. After waiting for few minutes, the table is turned vertically and the core is cast slowly into the mold. The mold is held vertically for few seconds to solidify the core glass and is finally turned horizontally for annealing as illustrated below

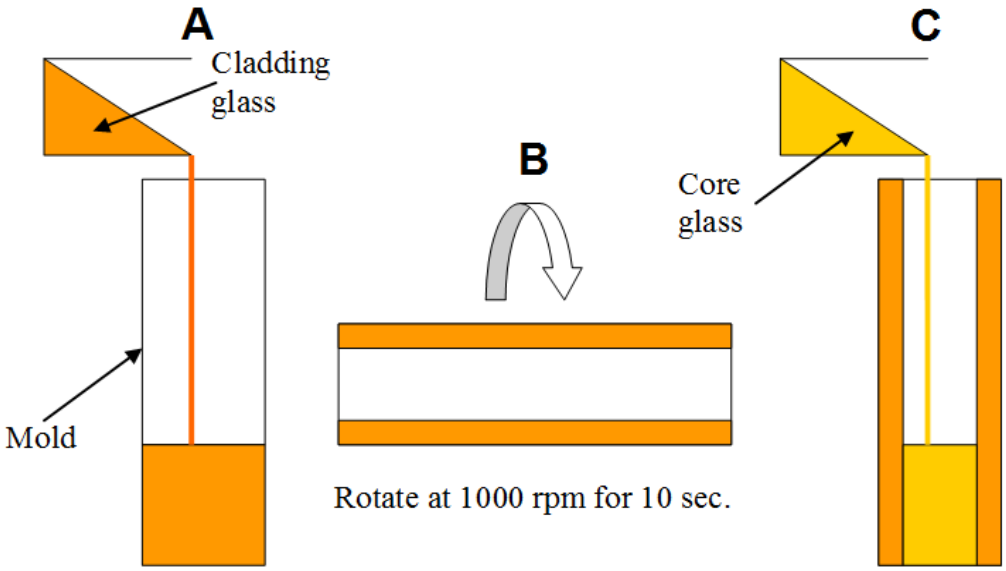

Figure II.22: Sequence of steps required for the rotational casting of preforms.

Direct core-clad fiber drawing process

Core-clad optical fibers can be drawn with a similar process than core fibers like the modified crucible drawing method shown in Figure II.23a. This process uses separate core and clad pieces. The core is placed inside the clad and both are preheated to the glass softening temperature under an argon gas controlled atmosphere. Figure II.23b presents the double crucible drawing method: this facility uses two concentric tubes for the molten core clad [Le,98].

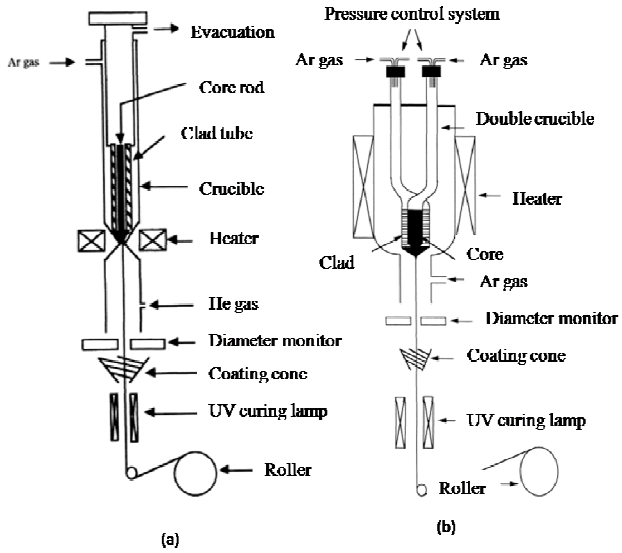

Figure II.23: (a) Draw tower: modified crucible method and (b) double crucible drawing method.

Different core-clad ratios can be obtained according to the gas pressure which can be independently controlled, within each part of the tube.

II.4.4 Currently available IR fibers

Infrared optical fibers transmitting in the 2-5 μm spectral region are highly desirable for a variety of military and civilian applications. A summary of the most important current and future applications and the associated candidate IR fiber that will best meet the need is given in Table II.3.

Table II.3: Examples of infrared fiber candidates for various sensor and power delivery applications [http://irfibers.rutgers.edu/it_rev_intro.html]

Application	Comments	Suitable IR fibers
1. Fiber optic sensors	Evanescent wave principle - liquids	AgBrCl, sapphire, chalcogenide, HMFG
2. Fiber optic chemical sensors	Hollow core waveguides - gases	Hollow glass waveguides
3. Radiometry	Blackbody radiation, temperature measurements	Hollow glass waveguides, AgBrCl, chalcogenide, sapphire
4. Er:YAG laser power delivery	3 μm transmitting fibers with high damage threshold	Hollow glass waveguides, sapphire, germanate glass
5. CO_2 laser power delivery	10 μm transmitting fibers with high damage threshold	Hollow glass waveguides
6. Thermal imaging	Coherent bundles	HMFG, chalcogenide
7. Fiber amplifiers and lasers	Doped IR glass fibers	HMFG, chalcogenide

Silica fibers

Most research projects have been focused on silica-based fibers, as these glasses are easy to process, specifically for optical fibers that carry large volumes of information transmitted by lasers. The silica glass structure exactly follows the Zachariasen rules [Sh,05]. SiO_4 tetrahedra are hence the main structural units [Ta,94]. The tetrahedra serve as building blocks in the network. This statement answers the second basic Zachariasen's rules. The tetrahedrons are linked at all 4 corners as required by the third and fourth basic Zachariasen's rules. This block building leads to 3D network. Due to the position of the oxygen in the structure and the valence of this one, oxygen are shared with 2 silicon atoms. The SiO_2 structure can be represented in 2-D as shown in Figure II.24:

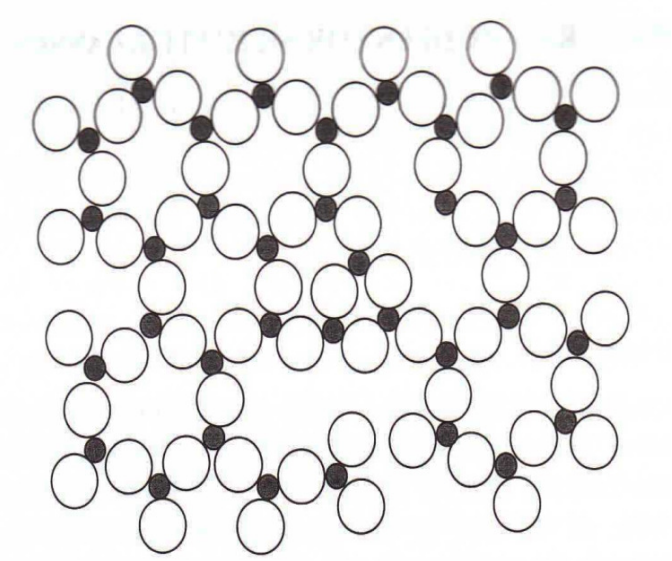

Figure II.24: Schematic drawing of a 2-dimensional structure for a SiO_2 glass [Sh,05]

Absorption losses in silicate-based fiber occur strongly both in the ultraviolet and infrared regions. Both UV and IR absorption mechanism exert residual effects in the visible and near infrared domain, and together with the scattering discussed in section II.4.2 produce a fundamental lower limit to the attenuation of silica fiber [Gr,98]. The lowest predicted value of this limit occurs near λ=1.55μm and is ~0.15dB/km for lightly doped silica [Gr,98]. Thus, an alternative has to be found to extend the spectral range where fibers can be used.

Fluoride fibers

Poulain et al. discovered the fluoride glasses accidentally in 1975 at the University of Rennes in France [Po,77]. In general, the typical fluoride glass has a lower glass transition temperature, T_g, than that of silica glass; is considerably less stable; and has failure strains of only a few percent compared to silica's greater than 5% [Po,77]. Also the temperature range for drawing fluorides is extremely small compared to the

drawing temperature for silicate fibers. Hence, even though numerous multicomponent fluoride glasses have been produced, only a few of these compositions have been drawn into fibers. The most popular heavy metal fluoride glasses for fabrication into fibers are the fluorozirconate and fluoroaluminate glasses of which the most common are ZBLAN (ZrF_4-BaF_2-LaF_3-AlF_3-NaF) and AlF_3-ZrF_4-BaF_2-CaF_2-YF_3, respectively. In fact, a perfect ZBLAN glass should transmit light near the theoretical minimum. Its attenuation coefficient can be as low as 0.001 dB/km, far less than silica's 0.2 dB/km. However, production problems now limit the best ZBLAN fibers to an attenuation coefficient of 10 dB/km or higher. Indeed the ZBLAN tend to crystallize during stretching of the fiber. The crystals act as mirrors, reflecting and bending the light [http://spacescience.spaceref.com/newhome/headlines/msad05feb98_1.htm]. Figure II.25 shows the loss recorded in a ZBLAN fiber as compared to the theoretical and silica fiber loss.

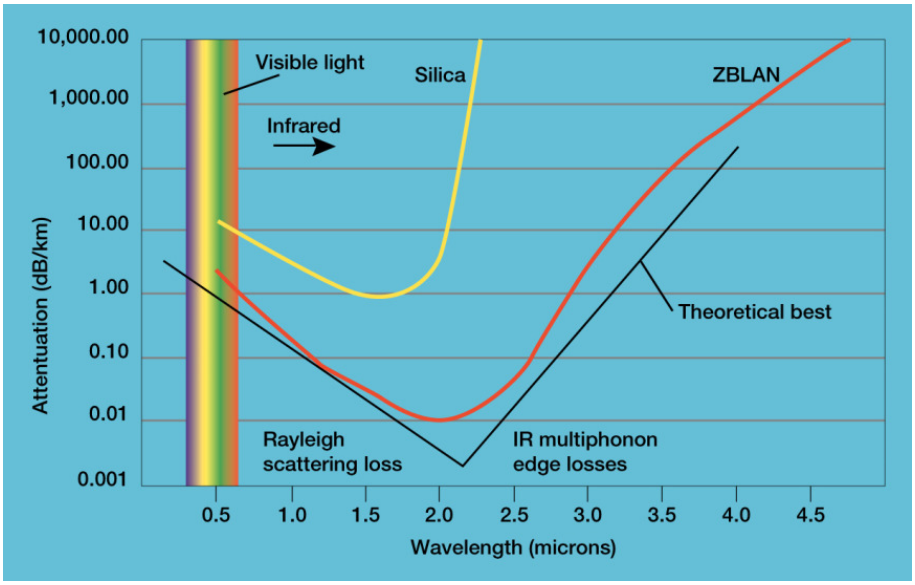

Figure II.25: Comparison of ZBLAN loss as a function of wavelength as compared to the theoretical and silica glass fiber loss [http://spacescience.spaceref.com/newhome/headlines/msad05feb98_1.htm].

Based on the extrapolations of the intrinsic losses resulting from Rayleigh scattering and multiphonon absorption, the minimum in the loss curves, or V-curves, is projected to be about 0.01 dB/km at 2.55 μm. Recent refinements of the scattering loss have modified this value slightly to be 0.24 dB/km or about 8 times lower than that for silica fiber, but still much higher than the theoretical minimum [Ca,90] In practice, extrinsic loss mechanisms still dominate fiber loss. The lowest measured loss obtained at British telecom on a 60-m-long fiber is 0.45 dB/km at 2.3 μm. The total minimum attenuation coefficient (0.65 dB/km at 2.59 μm) can be separated into an absorptive loss component equal to 0.3 dB/km and a scattering loss component equal to 0.35 dB/km. The challenge on this glass composition has been to reach the theoretical minimum absorption. However ZBLAN tends to crystallize, so long stretches cannot be drawn for communications fibers.

Germanate fibers

Heavy metal oxide glass fibers (HMFG) based on GeO_2 have recently shown great promise as an alternative to currently employed fibers for 3 μm laser power delivery [Ko,78]. The oxide germanate glasses have glass transition temperatures as high as 680^{o}C, good durability, and a relatively high refractive index of 1.84 (compared to silicate). GeO_2-based glass fibers are often composed of GeO_2 (30-76%) - RO (15-43%) - XO (3-20%) where R is an alkaline-earth metal and X an element of Group IIIA [Tr,93]. In Figure II.26, the loss V-curve is shown for a typical germanate glass fiber.

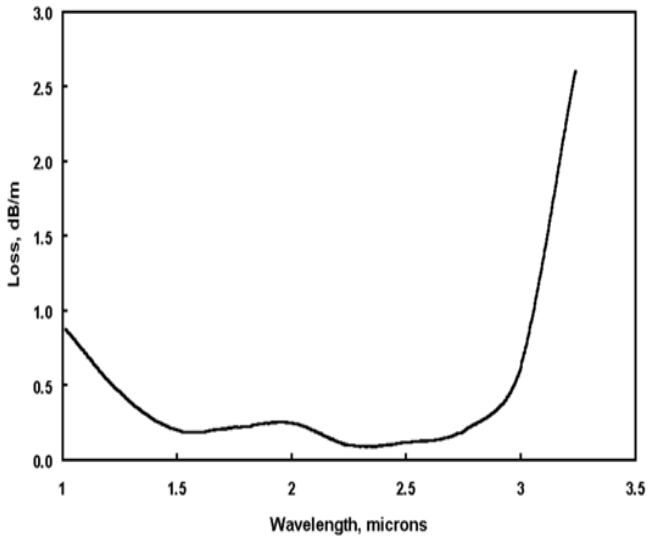

Figure II.26: Germanate glass fiber manufactured by Infrared Fiber Systems, Silver Spring, MD.

Even though the losses of the germanate fibers are not as low as losses in the fluoride glass fibers, they demonstrate a high damage threshold in the 2-3μm range. A power of ~20W has been launched into these fibers using a Er:YAG laser [Wa,02].

Chalcogenide fibers

The first chalcogenide glass fibers were drawn into essentially the first IR fiber in the mid 1960s [Ka,65]. Chalcogenide fibers fall into three categories: sulfide, selenide, and telluride [Ka,84]. One or more chalcogen elements are mixed with one or more elements such as As, Ge, P, Sb, Ga, Al, Si, etc. to form the glass. Chalcogenide glasses demonstrate low softening temperatures, which are more comparable with fluoride glasses than silica-based glasses. They are stable, durable, and insensitive to moisture. Even though they have an excellent transparency up to ~14μm in the case of selenide glass, they do not transmit light efficiently in the visible region. Arsenic trisulfide (As_2S_3) fiber, one of the oldest chalcogenide fibers, has a transmission range from 0.7 to about 6

μm [Ka,84]. The red coloration of this glass inhibit the transmission of light passes the 600nm wavelength. Additionally, most of the chalcogenide glasses, except for As_2S_3, have a rather large value of dn/dT [Ni,92]. This fact limits the laser power handling capability of the fibers. In general, chalcogenide glasses fibers have proven to be excellent candidates for evanescent wave fiber sensors and for IR fiber image bundles [Ni,92b]. The loss of two typical chalcogenide glass fibers is presented in Figure II.27.

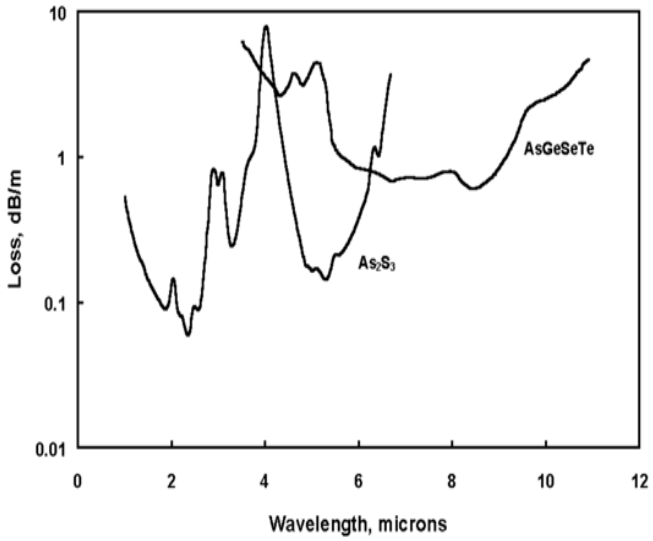

Figure II.27: Two common chalcogenide glass fibers: As_2S_3 and an AsGeSeTe fiber [Ni,92].

A key feature of almost all chalcogenide glasses is the strong extrinsic absorption resulting from contaminants such as hydrogen, H_2O, and OH bonding to the elemental cations [Wa,02]. The absorption peaks between 4.0 and 4.6 μm are due to S-H or Se-H bonds and those at 2.78 μm and 6.3 μm are due to OH (2.78μm) and/or molecular water. The hydride impurities are an issue due to the fact that in chemical sensing applications, the desired chemicals signature falls in the region of the extrinsic absorption of the fiber. Another important feature of most of the chalcogenide fibers is that their losses are in general much higher than the fluoride glasses. In fact at the important CO_2 laser

wavelength of 10.6µm, the lowest loss is still above 1 dB/m for the Se-based fibers [Ka,84]

Some of the optical and mechanical properties of the most common IR fibers are listed in Table II.8.

Table II.4: Selected physical properties of key IR fibers compared to conventional silica fiber [http://spie.org/x33604.xml].

Property	***Silica***	***ZBLAN***	***Germanate***	***Chalcogenide AsGeSeTe***
Glass transition or melting point, ^{o}C	1175	265	704	245
Thermal conductivity, W/m K	1.38	0.628	0.6	0.2
Thermal expansion coefficient, $10^{-6}K^{-1}$	0.55	17.2	9.6	15
Young's modulus, GPa	70.0	58.3	63.4	21.5
Density, g/cm^3	2.20	4.33	4.8	4.88
Refractive Index (λ, µm)	1.455 (0.70)	1.499 (0.589)	1.69 (3.80)	2.9 (10.6)
dn/dT, 10^{-5} K^{-1} (λ, µm)	+1.2 (1.06)	-1.5 (1.06)	+7 (3.8)	+10 (10.6)
Fiber transmission, range, µm	0.24-2.0	0.25-4.0	0.3-5	4-11
Loss* at 2.94 µm, dB/m	~800	~0.08	~0.9	~5
Loss* at 10.6 µm, dB/m	N/A	N/A	NA	2

The table above shows that fibers for application in the mid-infrared and infrared have higher loss, greater refractive indices and coefficient of thermal expansion. This means that the reflection or Fresnel loss exceeds 20% for two fiber ends. The higher

dn/dT and low melting or softening point leads to thermal lensing and, as a result, low laser-induced damage thresholds for the solid-core IR fibers [http://spie.org/x33604.xml].

II.4.5 Heavy metal oxide tellurite-based fibers

Heavy metal oxide (HMO) glasses containing TeO_2, PbO, Ga_2O_3 and Bi_2O_3 are known to have a good transparency in the visible and near infrared regions and high refractive indices [Wi,98] [Ru,92] [Mo,97b]. They exhibit moderate melting points as compared to silicate-based glasses, low glass transition temperatures, high dielectric constants and can be engineered with sufficient crystallization stability to be suitable for fiberization [El,92] [Ki,93] [El,00]. The successful fabrication of a single-mode Nd^{3+}-doped tellurite fiber laser in 1994 [Wa,94b] and the demonstration of a broadband Er^{3+}-doped tellurite fiber amplifier by the NTT opto-electronic group in 1997 [Mo,97] has led to extensive research activity in the use of tellurite-based glasses for a range of optical applications [El,00] [Wa,06]. The tellurite's resistance to moisture provides a better reliability than fluoride glass in telecommunication applications [El,00]. Recently, a tellurite fiber used by NTT opto-electronics was reported to have loss as low as 0.1dB/m which makes tellurite fibers promising materials for MIR optical applications [www.net-world.com].

The traditional view of the structure of glassy TeO_2 as a distorted lattice of the crystalline paratellurite phase α-TeO_2 has been challenged by the discovery of a new crystalline phase which is γ-TeO_2 [Bl,99]. Through MAS-NMR of ^{123}Te, it was found that the structure of the glass is constituted of TeO_m units where the tellurium atom can

be tetracoordinated (coordination number m=4) or three fold (m=3) [9-Sakida]. These structures have been denoted using the notation Q_n^m where m is the number of bonded O ions and n the number of bonded O ions bonded also to Te ions [Pi,08]. The different possible structure found in TeO_2 glasses are shown below:

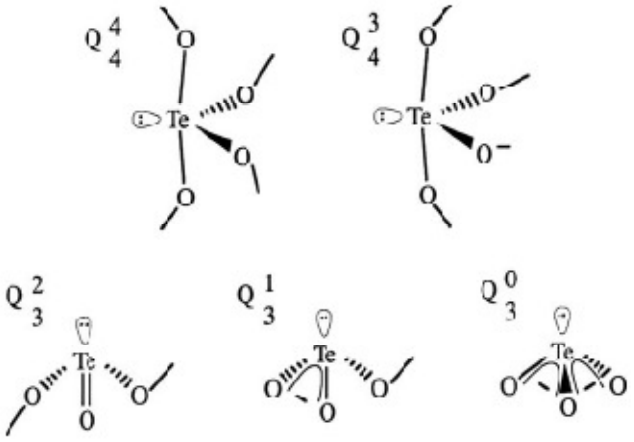

Figure II.28: Coordination polyhedra Q_m^n of Te atoms found in tellurite crystals, with m=number of bonded O atoms and n=number of bridging O atoms.[Pi,08]

Unlike silicate glasses, TeO_2-based glasses are composed of low-symmetry structural units such as TeO_4 trigonal bypyramids and TeO_3 trigonal pyramids [Ta,94]. A common representation of the TeO_2-based glass structure is illustrated in Figure II.29:

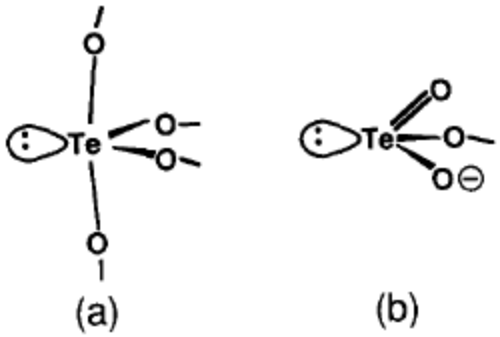

Figure II.29: (a) Structure of the TeO_4 trigonal bipyramid and (b) the TeO_3 trigonal pyramid in tellurite glasses [Ta,94]

In the TeO_4 units one equatorial site of the Te sp^3d orbitals is occupied by a lone pair electron and the two equatorial and axial sites are bonded to two oxygen atoms while in the case of TeO_3 units one of the Te sp^3 orbitals is occupied by lone pair electrons [Ta,94]. Addition of a modifier such as Bi_2O_3 or intermediates such as ZnO has leads to polymerization of the glass by creating chain-like structures of Te-O-Te increasing the tendency of glass formation [O'Do,04].

Recently, Hill and Jha showed promising results on TeO_2-BaO-Bi_2O_3 glass fibers [Hi,07]. They showed that glasses in the TeO_2–BaO–Bi_2O_3 system have a wide ranging stable glass forming region, displaying very little crystallization. These glasses have comparably high T_g values with respect to the other tellurite glasses and may be candidates for higher temperature applications (above 200^{o}C). They also have viscosities suitable for fiber drawing which lie well outside the crystallization temperature range, indicating that these glasses may be candidates for fiber drawing [Hi,07]. From the UV and IR edge data, the researchers concluded that the introduction of heavier compounds such as Bi_2O_3 in the tellurite glass structure has a limited effect on increasing the IR edge cut off to longer wavelengths, although there was a marked change in the total loss minimum, shifting it to longer wavelengths. The refractive index results showed that a wide range of refractive indices can be achieved within this glass system, ranging from 2.01 to 2.16, which indicates that this glass may be suitable for core clad structured fiber fabrication [Hi,07].

The study of the glasses in the TeO_2–Bi_2O_3–ZnO system by Youssef et al., showed high linear refractive indices in the range of 2.1–2.25 [Yo,07]. The experimental

Kerr susceptibility is in the range of 5.49–6.58×10^{-13}esu increasing with increasing Bi_2O_3 concentration. The glasses showed optical band gap energies in the range from 2.57 to 2.63eV and Urbach energies between 0.054 and 0.066eV. Youssef et al have reported that both optical band gap and Urbach energy are smaller than for other glass systems reported in the literature up to now revealing low defect concentrations in the glasses [Yo,07].

II.5 Main goal of the proposed work

While a large amount of research has been performed for mid-infrared optical applications, such as that shown in the previous sections, room for improvement still remains. New tellurite glass compositions for chemical sensing, lens or optical fiber applications are still needed. Furthermore, the impacts of controlled crystallization in tellurite-based glasses have not been extensively studied. To date, only a few papers have been published on the nucleation and growth behavior of tellurite-based glasses. Of major importance and special relevance to the present study here are the articles by Joshi et al and Oz et al.

- Joshi et al discussed the crystallization kinetics of the (x Na_2O - (100-x) TeO_2) glasses and the overall activation energies for the crystallization processes was measured to be in the range 190-240 kJ/mol [Jo,07]. The crystallized phases formed upon heat treatment of these glasses were identified by XRD. The partial T-T-T curves were derived from the JMA analysis. A new Na_2O 8 TeO_2 (NT8) crystal phase was observed when the sodium tellurite glass was heat treated above 600 K. Controlled heat treatment

of sodium tellurite glass was found to yield transparent glass-ceramics which exhibit the effects of line broadening from 80 nm to 130 nm [Jo,07].

- Oz et al. showed that an increase of the K_2O content in the binary $(1-x)TeO_2–xK_2O$ (x = 0.05, 0.10, 0.15, and 0.20 in molar ratio) glasses decreases the glass transition temperature, T_g. Further, the crystallization of these glasses takes place in the range between 327 and 421°C with one exothermic peak for the $0.95TeO_2–0.05K_2O$ and $0.90TeO_2–0.10K_2O$ glasses and two exotherms for the $0.85TeO_2–0.15K_2O$ and $0.80TeO_2–0.20K_2O$ glasses in the DTA curves [Oz,07]. Using XRD and Raman spectrometry, it was found that the crystalline phases present in the glass after heat treatment are distinct TeO_2-rich and $K_2Te_4O_9$ crystals. The Avrami constant, n, was calculated as 0.94 for the $0.95TeO_2–0.05K_2O$ glass, revealing that surface crystallization is the dominant crystallization mechanism [Oz,07] while the n values were found to vary between 1.7 and 1.87 for the exothermic peaks of the $0.90TeO_2–0.10K_2O$, $0.85TeO_2–0.15K_2O$ and $0.80TeO_2–0.20K_2O$ glasses, indicating that one dimensional growth of crystals (m= 1) is the dominant crystallization mechanism for these glasses. Using the modified Kissinger equation, the activation energy of crystal growth for the $0.95TeO_2–0.05K_2O$ glass was determined as 559.9 kJ/mol. and the activation energies for the other glasses were found to vary between 550 and 650 kJ/mol [Oz,07].

It is important to point out that no evaluation of the nucleation and growth rates nor the impact of the crystal formation on the optical, physical, thermal and mechanical properties have been performed in the studies from Joshi et al and Oz et al. It is of great interest to evaluate the crystallization kinetics in the tellurite-based glasses as well as the

impact of hydroxyl groups and of fiberization on the crystallization kinetics in order to reliably draw crystal-free low loss fiber.

As ternary tellurite glasses show excellent thermal resistance against crystallization when compared to the binary glasses [Ko,95], the tellurite glass composition of interest in the present study focuses on the TeO_2-Bi_2O_3-ZnO ternary glass system. Glasses of similar composition have been found to be of great interest for optical fibers, amplifiers and waveguides. Chung et al provide information on tellurite glass composite including $25(mol\%) \leq TeO_2 \leq 90(mol\%)$, $1(mol\%) \leq T_1O_3 \leq 55(mol\%)$ or $1(mol\%) \leq T_2O_3 \leq 40(mol\%)$, $0(mol\%) \leq ZnO \leq 35(mol\%)$, $0(mol\%) \leq M_2O \leq 35(mol\%)$, and $0(mol\%) \leq Bi_2O_3 \leq 20(mol\%)$, where T_1 includes a transition metal Mo, T_2 a transition metal W, M_2O Li_2O, Na_2O or two or more of Li_2O, Na_2O, K_2O, Rb_2O and Cs_2O including metals having +1 valence electrons and amount of M_2O and ZnO are never simultaneously 0 [Ch,09]. Chung et al. describe a tellurite glass composite able to increase the FWHM of Raman scattering so as to realize a wideband amplifier or a laser using a small number of excitation sources. This invention also provides an optical waveguide using the tellurite composite as core layer. Finally when used as a core layer this tellurite glass composite can be employed as an optical fiber or an optical waveguide [Ch,09]. While glasses in the TeO_2-Bi_2O_3-ZnO glass family is of great interest exemplified by the publication of a new study on the investigation of 2.0 μm emission in Tm^{3+} and Ho^{3+} co-doped TeO_2–ZnO–Bi_2O_3 glasses [Ga,09], no study exists on the crystallization mechanism on performance of optical fibers in this glass composition.

In this study we determined the kinetics of crystallization of glasses in the TeO_2–ZnO–Bi_2O_3 system. Our research focused on the determination of the Johnson-Mehl-Avrami exponent, activation energy and the nucleation and growth rate. Efforts in producing multimode core-clad fibers using a rotational caster are reported and performance of the resultant fibers and the effect of fiberization on the crystallization mechanism are discussed. Finally, we list various techniques to reduce the presence of hydroxyl groups in the glasses under investigation and we discuss the effect of OH content reduction on the nucleation and growth behavior of the tellurite-based glass.

CHAPTER III: GLASS PREPARATION AND DESCRIPTION OF THE CHARACTERIZATION TOOLS USED TO ANALYZE THE GLASSY BULK AND FIBERS.

III.1 Sample preparation

One of the main goals of this research was to define and optimize new glass compositions for mid-infrared applications. In order to achieve this goal a multitude of samples were prepared; attention was focused on those glass families that appeared to be most promising candidates for mid-infrared fibers. Small batches of glass were produced in order to i) assess the thermal mechanical resistance to fracture upon quenching and ii) evidence suitable glass compositions for mid-infrared applications. Glasses which did not crystallize after quenching have been fully characterized and glass candidates for fiber processing were selected upon their promising physical, thermal and optical properties.

Multiple tellurite based glasses in the TeO_2-Bi_2O_3-ZnO system were prepared with the compositions:

i) $(100\text{-}x)TeO_2\text{-}10Bi_2O_3\text{-}xZnO$ (x=15, 17.5, 20 and25),

ii) $(100\text{-}y)\ (0.70TeO_2–0.10Bi_2O_3–0.20ZnO)\text{-}\ yMO$ (MO= Li_2O, BaO and K_2O) (y=2 and 4).

iii) $(100\text{-}y)\ (0.70TeO_2–0.10Bi_2O_3–0.20ZnF_2)\text{-}\ 4BaO$

The raw materials used for the batch preparation were TeO_2 (Alfa Aesar, Tech), Bi_2O_3 (Alfa Aesar, 99%), ZnO (Alfa Aesar, 99%), BaO (Alfa Aesar, 88%), ZnF_2 (Alfa Aesar, 98%), Li_2CO_3 (Fisher, 99.5%), BaO (Alfa Aesar, 99.8%) and KCl (Fisher, 99.6%),

Compositional development was carried out via small test melts. A 7 g mixture of the raw materials was melted in a platinum crucible at 800-850 ^oC, depending on the composition, for 5 minutes. Some glasses were produced using raw materials containing carbonate (CO_3), chloride, (Cl), or fluoride (F) compounds. In order to evaporate these compounds, a pre-treatment of the batch at 400^oC or 450^oC, depending on the raw material to decompose, was performed prior to melting.

The molten glass was quenched on a Pt plate and then annealed for 15h, at 40^oC below the glass transition temperature. After annealing, the glasses were optically polished. All the tellurite glasses exhibited a yellowish coloration.

III.2 Thermal and physical properties

III.2.1 Differential thermal analysis (DTA)

The thermal properties of the investigated glasses were measured using a differential thermal analysis (DTA) calorimeter. The DTA records any difference in temperature between the sample and a reference. The DTA thermogram can be plotted either as $\Delta T=f(T)$ or heat flow=f(T). In our study, the differential thermal analysis was performed using a commercial DTA/TGA SDT 2940 apparatus from TA Instrument Inc. (www.tainstruments.com). The measurements were carried out on finely crushed samples placed in a hermetically sealed aluminum pan, or a platinum crucible when temperatures higher than 550^oC were needed. The glass transition temperature (T_g) and any evidence

of bulk glass crystallization (T_x) were determined at a heating rate of 10°C.min^{-1}. Shown in Figure III.1 is an example of a thermogram obtained for a glass of the composition $70TeO_2$-$10Bi_2O_3$-$20ZnO$.

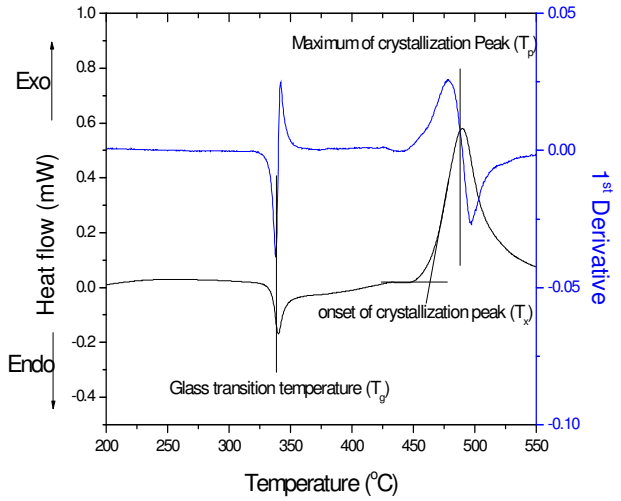

Figure III.1: DTA thermogram of the glass with the composition $70TeO_2$-$10Bi_2O_3$-$20ZnO$

The glass transition temperature (T_g) was taken at the inflection point of the endotherm (obtained by taking the first derivative of the curve), and the crystallization temperature (T_p) at the maximum of the exothermic peak. T_x was defined as the onset temperature of the crystallization peak as illustrated in Figure III.1. The accuracy of the measurement was estimated to be ±2°C.

III.2.2 Thermal mechanical analysis (TMA)

Thermal mechanical analysis is often used to assess changes in mechanical and/or dimensional properties of samples when they undergo changes in temperature. In our study, TMA analysis was performed using a commercial TMA 2940 apparatus from TA Instrument Inc. to quantify the volume expansion or contraction of a sample under load

as a function of temperature. Under negligible load, the thermal mechanical analysis experiment follows the free expansion or contraction of the material.

The samples studied were cut into cubes with a volume not below $0.5mm^3$ in order to have good accuracy of the coefficient of thermal expansion (CTE) measurement which was determined at a heating rate of $10°C.min^{-1}$ for each sample of interest. Figure III.2 presents an example of a TMA thermogram where the coefficient of thermal expansion, the glass transitions temperature (T_g) and the softening temperature (T_{soft}).

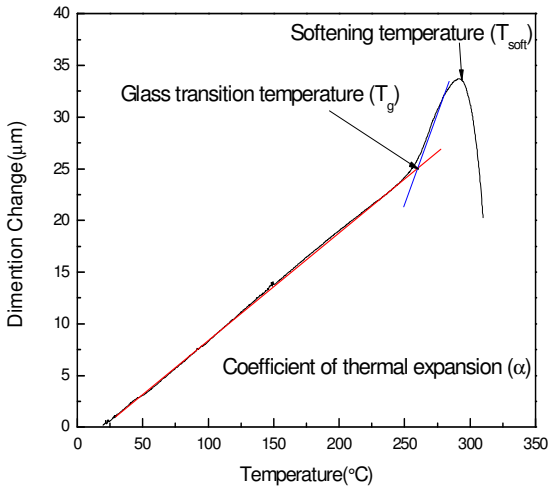

Figure III.2: Example of a TMA thermogram. Coefficient of thermal expansion α, glass transition temperature and softening temperature are shown.

To describe the overall deformation at a given temperature the following equation can be used:

$$\alpha_L = \frac{\frac{dL}{dT}}{L} \quad \text{and} \quad \alpha_V = \frac{\frac{dV}{dT}}{V} \qquad \text{eq. III.1}$$

where α is the coefficient of thermal expansion (CTE), the subscript L corresponds to measurement performed on the length of the sample and V on its volume. T is the temperature of interest [Br,07].

The coefficient of thermal expansion (CTE) is calculated on the linear sections of the curve as shown in Figure III.2 and T_{soft} is taken at the maximum of the thermogram. At temperatures above T_{soft} the dimension of the sample decreases due to both its own weight and the probe pressure. The accuracy of the measurement is $\pm 0.2\ 10^{-6}\ K^{-1}$

III.2.3 Density

Density is defined as the mass of the substance per unit of volume (g/cm^3). In our study, the density of the glasses was measured using the Archimedes' principle. The density of the samples were determined by using a diethylphtalate liquid with a known density as a function of temperature. The measurements were performed on polished samples. The density set up is represented in Figure III.3.

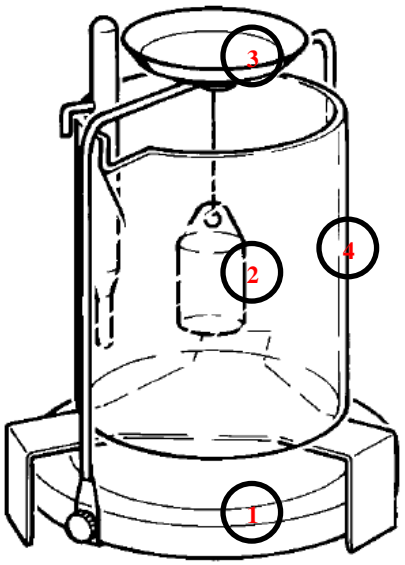

1: Weighing pan of balance
2: Sample holder for immersed weighing
3: Sample holder for air weighing
4: Diethylphtalate liquid

Figure III.3: Density determination kit

The polished glass is first weighed in air, and then while immersed. From these two weighings, density of the glass is calculated as follows:

$$\vec{P}_{liq} = \vec{P}_{air} + \vec{F}_{Archimedes} \qquad \text{eq. III.2}$$

where $\vec{P}_{liq}$: is the weight of the sample in the diethylphtalate liquid, $\vec{P}_{air}$:the weight of the sample in the air and $\vec{F}_{Archimedes}$:the Archimedes' force

The above expression can be re-written as follows:

$$B * g = A * g - V * \rho_0 * g \text{ with } V = \frac{A}{\rho_{sample}} \qquad \text{eq. III.3}$$

Hence,

$$\rho_{Sample} = \rho_0 \frac{A}{A - B} \qquad \text{eq. III.4}$$

With ρ_{sample} the density of the solid body (g/cm^2), ρ_0 is the density of the diethylphtalate liquid at a given temperature (g/cm^3), A is the weight of sample in air (g) and B is the weight of sample when immersed in the diethylphtalate liquid (g).The accuracy of the measurement was calculated to be ± 0.02g/cm^3

III.2.4 X-Ray diffraction (XRD)

X-Ray diffraction is a technique often used to determine the crystallographic properties or chemical composition of materials. The XRD spectra of the glasses were recorded using a Shimadzu XD-3A instrument with a Cu Kα X-ray source at 1.5418 Å, scanning from 5 to 80^o 2θ with a step size of 0.02^o. Samples were optically polished and mounted on an aluminum sample holder for measurement. The thickness of the sample was adjusted to fit the system requirement (~2mm). When a trace of crystallization was recorded, the position of the peaks (corresponding to a specific d-spacing) was searched over the ICDD database to identify the unknown crystal. The International Center

Diffraction Data (ICDD), formerly known as Joint Committee on Powder Diffraction Standards (JCPDS), is the organization that maintains the database of inorganic and organic spectra. The basics of the technique rely on the diffraction of an X-Ray beam on a parallel plan with a d-spacing as shown below.

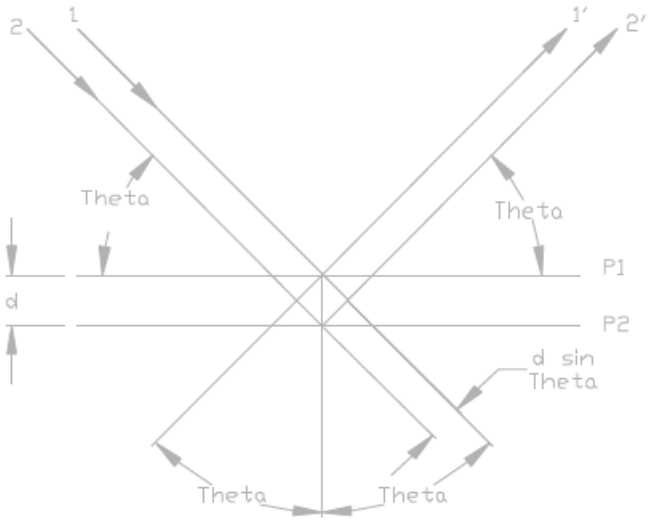

Figure III.4: Schematic of an X-Ray beam incident on a crystal.
[http://epswww.unm.edu/xrd/xrdbasics.pdf]

As illustrated in Figure III.4, the X-Ray beam hits the sample with an angle θ. A maximum in reflected beam intensity will occur if the diffracted X-ray wave is in phase with the original wave. For this phase matching between the diffracted and reflected beams to occur, the difference in path length between a wave diffracted from 2 different planes with d-spacing has to be an integer of the wavelength of the incident x-ray beam, as expressed by the Bragg's law [Al,93]:

$$2d*\mathrm{Sin}(\theta)=n\lambda \qquad \text{eq. III.5}$$

where θ is the angle of incidence of the X-Ray beam, d is the spacing between 2 atomic planes, n is an integer and λ is the wavelength of the X-ray beam. The dependence on the

d-spacing of the material implies that the angle of maximum intensity of diffracted X-Rays is a function of the size unit cell of the crystal.

III.2.5 Micro-hardness testing

One of the most important changes in a glass due to partial crystallization is the micro-hardness. Hardness is the measure of the amount of force required to plastically deform a material. These values range from 2000 GPa for hard materials such as sapphire or 7000 GPa for a diamond down to 4 GPa for a soft material. Micro-hardness measurements are performed through surface indentation or scratching of a given material. Many hardness testing methods can be used and a measured value can be compared only for measurements employing the same method of testing. Among all the technique the more frequently seen are:

- Vickers
- Brinell
- Rockwell (A, B and C)
- Knoop

The Brinell hardness, which was one of the first methods used (1900), consists of an indentation using a tungsten carbide (sometimes steel) ball. The hardness is defined as a function of contact area and load using the following equation [Ta,00]:

$$H_B = \frac{P}{\frac{\pi D}{2}(D - \sqrt{D^2 - d^2})} = \frac{3000}{157 - 15.7\sqrt{100 - d^2}} \qquad \text{eq. III.6}$$

where P is the load applied, D is the ball diameter (usually 1 cm) and d is the diameter of the indentation. This method requires sample with fairly large surface area and is mainly used for high hardness material.

The Rockwell hardness is a method that does not give hardness as a function of load/area. Instead, "The Rockwell test determines the hardness by measuring the depth of penetration of an indenter under a large load compared to the penetration made by a preload" [To,00]. Rockwell hardness increases with progressive increase of depth and time. The indenter can be either a steel ball or a diamond cone. The hardness value can be read directly from the instrument. This technique is mainly used for metals. The Rockwell hardness encompasses different types of measurements: Rockwell A, B, and C which depend on the materials of investigation and hence the load to apply. Rockwell A, B and C employ loads of 60, 100 and 150kgf, respectively. Rockwell A and B is used for softer metals or thin films while Rockwell C is used for hardened metals [Ro,19] .[Ro,22] [Ro,24]

The Knoop hardness test utilizes an elongated diamond indenter. This technique is useful for surface measurement and is especially useful in measuring anisotropic properties. This technique only measures the hardness on the long dimension of the indent and hence can be affected by texture, polycrystallinity and/or crystallographic axes. The Knoop hardness is calculated using the following equation [Kn,39]:

$$H_K = \frac{P}{A_p} = \frac{P}{L^2 C} \qquad \text{eq. III.7}$$

where P is the applied load, A_p is the projected area of indentation, L is the length of long diagonal and C is the constant relating the projected area to the length of the long diagonal. This constant depends upon the dimension of the indenter.

The Vickers method uses a diamond indenter with pyramidal shape. The technique consists of applying a load to a test piece to create an indentation. The surface area is then calculated through measurement of the length of the diagonal lines of the created indentation, after the removal of the load and following the method mentioned previously. The hardness as a function of indentation area can be calculated using the following equation [Sm,22]:

$$Hv = \frac{2P\sin(\frac{\Theta}{2})}{L^2} = \frac{1.854P}{L^2} \qquad \text{eq. III.8}$$

where θ is the angle between to opposite faces of the indenter, P is the applied load and L is the average diagonal length of the indentation. Knoop as well as Vickers hardness depends greatly upon surface condition.

This study employed a DUH-211S dynamic micro hardness tester (from Shimadzu) with a Vickers indenter. All of the experiments were carried on bulk glass samples with a thickness ranging from 1.5 mm to 5 mm. After the diamond indenter found the surface of a sample, a predetermined constant loading rate of 7.1 gF/sec was electromagnetically applied until reaching the final value of P = 25 grams. The indenter was left in place for an additional period of 5 seconds before it was lifted off the sample surface. The indentation diagonals were then measured using the eyepiece and a 50x objective and at this load were ~5μm in size. The Vickers hardness was calculated using the diagonal length information. The accuracy of the measurement was found to be better than 10% (set by the manufacturer)

III.2.6 Viscosity

The viscosity of a given glass material will change drastically with changing temperature. The temperature-viscosity relationship can give insight on such temperatures as melting, annealing or the temperature of devitrification and it allows one

to identify the temperature at which a glass rod must be heated in order to draw fiber, which corresponds to a viscosity of 10^5 Pa.s.

At a viscosity of 10 Pa.s the glass is fluid enough to be a consider a liquid, however it has to be mentioned that this is not the melting temperature associated with the crystal-melt phase transition. The viscosity of 10^3 Pa.s corresponds to the so-called "working point": at this viscosity the molten glass can be manipulated or formed/deformed into a final shape. Further, this viscosity is low enough to apply a shear processing but high enough to remain in the formed shape when the shear is removed. The Littleton softening point of the glass occurs at the temperature corresponding to $10^{6.6}$ Pa.s, and it is the temperature at which the glass can deform under its own weight. In order to remove the stress induced by the quenching of the melt the glass needs to be annealed. The annealing temperature is defined to be when the glass reaches a viscosity of 10^{12} Pa.s. At this optimum temperature the stress can be relieved in a few minutes. Finally, the "strain point" can be defined as the temperature at which the glass has a viscosity of $3*10^{13}$ Pa.s. At this temperature the stress can be relieved if the temperature is maintained for several hours. For temperatures below the "strain point" neither structural rearrangement nor permanent flow can be measured [Ca,07].

In this study, the viscosity of the glasses was measured using a beam bending and parallel plate viscometers

The beam bending technique was used to define the glass viscosity properties in the annealing range (η = Log 11.0 – Log 13.0 Pa s) using BBV-1000 beam bending viscometer form Orton Ceramics [OR,BBV]. The instrument components can be seen in the Figure III.5.

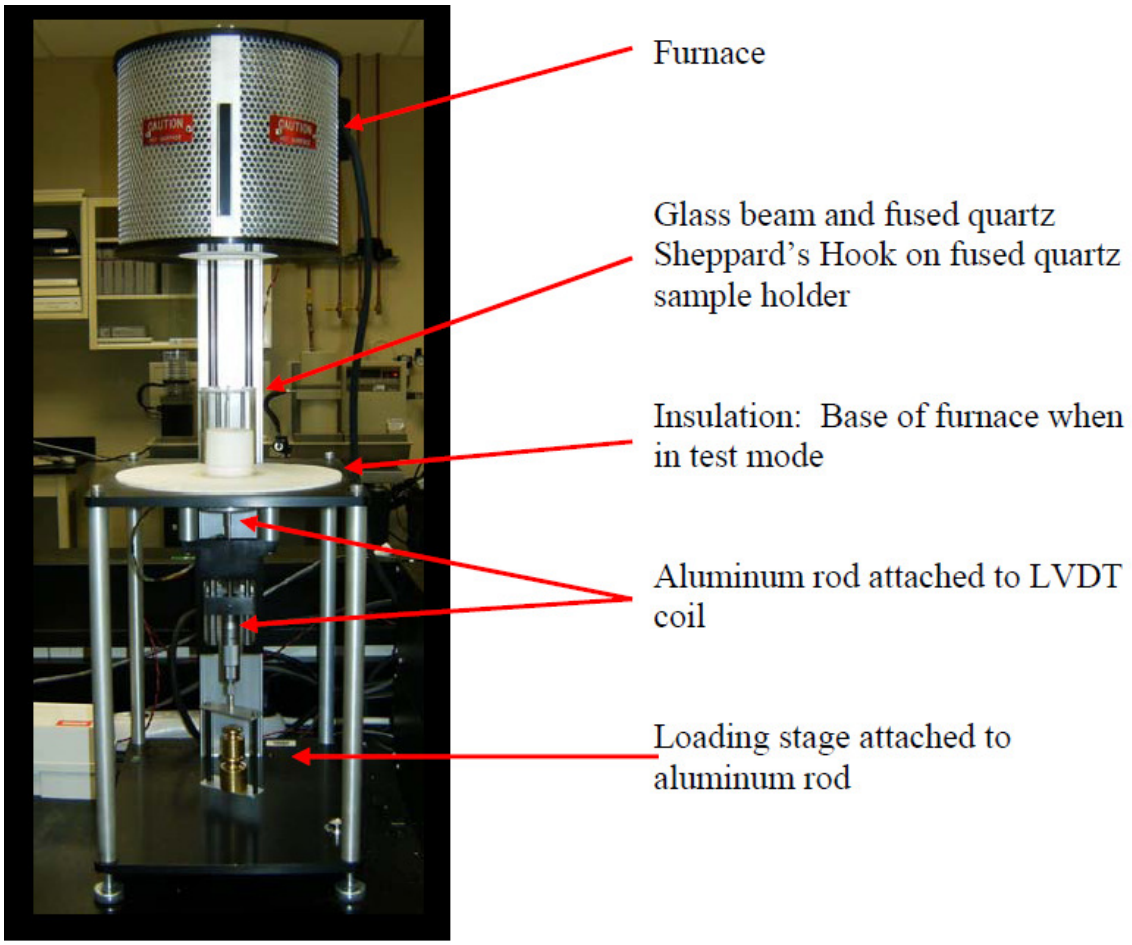

Figure III.5: BBV-1000 beam-bending viscometer, Orton Ceramics [OR,BBV]

The furnace element of the BBV is capable of reaching temperatures as high as 1000°C, and is equipped with a type "S" controller and sample thermocouple. A 50 mm diameter fused quartz sample holder supports a glass beam with square, rectangular, circular, or elliptical cross-section that must have dimensions maintaining a cross-sectional moment of inertia between 2 x 10^{-4} and 10 x 10^{-4} cm^4 [ASTM] [Sc, 08]. A "Sheppards hook" is placed at the midpoint of the glass sample and is attached to the LVDT coil beneath the furnace. In using this system, the deflection of the sample is measured using a given mass which is placed on an aluminum load-bearing stage attached at the base of the LVDT coil. The LVDT monitors the deflection rate of the

glass sample as a function of temperature (for rate-cooling or rate-heating measurements) or time (for isothermal measurements).

In order to determine the viscosity properties of the materials in the softening region (in the range of η = Log 4.0 – Log 8.0 Pa s) of the glass, a PPV-1000 **parallel-plate viscometer** from Orton Ceramics was employed [OR,PPV]. The instrument components are seen in Figure III.6.

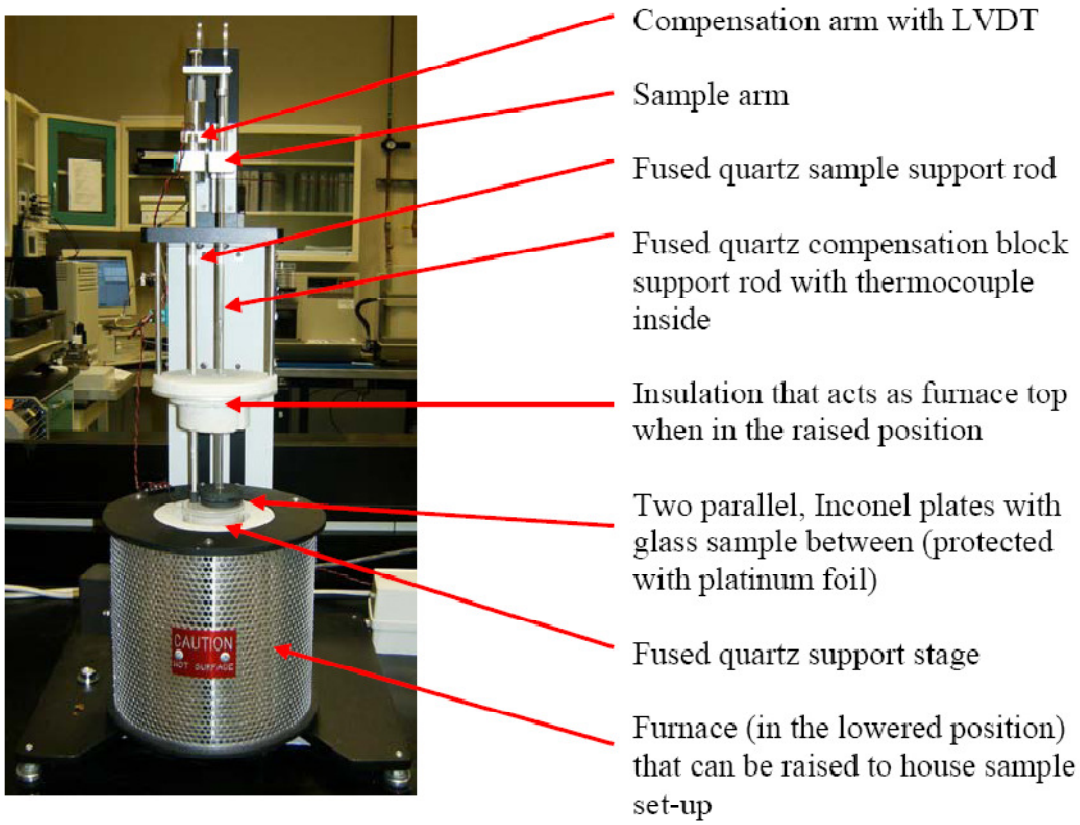

Figure III.6:PPV-1000 parallel plate viscometer, Orton Ceramics [OR,PPV].

The 1000°C Kanthal wound, ceramic fiber lined furnace (with type "S" control thermocouple) can be raised and lowered with a motor to house the glass sample [OR,PPV]. A cylinder of glass 3 – 6 mm in height and 6 – 12 mm in diameter finely ground finished resides between two parallel plates. The plates are made of inconel and

to avoid any contact, reaction and/or sticking between the plate and the glass sample, the glass disk is "sandwiched" in between two platinum foils. The top inconel plate is attached to a fused quartz sample support rod. The application of the load to the glass sample is done by attaching weights to the sample arm at the top of the instrument. The LVDT monitors the deflection rate of the glass sample as a function of temperature (for rate-cooling or rate-heating measurements) or time (for isothermal measurements).

III.3 Optical properties

III.3.1 UV-VIS spectroscopy

It is crucial to determine the absorption characteristics of a glass, specifically when it comes to optical materials, in order to evaluate their potential application. When light is incident on a dielectric boundary, some of the energy is reflected, some is absorbed and the rest is transmitted. The optical absorption of a glass varies with thickness and wavelength and is function of its physical and chemical structure [Bo,91].

In the work presented here, the UV-Vis-NIR absorption spectra of the samples have been measured with a dual beam UV-Vis-NIR Perkin Elmer Lambda 900 spectrophotometer at a scan rate of 1nm/s in the 200- 900 nm region. In the experimental set-up to obtain these spectra, the beam was focused onto the sample, with the light incident on the sample at normal angles. The sample was optically polished and thoroughly cleaned before any measurement. In this arrangement, the amount of light transmitted is compared with the source beam and the amount of light absorbed is calculated as a function of the wavelength of the beam to obtain the spectra. The absorption coefficient (α) measures the spatial decrease in intensity of a propagating

beam due to a progressive conversion of the beam into different forms of energy or matter [Sh, 08]. The extinction (or absorption) coefficient (α_e) translates the decrease in beam intensity due to all contributing processes and appears in the famous Beer-Lambert or Bouguer Law [In,88].

From Beer's law, the intensity decay along the propagation axis has the form

$$I(L)= I_o*\exp(-\alpha L) \qquad \text{eq. III.9}$$

where I_o is the initial intensity and α represents the absorption coefficient at each individual wavelength (cm^{-1}), and L is the sample thickness in cm. The absorption coefficient is given by

$$\alpha_{dB} = 10 * Log\left(\frac{I_0}{I}\right) \qquad \text{eq. III.10}$$

$$\frac{I_0}{I} = 10^{O.D.} \qquad \text{eq. III.11}$$

where O.D is the measurement of the optical density (i.e. absorbance) using the Perkin Elmer Lambda 900 spectrophotometer, after Fresnel reflection correction is applied.
The combination of the equations III.11 and III.10 yields:

$$\alpha = \frac{1}{L} Ln(10) * O.D. \qquad \text{eq. III.12}$$

This technique was used in the present study to observe the shift in the absorption band-edge of every bulk specimen evaluated.

III.3.2 Ellipsometry

The refractive index of a glass sample is of great interest for applications such as optical fibers for use in the IR region. According to Lloyd, their refractive indices must be

high and as independent of temperature as possible [Ll,75]. However materials with such indices required specific anti-reflection coatings to mitigate the corresponding high Fresnel losses that scale with index.

The technique of ellipsometry was invented by Paul Drude in 1887. He used this technique to measure the dielectric function of diverse materials such as metals and semi-conductors. The ellipsometry technique allows one to measure, with high reproducibility, the complex dielectric function $\varepsilon=\varepsilon_1+i\varepsilon_2$. Figure III.7 shows the set up of an ellipsometer.

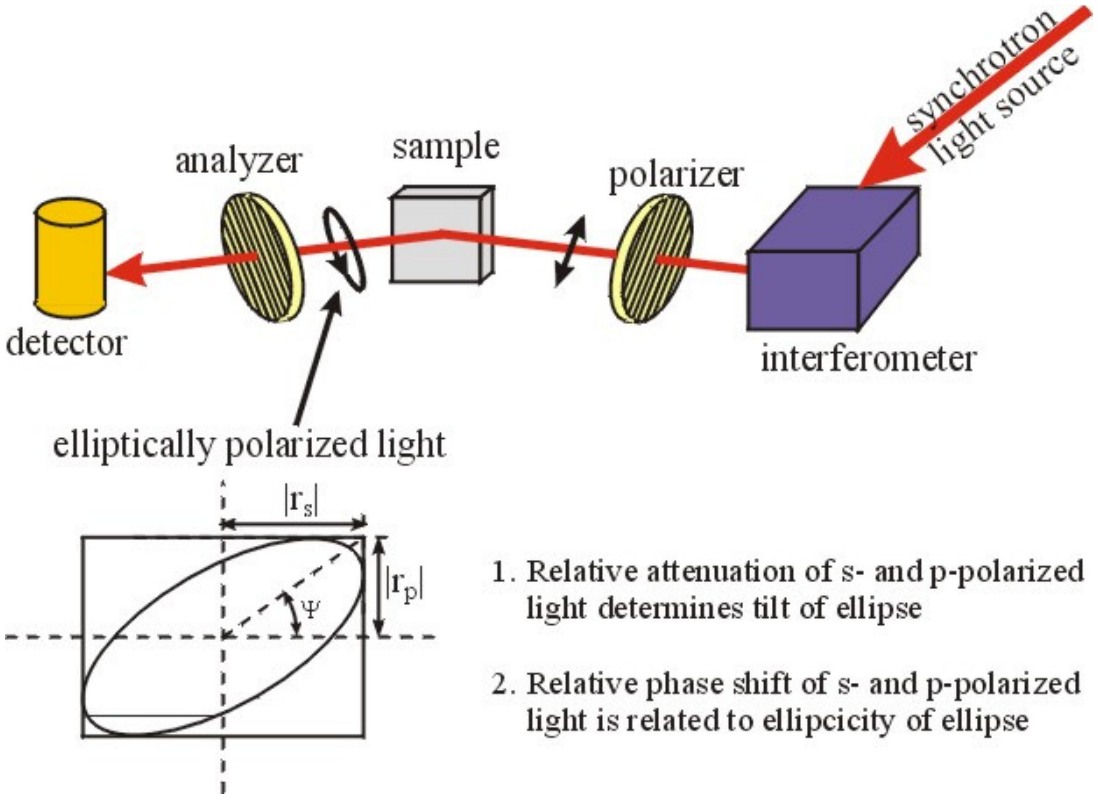

Figure III.7: Ellipsometer set-up [http://academic.brooklyn.cuny.edu/physics/holden/ellipsometry]

An incident beam is polarized with finite field components E_p and E_s in the directions parallel (p) and perpendicular (s) to the plane of incidence of the light. Due to interaction between the beam and the sample, the reflection will be attenuated and phase shifted as compare to the incident beam, according to the Fresnel equations [To,99]:

$$\frac{Rs}{Es} = -\frac{Sin(i-r)}{Sin(i+r)} \qquad \frac{Rp}{Ep} = -\frac{Tan(i-r)}{Tan(i+r)} \qquad \text{eq. III.13}$$

By combining those two equations we can then obtain the ratio of the parallel and perpendicular components [To,99]:

$$\frac{Rp}{Rs} = -\frac{Cos(i+r)}{Cos(i-r)} \qquad \text{eq. III.14}$$

where i is the angle of incidence, r is the angle of refraction, Rs is the reflected perpendicular component, Rp is the reflected parallel component, Es is the incident perpendicular component and Ep is the incident parallel component.

The general equation of ellipsometry is more often written as follows:

$$\rho = \frac{Rp}{Rs} = Tan(\Psi)e^{i\Delta} \qquad \text{eq. III.15}$$

where $Tan(\psi)$ is the amplitude ratio upon reflection and Δ is the phase shift [To,99].

A second polarizer will measure the ellipse of polarization of the reflected light. The degree of ellipticity can be used to calculate the dielectric function.

Two different ellipsometers were used during this study, depending on the accuracy of the measurement needed. The first instrument used, for gross refractive index measurement was a M44™ spectroscopic ellipsometer (from J.A. Woolam Co. Inc.) which incorporates a variable angle stage allowing adjustment of the incident angle. The instrument operates on a rotating polarizer principle, in which the polarization of incoming light is varied, and reflected intensity is recorded with a grating coupled CCD over a wavelength range of 600 to 1100 nm. Ellipsometric data was recorded at a 75 degree angle of incidence. The second system used was Metricon 2010M prism coupler (from Metricon Corporation) in collaboration with Politecnico di Torino. The Metricon

2010 prism coupled refractometer is fully automated. It was used to measure the refractive index of 4 mm thick glass samples at 630, 825, and 1533nm. All measurements were performed on optically polished samples. The precision on the measurement of the refractive index according to the manufacturer of the M44^{TM} is estimated to ±0.02 and the accuracy of the measurement of the Metricon 2010 is equal to ±0.0001.

III.4 Structural properties

Infrared (IR) and Raman spectroscopy both measure the vibrational energies of molecules but these methods rely on different selection rules. For a vibrational mode to be Raman active, there must be a change in polarizability of the molecule while to be IR active, the dipole moment of the molecule must change.

III.4.1 Raman spectroscopy

Raman spectroscopy is a technique used in condensed matter physics to evidence vibrational, rotational and other low frequency modes in a material. Raman scattering is the scattering of light via a coupling of optical and lattice vibrational modes. The oscillation of the molecule during nuclear vibration is quite slow compared to the very rapid oscillation of a light wave passing by. The molecules are thus affected by the very rapid oscillating electric field of light. Since the electronic cloud follows the nuclei, we find fluctuations in shape of the electronic cloud that surrounds the molecule from both the nuclear vibrations and the light wave. The light beam perturbs the electronic cloud and induces an instantaneous polarizability change with a frequency equal to the

perturbating light radiation. A picture of the principle of emission and excitation is given in Figure III.8.

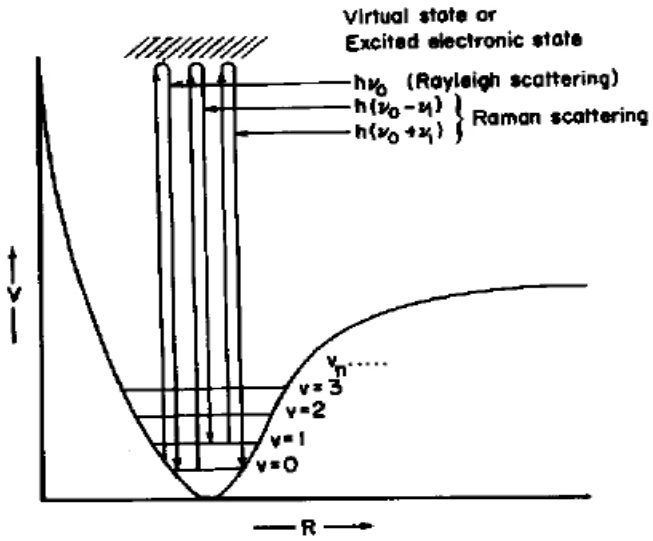

Figure III.8: Excitation and emission of photon [Fa, 91].

The levels of vibrations are represented by ν_0 (ground state), ν_1, ν_2 etc. The difference in energy between two states is what is directly observed in the IR spectrum and by the Raman shift in frequency from the Rayleigh line as shown in Figure III.9. Note that the molecule is first excited to a very high energy state ("virtual state" on the Figure). Three cases are then possible: return of the molecule to the ground state with emission of a photon of energy $h\nu_0$ (Rayleigh scattering), relaxation to a higher energy level than the ground state with emission of a photon of energy $h(\nu_0-\nu_1)$, and finally relaxation to the ground state after being excited from a higher energy level which creates the emission of a photon of energy $h(\nu_0+\nu_1)$. The last two cases correspond to Raman scattering. In Figure III.9 is shown a detection of scattering intensity in function of $h\nu$.

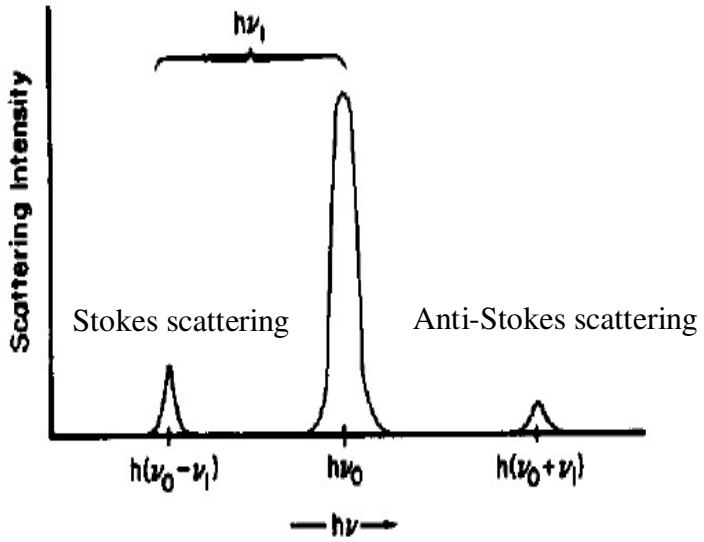

Figure III.9: The detection of scattering intensity as a function of hν. The displacement between the laser scattering $h\nu_0$, $h(\nu_0+\nu_1)$ and $h(\nu_0-\nu_1)$ is the Raman shift $h\nu_1$ [Fa,91].

The equipment needed to observe Raman scattering is simple. The emission and scattering from the sample are usually collected with a lens and focused into a monochromator. Gases, liquids and solids can be used as samples in Raman spectroscopy. The main problem of this technique comes from the fluorescence background, when light emitted from the sample is superimposed on the signal at frequencies close to the Rayleigh line.

In this study, the Raman spectra measurements were conducted using a LabRamHR Horiba Jobin Yvon micro-Raman system. The argon-ion 532 nm laser line was used as the excitation wavelength. The laser beam was focused onto the front polished surface of the sample via a 100x microscope objective, with a spatial resolution of about 2 µm. A backscattering geometry was used to collect the Raman signal, which was then spectrally analyzed with a spectrometer and a CCD detector. The Rayleigh line was reduced with a holographic notch filter.

III.4.2 Fourier transformed infrared spectroscopy(FTIR)

Using infrared (IR) spectroscopy, it is also possible to probe molecular vibration, sample homogeneity and, in some cases, the amount of chemical entity present in the material. IR spectroscopy measures the absorption of IR radiation by materials as the atoms undergo vibration. IR spectroscopy is primarily used to identify bond types, structures, and functional groups in organic and inorganic compounds

The energy of the IR radiation can be calculated using the following equation [Al,93]:

$$E=hf \qquad \text{eq. III.16}$$

where h is Planck's constant and f is the frequency of the incident radiation [Al,93].

Knowing the frequency of the radiation, it is possible to determine the wavelength of interest:

$$\lambda = \frac{c}{f} \qquad \text{eq. III.17}$$

where c is the speed of light in a vacuum.

In spectroscopic notation the wavelength is expressed in inverse centimeters (cm^{-1}) because of its proportionality with energy:

$$\frac{f}{c} = \frac{1}{\lambda} = \frac{E}{hc} \qquad \text{eq. III.18}$$

In conventional FTIR, infrared energy is emitted by a glowing black-body. The beam passes through an aperture that is set depending upon the sample under investigation. The aperture allows for a reduction or increase in the amount of energy incident on the sample and also for control of the amount of radiation incident on the detector. The IR beam enters an interferometer which will encode the signal. Following

the interferometer, the beam interacts with the sample in the sample compartment. The sample absorbs the energies resonant with the vibration of the structural unit present in the investigated sample. Finally the beam goes through the detector which measures the specific signal produced by the sample. The computer analyzes the signal received by the detector. A Fourier Transform is applied to the signal which converts this to a spectrum, where each peak corresponds to a precise vibration present in the sample during the irradiation. [Ma,04] [www. Thermonicolet.com]

In this study, the absorption spectra in the near-infrared (NIR) region were measured using a Magna-IR 560 spectrometer from Nicolet. The light source and mid-IR optics configuration (7,400-350 cm^{-1}) use an *ever-glo* source, KBr beamsplitter, DTGS detector and single detector optics. The system was carefully purged with nitrogen between each measurement in order to remove any atmospheric water or CO_2 within the spectrometer's sample chamber. The system's purge gas was previously run through a purge gas generator. The spectra were recorded over the range 4000-1500 cm^{-1} on optically polished samples. Following collection, the spectra were corrected for Fresnel loss and specimen path length (in cm).

III.4.3 X-Ray fluorescence (XRF)

The fluorine content in glass prepared using ZnF_2 and/or NH_4F-HF was determined by wavelength-dispersive x-ray fluorescence spectrometry (XRF). X-Ray fluorescence is the emission of characteristic secondary X-Rays (or fluorescent X-Rays) from a material that was excited by high energy X-Rays or gamma rays.

When a high energy X-Ray source impinges on the samples of investigation, the X-Ray can be either absorbed or scatter through the samples as illustrated in the figure below.

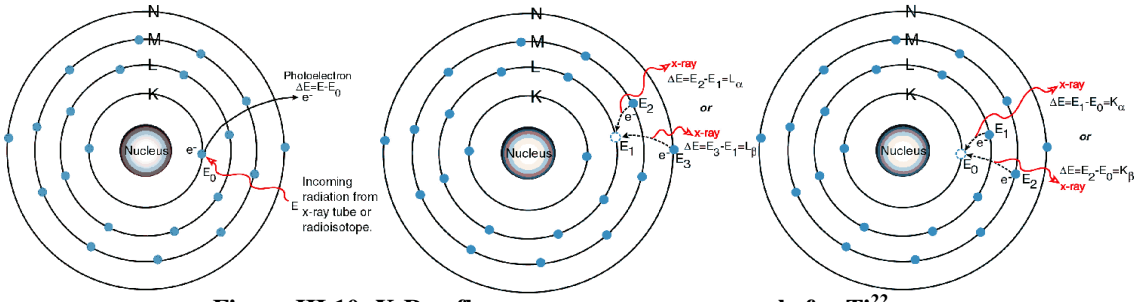

Figure III.10: X-Ray fluorescence process: example for Ti^{22}.

When the X-Ray is absorbed, a transfer of energy to an "innermost" electron occurs; this phenomenon is called "photo electric effect". If the X-Ray possesses sufficient energy, an electron will be ejected from the inner shell leading to a vacancy. This vacancy leaves the atom in an unstable state. In order for the atom to fall back to a more stable state, an electron from the outer shell must transfer to the inner shell giving rise to the emission of an X-Ray characteristic to the atom. The energy of this X-Ray corresponds to the difference in binding energy between the outer and the inner shells. The emission of this X-Ray is called X-Ray fluorescence.

XRF measurements were performed on a Bruker AXS S4 Pioneer X-ray fluorescence spectrometer relative to sodium trisilicate references doped with fluorine at SCHOTT RDD, Duryea (PA). The experiment was performed on optically polished samples. The fluorine concentrations of the references were characterized via an ion selective electrode technique with an accuracy of better than 5 at.%.

III.5 Microscopy

III.5.1 Optical microscopy

The optical microscope is often referred to as “light microscope”, as it uses a visible light and set of lenses to magnify the image of a sample. Despite limitations in resolution and in magnification, the optical microscope is still a fast way to investigate samples. Moreover, the optical microscope is an easy characterization tool to use and an economical apparatus. Figure III.11 shows a picture of the optical microscope used in this study.

Figure III.11: Nikon polarizing optical microscope

In this work, an optical microscope Nikon Type 115 optical microscope with a picture acquisition system was used to define the presence and size of crystals in heat treated bulk glasses. The samples were optically polished and thoroughly cleaned before analysis. As the resolution of the optical microscope depends on the eye piece used, the objective used, and the acquisition system, the accuracy of measurement will be reported in the results and discussion section depending upon the setting used.

III.5.2 Electron microscopy: elemental dispersive spectroscopy / scanning electron microscopy (EDS/SEM)

The composition of the investigated samples was checked using the scanning electron microscopy (SEM) coupled with an energy dispersive spectroscopy (EDS). Scanning Electron Microscopy (SEM) was also used for visual observation of an area of interest in a completely different way from that of the naked eye or even normal optical microscopy.

Energy Dispersive X-Ray Spectroscopy (EDS), sometimes referred to as EDAX or EDX, can be used to obtain semi-quantitative elemental results about very specific locations within the area of interest. Both SEM and EDS can be used for evaluating and / or analyzing samples, whether it's simply for screening purposes or for a failure related issue. Figure III.12a and b show an overview of the EDS /SEM system and of the detection system of the SEM respectively.

a) b)

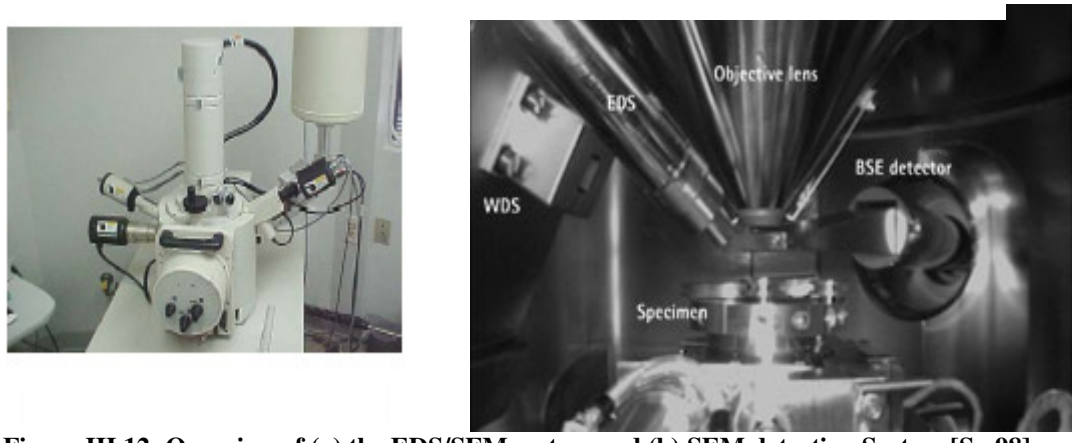

Figure III.12: Overview of (a) the EDS/SEM system and (b) SEM detection System [Su,98]

Typically, SEM provides the visual "answer" while EDS provides the elemental "answer". In both cases, areas of interest can be observed aerially or in cross section. In

scanning electron microscopy, an electron beam is scanned across a sample's surface. When the electrons strike the sample, a variety of signals are generated, and it is the detection of specific signals which produces an image or a sample's elemental composition. In Figure III.13 is shown the electron interaction with the materials.

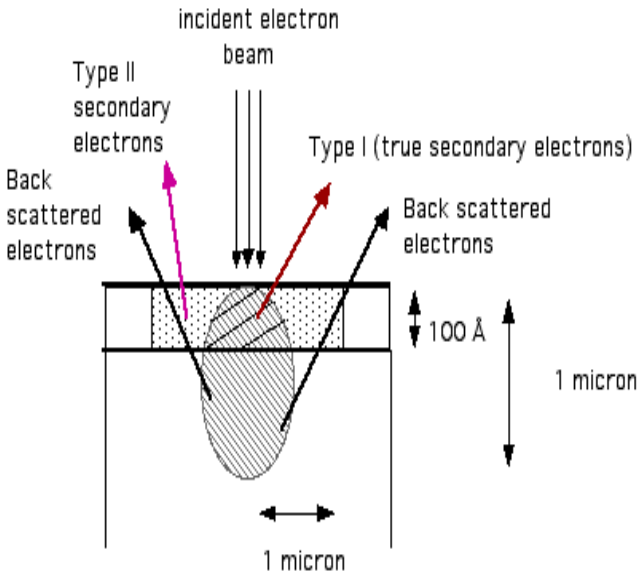

Figure III.13: Electron interactions with materials

The three signals which provide the greatest amount of information in SEM are secondary electrons, backscattered electrons, and X-rays [Ki,07] [Lu,08]:

- **Secondary electrons** are emitted from the atoms occupying the surface and produce a readily interpretable image of the surface. The contrast in the image is induced by the sample morphology. Due to the small diameter of the electron beam, a high resolution image is obtained.

- **Backscattered electrons** are primary beam electrons which are 'reflected' from atoms in the solid. The difference in the atomic number of each element produces a contrast on the image which therefore will show the distribution of different chemical

constituents in the sample. Because these electrons are emitted from a depth in the sample, the resolution in the image is not as good as for secondary electrons.

- Interaction of the primary beam with the atoms in the sample causes shell transitions which result in the **emission of an X-ray**. The emitted X-ray has an energy characteristic which is a function of the element atomic structure. Detection and measurement of the energy permits elemental analysis (Energy Dispersive X-ray Spectroscopy or EDS). EDS can provide rapid qualitative, or with adequate standards, quantitative analysis of elemental composition with a sampling depth of 1-2 μm. From the emission X-ray spectra, one can infer the elemental composition from the different shells (K, L, M) involved in addition to the element name. These characteristic lines are related to the Bohr model of the atom.

Figure III.14 shows a schematic of the origin of some characteristic lines.

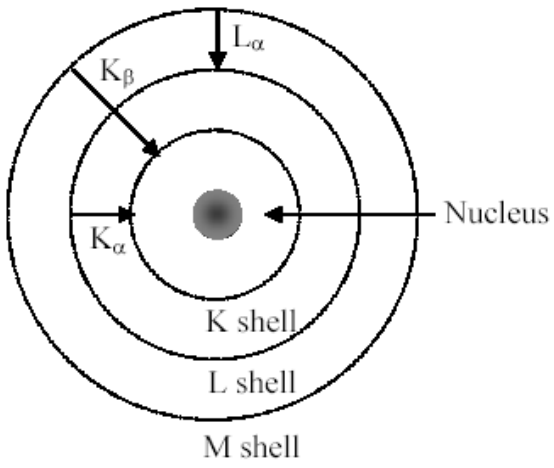

Figure III.14: Electron transitions in an atom producing characteristic X-rays.

In EDS, data are collected for all energies at once, and are displayed as a histogram of electronic counts versus x-ray energy as shown in Figure III.15.

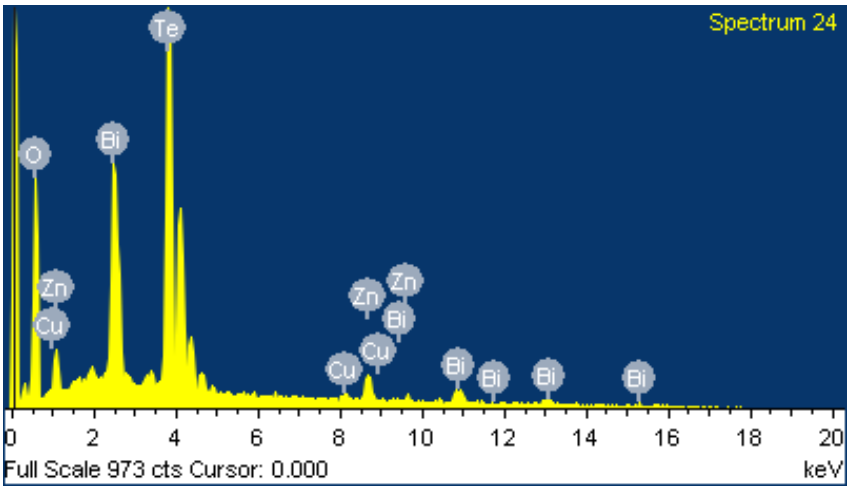

Figure III.15: histogram of electronic counts versus x-ray energy for a glass of composition 2.5%Cu_2O-97.5%(70TeO_2-10Bi_2O_3-20ZnO).

As a consequence, the analysis is both qualitative (for elements with atomic numbers between that of beryllium to uranium) and quantitative without any need of standards. The minimum detection limits is typically from 0.1 weight percent to a few percent and depends on the element and matrix. In this study, the SEM/EDS 3400N was used to analyze the composition of the investigated polished samples with an accuracy of measurement of ~2 at.%

III.6 Core, core-clad preform and fiber processing

III.6.1 Proof of concept for the fabrication of core-clad preform

III.6.1.1 Borophosphate glass system

The first step in developing core-clad fiber using rotational casting is to demonstrate the feasibility of rod (core preform) production. Such a process implies the control of parameters such as mold temperature, rotational speed, glass quenching temperature, etc. to process a preform with good homogeneity of composition and no defects along the length of the preform. As the presence of defects such as bubbles in

preforms can make the fiber weak and increase the loss propagation, it is crucial to prepare bubble-free preforms.

Borophosphate glasses were used for proof of concept as these glasses are easy to process, inexpensive and have been extensively studied [Du,92] [Pe,06] [Ha,00]. Borophosphate glasses were prepared using $Na_2B_4O_7$ (Alfa:Aesar, 98%) and $(NaPO_3)13$-Na_2O. A 30 g sample of molten glass was melted at 900°C for 30 min in a platinum crucible and quenched in a preheated brass mold at 375°C and annealed for 15 hours. Preforms with a diameter of 1.1-1.3 cm in the compositions $95NaPO_3–5Na_2B_4O_7$ were prepared as shown below

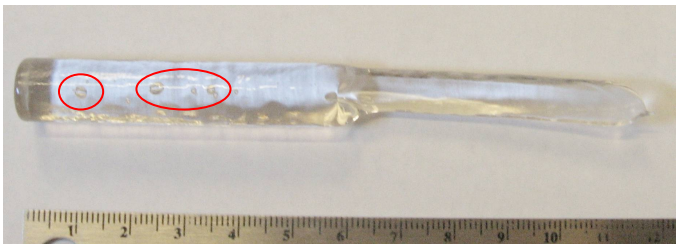

Figure III.16: Picture of a borophosphate preform

As seen above, the preform was full of bubbles the location of which are shown by the red circles in figure. It is of great importance to study the size and location of bubbles due to the repercussion of those defects on the subsequent fibers. In order to dtermine the location of bubbles in the preforms, the preforms were sliced into 4-5mm thick cross-sections which were polished and optically inspected using an optical microscope as illustrated below.

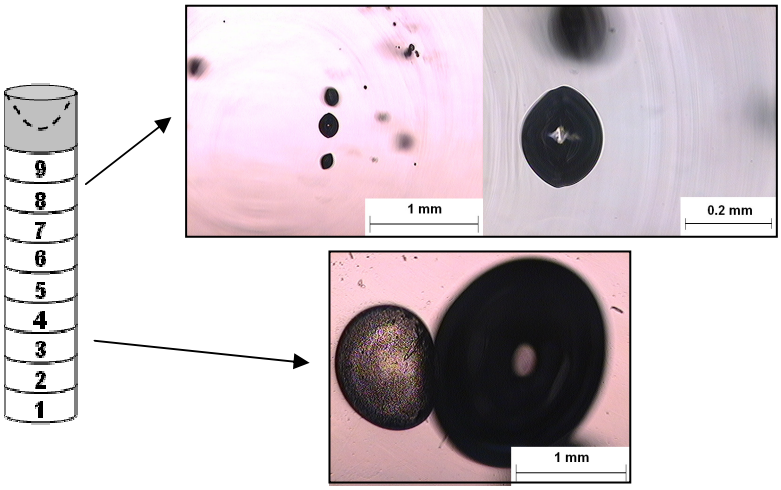

Figure III.17: Optical images of bubbles in a borophosphate core preform (200X and 500X magnification)

The slices were surveyed with an optical microscope to find trends in the appearance of bubbles. The majority of large bubbles were observed in the center of the preform at the top and at the bottom. Two main variables were identified through the optimization process to improve the preform quality: i) the temperature at which the mold is heated prior to casting and ii) the rate at which the melt is poured into the mold. We found that it is possible to prepare high quality preform (as shown below) by pouring the glass melt very slowly into the mold.

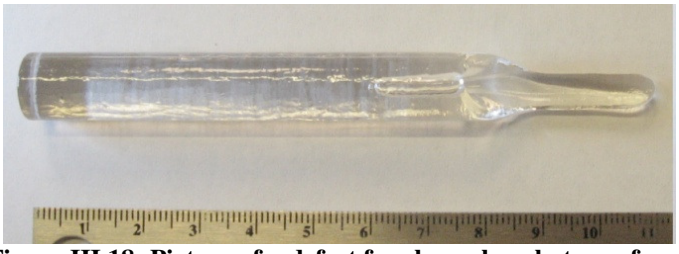

Figure III.18: Picture of a defect free borophosphate preform

III.6.1.2 Tellurite glass system

This optimized process (temperature of the mold, pouring rate and quenching temperature) was adapted to prepare bubble- and crack-free tellurite-based preforms. The

figure below shows bubble-free preforms with the composition $70TeO_2$-$10Bi_2O_3$-20ZnO, and $75TeO_2$-$5ZrO_2$-$20WO_3$.

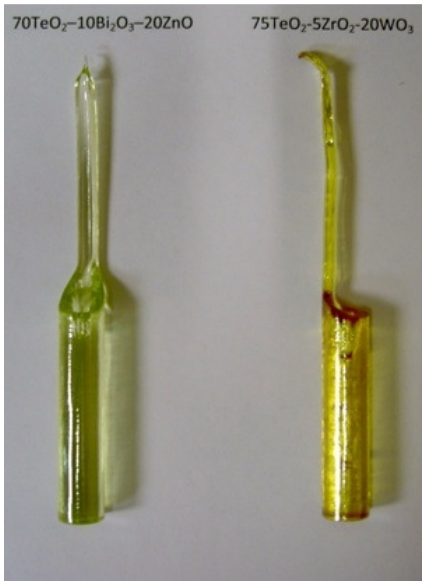

Figure III.19: Picture of tellurite preform in the composition $70TeO_2$-$10Bi_2O_3$-20ZnO (left) and $75TeO_2$-$5ZrO_2$-$20WO_3$ (right).

III.6.2 Core-clad preform

The core-clad performs used in the present work were processed using a rotational caster (illustrated in Figure III.20) following the method developed by Tran et al.[Tr,82].

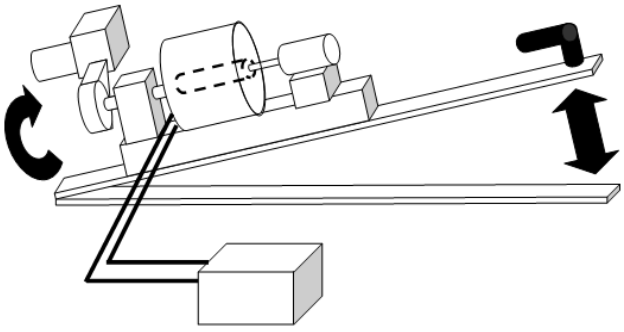

Figure III.20: Rotational casting rig

This process is based on individual preparation of both the core and cladding composition melts. In the first stage the mold is preheated in the furnace. When the

cladding glass is melted, the table is lifted up vertically and the glass is cast into the mold. The table is then quickly returned to a horizontal position and the mold is spun for few seconds. The spinning time was varied from 10 seconds to 45 seconds depending on the glass composition. After about 2 minutes, the table is turned vertically and the core glass is cast into the mold. The mold is held vertically for 30 seconds to solidify the core glass and is finally turned horizontally for annealing as illustrated below.

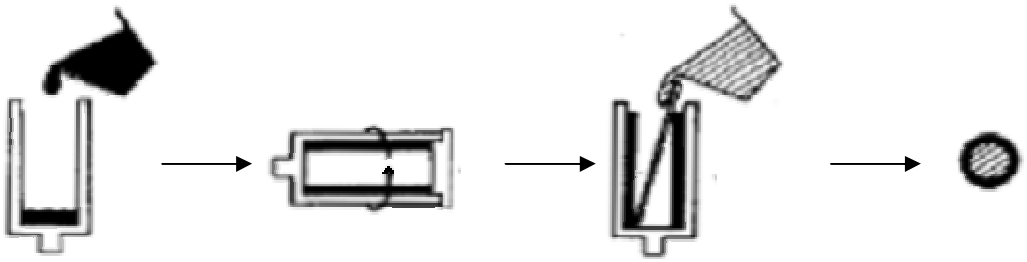

Figure III.21: Sequence of steps required for the rotational casting of preforms.

The first challenge was to obtain the "hollow tube" shape of the cladding by rotational casting. This hollow tube could be processed by optimizing **(i)** the **temperature at which the glass was quenched**, **(ii)** the **preheated mold temperature**, **(iii) spin speed**, and **(iv) spin duration**. Initial melting test were carried out which indicated that:

- The quench temperature most strongly affects cracking in the glass.

- The pre-heat temperature of the mold was determined by the necessary viscosity of the glass; when quenching the clad glass, low viscosity in the glass must be maintained long enough for the glass to coat the inside of the mold

After pouring the cladding melt into the mold, the mold had to be spun before the glass became too viscous to make the cladding shape. For this reason, the melt was

quenched as quickly as possible, and the mold was spun at maximum speed immediately after quenching the cladding glass.

Different spin speeds and mold quench temperatures were used in order to process a "borophosphate hollow clad tube" with a length of at least 5 cm. Figure III.22 presents pictures of the resulting clad's shapes.

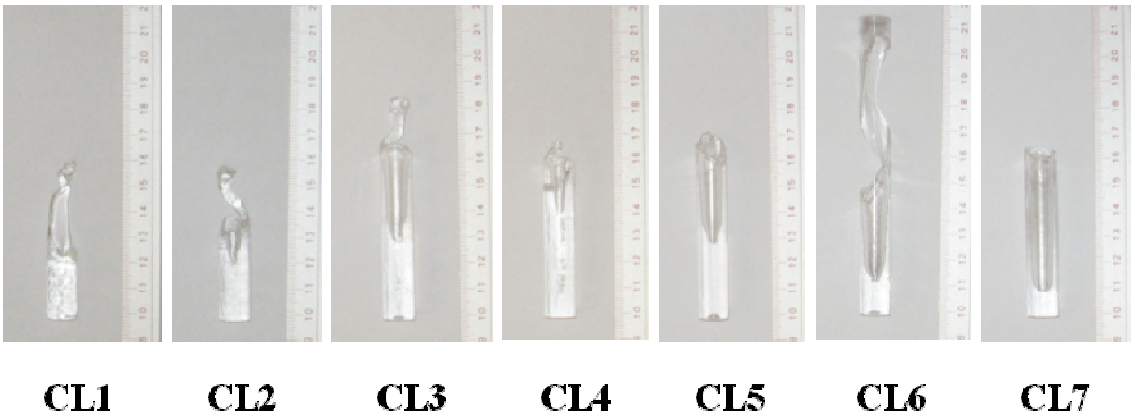

Figure III.22: Pictures of the borophosphate clad's shapes

The CL1 sample was prepared using a low quenching temperature (T_{quench}), a low pre-heat temperature for the mold, a low spinning speed and a short spin time. As a result, the clad is not clad shaped (i.e. not a tube shape). For the other samples, the spinning speed and T_{quench} were increased. The temperature of the mold was preheated to the temperature at which the log(viscosity of the clad material) = 12. The sample CL7 which is a "hollow clad tube" with a length of at least 5 cm was processed using the following parameters:

- mold preheated at $T_{log(\eta)=12}$

- T_{quench} = 50 ^{o}C below T_{melt}

- spinning speed = 2800 rpm

- spin for 30 seconds

After optimizing the quenching procedure and the mold temperature for the tellurite composition, the “hollow tube” shape, shown in Figure III.23, was consistently produced.

Figure III.23: Picture of "Hollow Tube" of $70TeO_2$-$10Bi_2O_3$-20ZnO glass

The final step to prepare a core-clad preform consists of pouring the melt of the glass used as the core in the hollow clad tube. As performed for the core preform, the core-clad preforms were sliced after annealing and each cross-section was optically inspected. The inspection of the cross-section with the optical microscope reveals the presence of bubbles located mainly at the core –clad interface as seen in Figure III.24.

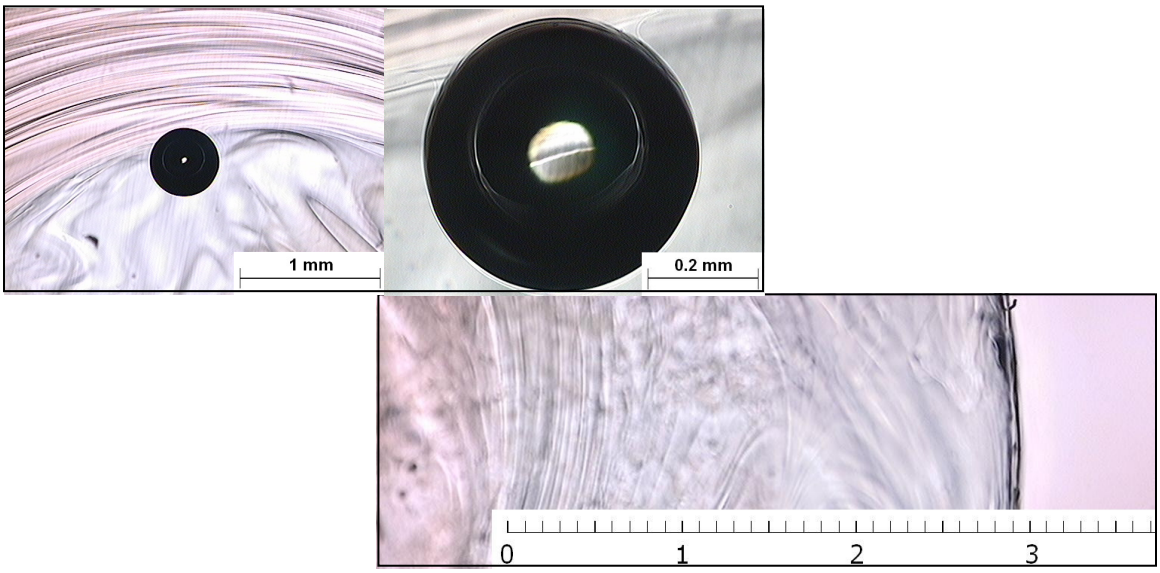

Figure III.24: Optical images of glass preform slices (500X magnification) in the doped cladding preform.

III.6.3 Fiber Drawing

Step-indexed optical fibers were drawn by pulling the tellurite core-clad preform using a Heathway drawing tower (Milton Keynes) shown below:

Figure III.25: COMSET fiber drawing tower

The diameter and length of the preforms used were 1 and 6 cm, respectively. The thermal gradient of the drawing furnace was specially designed to soften the preform just above its lower extremity. The drawing temperature, for glass in the $70TeO_2$-$10Bi_2O_3$-20ZnO composition, was found to be 370°C. At this temperature, a drop appeared and fell down under gravitational attraction, pulling the fiber in its wake. The pre-set fiber diameter was 125 μm to give strength to the fiber. The drawing speed was set at 5 m/min. More than 160 m of fiber were obtained for each drawing. Uncoated fibers were pulled in order to perform thermal and structural properties measurement and some UV cured polymer coated fibers, expected to have higher strength, were also pulled for the characterization of the fibers' optical properties.

III.7 Fiber characterization

The step index (Δn) of the core-clad fiber was estimated (± 0.002) by measuring the numerical aperture of the fiber using the far-field output pattern at 632 nm. From these measurements, the numerical aperture (θ) was determined:

$$\theta = \sqrt{2n * \Delta n} \qquad \text{eq. III.19}$$

where θ is the numerical aperture, n is the refractive index of the cladding glass (~2.15 in the case of the $70TeO_2$-$10Bi_2O_3$-20ZnO) and Δn is the refractive index difference between the fiber's core and the clad.

The cutback method was employed to characterize the fiber loss, as described by Kaminow *et al.* [Ka, 78]. This method allows one to neglect losses due to any reflection at the "launch fiber / fiber of investigation" junction and losses induced by the imperfect connection between the source and the fiber. The power readings from the meter were

recorded before and after a section of test fiber was removed. The loss was calculated from the difference of two readings and the length of fiber removed, using the following equation:

$$\frac{Log\left(\frac{P_1}{P_2}\right)}{L-l} = dB/m \qquad \text{eq. III.20}$$

where P_1 is the output power recorded using a fiber with length L (cm) and P_2 is the output power recorded using a fiber with length l (cm).

The losses were measured at 635 nm and 1.5 μm using a 635 nm pump laser diode (SDL) from Thorlabs [S1FC635] as a launching source and a HP 83438A Erbium ASE Source, respectively. A Spectra Physics model 404 power meter was used as detector.

III.8 Nucleation and growth

One of the goals of this study was to define the nucleation and growth behavior of the tellurite-based glasses of investigation. Hence, such parameters as nucleation rate, growth rate, activation energy of crystallization and the Avrami exponent were of particular interest.

III.8.1 Determination of the nucleation kinetics

The nucleation-like curves were determined using the method proposed by Marotta et al. [Ma,81]. The maximum of the first exothermic peak was measured at a heating rate of 20°C using the DTA with (T_p) and without (T_{p0}) an isothermal hold (30 minutes for tellurite glasses or 3 hours for lithium di-silicate glass) at T, a potential

nucleation temperature. The 20°C/min heating rate was chosen to prevent the formation of nuclei during the heating of the glass. The nucleation-like curve was then obtained by plotting $\frac{1}{T_p}$ as a function of the temperature used for the isothermal as shown by the equation below:

$$Ln(I_0) = \frac{E_c}{R}\left(\frac{1}{Tp_0} - \frac{1}{Tp}\right) + C \qquad \text{eq. III.21}$$

where I_0 is the steady state nucleation rate, E_c is the activation energy for crystallization which represents the minimum amount of energy to input in order to initiate a reaction, C is a constant term, and R is the gas constant.

The activation energies associated with the glass transition temperature (E_a) and with the crystallization peak (E_c) can be determined by measuring the glass transition temperature, T_g and the maximum of the exothermic peak, T_p, respectively, at different heating rates using the Kissinger equation [El,00].

$$Ln\left(\frac{q}{T_g^{\,2}}\right) = -\frac{E_a}{RT_g} + C \qquad \text{eq. III.22}$$

where q is the heating rate, T_g is the glass transition temperature (T_g in the equation can be replaced by T_p to determine E_c) measured at 5, 10, 15 and 20°C/min, R is the gas constant, and C is a constant term. While this nucleation-like curve does not represent the fully quantitative nucleation rate due to the constant terms which cannot be determined, the temperature dependence remains accurate.

III.8.2 Determination of the growth rate

The growth-like curve was determined using the technique proposed by Ray et al. [Ra,01]. Between 30 to 60 mg of glass powder was heated in the DTA at a heating rate of 20°C/min from room temperature to T, a growth temperature. After 5 minutes at this temperature, the temperature was decreased to a temperature lower than T_g and held for 5 minutes to allow stabilization of the glass and finally the temperature was ramped up to a temperature higher than T_p, the crystallization temperature but lower than T_m, the melting temperature. The area of the exothermic peak (A_T) was then measured. The same experiment was reproduced using various growth temperatures and the growth like curve was then obtained by plotting $\Delta A = A - A_T$, where A is the area of the exothermic peak when no thermal hold at any potential growth temperature is used (i.e. A is the area of the exotherm when the DTA curve is obtained applying a constant heating rate). The changes in the area of the exothermic peak after isothermal hold at a growth temperature can be related to the speed at which the crystals grow in the glass.

III.8.3 Nucleation and growth dimensionality

The Avrami exponent, n, was determined using a DTA. The glass powder, placed in a Pt crucible, was heated to a temperature at which the growth is expected to be relatively slow (based on the growth like curve) and hold for t minutes. The area (A) of the exothermic peak between the on-set time (when crystallization starts) and the time where the peak ends (t_{end}) was then recorded. On the same curve, the area of the curve for time lower than t_{end} was recorded and called A_t. χ was calculated as follow:

$$\chi = \frac{A_t}{A} \qquad \text{eq. III.23}$$

Shown in Figure III.26 is an example illustrating the determination of A_t with t = 20 minutes.

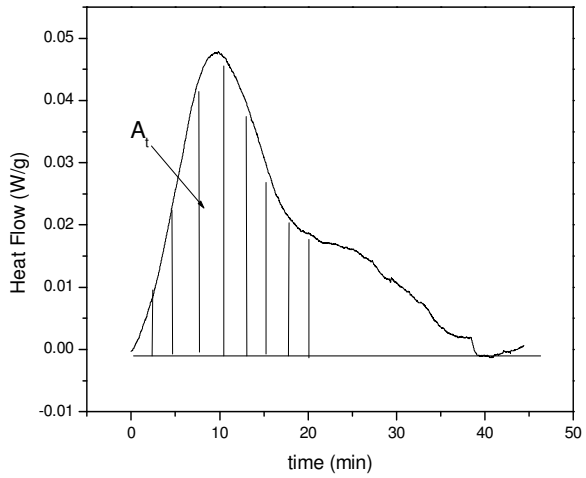

Figure III.26: Heat flow as a function of time for the glass with the composition $70TeO_2$-$10Bi_2O_3$-20ZnO after an isothermal at 410°C

The Avrami exponent, n, can be determined using the equation below [Sa,00] known as the Johnson-Mehl-Avrami equation

$$\chi = 1 - \exp(-Kt^n) \qquad \text{eq. III.24}$$

where χ is the fraction crystallized which reflects the rate of crystallization that includes both the nucleation and growth rate, k is the overall rate of crystallization and t is the duration of the heat treatment. n is determined by plotting Ln(-Ln(1-X))=f(Ln(t)). The plot obtain must be a straight line with slope n. These methods to determine χ and n assume that no nuclei are formed during the heating of smaples.

As mentioned in the previous section the Avrami exponent, n gives an insight of the kind of crystal growth in the glass sample of investigation. Crystals can form at the surface or within the bulk. When the crystals grow within the bulk, crystallization can be 1D, 2D or 3D. The crystallization is labeled 1D when the crystals have a needle like

shape and 3D when the crystals are spherical. The table below lists the various crystallization mechanisms as a function of n. The table proposed by Oz et al. demonstrates the kind of growth as a function of the value of n [Oz,07].

Table III.1: Values of n and m for different crystallization mechanisms during the heat treatment of glass system [Oz,07]

Crystallization mechanism	Kind of growth	n
Bulk crystallization with constant number of nuclei (i.e. the number of nuclei is independent of the heating rate)	1D	1
	2D	2
	3D	3
Bulk crystallization with an increasing number of nuclei (i.e. the number of nuclei is inversely proportional to the heating rate)	Surface Crystallization	1
	1D	2
	2D	3
	3D	4

If n is greater or equal to 2 the growth most probably occurs in the bulk, while if n=1, depending upon the dependence or not of the number of nuclei with heating rate, the growth can be bulk or surface. Christian et al. proposed a more complete table (see table II.1), however it has to be mentioned that none of those tables are exhaustive [Ch,65].

CHAPTER IV: RESULTS

IV.1 Tellurite-based glass processing and characterization

This section focuses on the measurement of the physical, thermal, optical and structural properties of glasses in the TeO_2–Bi_2O_3–ZnO system. The viscosity curves of the various glasses were measured to understand the impact of the changes in the glass structure on the fragility of the glass network and to ascertain evidence of such variation on viscous flow.

IV.1.1 Thermal and physical properties of the investigated glasses

Glasses with the compositions (90-x)TeO_2–10Bi_2O_3–xZnO with x= 25, 20, 17.5, 15 were processed as explained in detail in §III.1. The thermal properties of the glasses, such as the glass transition temperature T_g, the onset of crystallization T_x and the crystallization temperature T_p were measured using a differential thermal analysis (DTA). Figures IV.1a and b present, respectively, the DTA thermogram which shows the position of T_g, T_x and T_p for the glass with x=20, taken as an example and the DTA thermogram of the investigated glasses

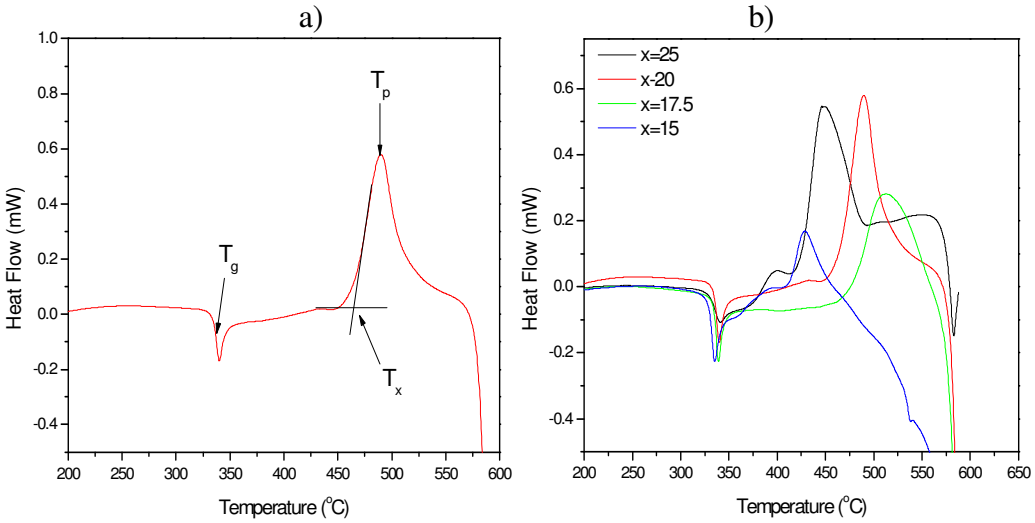

Figure IV.1: (a) DTA thermogram of the glass with x = 20 and (b) of the investigated glasses in the (90-x)TeO_2-10Bi_2O_3-xZnO system using a heating rate of q=10°C/min

The glass transition temperature (T_g) is taken at the inflection point of the endotherm (obtained by taking the first derivative of the curve), and the crystallization temperature (T_p) at the maximum of the exothermic peak. T_x is defined as the onset temperature of the crystallization peak as illustrated in Figure IV.1a. The DTA curve in Figure IV.1b shows only one exothermic peak for the glasses with x=17.5 and 20 and two crystallization peaks for the glasses with x=25 and 15. Table IV.1 summarizes the thermal properties of the glasses under investigation.

Table IV.1: Physical and thermal properties of glasses in the (90-x)TeO_2-10Bi_2O_3-xZnO system

Composition	Density (g/cm^3) ±0.02 g/cm^3	T_g (°C) ±2 °C	1st exothermic peak		2nd exothermic peak		ΔT (T_x-T_g) ±4 °C	CTE (10^{-6}/K) ±0.2x10^{-6}/K (25-300°C)
			T_{x1} (°C) ±2 °C	T_{p1} (°C) ±2 °C	T_{x2} (°C) ±2 °C	T_{p2} (°C) ±2 °C		
x=15	6.18	330	381	405	414	444	T_{x1}-T_g=51	15.0
x=17.5	6.17	333	N/A		476	512	T_{x2}-T_g=143	15.1
x=20	6.16	337	N/A		463	490	T_{x2}-T_g=126	15.4
x=25	6.15	337	376	404	424	457	T_{x1}-T_g=39	15.6

As seen above, T_g increases with increasing x. T_{x1} is higher for the glass with x=15 whereas T_{p1} does not seem to vary when x increases from 15 to 25. T_{x2} and T_{p2} decrease when x increases from 17.5 to 25. The glass with x = 15 exhibits the lowest T_{x2} and T_{p2}. The density of the glasses decreases and the coefficient of thermal expansion (CTE) increases when x increases.

The activation energies associated with the glass transition temperature (E_a) and with the crystallization peak (E_c) were determined using the Kissinger equation by measuring at different heating rates, T_g and T_p, respectively [Ki,57].

$$Ln\left(\frac{q}{T_g^{\,2}}\right) = -\frac{E_a}{RT_g} + Constant \qquad \text{eq.IV.1}$$

where q is the heating rate, T_g is the glass transition temperature measured at 5, 10, 15 and 20^{o}C/min and R is the gas constant. (T_g in equation IV.1 can be replaced by T_p to determine E_c)

DTA scans were measured using 5, 10, 15 and 20 ^{o}C/min heating rates. Figure IV.2a presents the DTA thermograms of the glass with x =20, taken as an example, measured using various heating rates.

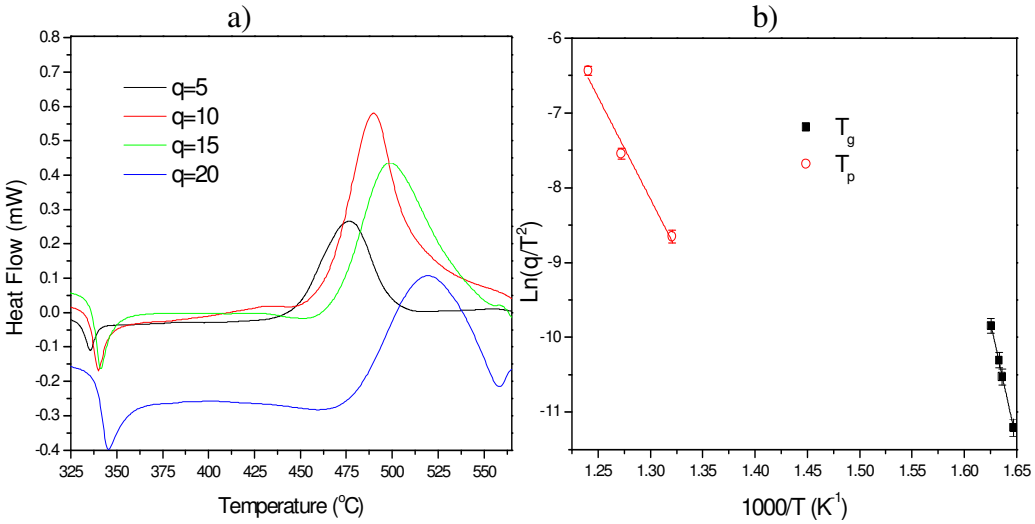

Figure IV.2: (a) DTA thermogram of the glass with x =20 as a function of the heating rate and (b).plot of $Ln\left(\frac{q}{T_p^2}\right)$ and $Ln\left(\frac{q}{T_g^2}\right)$ as a function of Tp^{-1} and Tg^{-1}

As the heating rate increases, T_g and T_p shift toward higher temperature as one would expect due to the thermal lag in the similar size samples of glass (50 mg) with increasing heating rate[Mo,93]. The baseline offset seen for the thermogram obtained using q= 20°C/min is an artifact of the measurement. Figure IV.2b presents the plot of $Ln\left(\frac{q}{T_p^2}\right)$ as a function of $1000/T_p$ (in red) and of $Ln\left(\frac{q}{T_g^2}\right)$ as a function of $1000/T_g$ (in black) for the glass with x=20, taken as an example. These plots results in a straight line which, from Equation IV.1, yields a slope corresponding to $-\frac{E_c}{R}$ and $-\frac{E_a}{R}$, respectively [Ki,57]. The same experiment was repeated for all the investigated glasses and values determined for (i) E_a, the activation energy for T_g, and (ii) E_{c1} and E_{c2} the activation energies for T_{p1} and T_{p2}, respectively, are summarized in Table IV.2.

Table IV.2: Activation energies associated with the glass transition temperature (E_a) and with the crystallization peaks (E_{c1} and E_{c2}) of the glasses in the (90-x)TeO_2-10Bi_2O_3-xZnO system

Composition	E_a (KJ.mol^{-1}) (±50 KJ.mol^{-1})	E_{c1} (KJ.mol^{-1}) (±50 KJ.mol^{-1})	E_{c2} (KJ.mol^{-1}) (±50 KJ.mol^{-1})
x=15	476	305	195
x=17.5	476	N/A	144
x=20	531	N/A	128
x=25	602	257	241

The activation energy E_a increases progressively with increasing x whereas E_{c1} decreases when x increases from 15 to 25. The glasses with x =17.5 and 20 exhibit similar E_{c2}, as do glasses with x=15 and 25, within the accuracy of the measurement (50 KJ/mol)

IV.1.2 Optical properties of the investigated glasses

The visible and near-infrared absorption spectra of the glasses are reported in Figure IV.3a and b, respectively. Shown is the absorption coefficient as a function of wavelength for the glasses of investigation.

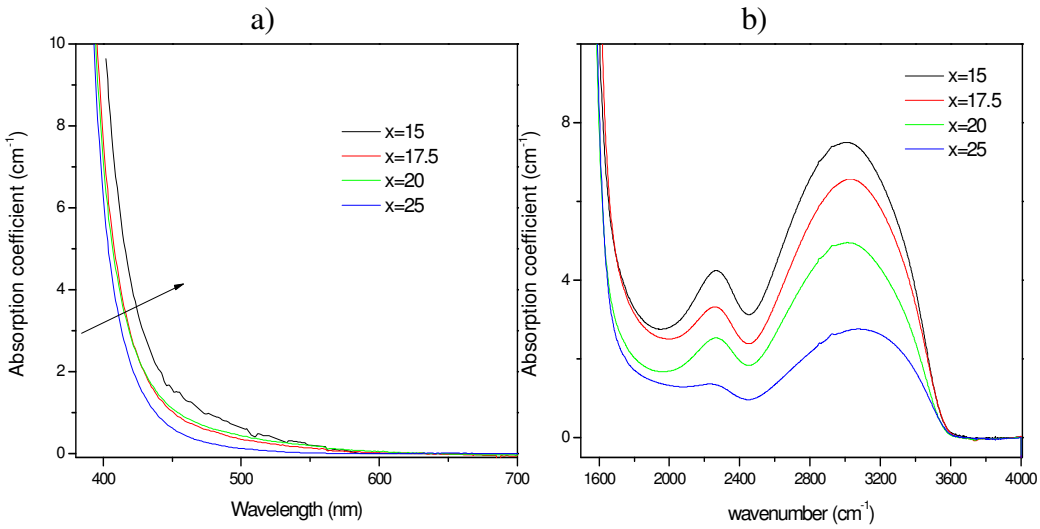

Figure IV.3: (a) Visible and (b) near-infrared absorption spectra of the glasses in the (90-x)TeO_2-10Bi_2O_3-xZnO system

When x decreases, the optical band gap progressively shifts to longer wavelength. The shift of the band gap wavelength of the investigated samples defined as the wavelength for which the linear absorption coefficient is 10 cm^{-1} (λgap) was estimated to be ~ 10nm. As seen in Figure IV.3b, all spectra exhibit a similar broad absorption band between 2,500 cm^{-1} and 3,700 cm^{-1} and an absorption band centered at ~2,250cm^{-1}. The amplitude of both bands decreases in intensity with the progressive increase of x.

The refractive index dispersion was studied as a function of x. The measurements were conducted in collaboration with Dr. C. Rivero-Baleine at Lockheed-Martin. Figure IV.4 presents the refractive index of the investigated glasses as a function of the wavelength.

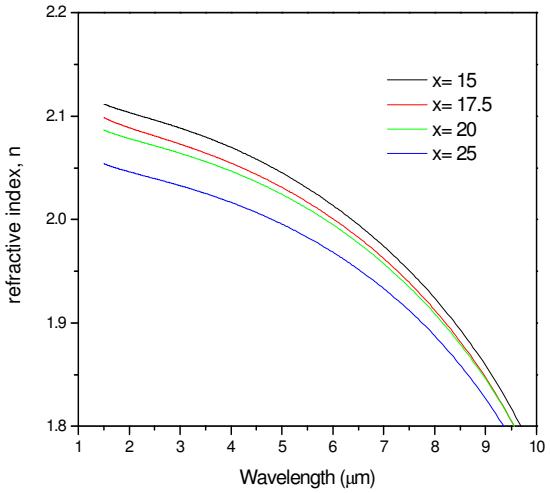

Figure IV.4: Refractive index dispersion of the glasses in the (90-x)TeO_2-10Bi_2O_3-xZnO system

As seen above, the refractive index progressively decreases with an increase of x.

IV.1.3 Structural properties of the investigated glasses

The structural properties of the glasses as a function of x were investigated using Raman spectroscopy. The measurements were conducted in collaboration with Dr. C. Rivero-Baleine at Lockheed-Martin using a 532nm excitation. The Raman spectra of the glasses are shown in Figures IV.5. All the spectra were normalized to the band located at 770cm^{-1}.

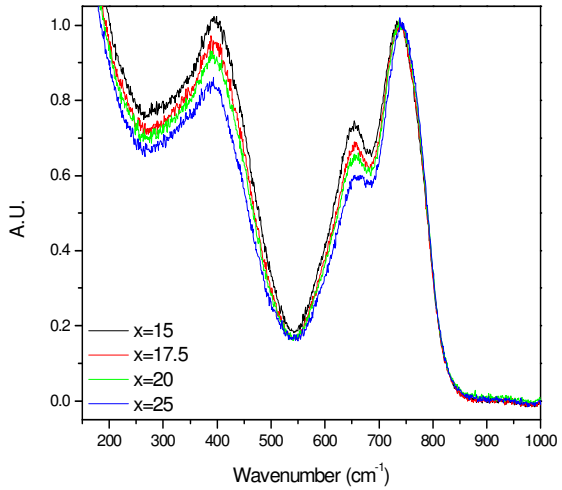

Figure IV.5: Raman spectra of the glasses in the (90-x)TeO_2-10Bi_2O_3-xZnO system.

Several bands can be seen in three main wavenumber ranges: 720-780, 610-680, and 380-450 cm^{-1}. As seen in Figure IV.5, when x increases, the intensity of the band at 415 cm^{-1} decreases while the band at 730 cm^{-1} increases in amplitude and shifts to higher wavenumber when compared to the band at 660 cm^{-1}.

IV.1.4 Measurement glass viscosity

The viscosity of the investigated glasses was measured from Log 5 Pa.s to Log 12 Pa.s using a beam-bending and a parallel-plate viscometer. Figure IV.6 shows the Log η of the investigated glasses as a function of temperature.

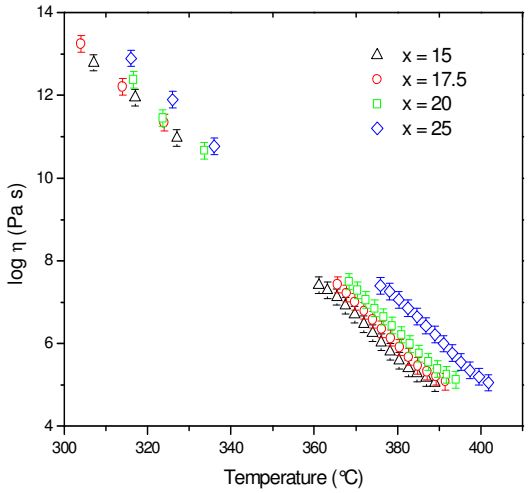

Figure IV.6: Log η of the glasses in the (90-x)TeO_2-10Bi_2O_3-xZnO system as a function of the temperature

It can be noted that as x increases, the Log η of the glasses shifts to higher temperatures.

The activation energy for viscous flow, E_η, an indication of the energy required to sever sufficient bonds within the glass network to initiate "flow", was calculated in the range of Log 9.0 Pa.s and Log 13.0 Pa.s using the following equation [Sh,05]

$$\eta = A_\eta \exp\left(\frac{E_\eta}{RT}\right) \qquad \text{eq. IV.3}$$

where η is the viscosity, A_η is a constant, R is the ideal gas constant, and T is the temperature (K).

Figure IV.7 shows the Ln η as a function of 1/T in the Log 9 Pa.s – Log 13 Pa.s range of the investigated glasses.

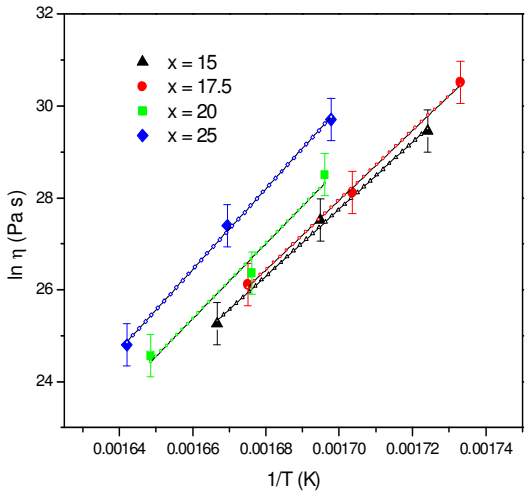

Figure IV.7: Ln η as a function of 1/T in the range Log 9 – Log 13 Pa.s of the glasses in the (90-x)TeO_2-10Bi_2O_3-xZnO system . Also shown are the linear fits

These plots yield a straight line which, from Equation IV.3, possesses a slope corresponding to $-\frac{E_a}{R}$. From the activation energy for viscous flow, it is possible to calculate the fragility parameter, which is a common classification of the sensitivity in the temperature dependence of the viscosity for glass-forming liquids. The fragility parameter, m, was calculated using the following equation [Mc,00] [Du,06]

$$m \cong \frac{E_\eta}{RT_{12}Ln(10)} \qquad \text{eq.IV.4}$$

where T_{12} is the temperature corresponding to a viscosity of Log 12 Pa.s, known as the annealing point temperature.

Table IV.3 summarizes the values of the activation energy for viscous flow E_η, T_{12} the temperature corresponding to Log 12 Pa.s, referred to as the glass' annealing point temperature, and the kinetic fragility parameter, m, of the investigated glasses.

Table IV.3: Activation energy, E_η, T_{12}, and the kinetic fragility parameter, m for glasses in the (90-x)TeO_2-10Bi_2O_3-xZnO system

Composition	m±2	E_η ±16(KJ·mol^{-1})	T_{12}±2 (^{o}C)
x = 15	54	609	316
x= 17.5	56	630	317
x = 20	60	679	319
x = 25	64	731	325

In agreement with the shift of the Log η of the glasses to high temperatures with an increase of x seen in Figures IV.6, T_{12} increases when x increases. One can notice also that the activation energy for viscous flow, E_η, and m increase with an increase of x.

IV.2 Nucleation and growth behavior of the glasses

This section focuses on the determination of the nucleation and growth temperature ranges and on the maximum of nucleation and growth rates of the investigated glasses. First the methods used in this study to define the nucleation- and growth-like curves of the investigated glasses were tested using lithium di-silicate as a reference material since this glass has been well studied. Then, we present the study of the nucleation and growth behavior of glasses in the (90-x)TeO_2-10Bi_2O_3-xZnO system with the determination of the parameters such as activation energy for crystallization, Johnson-Mehl-Avrami (JMA) exponent, and nucleation and growth regimes and rates of these glasses have not been discussed.

IV.2.1 Validation of method using lithium disilicate

Lithium di-silicate glass (LS2) was used as a reference sample to validate the techniques used to define the nucleation and growth behavior of the investigated glasses.

Nucleation-like curve of Lithium Disilicate (LS2)

Marotta et al. and Ray et al. developed various methods to rapidly provide semi- or fully quantitative estimates of crystal nucleation rates with a minimum of effort [Da,03] [Ma,81] [Ra,00]. A complete description of the techniques can be found in §III. Differential thermal analysis (DTA) was employed to determine the nucleation-like curves. Figure IV.8 presents the DTA scan obtained for a LS2 powder heated up to 1000°C using a heating rate of 20 °C/min.

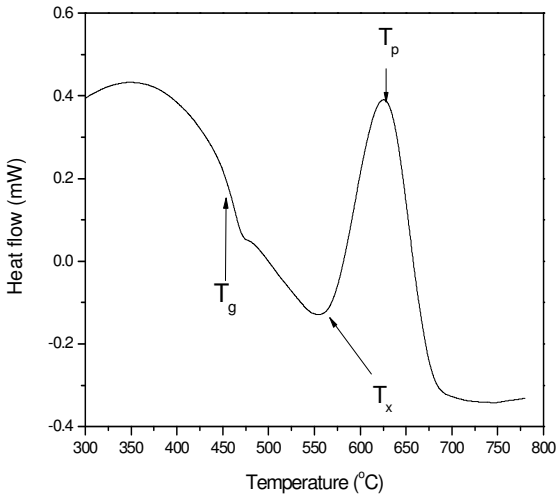

Figure IV.8: DTA thermogram of the lithium disilicate glass.

The DTA curve shows only one exothermic peak. T_g was measured at (457±2) °C, T_x at (581±2) °C and T_p at (642±2) °C. As suggested by Ray et al. [Ra,97] and Marotta et al [Ma,81], the nucleation-like curve was obtained by tracking the position of T_p and the height of the exotherm peak (δT_p) when the glass powder is heated using a 20 °C/min heating rate in the DTA to T_n, a temperature ranging from T_g to 500 °C and was hold at this temperature for a period of time of 3 hours to nucleate the glass [Ra,97]. Figure IV.9 presents the plots of δT_p and T_p^{-1} as a function of T_n.

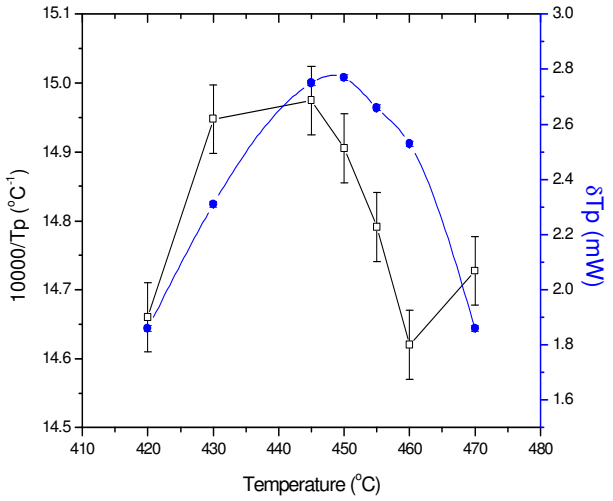

Figure IV.9: Tp^{-1} and δT_p of LS2 glass as a function of temperature.

Both curves exhibit, in the accuracy of the measurement, the same maximum measured at (445±2) °C and slightly different temperature range.

Growth-like curve of Lithium Disilicate (LS2)

As explained in the §III.8, to obtain the growth-like curve, the glass was heat treated using a heating rate of 20°C/min to various potential growth temperatures and held at these temperatures for 5 minutes. The growth-like curve is obtained by plotting $\Delta A = A - A_T$, where A_T and A are the area of the exothermic peak with and without a thermal hold at the potential growth temperatures. ΔA of LS2 glass is plotted in Figure IV.10 as a function of the heat treatment temperature.

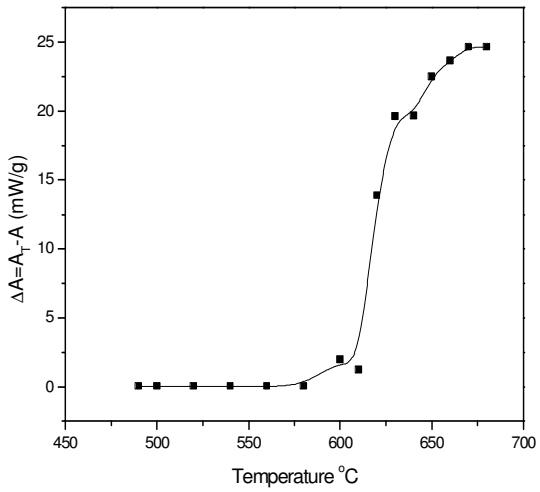

Figure IV.10: ΔA of LS2 glass as a function of temperature.

As seen above, the growth-like curve of LS2 does not exhibit a maximum. The onset of the growth-like curve occurs at (571±2) °C.

IV.2.2 Nucleation and growth behavior of (90-x)TeO_2-10Bi_2O_3-xZnO glasses

Nucleation- and growth-like curves

As performed for LS2 glass, the nucleation- and growth-like curves of the investigated glasses were determined using Ray's and Marotta's methods. The glasses were heated using a 20 °C/min heating rate to T_n, a temperature ranging from T_g to 500°C and were held at this temperature for a period of time of 3 hours. Figure IV.11 presents a plot of δT_p and T_p^{-1} as a function of T_n for the glass with x=20, taken as an example.

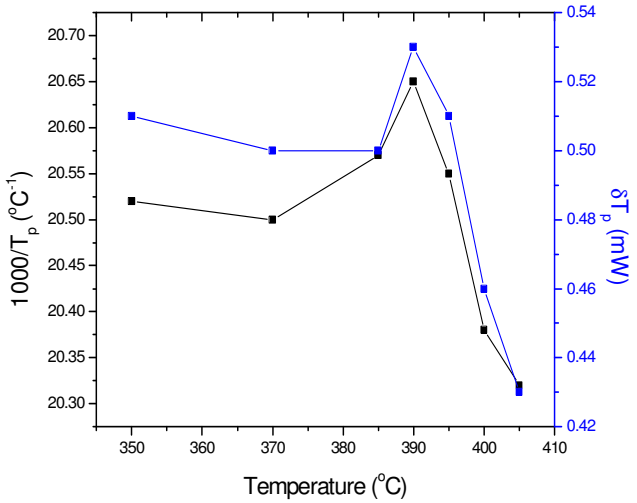

Figure IV.11: Tp^{-1} and δT_p of the glass with x = 20as a function of temperature

As seen for LS2, the 2 curves exhibit similar shape and within the accuracy of the measurement, the same maximum measured at (390±2) ^{o}C. The same experiment was reproduced for all the glasses and no differences between the two plots could be seen for any of the glasses. The nucleation- like curves of the investigated glasses are presented in Figure IV.12.

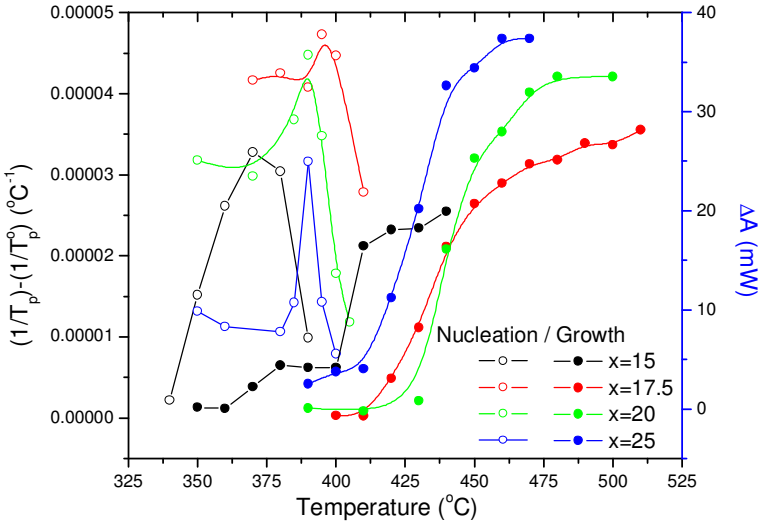

Figure IV.12: Nucleation- and growth-like curves of the investigated glasses in the (90-x)TeO_2-10Bi_2O_3-xZnO system

All the nucleation-like curves present a maximum, commonly called the temperature of maximum nucleation ($T_{n\ max}$), which decreases from (397±2) °C to (389±2) °C when x increases from 17.5 to 25. The glass with x=15 exhibits its temperature of maximum nucleation at (370±2) °C which is the lowest of the $T_{n\ max}$.

As performed for LS2, the growth-like curves of the tellurite-based glasses were determined by heat treating the glasses using a heating rate of 20°C/min to various potential growth temperatures and holding the glasses for 5 minutes at these temperatures. The growth-like curves, presented in Figure IV.12, were obtained by recording the areas of the exothermic peak with and without thermal hold at the potential growth temperatures. As seen above, though the growth like curves of the glasses do not exhibit maxima, they do show a pronounced increase in growth rate at a temperature just over 400°C.

Crystal growth rate

Glass samples were heat treated in a furnace, at their respective $T_{n\ max}$ for various times, and examined with an optical microscope for evidence of crystals. Figures IV.13a, b and c present optical micrographs of the glass with x=20, taken as an example, heat treated at 390°C, its temperature of maximum nucleation, for 4, 8 and 39h, respectively.

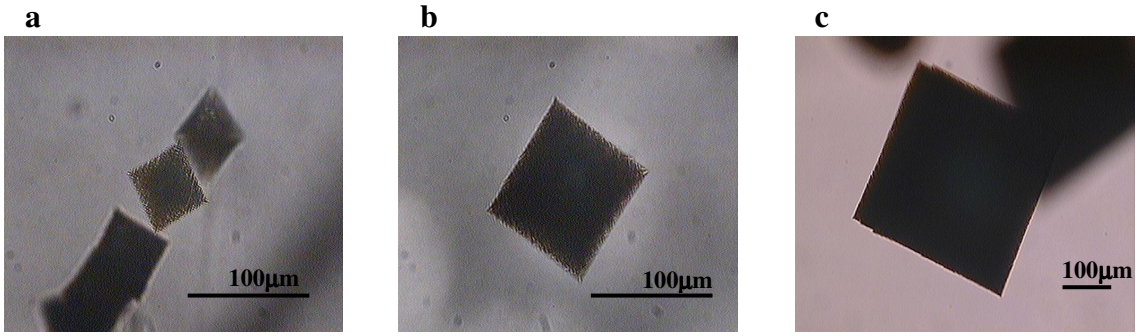

Figure IV.13: Optical microscope images of crystal seen in the glass with x = 20 heat treated at 390°C for (a) 4, (b) 8 and (c) 39hrs. These micrograph were taken using plane polarized light with a 50X (a and b) and a 20X objective (c)

The micrographs depict crystals with a square shape in the glass after heat treatment with a size that increases from (~68±7) µm to (~408±54) µm when the heat treatment time increases from 4 to 39 hours. The same experiment was conducted when the glass was heat treated at both 400 and 405°C and crystals diagonals were measured at each temperature as a function of heat treatment time, and a growth rate calculated. Figure IV.14a presents the variation of the crystal size observed in the glass with x = 20 when heat treated at 390, 400 and 405 °C as a function of the heat treatment duration.

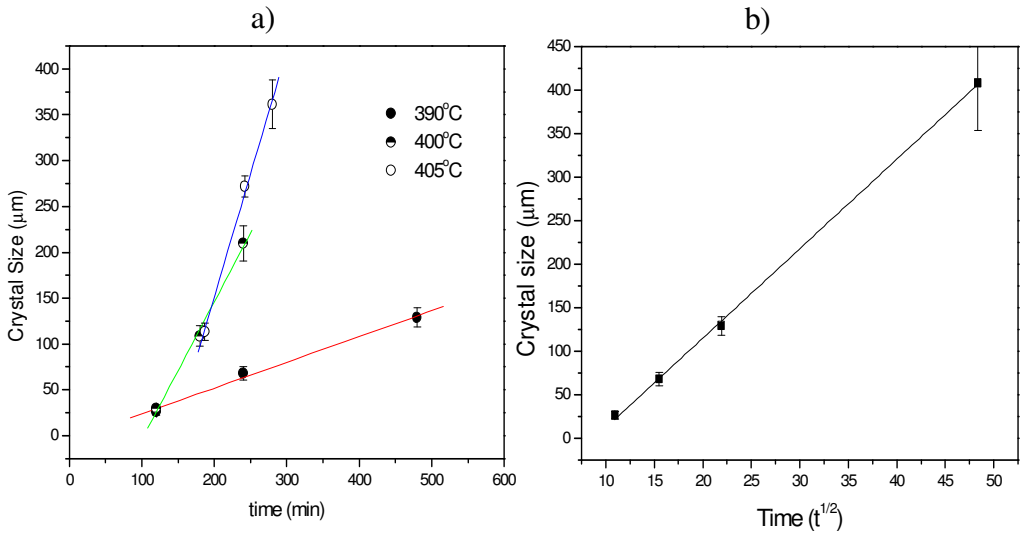

Figure IV.14: (a) Crystal size as a function of t and (b) as a function of $t^{1/2}$

For short heat treatment times, the crystal size as a function of the heat treatment duration (t) is well supported by a straight line. However this linearity is no longer true for long heat treatment times (not shown here). Figure IV.14b presents the variation of the crystal size observed in the glass with x = 20 when heat treated at 390 °C as a function of $t^{1/2}$ for an extended heat treatment duration (>39 hrs). It is clearly shown that the crystal size is well supported by a straight line when plotted as a function of $t^{1/2}$.

The slope of the linear fit for short heat treatment represents the growth rate (U) as suggested by [Ma,06]; it increases from (0.26±0.02) µm/min when the glass is heat treated at T=390 °C to (2.80±0.02) µm/min when the temperature of the heat treatment is increased to 405°C. The same experiments were repeated for all the investigated samples heat treated at various heat treatment temperatures and Figure IV.15 shows the resulting growth rate of the crystals forming as a function of the heat treatment temperature.

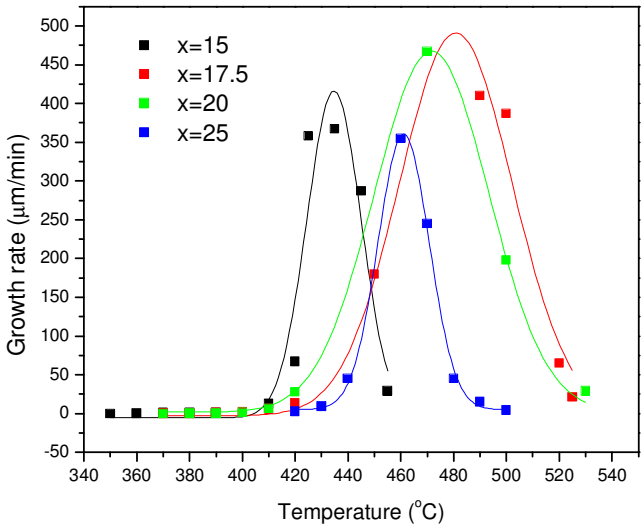

Figure IV.15: Growth rate of the crystal forming in the investigated glasses in the (90-x)TeO_2-10Bi_2O_3-xZnO system as a function of temperature

One can notice that the temperature of maximum growth rate progressively decreases from (481±2) °C to (461±2) °C and the maximum growth rate at these temperatures decreases, progressively, from (489±4) to (360±19) µm/min when x increases from 17.5 to 25. The glass with x =15 exhibits the lowest temperature of maximum growth measured at (435±2°C) and a maximum growth rate of (417±17) µm/min at this temperature. The temperature width of the growth rate curve is the largest for the glasses with x = 17.5 and 20.

Nucleation rate

As explained in detail in §III.8, the quantitative nucleation rate was obtained using the method developed by Ranasinghe et al. [Ra,02]. The glasses were first heat treated at a potential nucleation temperature T_n for t_n minutes to form nuclei and then at T_G, a higher temperature in the growth range temperature, for a time t_G to grow the

crystals. Finally, the glasses were heated up to 600 °C using a 20 °C/min heating rate to measure the exothermic peak which is the thermal signature of the partially crystallized sample. If reproduced for various t_n, it is then possible to determine I_n and N_q by plotting $I_n t_n+N_q$ as a function of t_n using the Equation II.32. Figure IV.16a shows the plot of $I_n t_n+N_q$ as a function of t_n when the glass with x = 20 was nucleated at 390°C.

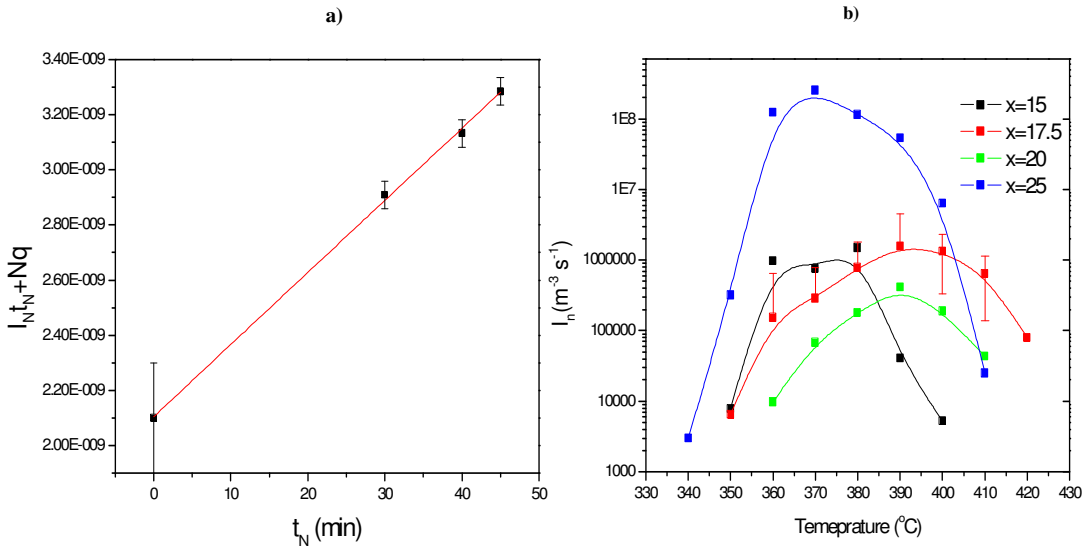

Figure IV.16: (a) Number of nuclei ($I_n t_n+N_q$) formed at 390°C in the glass with x =20 as a function of nucleation heat treatment time (t_n) and (b) nucleation rates of the investigated glasses in the (90-x)TeO_2-10Bi_2O_3-xZnO system as a function of temperature.

As seen above, the plot of $I_n t_n+N_q$ as a function of t_n describes a straight line, the slope of which corresponds to I_n, the nucleation rate, and the intercept is representative of N_q, the number of nuclei present in the as-quenched glass. When reproduced for diverse temperatures of nucleation (T_n), it is then possible to fully determine the nucleation rate curve as a function of the nucleation temperature as illustrated in Figure IV.16b. Similar experiments were reproduced for all of the investigated glasses and Table IV.4 lists the value of N_q, the number of nuclei in the as-quenched glass and I_n, the nucleation rate determined at a specific isothermal temperature T_n, and over a wide temperature range.

Table IV.4: Maximum Nucleation rates ($I_{n\text{-}max}$) and number of quenched-in nuclei (N_q) determined for a specific nucleation temperature and for a wide range of potential nucleation temperatures of glasses in the (90-x)TeO_2-10Bi_2O_3-xZnO system

Glass Composition	Isothermal			Over the nucleation range		
	T (^oC)	$I_{n\text{-}max}$ ($m^{-3}.s^{-1}$)	N_q (m^{-3})	T (^oC)	I_n($m^{-3}.s^{-1}$)	N_q (m^{-3})
x=15	370	$8.7\ 10^5$	$7.99\ 10^6$	350-400	$7.96\ 10^3$ – $9.54\ 10^6$	$7.22\ 10^6$ – $15.0\ 10^6$
x=17.5	390	$1.45\ 10^6$	$1.21\ 10^{10}$	350-420	$6.4\ 10^3$ – $1.6\ 10^6$	$0.98\ 10^{10}$- $1.76\ 10^{10}$
x=20	390	$3.16\ 10^5$	$2.19\ 10^9$	360-410	$9.3\ 10^3$ – $3.91\ 10^5$	$1.9\ 10^9$ – $2.38\ 10^9$
x=25	370	$2.07\ 10^8$	$3.97\ 10^{12}$	340-410	$2.7\ 10^3$ – $2.68\ 10^8$	$3.6\ 10^{12}$- $4.23\ 10^{12}$

While the nucleation rates (I_n) lie in the same range of values for x varying between 15 to 20, it increases dramatically for the glass with x = 25. The number of nuclei in the as-quenched glass is the lowest in the glass with x=15 and the largest in the glass with x=25.

JMA exponent

As explained in the §III.8.3, the JMA exponent was determined from the volume of glass crystallized using the Equation III.24 which can be measured by heat treating the glass for a time t at a temperature high enough to induce the formation of crystals. Typically, the temperature of the isothermal is close to T_p. Figure IV.17a illustrates the DTA scan of the glass with x = 20 heat treated during t min at 420^{o}C. From this heat flow curve, it is possible to estimate the volume of glass crystallized, using the equation III.24, from the beginning to the end of the isothermal hold at 420^{o}C. Figure IV.17b shows the plot Ln(-Ln(1-χ)) as function of Ln(t).

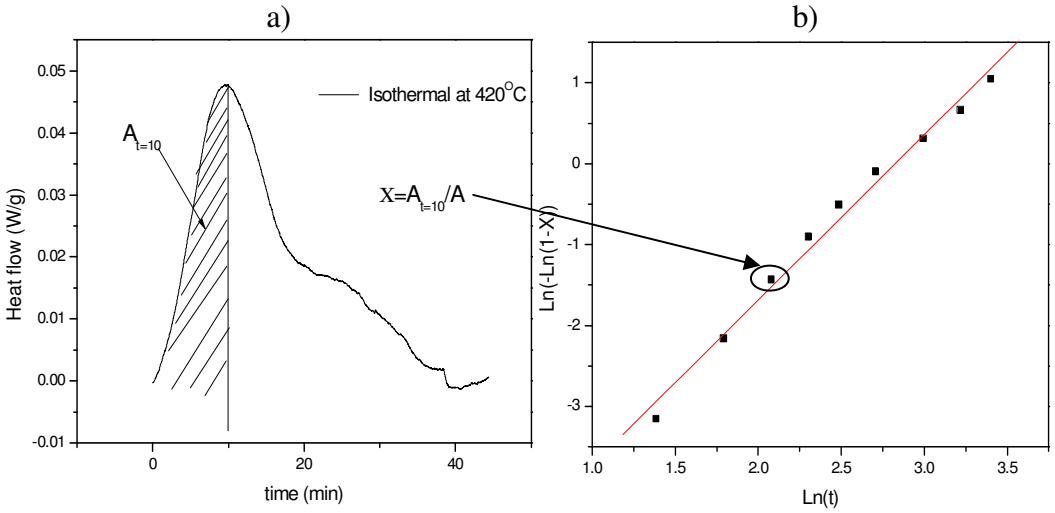

Figure IV.17: (a) Example of a DTA thermogram of the glass with x = 20 heat treated at 420°C for t minutes and (b) Ln(-Ln(1-χ)) as function of Ln(t).

As predicted by the Avrami's equation (Equation III.24), the plot Ln(-Ln(1-χ)) as function of Ln(t) yields a straight line, the slope of which is the Avrami exponent or also called JMA exponent, n. The JMA exponent of the glass with x = 20 was measured at 2.0 when heat treated at 420°C. The same experiments were reproduced for all the investigated glasses and the values of their respective n are listed in Table IV.5.

Table IV.5: JMA exponent of the investigated glasses in the (90-x)TeO_2-10Bi_2O_3-xZnO system

Composition	JMA exponent 1st exothermic peak ±0.1	JMA exponent 2nd exothermic peak ±0.1
x=15	1.55	1.7
x=17.5	N/A	1.9
x=20	N/A	2.0
x=25	1.61	2.2

n slightly increases with an increase of x.

Crystalline phase identification.

Hot stage XRD measurements were performed on the glasses to define the crystalline phases formed during the heat treatment at various temperatures, in collaboration with Dr. S. Misture at Alfred University. The samples were heat treated in-situ at 20^{o}C/min and were held for 5 minutes at various temperatures in the 350-600 ^{o}C range. The XRD patterns of the glasses are presented in Figures IV.18.

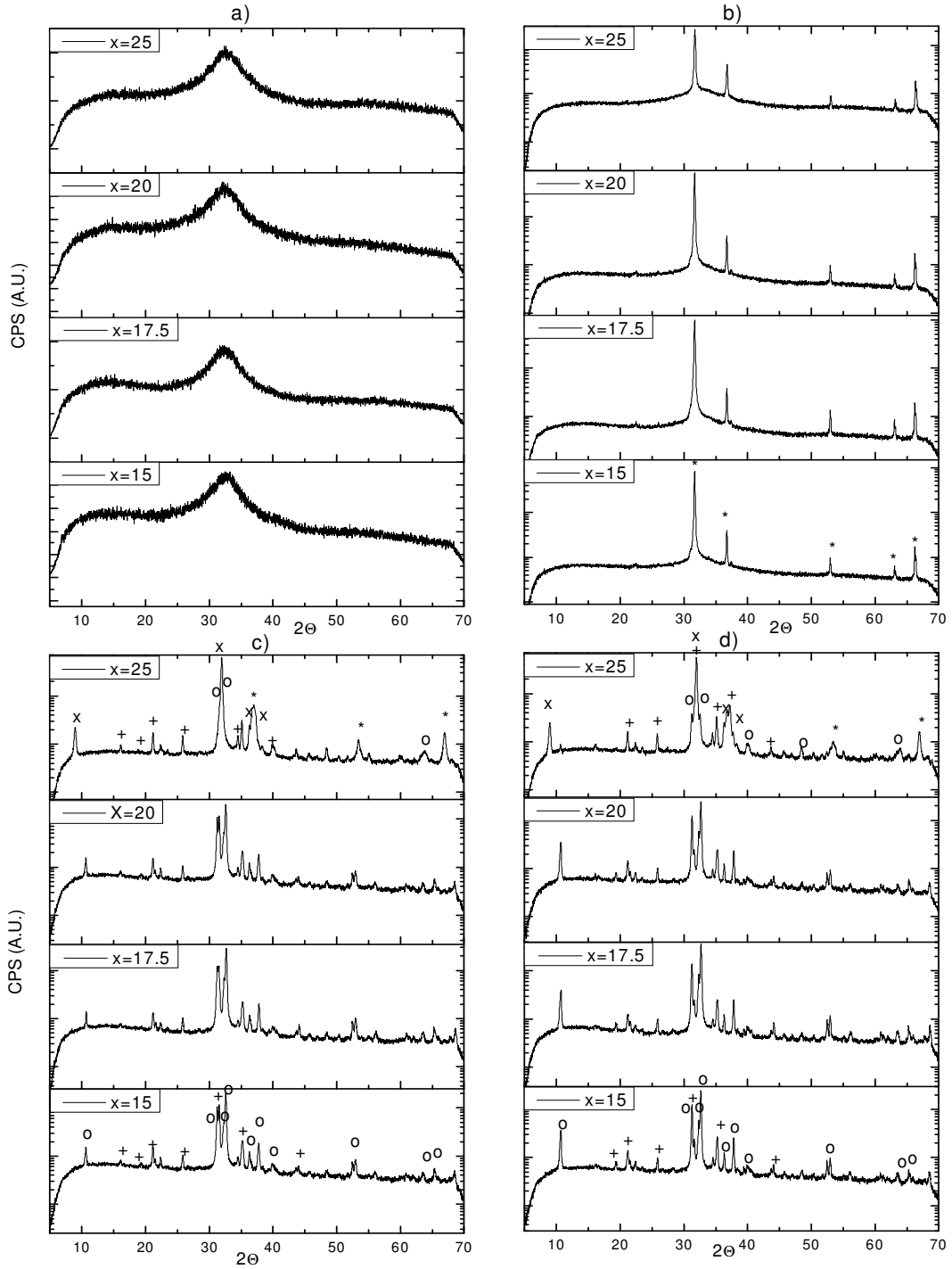

Figure IV.18: XRD patterns of the investigated glasses in the (90-x)TeO_2-10Bi_2O_3-xZnO system measured (a) at room temperature and (b) when heat treated at the glasses respective temperature of maximum nucleation rate, (c) at 425°C and (d) at 500°C. (Peak attributions: * Bi_2O_3, + $Zn_2Te_3O_8$, o $Bi_2Te_4O_{11}$ and x $Bi_2Te_2O_7$)

Figures IV.18a present the XRD patterns recorded at room temperature. The patterns show a broad peak centered at $2\Theta=32.3^{o}$ for all 4 glasses. Figures IV.18b illustrates the XRD patterns of the glasses heat treated at their respective temperatures of maximum nucleation. Compared to the spectra in Figure IV.18a, the broad band decreases in intensity and sharp peaks at $2\Theta=$ 31.69, 36.79, 52.94, 63.02 and 66.23^{o} appear. Shown in Figure IV.18c are the XRD patterns of the glasses heat treated at 425^{o}C. Compared to the XRD patterns shown in Figure IV.18b, new peaks at $2\Theta=$21.06, 25.79, 31.45, 36.64 and 40.01^{o} and $2\Theta=$ 10.67, 19.35, 31.18, 32.59, 36.29, 37.77, 39.93, 43.67, 44.00, 65.29 and 68.48^{o} appear. The XRD pattern of the glass with x =25 exhibits additional peaks located at $2\Theta=$8.95, 36.29, 37.29 and 53.40^{o}. Lastly, the XRD patterns of the glasses heat treated at 500^{o}C are depicted in Figure IV.18d. Compared to the peaks exhibited in the XRD patterns in Figure IV.18c, the peaks at 31.69, 36.79, 52.94, 63.02 and 66.23^{o} decrease in amplitude. These peaks were found to completely disappear when the heat treatment temperature increased to 550^{o}C (not shown here). The peaks at $2\Theta=$ 10.67, 19.35, 31.18, 32.59, 36.29, 37.77, 39.93, 43.67, 44.00, 65.29 and 68.48^{o} as well as the peaks at $2\Theta=$21.06, 25.79, 31.45, 36.64 and 40.01^{o} increase in intensity compared to those shown in Figure IV.18c.

IV.2.3 Effect of controlled nucleation and growth on the physical/thermal and optical properties of glasses with x=20.

Glasses with x = 20 were heat treated at 390^{o}C, the temperature of maximum nucleation from 4 to 39 hours. As expected, crystals formed in the glasses. Using an optical microscope, the size of the crystals was measured. The table below summarizes

the size of the crystals formed as a function of the heat treatment duration as well as the physical, mechanical and thermal properties of the heat treated glasses.

Table IV.6: Physical, thermal and mechanical properties of glasses with x = 20 as a function of heat treatment time at T=390°C

duration of the heat treatment	Crystal Size µm	Density (g/cm^3) ±0.02 g/cm^3	T_g (°C) ±2°C	T_p (°C) ±2°C	CTE (10^{-6}/K) ±0.2x10^{-6}/K 25°C≤T≤250°C	H_v (MPa)
70TeO_2-10Bi_2O_3-20ZnO, T=390°C						
0h	NA	6.16	334	482	15.1	301±21
4h	68±7	6.16	331	483	16.1	326±16
8h	129±19	6.20	330	481	16.2	339±8
39h	408±54	6.25	329	475	16.0	344±11

As seen in the table above, the size of the crystals, the density and the hardness increase as the duration of the heat treatment increases. It is interesting to notice that the density does not vary when the glass sample is heat treated for only 4h. The T_g and T_p of the glass decreases slightly from (334±2) °C to (329±2) °C with the progressive increase in the heat treatment duration. Lastly the thermal expansion coefficient (CTE) of the glass sample increases after a short heat treatment time (4 hours) and then remains constant when the glass is heat treated up to 39 hours. .

Figures IV.19a and b present the IR spectra and the UV-VIS spectra of the heat treated glasses, respectively. Also shown are the spectra of a glass heat treated at 405°C for 4 hours.

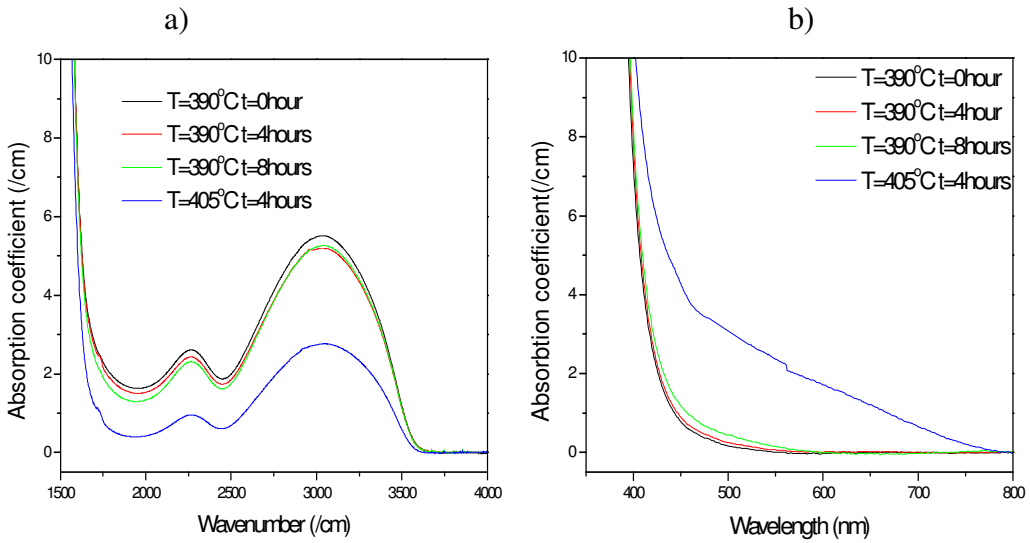

Figure IV.19: (a) Visible and (b) near-infrared absorption spectra of glasses with x = 20 heat treated at 390°C for t hours and heat treated at 405°C for 4 hours.

The spectra in Figure IV.19a exhibit similar bands seen in Figure IV.3b. The amplitude of the absorption band centered at 3,025 cm^{-1} decreases progressively as the heat treatment duration increases. As seen in Figure IV.19b, there is no significant variation in the optical band gap when the glass is heat treated at 390°C. However, a shift of the optical band gap was measured when the glass is heat treated at 405°C. (The band gap of the sample heat treated for 4 hours at 405°C exhibit a tail in the 400-700nm wavelength range.

IV.3 Fiber processing and characterization

In this section, we explain how to prepare core and core-clad preforms and fibers in the TeO_2-Bi_2O_3-ZnO system. The effect of fiber drawing on the thermal and structural properties of the glass is studied. The optical properties of a core-clad fiber, such as numerical aperture and loss at 632 nm and 1.55 μm, are presented. Lastly, the nucleation and growth behavior of glass-fibers are compared with that of the preform.

IV.3.1 Core preform and fiber processing

Core preforms with the composition $70TeO_2$-$10Bi_2O_3$-$20ZnO$ (x = 20) were processed using the technique described in the §III.6. The preforms within this glass composition were found to exhibit good thermal mechanical resistance to casting (shock, fracture). After annealing, the preforms were sliced into cross-sections which were polished and inspected using an optical microscope. No apparent crystallization in the rods was observed in the core preform using an optical microscope and no crystallization peak was observed in the XRD pattern of the cross-sections confirming the absence of crystallization in the core preform. No variation in the density and absorption band gap, within the accuracy of the measurements, were measured between the cross-sections.

The preforms were drawn into fibers with a diameter of 125 µm using the technique described in the §III.6.3.

The thermal properties such as the glass transition temperature T_g, the onset of crystallization T_x and the crystallization temperature T_p of the fiber were measured using a DTA and were compared to those of the corresponding bulk. Figure IV.20 presents the DTA thermograms of the bulk and fiber glasses with x=20. In order to compare the thermal properties of the fiber with those of the bulk glass, both materials were crushed into powder having similar grain size (~400µm).

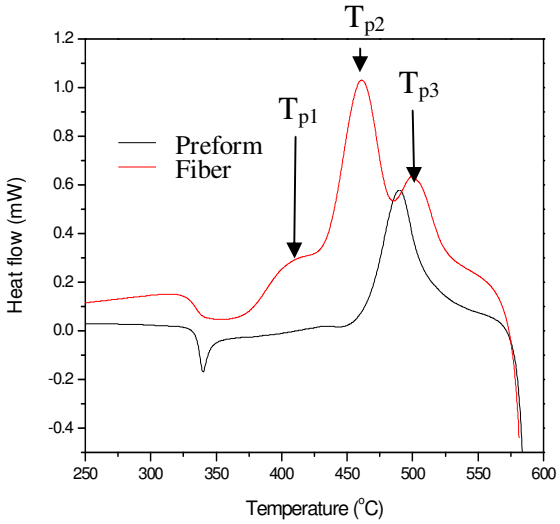

Figure IV.20: DTA thermograms of the bulk glass with x=20 and the corresponding fiber.

The DTA curve for the bulk glass shows only one exothermic peak while 3 crystallization peaks can be seen for the glass fiber. Table IV.7 summarizes the thermal properties of the preform and fiber.

Table IV.7: Thermal properties of the glass with x=20 and the corresponding fiber.

Material	**T_g (°C) ±2 °C**	**1st exothermic peak**		**2nd exothermic peak**		**3rd exothermic peak**		**$\Delta T=T_x-T_g$ (°C) ±4 °C**
		T_{x_1} (°C) ±2 °C	**T_{p1} (°C) ±2 °C**	**T_{x_2} (°C) ±2 °C**	**T_{p2} (°C) ±2 °C**	**T_{x_3} (°C) ±2 °C**	**T_{p3} (°C) ±2 °C**	
Preform	336	NA	NA	463	490	NA	NA	$T_{x2}-T_g=127$
Fiber	334	371	399	423	447	465	480	$T_{x1}-T_g=39$

The preform and fiber exhibit similar T_g., within the accuracy of the measurement. However, T_{x2} and T_{p2} of the fiber are lower than those of the bulk glass.

Moreover, one can notice that ΔT, the difference between T_g and the first onset of crystallization peak, decreases from 127 to 39°C when the preform is drawn into fiber.

As explained in §IV.1.1, the activation energy can be obtained through the measurement of the glass transition and crystallization temperatures at various heating rates. The value of E_a, the activation energy for T_g, E_{c1}, E_{c2} and E_{c3} the activation energies for T_{p1} T_{p2} and T_{p3} respectively, of the preform and fiber are summarized in table IV.8.

Table IV.8: Activation energies associated with the glass transition temperature (E_a) and with crystallization peaks (E_{c1},E_{c2} and E_{c3}) of the glass with x=20 and the corresponding fiber.

Material	E_a (KJ.mol^{-1}) (±50 KJ.mol^{-1})	E_{c1} (KJ.mol^{-1}) (±50 KJ.mol^{-1})	E_{c2} (KJ.mol^{-1}) (±50 KJ.mol^{-1})	E_{c3} (KJ.mol^{-1}) (±50 KJ.mol^{-1})
Preform	531	N/A	128	N/A
Fiber	636	290	198	131

The activation energies E_a and E_{c2} increase after drawing the preform into fiber. It is interesting to point out that the activation energy E_{c1} of the fiber is greater than E_{c2} and E_{c3}.

IV.3.2 Core-clad preform and fiber processing

Core-clad preforms with the composition $70TeO_2$-$10Bi_2O_3$-20ZnO (x =20) and $72.5TeO_2$-$10Bi_2O_3$-17.5ZnO (x=17.5), respectively for the clad and core glasses, were processed using the rotational casting process described in §III.6.2. As performed for the core preforms, the core-clad preforms were sliced into cross-sections which were polished and optically inspected using an optical microscope. No apparent crystallization

was observed in the cross-sections and no crystallization peak was observed in the XRD pattern of the cross-sections confirming the absence of crystallization in the core-clad preform. As seen in the core preform, no variation in the density and absorption band gap were measured between the cross-sections. The refractive indices at 630, 825, 1533 nm of each cross-section was measured with an accuracy of ±0.0001 in collaboration with Dr. M. Ferraris and Dr. D. Milanese at Politecnico di Torino (Italy). No variation in the refractive index between cross-sections was observed. The Table IV.9 lists the refractive indices at 630, 825, 1533 nm when measured in the clad and core glasses.

Table IV.9: Refractive indices of the bulk cladding and core glass compositions and subsequent Δn at 630, 825, and 1533 nm.

Wavelength (nm)	Refractive index (n_{clad}) of cladding glass of composition $70TeO_2$-$10Bi_2O_3$-$20ZnO$ (x=20)	Refractive index (n_{core}) of core glass of composition $72.5TeO_2$-$10Bi_2O_3$-$17.5ZnO$ (x=17.5)	$\Delta n=n_{core}-n_{clad}$
630	2.1492±0.0001	2.1583±0.0001	0.0091
825	2.1165±0.0001	2.1261±0.0001	0.0096
1533	2.0847±0.0001	2.0925±0.0001	0.0078

In agreement with the data presented in Figure IV.4, the refractive index decreases with increase of x. The difference between the refractive index of the core and that of the clad (Δn) slightly decreases with increasing wavelength of the incident light.

To probe the uniformity of the interface between the core and the clad glasses, the core or the clad glass of the preform was doped with 2 mol% CuO, used as a tracer ion. The Cu-doped core-clad preforms were sliced into cross-sections. Figure IV.21(a) presents a photograph of cross-sections of Cu doped core-clad and a core-Cu doped clad preforms.

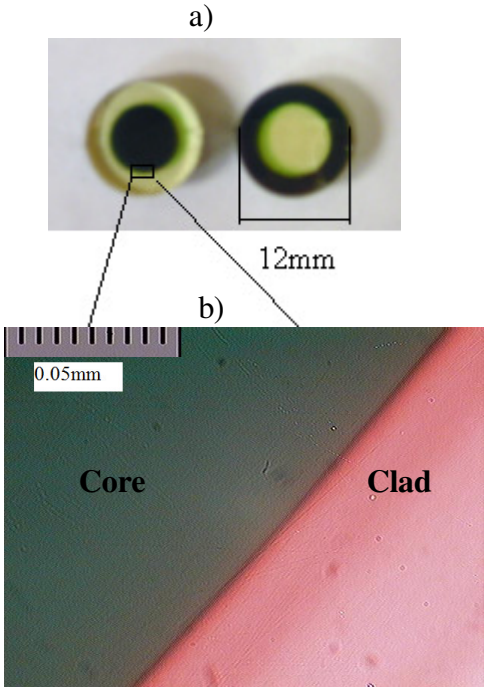

Figure IV.21: (a) Photograph and (b) optical image of the Cu-doped core-clad interface

As seen above, the doping with Cu leads to a dark green coloration of the glass allowing the measurement of the cladding thickness. As can be seen in Figure IV.21a, the undoped glass remains colorless compared to the Cu doped glass. Each of the individual slices was inspected and the diameter of the core and of the clad measured. The outer diameter of the preform was measured to be (12±0.1) mm with a core diameter of (2.9±0.1) mm. The variation of the core and clad dimensions over the 65 mm length of the preform is presented in the figure below.

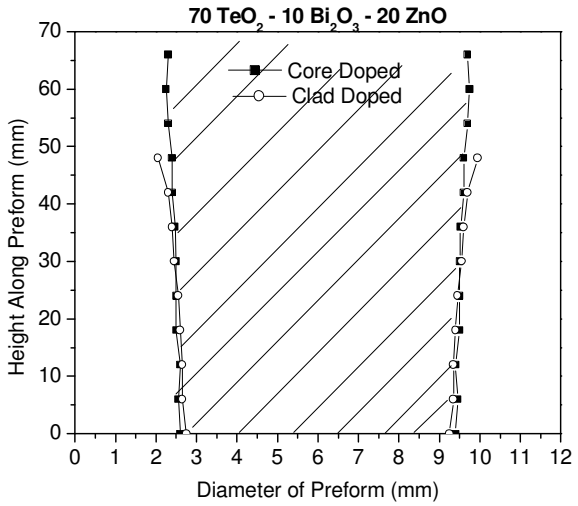

Figure IV.22: Core thickness uniformity over the length of the preform, measured at multiple cross-section locations

As seen above, there is less than 3% of core thickness variation on a length of ~45mm within the complete 65mm length of the preform. The optical microscope image of the interface region (across the white to colored boundary), taken with a 100X magnification with an optical resolution of 0.18 μm, is presented in Figure IV.21b. The pink coloration is only due to an illumination effect. No apparent diffusion between the doped and undoped glasses can be seen as the undoped glass at the interface with the doped glass remains colorless. In order to verify the absence of low levels of Cu diffusion, the absorption spectra of the Cu doped and undoped glasses were measured using a 2 nm slit to measure independently the absorption spectrum of the core and of the clad glasses near the interface. The absorption spectra are shown below:

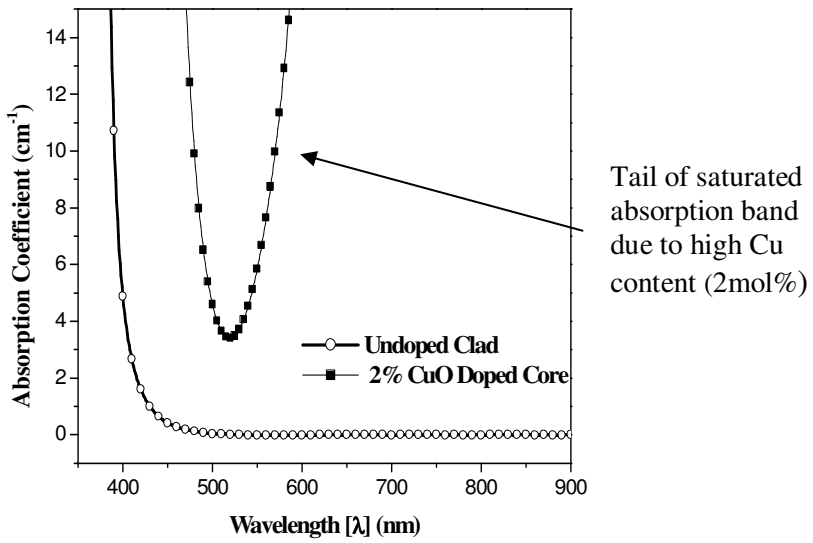

Figure IV.23: Absorption spectra of the Cu-doped core (2 mol %) and the undoped clad of a core-clad preform cross-section.

The spectrum of the undoped glass shows no absorption in the visible range while the spectrum of the Cu-doped glass exhibits the tail of an absorption band expected to be centered at 790 nm. The composition of a cross-section of the Cu-doped-core clad preform was analyzed using an EDS/SEM in order to assess Cu or Te diffusion in atomic level which might occur during the core-clad preform processing. Figure IV.24 shows the atomic percent of Te and Cu along a line crossing the full diameter of the core-clad preform.

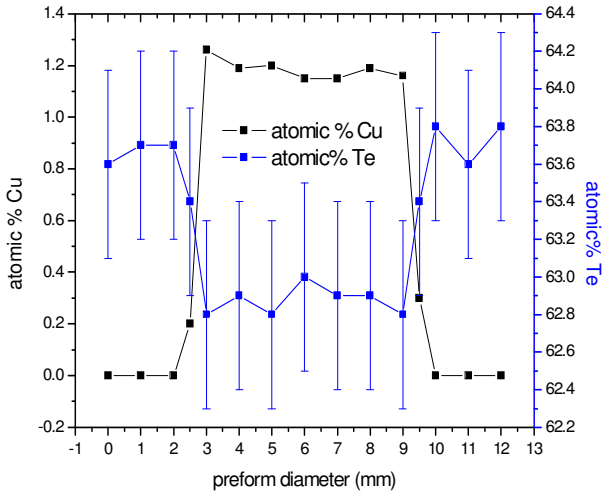

Figure IV.24: Atomic percent of Te and Cu along a line crossing the full diameter of the core-clad preform

As can see above, there is no significant diffusion of Cu from the doped glass to the undoped glass

The core-clad preforms with the composition $70TeO_2$-$10Bi_2O_3$-20ZnO and $72.5TeO_2$-$10Bi_2O_3$-17.5ZnO, respectively for the clad and core glasses, were drawn into fibers in collaboration with Drs. J. Ballato and P. Foy at COMSET (SC, USA), using the fiberization parameters described in the §III.6.3. At least 160 m of uncoated and polymer coated core-clad fibers with a diameter of 125 µm were obtained from each draw. An optical micrograph of an uncoated core-clad fiber cross-section taken with a 500X objective is presented below.

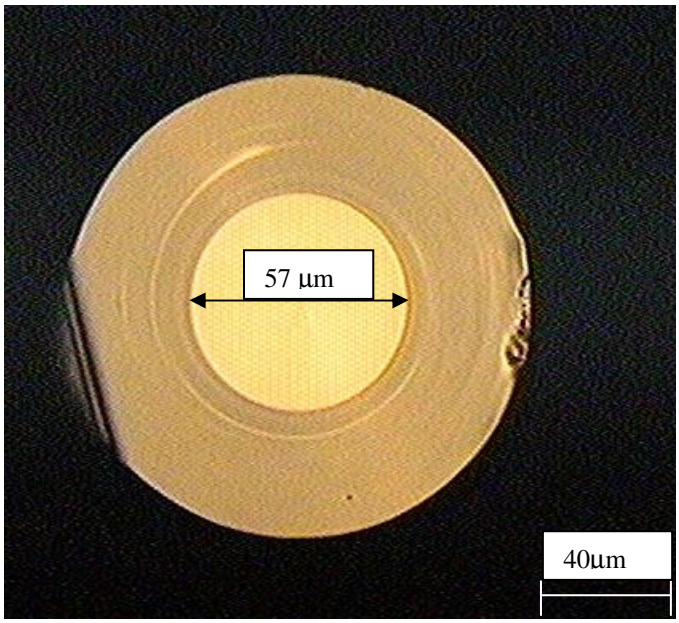

Figure IV.25: Optical micrograph of the core-clad fiber cross-section using 50X magnification.

The fiber has a diameter of (124±1) µm with a core diameter of (57±1) µm. As can be seen in the micrograph, the core remained circular during the drawing process. Multiple fibers were examined in a similar manner and no variation in the core diameter, within the accuracy of the measurement, or in the shape of the core was observed.

Figures IV.26a and b present the normalized micro-Raman spectra of core and clad glasses, respectively, measured in the fiber and in the preform measured using an excitation wavelength of 785 nm. Figure IV.26c shows a schematic of the 2 µm laser spot and position of the measurement on the fibers cross-section.

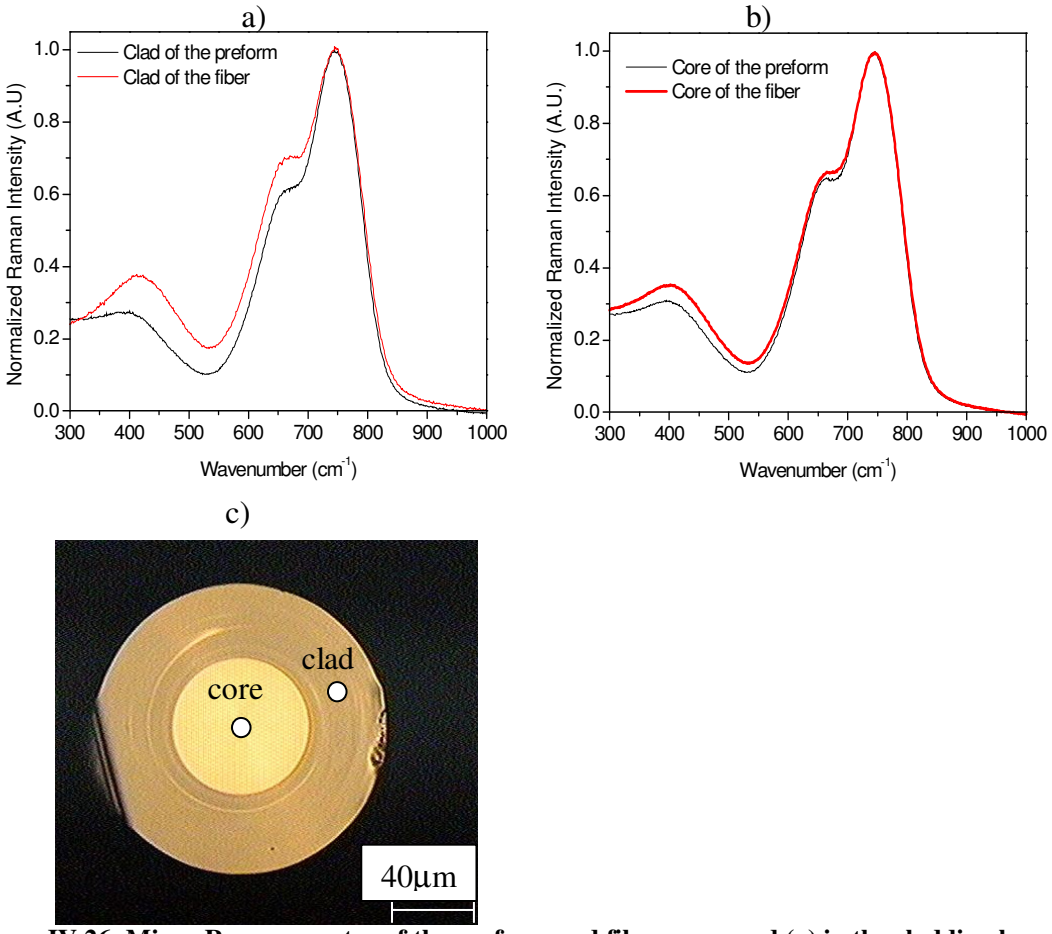

Figure IV.26: Micro-Raman spectra of the preform and fiber measured (a) in the cladding layer and (b) in the core. (c) Schematic of the laser spot and localization of the Raman measurement on the fiber cross-section.

The spectra exhibit similar bands in the 400–800 cm^{-1} range seen in Figure IV.5. Compared to the Raman spectra of the preform, the intensity of the band at ~400 and at 650 cm^{-1} in the Raman spectra of the fiber increases slightly in intensity and shifts toward higher wavenumbers.

To quantify the optical properties of the as-drawn fibers such as numerical aperture and propagation loss, the core-clad fiber was drawn with a UV curable polymer coating to increase the strength of the fiber. The core-cladding index difference (Δn)

obtained from the NA calculation was found to be (0.009± 0.002). From the numerical aperture (NA), it is possible to estimate the approximate number of modes, m, which can travel in the optical fiber, using the following equation [O'Do,07]:

$$m \approx \left(\frac{NA * d}{\lambda} \right)^2 \qquad \text{eq. IV.10}$$

where d is the diameter of the core and λ the wavelength of interest.

The number of mode traveling at 1.55 μm in the core-clad fiber with a core diameter of (57±1) μm is ~51.

The propagation losses at 632 nm and 1.5 μm for the core-clad fiber were measured using the cutback method described in §III.7. The propagation losses at 632 nm and 1.5 μm were measured at m (3.2±0.1)dB/m and (2.1±0.1)dB/m, respectively.

IV.3.3 Effect of fiber drawing on the nucleation and growth behavior

The nucleation- and growth-like curves of the preform and of the core fiber with x=20 were determined using the techniques described in §II.2 and are presented in Figure IV.27.

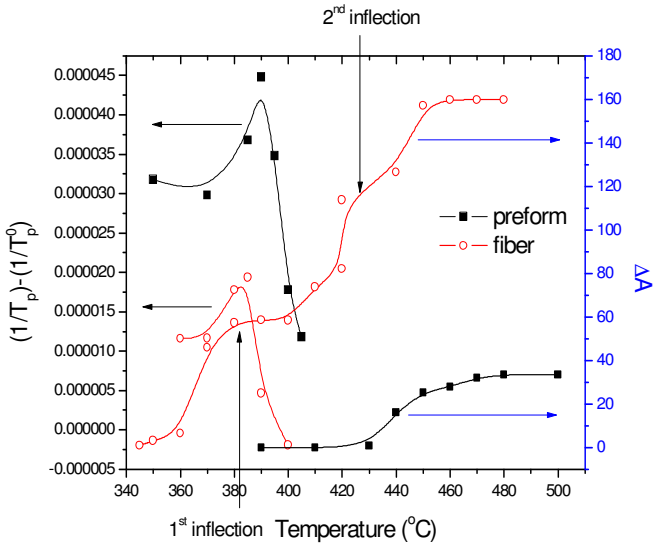

Figure IV.27: Nucleation- and growth-like curves of the bulk glass with x=20 and the corresponding fiber

The nucleation-like curves present a maximum, commonly called the temperature of maximum nucleation ($T_{n\ max}$), which decreases from (390±2°C) to (384±2°C) when the glass is drawn into fiber. The growth-like curve of the glass is shifted to lower temperature after drawing and a large overlap between the nucleation- and growth- like-curves of the fiber can be seen, While the growth-like curve of the bulk glass does not show any maximum, the growth-like curve of the fiber exhibits two inflection points measured at (382±2) °C and (426±2) °C.

The JMA exponent, which gives an indication of the predominant crystallization dimensionality, was calculated using Equation III.24. Table IV.10 lists the JMA exponent of the preform and of the fiber with x =20.

Table IV.10: JMA exponent of the glass with x=20 and the corresponding fiber

Material	JMA 1st crystallization peak ±0.1	JMA 2nd crystallization peak ±0.1	JMA 3rd crystallization peak ±0.1
Preform	N/A	n=2	N/A
Fiber	n= 1.29	n=2.07	n=1.77

As seen above, the fiber drawing process has no effect on the JMA exponent of the 2nd crystallization peak. However it is interesting to notice that while the value of n for the 3rd crystallization peak remains in the range 1.5<n<2.5, the value of n for the 1st crystallization is less than 1.5.

IV.4 Hydroxyl group reduction in TeO_2-based glasses

In this section, we first present the physical, thermal, optical and structural properties of tellurite glasses prepared with various modifiers and melted in various atmospheres in order to process a bulk glass and fiber with reduced OH content. The effect of the OH content reduction on the nucleation and growth behavior of bulk glasses and fiber is studied.

IV.4.1 Processing and characterization of glasses in the $70TeO_2–10Bi_2O_3–20ZnO$ system with various OH content

Processing and characterization of bulk glasses

Glasses with the compositions (100-x) $(0.70TeO_2–0.10Bi_2O_3–0.20ZnO)–xMO$ with MO= Li_2O, BaO and K_2O and x = 0, 2 and 4 and $(0.70TeO_2–0.10Bi_2O_3–0.20ZnF_2)$ were prepared in regular and oxygen-rich environment using the technique described in §III.1. The near infrared absorption spectra of the investigated glasses are shown in Figure IV.28a and b.

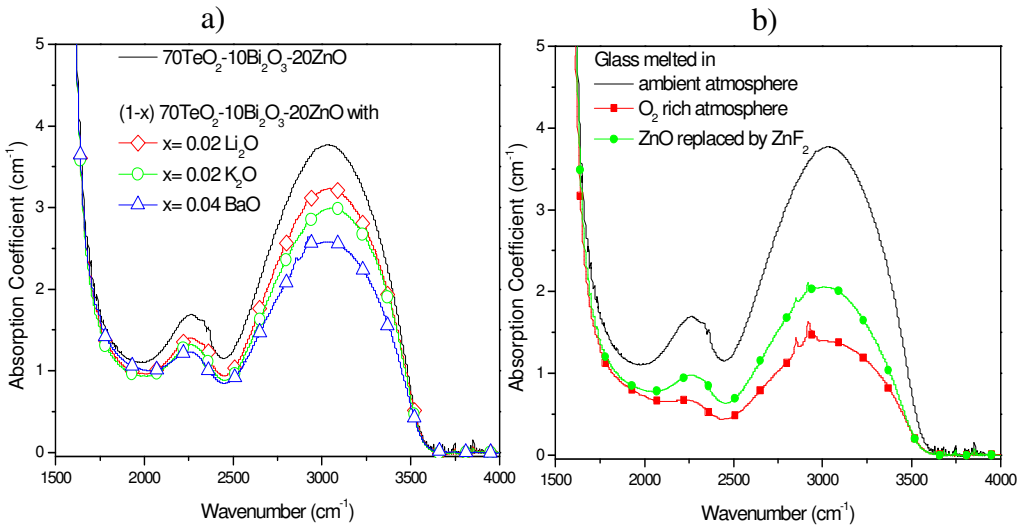

Figure IV.28: (a) Near infrared absorption spectra of glasses prepared with alkaline and alkaline-earth and (b) with ZnF_2 instead of ZnO and of the glass melted in an oxygen-rich environment.

All the spectra in the Figures above exhibit a broad absorption band between 2,500 cm^{-1} and 3,700 cm^{-1}. The amplitude of the bands in the 2,000-3,500 cm^{-1} range decreases progressively with the addition of Li, K and Ba at low levels as compared to the based ternary composition shown by the solid line. It is important to notice that the decrease of these absorption bands is more pronounced as the size of the alkaline or alkaline-earth ion increases. In Figure IV.28b, one can notice that the replacement of ZnO

by ZnF_2 and also the melting in O_2-rich-environment leads to a decrease of the amplitude of these OH related bands. It is interesting to point out that the intensity of these absorption bands is the lowest when the glass is melted in O_2-rich-environment. The number of hydroxyl group per cm^3 in the glass network can be estimated using the following equation [Fe,01]:

$$N_{OH} = \frac{N}{\varepsilon * L} Ln\left(\frac{1}{T}\right) \qquad \text{eq.IV.1}$$

where N is the Avogadro constant, L is the sample thickness (cm), T is the transmittance and ε is the molar absorptivity of the free OH groups in the glass. ε used here is the molar absorptivity corresponding to OH groups in silicate glasses, $49.1*10^3$ cm^2/mol [Fe,01]. The concentration of hydroxyl groups can also be estimated in part per million (ppm) using the equation reported by [Ch,82]::

$$C_o = \frac{N_{OH}.W_{OH}}{N_{OH}.W_{OH} + N_{Glass}.W_{Glass}} \qquad \text{eq. IV.2}$$

where N_{OH} and N_{Glass} are OH units and glass molecular units in 1 cm^3, respectively. W_{OH} and W_{Glass} are the molecular weight of OH and glass, respectively.

Table IV.1 summarizes the OH content in the glasses as well as the density, molar volume and glass transition temperature (T_g) of the newly developed glasses. The molar volume of the glasses, which represents the volume occupied by one mole of the glass, was calculated from the density values according to $V_m=M/\rho$, where M and ρ are the molar weight (g/mol) and density (g/cm^3) of the glass, respectively [Ha,02].

Table IV.10: Density, molar volume and glass transition temperature of the new developed glasses

Glass composition	Density (g/cm^3) ($\pm 0.02 g/cm^3$)	Molar Volume (cm^3/mol) ($\pm 0.09\ cm^3/mol$)	T_g (^oC) ($\pm 2^oC$)	OH (10^{19} ions/cm^3) (± 0.01 ions/cm^3)
$70TeO_2$–$10Bi_2O_3$–$20ZnO$	6.12	28.53	336	4.72 (213ppm)
0.98 ($70TeO_2$–$10Bi_2O_3$–$20ZnO$) – $0.02Li_2O$,	6.06	28.33	326	3.95 (184ppm)
0.98 ($70TeO_2$–$10Bi_2O_3$–$20ZnO$) – $0.02\ K_2O$	5.93	29.17	331	3.64 (172ppm)
0.96 ($70TeO_2$–$10Bi_2O_3$–$20ZnO$) – $0.04BaO$	6.12	28.02	340	3.15 (144ppm)
$70TeO_2$–$10Bi_2O_3$–$20ZnF_2$	6.18	28.25	305	2.51 (115ppm)
$70TeO_2$–$10Bi_2O_3$–$20ZnO$ melted in O_2-rich-environment	6.23	28.02	341	1.71 (77.5ppm)

As can be seen above, the OH content can be reduced to 77.5 ppm by melting the glass batch in O_2-rich-environment. The introduction of Li_2O and K_2O in the tellurite-based network leads to a decrease of the density and T_g while the introduction of BaO in the matrix has no significant influence on the density but does increase slightly the T_g of the glass. When the glass is prepared using ZnF_2 as a replacement of ZnO, its density increases and its T_g decreases whereas the melting of the glass in O_2- rich-environment leads to a glass with a larger density and higher T_g.

Figure IV.29 present the Raman spectra of the investigated glasses, measured using a 785 nm excitation in collaboration with Dr. C. Rivero-Baleine at Lockheed-Martin, Orlando FL.

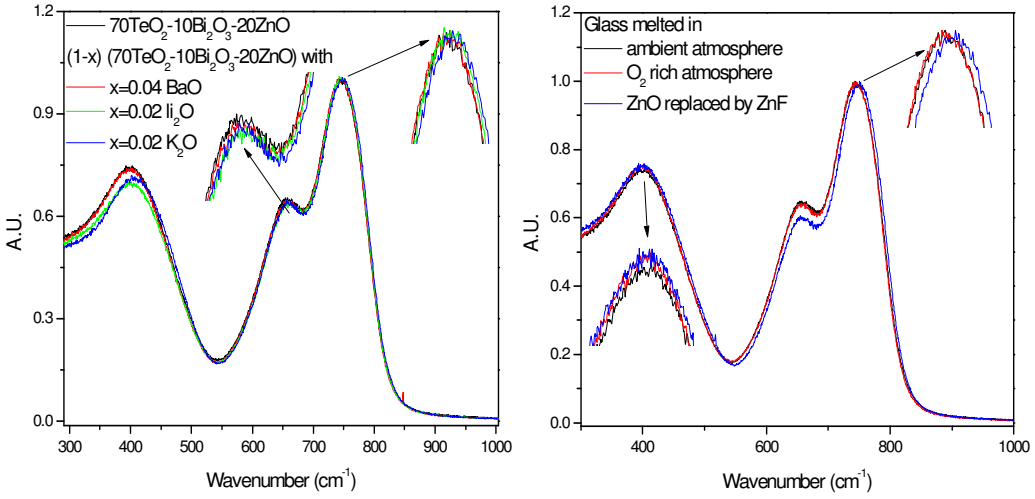

Figure IV.29: (a) Raman spectra of glasses prepared with alkaline and alkaline-earth and (b) with ZnF_2 instead of ZnO and of the glass melted in an oxygen-rich environment.

In each spectrum, several bands are observed in three main wavenumber ranges: 720-780, 610-680 and 380-430cm^{-1} as seen in Figure IV.5

In Figure IV.29a, the amplitude of the bands in the 610-680 cm^{-1} and 380-430cm^{-1} ranges slightly decreases at the expense of the bands at around 720-780cm^{-1} and the position of the bands at 740 and at 400cm^{-1} shifts slightly to larger wavenumbers with the introduction of Li_2O and K_2O in the tellurite network. Note that each spectra are normalized to the Raman band with maximum intensity. However, the addition of BaO does not change significantly the Raman spectrum of the glass. The introduction of K_2O leads to larger variation in the Raman spectrum than Li_2O.

Figure IV.29b, depicts the Raman spectra of the glasses prepared using ZnF_2 and melted in O_2 rich atmosphere. It is clearly shown that the melting in O_2 rich atmosphere has no

significant influence on the Raman spectrum of the glass except for a slight increase of the band at 400 cm^{-1} compared to that of at 740cm^{-1}. However, the replacement of ZnO by ZnF_2 leads to a small shift to higher wavenumber of the band at 740 cm^{-1}, a decrease of the amplitude of the band at 660 cm^{-1} , and an increase of the amplitude of the 400cm^{-1} band compared to that at 740 cm^{-1}.

Processing and characterization of the fiber

As shown in Figure IV.28b, melting of the glass batch in oxygen-rich-environment reduces the OH content in the glass. Thus, 30g batch of glasses with the composition 70TeO_2-10Bi_2O_3-20ZnO were melted in regular and O_2-rich-environment in order to prepare fibers with various OH amounts. As explained in §III.6.1, the glasses were quenched in a cylindrical mold preheated below the T_g of the glasses and the mold was quickly annealed at 285 ^oC for 15 hours. Fibers were drawn by pulling the 5-7cm long preform with a diameter of 12mm using a Heathway drawing tower (Milton Keynes). A pre-set fiber diameter of 125 μm was used to give strength to the fiber and to allow us to continuously pull it using rotational take-up on a drum. Nominally 110 m of core-clad fiber was obtained for each drawing run from a 5 cm long preform. UV cured polymer coatings were applied to protect the fibers from handling. The attenuation in dB/m was measured in ~2 meters long fibers prepared in air and in O_2-rich-environment in collaboration with Teemu Kokki, at nLight (Finland). Figure IV.30 exhibits the losses in the fibers drawn from preforms prepared in regular and oxygen-rich-environment as a function of wavelength.

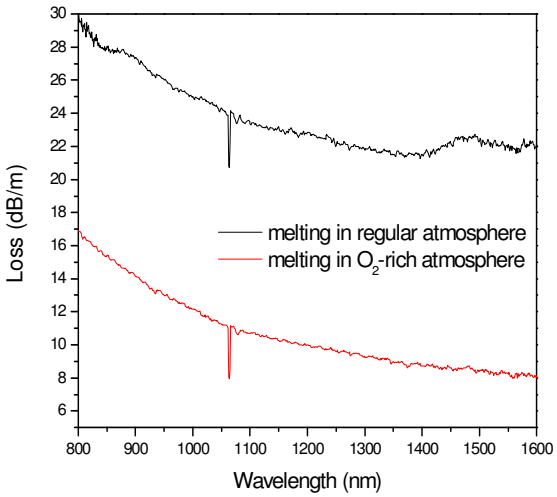

Figure IV.30: Loss spectrum of fibers drawn from a preforms melted in air and in an oxygen-rich environment

High background losses were measured for both fibers. The shape of the fibers' losses is similar; the losses in the fiber prepared in O_2-rich environment are lower than in the fiber prepared in regular environment. Both spectra present a sharp peak at 1075 nm which is a measurement artifact caused by the light source. The spectrum of the fiber melted in regular environment, expected to have a larger amount of OH than the fiber processed in O_2-rich-environment, shows a band located at 1470 nm.

IV.4.3 Effect of OH reduction on the nucleation and growth behaviors of bulk glass and fiber.

Bulk and fiber were prepared by melting the glass (x=20) in regular and O_2-rich environment in order to prepare bulks and fibers with high and low OH contents, respectively. The thermal properties of the bulks and fibers were measured and compared. Figures IV.31a and b present the DTA thermograms of the bulk glasses and fibers melted in regular and O_2 rich-environment. Note that in order to compare the bulk

glass and the fiber both materials were crushed into powder having similar grain size (~400µm).

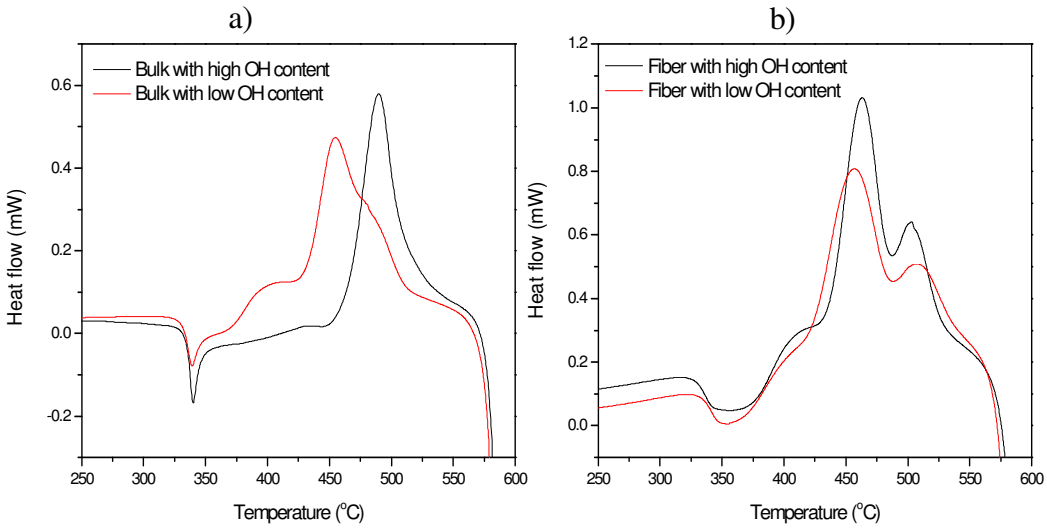

Figure IV.31: DTA thermograms of (a) bulk glasses and (b) the fibers processed with high and low OH content.

The DTA curve of the bulk glass melted in regular atmosphere shows only one exothermic peak while 3 crystallization peaks appear in the DTA scan of the glass melted in oxygen-rich-environment. The DTA curves of both fibers exhibit 3 exothermic peaks. Table IV.11 summarizes the thermal properties of the glasses and fibers processed with low and high OH content.

Table IV.11: Thermal properties of the bulk glasses and fibers processed with high and low OH content

Material	T_g (^oC) ±2 ^oC	1st exothermic peak		2nd exothermic peak		3rd exothermic peak		$\Delta T=T_x-T_g$ (^oC) ±2 ^oC
		T_{x_1} (^oC) ±2 ^oC	T_{p1} (^oC) ±2 ^oC	T_{x_2} (^oC) ±2 ^oC	T_{p2} (^oC) ±2 ^oC	T_{x_3} (^oC) ±2 ^oC	T_{p3} (^oC) ±2 ^oC	
Bulk glass with high OH content	336	NA	NA	463	490	NA	NA	$T_{x2}-T_g$=127
Bulk glass with low OH content	341	376	405	430	454	473	480	$T_{x1}-T_g$ =35
Fiber with high OH content	334	371	410	433	464	490	502	$T_{x1}-T_g$ =37
Fiber with low OH content	336	365	407	421	456	494	506	$T_{x1}-T_g$ =29

As seen above, the T_g of the bulk glass with low OH content is slightly higher than that of the glass with high OH content whereas no significant variation in the T_g of the fiber was measured when the OH content in the fiber is reduced. Moreover, one can notice that a reduction in the OH content in both the bulk glass and fiber leads to a decrease of T_p and T_x except for the 3rd T_p and T_x of the fiber, which in the accuracy of measurement, does not vary when the fiber is prepared with low OH content. Thus ΔT, the difference between T_g and the first onset of crystallization peak, decreases from $(127\pm2)^oC$ to $(35\pm2)^oC$ and from $(37\pm2)^oC$ to $(29\pm2)^oC$ when the glass and the fiber are prepared with reduced OH content, respectively.

As explained in §IV.1.1, the activation energy can be obtained from the measurements of the glass transition and crystallization temperatures at various heating

rates. The value of E_a, the activation energy for T_g, E_{c1}, E_{c2} and E_{c3} the activation energies for T_{p1} T_{p2} and T_{p3} respectively, of the bulk and fibers processed with high and low OH content, are summarized in Table IV.12.

Table IV.12: Activation energies associated with the glass transition temperature (E_a) and with the crystallization peaks (E_{c1},E_{c2} and E_{c3}) of the bulk glass and fiber processed with high and low OH content.

Material	E_a (KJ.mol^{-1}) (±50 KJ.mol^{-1})	E_{c1} (KJ.mol^{-1}) (±50 KJ.mol^{-1})	E_{c2} (KJ.mol-1) (±50 KJ.mol-1)	E_{c3} (KJ.mol-1) (±50 KJ.mol-1
Bulk glass with high OH content	531	N/A	128	N/A
Bulk glass with low OH content	525	209	171	97
Fiber with high OH content	636	290	198	131
Fiber with low OH content	621	142	179	101

In the accuracy of measurement, there is no effect of the OH content reduction on the E_a, the activation energy for T_g, T_{p2} and T_{p3} of the bulk glass and fiber whereas the activation energy for T_{p1} of the fiber decreases when the fiber is prepared with low OH content.

The nucleation- and growth-like curves of the glasses and fibers processed with low and high OH contents were determined using the techniques described in §II.2 and are presented in Figures IV.32a and b, respectively.

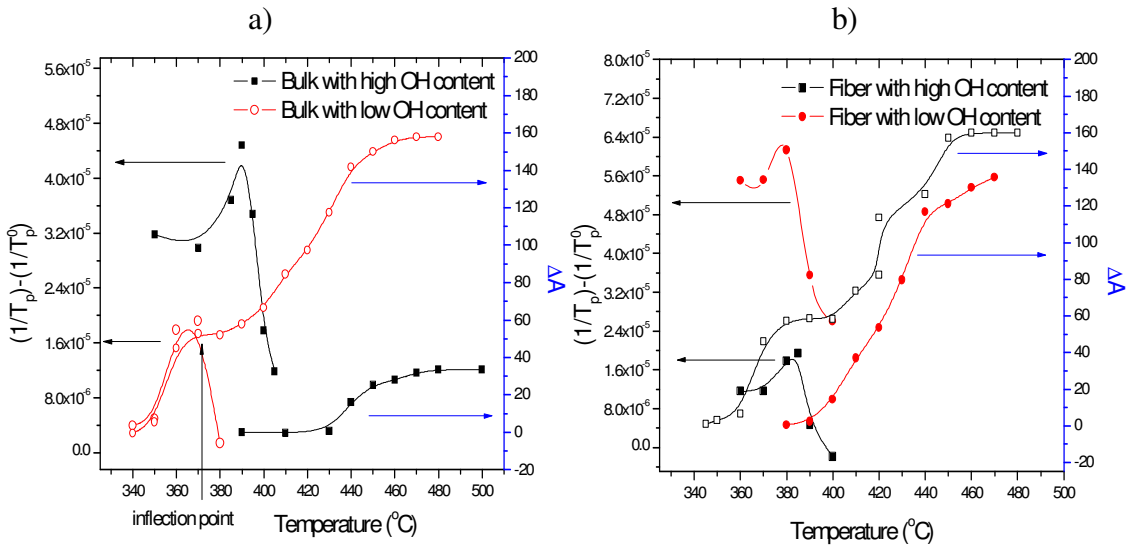

Figure IV.32: Nucleation- and growth-like curves of (a) bulk glass and (b) fiber processed with low and high OH content

The nucleation-like curves of the bulk and of the fiber present a maximum which decreases from (390±2) °C to (366±2) °C and (384±2) °C to (381±2) °C when the bulk glass and fibers are prepared with lower OH content, respectively. The nucleation-like curve of the glass is shifted to lower temperatures when the glass is prepared with lower OH content. However the growth-like curve of the fiber produced with low OH shifts to higher temperatures as compared to the fiber with high OH content. Furthermore, one can notice in Figure IV.32a that while the growth-like curve of the bulk glass processed with high OH content does not show any maximum, the growth-like curve of the glass prepared with low OH content exhibits one inflection points at (370±2) °C. As seen in Figure IV.32b, the growth-like curve of the fiber prepared with high OH exhibits two inflection points and the growth-like curve of the fiber with low OH content presents no maximum. Lastly, a large overlap between the nucleation- and growth- like-curves of the low OH-containing bulk glass is present, whereas the overlap between the nucleation-

and growth- like-curves of the low OH-containing fiber is lower than that of the fiber prepared with high OH content

The JMA exponent, which gives an indication of the predominant crystallization dimensionality, was calculated using the equation III.24. Table IV.13 lists the JMA of the investigated glasses and fibers.

Table IV.13: JMA exponent of the glass and the fiber processed with high and low OH content.

Material	JMA 1st crystallization peak ±0.1	JMA 2nd crystallization peak ±0.1	JMA 3rd crystallization peak ±0.1
Bulk glass with high OH content	N/A	n=2	N/A
Bulk glass with low OH content	n= 1.21	n=2.5	n=1.67
Fiber with high OH content	n= 1.29	n=2.07	n=1.77
Fiber with low OH content	n= 1.21	n=2.11	n=1.75

As seen above, there is no significant effect of the OH reduction in both bulk glass and fiber on the JMA exponent of the crystallizations. It is interesting to notice that while the n of the 3rd crystallization peak remains in the range $1.5<n<2.5$, the n for 1st crystallization is <1.5 and for the 2nd crystallization >2.

The bulk glasses prepared with low and high OH contents were heat treated at 365°C for 2 to 40 hours to determine the nucleation and growth rates of the crystals as

explained in the section §II.2.1. Figure IV.33 shows the nucleation and growth rates of the crystals in the bulk glasses.

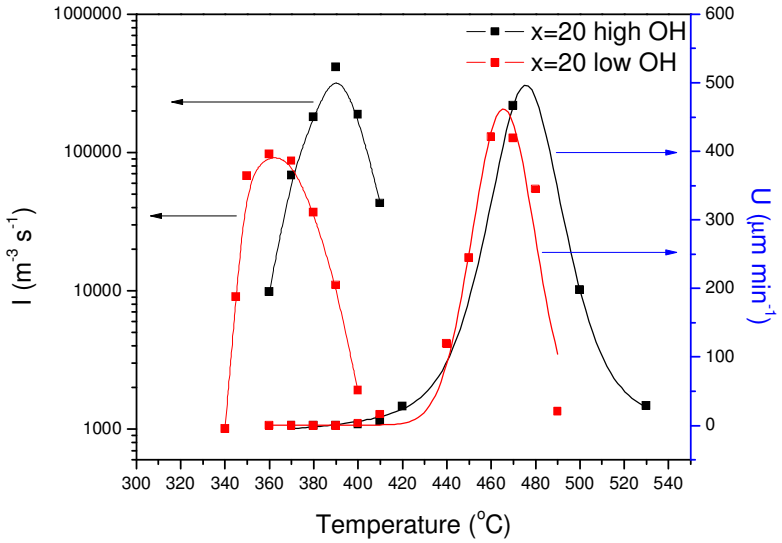

Figure IV.33: Nucleation (I) and growth (U) rates of the crystal in bulk glasses prepared with high (213ppm) and low OH (77.5ppm) content as a function of temperature

A reduction of the OH content leads to a shift to lower temperature of the nucleation and growth rates curves. The temperature of maximum growth rate slightly decreases from (476±2) °C to (468±2) °C and the maximum growth rate at these temperatures from (498±31) µm to (461±16) µm when the glass is prepared with lower OH content. From the curves in Figure IV.33, the averaged amount of nuclei in the as-quenched glass (N_q) was quantified using the technique described in §II.2.1 and was found to increase from 1.98 10^{10} m^{-3} to 3.65 10^{11} m^{-3} over the entire nucleation temperature range when the glass is prepared with a lower OH content.

CHAPTER V: DISCUSSION

V.1 Effect of the glass network on the physical, thermal, optical and structural properties of the glasses.

In this study, glasses with the composition (90-x)TeO_2–10Bi_2O_3–xZnO with x= 25, 20, 17.5, 15 were processed and the physical, thermal, optical and structural properties of these glasses were studied as a function of the glass composition. The following question was addressed: *what is the compositional effect on the variation of physical, thermal, optical and structural properties within the TeO_2-Bi_2O_3-ZnO system?* To conduct this study, bars of 1x1x6 cm were cast from 30 g melts. Long bars (~6 cm) and disks (~3 mm in diameter) were fabricated for the viscosity measurements as described in §III.2.6. After annealing, the samples were optically polished and visually inspected to determine the presence of any evident crystallization or defects such as bubbles.

Before discussing the variation of the physical, thermal and optical properties of the investigated tellurite glasses within the composition series (90-x)TeO_2 – 10Bi_2O_3 – xZnO with x = 15, 17.5, and 20, the structure of the glasses is first discussed. The structure of the glasses was investigated using Raman spectroscopy. The Raman spectra of the investigated glasses are depicted in Figure IV.5 as a function of x, the concentration of ZnO. When the concentration of ZnO increases (from x = 15 to 25 mol%), the intensity of the band at 415 cm^{-1} decreases while the band at 730 cm^{-1} increases in amplitude and shifts to higher wavenumber when compared to the band at

660 cm^{-1}. Note that all spectra were normalized to the band with highest intensity. In order to interpret the spectra, focusing only on one broad band in each wavenumber region is often sufficient to obtain an outline of structural change with composition in agreement with [Ta,94]. In both systems, three main bands corresponding to the TeO_2 network exist near 730, 660, and 415-450 cm^{-1}. The band at 730 cm^{-1} has been ascribed to the stretching mode of the [TeO_3] containing terminal Te-O bonds with non-bridging oxygens (NBO) such as Te=O and Te-O^- and the shoulder at 780 cm^{-1} to the Te-O^- stretching vibrations in the [TeO_{3+1}] units, and [TeO_3] units containing NBO [Hi,07] [Se,94] [Ma,03]. The band at 660 cm^{-1} has been assigned to the stretching modes of the [TeO_4] units with bridging oxygens (BO) [Se,92] and the shoulder at 600 cm^{-1} to the vibration of the continuous network consisting of [TeO_4] tetrahedral bipyramidal (tbps) units as explained by [Hi,07]. The band in the range 415-450 cm^{-1} has been attributed to the bending modes of Te-O-Te or O-Te-O linkages [Se,92] and the shoulder at 380 cm^{-1} to the Bi-O-Bi vibration in [BiO_6] octahedral units [Ha,97]. The band at 400 cm^{-1} may also be related to the Zn-O vibration as suggested by [Oz,07b] [Tz,01]. The variations in the Raman spectra may indicate that the progressive replacement of TeO_2 by ZnO leads to a decrease of the [TeO_4] units with an increase of the [TeO_3] and [TeO_{3+1}] units as suggested by [Ko,86] [Sh,97] [O'Do,04].

V.1.1 Thermal and physical properties of the investigated glasses

From Table IV.1, and T_g increases when x, the concentration of ZnO, increases from 15 to 25. The increase of T_g with an increase of x can be related to the role of ZnO

in the structure of the glass which is believed to enter the network behaving like a network-former [El,00]. Consequently, the network of the glasses with high ZnO content is believed to be more cross-linked than the glasses with lower ZnO content. Hence the T_g of the glasses of investigation shifts to high temperature as the ZnO content increases [Ch,07b] [Bü,92]. The density slightly decreases. It is conceivable that the depolymerization (decrease of the $[TeO_4]$ units with an increase of the $[TeO_3]$ and $[TeO_{3+1}]$ units) of the tellurite network leads to a significant decrease of the density partially compensated by the cross-linking induced by the ZnO incorporation in the glass network.

Table IV.1 also lists the temperature difference, ΔT, between the first crystallization temperature T_x, and the glass transition temperature which provides a gauge of the glass' resistance to crystallization, and should be as large as possible in order to form fiber of good optical quality with minimal scatter loss from microcrystallites [So,93]. Typically a ΔT value larger than 100^oC suggests reasonable glass stability. As the preform must sit within a heated furnace during drawing, this stability becomes important for realizing crystallite-free fiber, as the length of the "hot-zone" within the furnace (between the orifice where the first glass bead "drops" and the length of the preform) can be large. The DTA curves presented in Figure IV.1 exhibit one exothermic peak for the glasses with x = 17.5 and 20 which is larger than that of the glasses with x = 15 and 25. A second exothermic peak can be seen at lower temperature in the DTA curves of the glasses with x = 15 and 25. The ΔT of the glasses with x=17.5 and 20 is larger than 100^oC whereas, due to this second exothermic peak, it is smaller than 90^oC for the glasses with x = 15 and 25 as seen in Table IV.1. This clearly shows

that the glasses with x = 17.5 and 20 possess a better stability (resistance) to crystallization and thus are better glass candidates for fiberization than the glasses with x = 15 and 25. The lowestT_{x2} and T_{p2} of the glasses with x = 15 and 25 seen in Table IV.1 indicate that these glasses crystallize at lower temperature than the glasses with x = 17.5 and 20 [Po,96].

The shift of T_g, T_{p1} and T_{p2} with respect to the heating rate allows using the equation IV.1 for the determination of the activation energies related to the glass transition and to the crystallization phenomenon [Ki,57]. As seen in Table IV.2, the activation energy E_a increases with an increase of x indicating an increase in bond strength and in glass connectivity with an increase of the ZnO content as suggested by [Jo,97]. Since the activation energy of crystallization is an indication of the speed of crystallization [Ti,06], the glasses with x = 15 and 25 are expected to have a higher rate of crystallization than the glasses with x = 17.5 and 20 as their E_{c2} is lower than that of the glasses with x = 15 and 25 confirming a higher crystallization ability of the glasses with x = 15 and 25 than the glasses with x = 17.5 and 20.

V.1.2 Optical properties of the investigated glasses

From Figure IV.3a, when TeO_2 is progressively replaced by ZnO up to x=25 in the glass system (90-x)TeO_2-10Bi_2O_3-xZnO, the optical band gap exhibits a monotonic shift to shorter wavelengths. The shift of the band gap with an increase of ZnO content can be related to a an increase of the Te-O bonds with non-bridging oxygens, such as an increase of the [TeO_3] and [TeO_{3+1}] units in agreement with [Fa,98]. Note that the 10 nm

shift of the band gap wavelength indicates that the addition of ZnO in the glass network does not subsequently affect the transparency of the glass in the visible region.

Figure IV.3b presents the IR absorption spectrum of the investigated glasses. The spectra exhibit a broad band between 2,500 cm^{-1} and 3,700 cm^{-1}. In agreement with [17], these bands can be assigned to the stretching vibration of OH groups. [Na,03]. As the glasses were processed using the same melting technique and the same raw materials, it is possible to compare the amount of OH in the glasses as a function of the glass composition. The number of hydroxyl group in the glass network has been estimated using the following equation [Fe,01]:

$$N_{OH} = \frac{N}{\varepsilon * L} Ln\left(\frac{1}{T}\right) \qquad \text{eq.V.1}$$

where N is the Avogadro constant, L is the sample thickness (cm), T is the transmittance and ε is the molar absorptivity of the free OH groups in the glass. ε used here is the molar absorptivity corresponding to OH groups in silicate glasses, $49.1*10^3$ cm^2/mol [Fe,01].
The concentration of hydroxyl groups can also be estimated in part per million (ppm) using the equation reported by [Ch,82]. Here, the OH ion contamination in the glass bulk can be expressed as follows:

$$C_o = \frac{N_{OH}.W_{OH}}{N_{OH}.W_{OH} + N_{Glass}.W_{Glass}} \qquad \text{eq.V.2}$$

where N_{OH} and N_{Glass} are OH units and glass units in 1 cm^3, respectively. W_{OH} and W_{Glass} are the molecular weight of OH and glass, respectively. Table V.1 summarizes the amount of hydroxyl group in the glasses as a function of x.

Table V.1: Calculated hydroxyl content in glasses in the (90-x)TeO_2 – 10Bi_2O_3 – xZnO system

Composition	OH (10^{19} ions/cm^3) (±0.01 ions/cm^3)
x=15	9.18 (419 ppm)
x=17.5	8.05 (368 ppm)
x=20	4.72 (216 ppm)
x=25	3.38 (155 ppm)

The number of hydroxyl groups is found to depend highly on the glass composition, decreasing progressively with the progressive ZnO introduction in the tellurite network. As proposed by El Mallawany et al. [El,00], the introduction of ZnO in the glass system is expected to connect the non-bridging oxygen of the [TeO_3] and [TeO_{3+1}] groups, leading in turn to a decrease of the possible sites where the OH groups can bond and to a decrease of the refractive index as seen in Figure IV.4

V.1.3 Viscosity properties of the investigated glasses

The viscosity of the investigated glasses was measured from Log 5 Pa.s to Log 12 Pa.s using beam-bending and parallel-plate viscometers. Figure IV.6 shows the Log η as a function of temperature for the investigated glasses. As the ZnO concentration increases, the Log η of the glasses shifts to higher temperatures indicating that the tellurite-based fibers with high ZnO concentration need to be drawn at higher temperature than the fibers with a lower concentration of ZnO. The shift to higher temperatures of the viscosity behavior of the glass when the concentration of ZnO increases is in agreement

with the increase of T_g with an increase of x in Table IV.1 and can be related to the role of ZnO which is believed to cross-link the tellurite network [Ch,07b] [Bü,92].

The activation energy for viscous flow, E_η, an indication of the energy required to sever sufficient bonds within the glass network to initiate "flow", was calculated in the range of Log 9.0 Pa.s and Log 13.0 Pa.s using Equation IV.3 [Sh,05]. From the activation energy, it is possible to calculate, using Equation IV.4, the fragility parameter, which is a common classification of the sensitivity in the temperature dependence of the viscosity for glass-forming liquids, first described by Angell [An,91]. Table IV.3 summarizes the values of E_η, the temperature corresponding to Log 12 Pa.s, referred to as the glass' annealing point temperature (T_{12}), and the kinetic fragility parameter, m, of the investigated glasses. As the concentration of ZnO increases, the activation energy for viscous flow, E_η, T_{12} and m increase. It is important to mention that a 'strong' glass has a *rigid* glass network (a glass network that is over constrained), where the viscosity exhibits less of a temperature-dependence near T_{12} than that for a 'fragile' glass with a *floppy* glass network (a glass network where the number of constraints is less than the number of degrees of freedom) [Du,06] [An,91] [Ca,97]. An example of a 'strong' glass, such as SiO_2, exhibits covalent directional bonding forming a spatial network with m = 17.9 [Na,07]; whereas, a polymer such as poly (methylmethacrylate), PMMA, is considered a 'fragile' glass-forming liquid with molecular-like units interacting via isotropic bonds with Van der Waals forces with an m = 145 [Bo,93]. The increase in the E_η, T_{12} and m with an increase of ZnO content indicates that the glass becomes more fragile when TeO_2 is progressively replaced by ZnO. This is probably due to a reduction in the $[TeO_4]$ units and an increase of the $[TeO_3]/[TeO_{3+1}]$ units

The physical, thermal, optical and structural properties of the glasses with the composition (90-x)TeO_2 – 10Bi_2O_3 – xZnO (with x = 15, 17.5, 20 and 25) were discussed with respect to the structure of the glass network as characterized using Raman spectroscopy. As the ZnO content increases, the density decreases and the Log viscosity curve as a function of temperature as well as T_g and T_{12} shift to higher temperature probably due to ZnO which is believed to cross-link the tellurite network. The decrease of the glasses' refractive index and the increase of the fragility parameter with an increase of ZnO content can be related to the increase of the [TeO_3]/[TeO_{3+1}] units and the decrease of the [TeO_4] units. From the thermal properties measurement, the glasses with x = 17.5 and 20 are expected i) to possess a better stability (resistance) to crystallization and ii) to crystallize at higher temperature than the glasses with x = 15 and 25. Thus, the glasses with x = 17.5 and 20 are better glass candidates for fiber drawing than the glasses with x = 15 and 25.

V.2 Crystallization kinetics of (90-x)TeO_2-10Bi_2O_3-xZnO glasses

Before discussing the nucleation and growth behavior of tellurite glasses as a function of the glass composition, we first validate the methods used in this study to define the nucleation- and growth-like curves using LS2 glass as a reference glass. Here, we will answer the following question: *What is the effect of the glass composition on the nucleation and growth behavior of glasses within the TeO_2-Bi_2O_3-ZnO system?*

V.2.1 Validation of method using lithium disilicate

LS2 glass was chosen as a reference glass as its nucleation and growth-like curves were published and well studied by many authors [Ja,82] [Ra,97] [Ra,01] and extensively reviewed by Zanotto et al. [Za,02].

In this study, the nucleation-like curves were determined using the methods proposed by Ray et al [Ra,97] and Marrota et al [Ma,81]. A complete detail of these methods is presented in §III.8 Differential thermal analysis (DTA) was also employed to determine the nucleation-like curve. The thermal properties of LS2 glass were measured using the DTA and the characteristic temperatures were found to be: T_g=(457±2) ^oC, T_x=(581±2) ^oC and T_p=(642±2) ^oC which are, in the accuracy of measurement, in agreement with those already reported in [Ra,97] [Fo,05].

The nucleation-like curve was obtained by measuring the maximum of the first exotherm and also the height of this peak by heat treating the LS2 glass using a heating rate of 20 ^oC/min to T, a potential nucleation temperature, and holding the glass at this temperature for 3 hours. As seen in Figure IV.9, the nucleation like curves of LS2, obtained using the two techniques, exhibit a similar maximum at (445±2) ^oC which is in agreement with data published by Ray et al. validating the two methods used in this study [Ra,97]. This temperature is commonly called the temperature of maximum nucleation and corresponds to the temperature the glass needs to be heat treated to nucleate a maximum number of nuclei. One can notice that the temperature range at which the nucleation occurs seems to be slightly narrower when the nucleation-like curve is obtained from the measurement of the peak heights. As suggested by [Ra,97], this can be

attributed to slight surface crystallization as the peak height of the exotherm is more sensitive to the surface crystallization than the position of the exotherm peak. Thus, in this study, the nucleation-like curve of the tellurite glasses was obtained by measuring the position of the exotherm peak.

The growth-like curve was determined using the method defined by Ray et al. by measuring the area of the exothermic peak (A_T) when the LS2 glass is heat treated for 5 minutes to T, a growth temperature. A complete detail of the technique can be found in §III.8.2. The growth-like curve of LS2, in Figure IV.10, exhibits an onset of the growth rate at (571±2) ^oC but no maximum could be obtained. The same results were obtained by Ray et al., validating our technique to determine the growth-like curve of the investigated glasses. It is interesting to mention that a complete growth-like curve as a function of temperature could be obtained for ZBLAN [Sm,95] or Chalcohalide [Ma,97] using this technique whereas only a partial curve could be obtained for LS2. As postulated by Ray et al [Ra,01], this can be related to the fast growth rate of the crystals in LS2 at temperatures around 680^oC. If the growth rate of the crystals is high enough to transform most or all of the glass into crystal during the 5 minute heat treatment, no or very small amount of glass samples remains for further crystallization on the last step of the DTA analysis.

In this study we demonstrated that we could reproduce data obtained for a known glass. However, studying LS2 brought to light an important conclusion: the DTA method can produce a realistic nucleation-like curve while the growth-like curve obtained

matches the "true" growth rate as a function of temperature curve only if the growth rate is slow enough to allow the measurement of the fraction crystallized at temperature close or higher than the maximum growth rate. The method proposed by Ray et al cannot be applied to glasses with high crystals growth rates.

V.2.2 Nucleation and growth behavior of glasses in the (90-x)TeO_2-10Bi_2O_3-xZnO

Nucleation- and growth-like curves

The DTA methods of defining the nucleation temperature range and temperature of maximum nucleation rate were applied to the tellurite-based glasses under investigation. Both δT_p and T_p^{-1} were obtained as a function of temperature for all glasses of investigation. No variation in the temperature of maximum nucleation rate and nucleation temperature range was observed as seen in Figure IV.11 which shows the plots of δT_p and T_p^{-1} as a function of temperature for the glass with x=20 taken as an example. This clearly shows that the surface crystallization, while occurring in the glass during the heat treatment, is negligible in this glass system. It is interesting to point out that there is no substantial change occurring in δT_p or T_p^{-1} at temperature below ~370-375^oC suggesting that the initial concentration of nuclei present in the as-quenched glasses remains constant when the glasses are heat treated at temperatures below 375^oC. For temperature between T_g and 375^oC, the nucleation rate is too slow to produce any additional nuclei [Ar,99] whereas heat treatment above this temperature leads to the formation of nuclei in the glass. As seen in Figure IV.11, a heat treatment of the glass with x = 20 at 390^oC for 30 minutes is expected to form a maximum of nuclei in the

glass. Figure IV.12 shows the nucleation-like curves of the glasses. One can notice that the temperature of maximum nucleation slightly decreases from (395±2) ^{o}C to (390±2) ^{o}C when x increases from 17.5 to 25. The glass with x = 15 exhibits the lowest temperature of maximum nucleation measured at (370±2)^{o}C.

The growth-like curves of the investigated are also shown in Figure IV.12. One can observe that there is no clear maximum in the growth-like curve of the glasses of investigation, as seen in the curve of LS2 glass. In agreement with Ray et al, the reason for the lack of maximum in the curve is probably due to the high growth rate of the crystals forming the tellurite network. As seen in Figure IV.12, there might be some overlap between the nucleation and growth like curves.

Crystal growth rate

In order to confirm if there is an overlap between the nucleation- and growth-like curves and to assess if the crystallization is surface or diffusion-controlled, the glasses were heat treated at their respective temperatures of maximum nucleation for different durations. Any formation and growth of the crystals with an increase of the heat treatment duration at this specific temperature would confirm the overlap between the nucleation and growth like curves.

Crystals with a square shape were observed in all the glasses after the heat treatment as illustrated in Figures IV.13a, b and c which present the optical micrographs of the glass with x=20 heat treated at 390°C for 4, 8 and 39h, respectively. One can notice an increase in the crystal size with increasing heat treatment time confirming the overlap between the nucleation and growth regimes. The size of the crystals forming in

the tellurite glasses was recorded as a function of the heat treatment duration and Figure IV.14a presents the variation in crystal size as a function of time for the heat treatment temperature of 390, 400 and 405^{o}C for the glass with x = 20, taken as an example. For short heat treatment durations (<39hours), the crystal size was found to increase linearly with t, the duration of the heat treatment whereas, it increases with $t^{1/2}$ for longer heat treatment (>39hours) as seen in Figure IV.14b. In agreement with [Di,07], this suggests that the glasses exhibit diffusion-controlled crystal growth. From the dependence of the crystal growth with $t^{1/2}$ and the values obtained for the JMA exponent (1.5<n<2.5) (Table II.1), we conclude that the crystal growth occurs in 3D and inside the bulk samples, even though some degree of surface crystallization may be expected due to the presence of surface flaws; we expect, however, this latter contribution to be small. Heat treated samples were examined using XRD with and without removal of the samples surface and no variation in the XRD pattern (not shown here) was found. This observation confirms the lack of measurable surface crystallization at temperature up to 410^{o}C.

From the variation in crystal size as a function of time for short heat treatment, it is possible to estimate the growth rates (U) as a function of the heat treatment temperature. The complete nucleation-like curve and the growth rate curves in Figures IV.12 and IV.16 clearly show that crystals in the glasses with x = 15 and 25 exhibit some differences compared to the glasses with x=17.5 and 20. Specifically these glasses exhibit (i) crystal formation at lower temperature and (ii) growth at a lower rate, and over a smaller temperature range than that seen in the glasses with 17.5 and 20. The difference in nucleation and growth behavior of the investigated glasses as a function of the glass

composition can be correlated to the position of these glasses in the ternary diagram proposed by [Ch,07b]. As seen in the Figure V.1, the glasses with x=15 and 25 are found to be near the limit of the glass formation region while the glasses with x = 17.5 and 20 are much closer to the middle of the glass forming region and hence have a higher stability to crystallization.

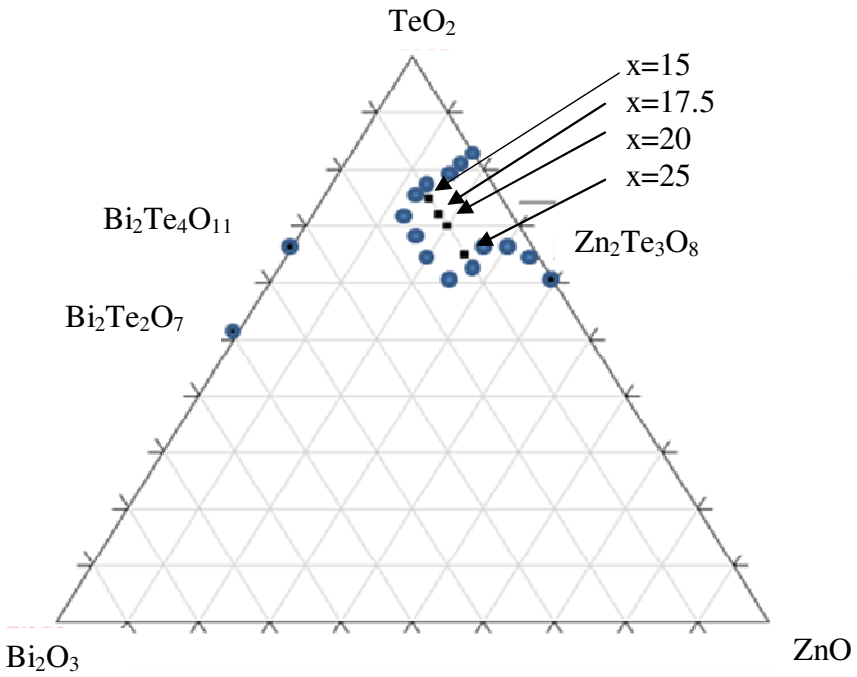

Figure V.1: Vitreous domain diagram for the TeO_2-Bi_2O_3-ZnO system (blue dots=limit of glass formation)

Nucleation rate

The nucleation rate of the crystals forming in the tellurite glasses was obtained using the method proposed by Ranasinghe et al [Ra,02] by heat treating the glass at a potential nucleation temperature to form nuclei and then at a higher temperature to grow the crystals. A complete description of the method can be found in §II.2.1. Figure IV.16b presents the nucleation rate of the investigated glasses. From the nucleation rate, it is possible to estimate N_q, the number of nuclei present in the as-quenched glass and I_n,

nucleation rate. It is important to remember that the number of quenched-in nuclei, N_q, should be constant independent of the nucleation temperature of investigation as suggested by [Ra,02]. However, N_q depends on the glass melting process (temperatures of melting and quenching, crucible used for the melting, purity of the raw materials, etc….). As the investigated glasses were processed using the same crucible, raw materials and melting and quenching processes, it is possible to compare the N_q of the glasses. As seen in Table IV.4, the glasses exhibit a small variation in N_q over the nucleation range except the glass with x = 15 which possesses the greatest variation in N_q. This indicates that the overlap between the nucleation and growth curves of the glasses with x = 17.5, 20 and 25, while existent, is smaller than that of the glass with x = 15 according to [Ra,02]. Thus, crystals are expected to form with large distribution of sizes during the heat treatment of the glass with x = 15 [Ra,02]. Moreover, one can notice that the glass with x=25 has the highest N_q and I_n indicating this glass has a tendency to crystallize in a narrower temperature range as expected from the small bandwidth of its nucleation and growth curve presented in Figure IV.16b and IV.15. Note that the glass with x=15 exhibit the lowest values of N_q while having a similar nucleation rate than the glasses with x=17.5 and 20. This can be attributed to the increased viscosity of the glass at the temperature of the maximum nucleation rate impeding the formation of quenched-in nuclei during the glass formation.

JMA exponent

It is also important to define the kind of growth (surface or bulk, 1D "needle-like", 2D "platelets" or 3D cubic or spherical crystals) occurring in the glass during the

heat treatment. The JMA parameter, n, gives insight into the growth dimensionality occurring in the glass system during crystallization [Ch,65]. The JMA parameter n, taken as the slope of the linear fit of the plot Ln(-Ln(1-χ)) as function of Ln(t) in Figure IV.17b as explained in §III.8.3, was found to vary from 1.7 to 2.2 for x increasing from 15 to 25, is summarized in Table IV.5. As proposed by Christian et al., these values can be grouped: "n" in the range $1.5<n<2.5$ is considered to represent crystal growth which is diffusion controlled, whereas growth character n=2 represents grain edge nucleation after saturation for an interface controlled process [Ch,65]. From the dependence of the crystal growth with $t^{1/2}$ and the values obtained for the JMA exponent, the crystal growth is expected to be diffusion controlled and hence is expected to occur in 3D, even though some degree of surface crystallization is expected.

Crystalline phase identification

The crystals phases formed in the glasses were determined using hot stage XRD in collaboration with Dr. S. Misture at Alfred University. In all studies, the samples were held for 5 minutes at various temperatures before recording the XRD pattern. The presence of a broad peak in the XRD pattern of the annealed glasses seen in Figure IV.18a confirms that after quenching, no significant crystals are present in the glass, even though nuclei are present in the as-quenched glass. These nuclei are probably not large enough and/or numerous enough to induce measurable X-ray diffraction. It is important to mention that no variation in the resulting XRD patterns was observed when the glasses were heat treated at temperatures below 350°C. However, when heat treated at their respective temperature of maximum nucleation, the XRD pattern of the glasses exhibit

sharp peaks at 2Θ= 31.68, 36.74, 52.95, 63.04 and 66.2° shown in Figure IV.18b. These sharp peaks can be attributed to the formation of Bi_2O_3 crystals in agreement with ICCD card #00-057-0400. Senthil et al. showed the formation of $Bi_{3.2}Te_{0.8}Zn_{6.4}$ crystal in glasses with similar composition ((100-2x)TeO_2-xBi_2O_3-xZnO with x=5, 10 and 15) when heat treated at 375°C for 6 hours [Se,04]. The positions of the diffraction peaks of both crystals are quite close; however in the experiment presented here, the position of the peaks has a better match with those of Bi_2O_3 than with those of $Bi_{3.2}Te_{0.8}Zn_{6.4}$. As shown in Figure IV.18c, when the samples are heat treated at 425°C, the peak intensity corresponding to Bi_2O_3 crystals decreases in intensity and new peaks appear. The peaks at 2Θ=21.06, 25.79, 31.45, 36.64 and 40.01° are present in the XRD pattern of all the investigated glasses and can be attributed to $Zn_2Te_3O_8$, in agreement with phases seen in the lower Zn-containing glasses seen by Chagraoui et al. [Ch,07b]. The peaks at 2Θ= 10.67, 19.35, 31.18, 32.59, 36.29, 37.77, 39.93, 43.67, 44.00, 65.29 and 68.48° can be related to $Bi_2Te_4O_{11}$ in agreement with [Sz,96]. It is believed that at temperature between $T_{n\ max}$ and 425°C, Te in these glass compositions is sufficiently mobile to react with the Bi_2O_3 crystals to form $Bi_2Te_4O_{11}$ [Sz,96]. Additional peaks located at 2Θ=8.95, 36.29, 37.29 and 53.40° can be seen in the XRD pattern of the glass with x=25. These peaks are ascribed to $Bi_2Te_2O_7$ in agreement with [Me,98]. The XRD patterns of the glasses heat treated at 500°C (Figure IV.18d) do not exhibit the peaks corresponding to Bi_2O_3 except the XRD pattern of the glass with x=25. Only the peaks related to $Zn_2Te_3O_8$ and $Bi_2Te_4O_{11}$ crystals remain in the patterns of the glasses. Samples were studied via XRD with and without removal of the samples surface after heat treatment and no

variation in the XRD pattern of the partially crystallized sample (not shown here) were evidenced, confirming the lack of significant surface crystallization.

V.2.3 Effect of controlled nucleation and growth on the physical/thermal and optical properties of glasses with x=20.

In order to study the effect of partial crystallization on the physical, thermal, mechanical and optical properties of the glasses, glasses with x = 20 were heat treated at 390°C, their temperature of maximum nucleation from 4 to 39 hours. As explained in §V.2.2, crystals are expected to form and grow in this glass during the heat treatment due to an overlap between the nucleation- and growth-like curves. As seen in Figure IV.13, the heat treatment of the glass lead to the formation with crystals with a size increasing from (68±7) to (408±54)μm. Table IV.6 lists the physical, thermal and mechanical properties of the glasses after heat treatment for 4 to 39 hours. The increase of the glass density from (6.16±0.02) g/cm^3 to (6.25±0.02) g/cm^3 after heat treatment for 4 to 39 hours can be related to the Bi_2O_3 crystals forming in the tellurite network which have a density of 8.929 g/cm^3, greater than the density of the investigated glass measured at (6.16±0.02) g/cm^3 [Ma,06b]. From the density of the glass and of the crystal nucleating in the glass, it is possible to calculate an approximate volume of glass crystallizing during the heat treatment using the following equation [Pa,02]:

$$\rho_{gc} = \rho_c \alpha_c + \rho_c (1- \alpha_c) \qquad \text{eq. V.3}$$

where ρ_{gc} is the density of the crystal containing glass, ρ_g and ρ_c are the density of the glass and crystal, respectively and α_c is the volume fraction of samples that crystallized during the heat treatment.

The volume fraction of crystallized glass gives an insight on the amount of the volume that undergoes crystallization as compared to the volume that remains glassy [Go,80]. Table V.2 presents the volume fraction of glass crystallized in glasses heat treated at 390°C for 4 to 39 hours.

Table V.2: Volume fraction crystallized in the glasses with composition x = 20 as a function of heat treatment time at T=390°C

Heat treatment duration	$\alpha_{c\ \%}$
0h	0
4h	N/A
8h	1.5%
39h	3.3%

As expected, the volume of glass crystallized is larger for longer heat treatment. It is important to mention that the values reported in the table above cannot be taken as a "real" number. Indeed as the glasses are quenched to room temperature at the end of the heat treatment, a decrease of the density is expected, due to the fast quench which is expected to lead to a larger volume and consequently to a lower density than expected [Sh,05].

As seen in Table IV.6, T_g decreases with an increase of the heat treatment time duration. This can be attributed to changes in the glass composition; as Bi_2O_3 forms, the surrounding glass is expected to be deficient in bismuth and hence the T_g decreases. We also noticed a decrease in T_p when the glass is heat treated for 4 to 39 hours. As suggested by Marotta et al and Ray et al, the variation in T_p can be directly related to the quantity of nuclei in the glass [Ma,81]: a large decrease in T_p revealing the formation of a large number of nuclei in the glass after heat treatment.

As seen Table IV.6, the thermal expansion coefficient (CTE) increases from $15.1\pm0.2x10^{-6}$/K to ~$16.1\pm0.2x10^{-6}$/K with the formation of crystals which have a larger thermal expansion coefficient (CTE) than the glass with x = 20 [Ya,05]. An increase of the glasses' Vickers hardness from (301±21) MPa to (344±11) MPa was observed after heat treatment for 39 hours at 390°C. The crystals forming in the glass are expected to inhibit the propagation of cracks increasing in turn the hardness of the material as suggested by Takebe et al. who showed that the formation of crystals with size larger than a micrometer induce an increase of the Vickers hardness [Ta,06].

Figures IV.19a and b present the IR spectra and the UV-VIS spectra of glasses $70TeO_2$-$10Bi_2O_3$-20ZnO as a function of heat treatment duration at 390°C, respectively. The decrease in OH content (absorption band at 3,025 cm^{-1}) is probably due to a higher annealing temperature rather than crystal formation. As seen in Figure IV.19b, there is no significant shift of the optical band gap when the glass is heat treated at 390°C up to 8 hours. This shows that the crystals with a size of (129±19) µm while large enough to induce light scattering are not numerous enough to have a significant impact on the absorption cross-section. However, a shift of the band gap with a visible tail was observed when the glass is heat treated at 405°C for 4 hours. Crystals are expected to form and grow up to (263±27) µm when the glass is heat treated for 4 hours at 405°C as seen in Figure 14a. These crystals are large enough to induce light scattering.

In this section, the nucleation and growth regimes and rates as well as the Johnson-Mehl-Avrami exponent were determined and discussed as a function of the glass composition. We showed that these parameters depend on the glass composition. The

glasses with x=15 and 25 are probably not appropriate materials for applications which require controlled nucleation and growth as i) crystals with a large distribution of size are expected to form in the glass with x = 15 when heat treated at its temperature of maximum nucleation and ii) the glass with x = 25 is expected to fully crystallize on a shorter temperature range than the other glasses. These variations of the nucleation and growth behavior as a function of the glass composition can be related to the domain of glass formation in the TeO_2-Bi_2O_3-ZnO ternary glass system: the glasses with x = 15 and 25 are at the limit of the glass formation domain while the glasses with x = 17.5 and 20 are in the middle of the glass forming region. The predominant crystallization in the investigated glasses is expected to be 3D bulk crystallization governed by diffusion, this statement is supported by the lack of surface crystallization and the non-stoichiometric nature of the crystal formed. Using XRD, we found that Bi_2O_3 crystals are the first crystals to form in the glasses when heat treated at their respective temperature of maximum nucleation. When heat treated at higher temperature, new crystals such as $Bi_2Te_4O_{11}$ and $Zn_2Te_3O_8$ form in the glasses. Lastly, the formation of crystals in the glass with x = 20 when heat treated at 390°C for various time ranging from 4 to 39 hours was found to induce a decrease in T_g, and T_p and an increase in the thermal expansion coefficient (CTE) and density attributed to the higher CTE and density of the crystal as compared to those of the glass. We also showed that the crystals with a size of (129±19) μm do not lead variation in the optical band gap due to the too low amount quantity of such crystals.

V.3 Preform/Fiber processing and characterization

In this section, we present, for the first time to our knowledge, the fabrication and the characterization of novel tellurite-based core-clad preform and fiber. We first explain the choice of the glasses in the TeO_2-Bi_2O_3ZnO glass system used as the core and clad glasses for the drawing of core-clad fibers. Using small quantities of Cu as a tracer, we measured the core dimension uniformity in the preform and we ascertained if diffusion across the core-clad interface occurs during the core-clad preform processing using a rotational caster. The key attributes of the fiber such as its numerical aperture and its propagation losses at 632 nm and 1.55 μm are reported. Lastly, we discuss the effect of the fiber drawing process on the thermal and structural properties as well as on the nucleation and growth behavior of the glasses. Specifically, we will answer the following question: *What significant differences, if any, exist between bulk glass and the corresponding fiber?*

V.3.1 Core preform and fiber processing and characterization

To be considered a suitable candidate for fiberization, the glass must have a good thermal mechanical resistance to casting (shock, fracture) and a good stability (resistance) to crystallization. This resistance to crystallization can be estimated by measuring the glass' thermal properties such as its glass transition temperature, T_g and crystallization temperature, T_x. The difference between these values, $\Delta T=T_x-T_g$, provides a gauge of the glass' resistance to crystallization, and should be as large as possible to suggest that the glass can form fiber of good optical quality with minimal scatter loss from microcrystallites [So,93]. Typically a ΔT value larger than 100°C suggests reasonable

glass stability. As the preform must sit within a heated furnace during drawing, this stability becomes important for realizing crystallite-free fiber, as the length of the "hot-zone" within the furnace (between the orifice where the first glass bead "drops" and the length of the preform) can be large. In the fiber draw system used in this study, the distance is 25 mm. Based on §IV.1 and §IV.2, the glasses with x = 17.5 and 20 can be considered as good candidates for fiberization as their ΔT values are larger than 100°C (see Table IV. 1). Thus, core preforms with x=20 were processed as explained in §III.6 and were drawn into 125 µm diameter fibers. From the viscosity properties of the glass the draw temperature was set to 370°C. Figure V.2 presents the Ln (U) as a function of temperature.

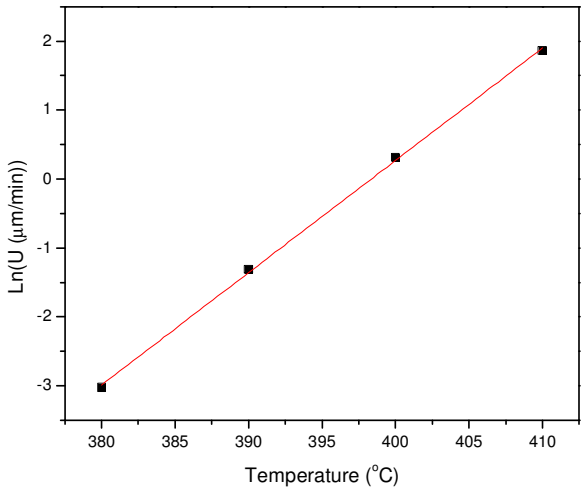

Figure V.2: Ln (U) as a function of temperature

Figure V.2 yield a straight line equation of which can give an insight of the expected crystal growth at low temperatures. At the drawing temperature, the growth rate is expected to be as low as 4nm/min. Thus, no significant crystallization should occur during the drawing of the preform. As confirmed by the lack of crystallization peak in the

x-ray diffraction pattern of the core fiber. These results however, do not exclude the possible low level formation of a second phase after drawing.

The thermal properties of the fiber were measured and compared with those of the preform. The T_g of the fiber was found to be identical to that of the preform indicating that the fiber drawing has no or little impact on the overall bond strength in the tellurite network. However, while the preform was found to have only one exothermic peak, the fiber possesses 3 exothermic peaks as seen in Figure IV.20. Due to its first crystallization peak, with an onset temperature T_{x1} at (371±2) ^{o}C, the fiber exhibits a lower ΔT than the preform indicating a decrease in the glass stability against crystallization after the fiber drawing process. The presence of the 3 exothermic peaks in the DTA scan of the fiber can be related to the XRD pattern of the bulk glass with x=20 presented in Figure IV.18. It is possible to assume that the 3 crystallization peaks correspond to the 3 crystals forming at various temperatures: Bi_2O_3, $Bi_2Te_4O_{11}$, and $Zn_2Te_3O_8$. In the case of the preform, it is believed that these three crystallizations are encompassed in the unique crystallization peak.

As seen in Table IV.8, the fiber exhibits smaller E_a and larger Ec_2 than the preform. As E_a can be related to the activation energy for viscous flow, the decrease of E_a after fiber drawing can be related to changes in the viscous flow behavior of the glass probably due to the change of the thermal history of the glass occurring during the drawing. As explained in §IV.1.1, the activation energy of crystallization is an indication of the speed of crystallization [Ti,06]. The larger Ec_2 of the fiber compared to that of the preform indicates that the fiber has the maximum rate of crystallization and thus has a higher tendency to crystallize than the glass. Because of the appearance of a

crystallization peak at lower temperature in the DTA scan of the fiber compared to that of the preform, it is possible to think that the fiber crystallizes at lower temperature than the preform indicating that the fiber drawing process does change the thermal properties of the glass and consequently its stability to crystallization

V.3.2 Core-clad preform and fiber processing and characterization

For the processing of the optical core-clad fibers, it is crucial for the glasses used for the core and clad of the fiber to have similar thermal properties (T_g and viscosity/temperature response) as well as minimum mismatch in CTE (coefficient of thermal expansion) [Eb,05]. Large CTE mismatch between the core and the clad compositions can yield stresses that can ultimately lead to fracture of the preform and/or fiber. The refractive index of the core material needs to be slightly larger than that of the clad to allow guiding within the core via total internal reflection [Ka,00]. As explained in §IV.1, an increase in TeO_2 content can increase the refractive index of the glass. As shown in the previous paragraph, the glass with x = 20 can be drawn into fiber. For the processing of a core-clad fiber, the glass with x= 25 cannot be used as a core material as this glass was found to have a higher tendency to fully crystallize over a short temperature range than the other glasses. Thus, the glass with the composition $72.5TeO_2$–$10Bi_2O_3$–17.5ZnO was chosen as a core glass composition as this glass was found to exhibit a good resistance to crystallization: its T_g was measured at (333±2) ^oC and T_x at (476±2) ^oC (Table IV.1). Thus, core-clad preforms with the composition $72.5TeO_2$-$10Bi_2O_3$-17.5ZnO and $70TeO_2$-$10Bi_2O_3$-20ZnO, respectively for the core and clad

glasses, were processed using a rotational caster. Since the quality and light-guiding efficiency of a fiber is highly dependent upon the quality of the preform, it is crucial to process core-clad preform with i) controlled wall thickness, ii) a highly uniform Δn between core and clad along the length of the preform and iii) low surface and bulk defects both within each respective glass and at their interface. Defects such as cracks and bubbles can cause light scattering that compromises the guiding quality of the fiber, inducing large loss and degrading the mechanical integrity of the resulting fiber [Ni,81]. In order to obtain bubble- and crack-free core-clad preforms, the process variables of the rotational caster (spinning speed, spinning time, glass quench temperature and mold temperature) were evaluated and optimized for the defined compositions as explained in §III.6.

During the casting of the core in the clad tube, diffusion from the hot core to the cold clad, may occur due to a re-melting or softening of the cladding glass. To assess the core-clad interface uniformity and the probable diffusion between the core and clad glasses, the core or clad glasses were doped with Cu, used as a tracer. The preforms were sliced into cross-section and optically polished for visual inspection. As seen in Figure IV.22, a good uniformity of the cladding layer thickness, with less than 3% thickness variation, can be observed along 40 mm of the preform. As can be seen in Figure IV.21, the undoped glass remains colorless compared to the Cu doped glass showing the absence of an apparent diffusion of Cu from the doped glass to the undoped glass during the casting of the core glass into the clad glass. This was confirmed by measuring the absorption spectra in both doped and undoped glasses near the core-clad interface. As seen in Figure IV.23, the absorption spectrum of the undoped glass shows no absorption

band in the visible range related to the Cu dopant while the spectrum of the Cu-doped glass exhibits the tail of an absorption band expected to be centered at 790 nm which can be attributed to CuO [Ku,95]. The absence of an absorption band at 790 nm in the absorption spectrum of the undoped section suggests the absence of an extensive diffusion of Cu across the interface occurring during the casting of the core glass into the clad glass. In order to verify the absence of diffusion at the atomic level, elemental analysis using an EDS/SEM was performed on a cross-section of the Cu-doped-core clad preform in order to assess small diffusion occurring during the core-clad preform processing. Figure IV.24 provides the atomic percent of Te and Cu along a line crossing the full diameter of the core-clad preform. No significant diffusion of Te or Cu was confirmed as shown in Figure IV.24 confirming that it is possible to maintain the desired index step in the core-clad preform processed using the rotation casting method.

The core-clad preforms with the composition $70TeO_2$-$10Bi_2O_3$-20ZnO and $72.5TeO_2$-$10Bi_2O_3$-17.5ZnO, respectively for the clad and core glasses were drawn into fiber as explained in §III.6.3. The step index difference between the core and the clad is clearly represented on the micrograph in Figure IV.25 by the bright coloration of the core compared to that of the cladding. Similar micrographs of core-clad fiber were reported by Prassad *et al* in $KNbO_3$-doped TeO_2- Na_2O- ZnO glass fibers drawn using the rod in tube method [Sy,06]. The composition of the resulting drawn fiber was analyzed using EDS. Within the accuracy of the measurement (±2 at.%), the fiber composition was found to be identical to that of the preform. Similarly, the glass transition temperature (T_g) of the fiber was measured and found to be (332±2)^oC, which is identical to the T_g of the

corresponding preform. No crystallization peak could be seen in the x-ray diffraction of the core-clad fiber indicating the absence of the crystallization during the fiber drawing. These results however, do not exclude the possible low level formation of a second phase after drawing.

The effect of the drawing process on the structure was investigated using micro-Raman spectroscopy. The Raman spectra in Figures IV.26a and b reveal three major bands in the 400–800 cm^{-1} range. It can be seen that the Raman bands located in the 400-500 cm^{-1} region and the shoulder at 650cm^{-1} have a higher intensity for the core glass composition as compared to the cladding glass composition as expected due to the larger amount of TeO_2 in the core glass as discussed in §IV.1. The large intensity of the band at 770 cm^{-1} can be explained by the distortion of the TeO_4 site resulting in TeO_{3+1} polyhedra [Ch,04] [Ko,95]. Compared to the Raman spectra of the clad and core glasses in the preform, the intensity of the band at ~400 cm^{-1} in the spectra of the clad and of the core glasses in the fiber increases slightly in intensity and shifts to higher wavenumbers. As observed in [Ro,02], these variations might reflect an increase of the linkages O–Te–O and Te–O–Bi in the network of the fiber. A larger increase in intensity is seen for the band located at ~660 cm^{-1} as compared to that of the band at 770 cm^{-1} suggesting an increase of the TeO_4 units after fiber drawing. The fiber drawing process leads to the formation of a fiber with a more connected structure than the preform. This structural variation can be related to the changes in the glass network upon variation of the glass' thermal history and to a physical orientation of the molecular units within the glass. It is interesting to note that the variations in the Raman spectra induced by the drawing process are more pronounced in the spectra of the clad glass, most likely due to the more

rapid quenching of the outer fiber surface, as compared to the core of the fiber which sees a "slower cooling rate" than the outer fiber surface.

As changes in the structure can be seen after the drawing of the fiber, it is of great importance to asses any changes in refractive index induced by the fiberization process. The core-cladding index difference (Δn) obtained from the NA calculation was found to be (0.009 ± 0.002) using Equation III.19, this value for the index difference in the fiber is similar to that measured in the perform glasses, as shown in Table IV.9. This result suggests that the drawing process leads to no noticeable change in the refractive index difference between the core and the clad glasses. Using Equation IV.10, the number of modes traveling in the fiber is estimated at 51, revealing that the fiber is multimode. In order to obtain a single-mode fiber at 1.55 μm, the core diameter of the fiber should be reduced to approximately 8 μm.

The propagation losses at 632 nm and 1.5 μm for 60 cm long core-clad fibers were measured using the cutback method, described in §III.7, and were found to be (3.2 ± 0.1)dB/m and (2.1 ± 0.1)dB/m, respectively. Similar losses were reported in fiber in the ternary glass system TeO_2-ZnO-Na_2O doped with $KNbO_3$ by Prasad et al. [Sy,06] but larger than those reported for commercial monomode tellurite based fiber having a propagation loss <0.1 dB/m [Oh,02]. The high losses in our fiber can be related to some surface and volume defects within the glass such as bubbles and/or impurities such as Fe, Cu, Co, Ni, Mn, and Cr which absorb strongly in the 600 – 1600 nm wavelength range [Gl,79]. These impurities are present in the raw materials and can come from the crucible. Water can be also a possible origin for high loss at 1.5 μm as suggested by

[Gu,05][Ts,03][Fe,01]. From the IR absorption spectra of the glass with x = 17.5 presented in Figure IV.3b and the Equation V.1, the OH^- content is ~8.05.10x10^{19} ions/cm^3, which is similar to that reported by Feng et al. in germano-tellurite glasses and Dai et al. in Er_2O_3 doped TeO_2-ZnO-La_2O_3 glasses made using high purity raw materials with no special heat treatment to reduce the OH^- content in the raw materials [Fe,01] [Da,06]. This suggests that while high purity ingredients can reduce losses in the visible, OH reduction requires dedicated processing steps to both raw materials prior to melting and to the melt environment during melting. We believe that the use of raw materials with higher purity, of a pure Pt or Au crucible and melting in controlled atmosphere would significantly decrease the losses in the fiber.

V.3.3 Effect of the fiberization process on the nucleation and growth behavior

The nucleation- and growth- like curves of the core preform with x = 20 were obtained using Marotta's and Ray's methods and were compared with those of the bulk glass. As can be seen in Figure IV.27, the maximum for the nucleation curve decreases from (390±2°C) to (384±2°C) after fiber drawing indicating that the fiber crystallizes at slightly lower temperature than the bulk glass. This is in agreement with the presence of a crystallization peak in the DTA scan of the fiber at lower temperature than in scan of the preform. It is important to point out that the fiber drawing process increases also the overlap between the nucleation- and growth-like curves. Crystals with a large distribution of size are expected to form in the fiber when heat treated at its temperature of maximum nucleation. The growth-like curve of the fiber exhibits 2 inflection points at (382±2) °C,

(426±2) ^{o}C while none was detected on the growth-like curve of the preform. As seen in the DTA data reported in Table IV.7, 3 crystals are expected to form in the glass fiber at 3 distinct temperatures and over 3 distinct temperature ranges. Hence the 2 inflection points can be attributed to either the growth of two distinct crystals and/or the growth of a single crystal growing in two different dimensionalities (i.e. surface and bulk crystallization) as suggested by the JMA exponents of the fiber listed in Table IV.10. The low value of n for the 1st exothermic peak, may indicate that the first crystals form first at the surface of the fiber [Ch,65] while the larger value of n for the 3rd exothermic peak suggests the formation of crystals in the volume of the fibers. From the JMA parameters and the DTA analysis of the fiber, it is possible to think that a surface crystallization occurs in the fiber when heat treated at low temperature, having a maximum growth rate at about ~382^{o}C. The crystal forming is believed to be in the Bi_2O_3 crystal composition. When heat treated at higher temperatures, we think that Bi_2O_3 crystals form in 3 dimensions in the bulk of the fiber, then transform into the $Bi_2Te_4O_{11}$ crystal having a maximum growth rate at about 426^{o}C. Finally, crystallization of the fiber is expected to end with the formation of $Zn_2Te_3O_8$ crystals, whose maximum cannot be seen in the growth-like curve probably due to a fast growth rate of these crystals and/or due to the presence of other crystal composition at temperature around 460^{o}C. As performed for the bulk glasses, the fiber was heat treated between 380^{o}C to 400^{o}C between 1 and 8 hours. No heat treatment could be performed at temperature higher than 400^{o}C due to the small size of the fiber which sagged under its own weight. Crystals are expected to form at the surface and in the volume and grow simultaneously in the fiber. However, after carefully polishing the cross-section of the fiber as the surface crystallized rapidly, no crystals

could be seen inside the fiber using an optical microscope and SEM, probably due to the brittleness and the small size of the fiber optical microscopy and/or SEM.

In this section, we report results on the processing and characterization of novel core and core-clad preforms and fibers within the TeO_2-Bi_2O_3-ZnO glass system. The core-clad fiber was drawn from a core-clad preform prepared via rotational casting. Using Cu ions as a tracer, we showed excellent cladding layer thickness uniformity across lengths of up to 40 mm in a 65 mm long perform with no detectable diffusion of elements between the core and the clad glasses occurring during the processing of the preform. Using micro-Raman spectroscopy, the structure of the fiber is thought to be more connected with a larger number of [TeO4] units than that of the preform. These changes were attributed to modification to the bulk glass' thermal history upon drawing and small scale molecular orientation of chain units within the tellurite glass matrix upon fiberization. The resulting multimode core-clad fiber was found to have an index step of (0.009±0.002) at 632 nm between the fiber core and clad composition with losses at (3.2±0.1) and (2.1±0.1) dB/m at 632 nm and 1.5μm, respectively. We showed that the fiber drawing of the glass with the composition $70TeO_2$-$10Bi_2O_3$-20ZnO increases the tendency of the glass to crystallize at lower temperature. Three crystalline phases at 3 distinct temperatures and over distinct temperature range are expected to form in the fiber. From the JMA parameters, surface crystallization will occur in the fiber with maximum growth rate around (382±2)^oC while bulk crystallization will occur when the fiber is heat treated at higher temperature with a maximum growth rate at about (426±2)^oC. Crystals forming in the fiber were found to be difficult to analyze due to the

overlap between nucleation and growth as well as overlap between the growth of the various crystals. .

V.4 Hydroxyl group reduction in TeO_2-based glasses

As discussed in §II.4.2, impurities such as hydroxyl (OH^-) are one of the origins for the high propagation loss at 1.5 μm in the fiber investigated in this study. Thus, efforts were focused on the reduction of OH^- groups in the TeO_2–Bi_2O_3–ZnO system. In this section, we investigate the processing of tellurite bulk glass and fiber with x = 20 with low OH content using fluorine based raw materials, adding modifiers in the tellurite network and melting in various environments. We discuss the effect of OH reduction in the network on the physical, thermal, optical and structural properties as well as on the nucleation and growth behavior of bulk glasses and fiber. Specifically, we will answer the following question: *How can the water be reduced in the glasses and in the resulting fiber and what is the impact of OH reduction on the physical, thermal, optical and structural as well as the nucleation and growth behavior of the glass with x = 20?*

V.4.1 Processing and characterization of glasses with various levels of OH content

In order to reduce the OH content in the tellurite network, glasses with the compositions (100-x) ($0.70TeO_2$–$0.10Bi_2O_3$–$0.20ZnF_2$)- xMO and (100-x) ($0.70TeO_2$–$0.10Bi_2O_3$–0.20ZnO)–xMO with MO= Li_2O, BaO and K_2O and x = 0, 2 and 4 were

processed using a standard melting method detailed in §III.1 in regular and oxygen-rich environment.

As seen in Table IV.10, Figures IV.28a and IV.29a, the introduction of alkaline or alkaline earth materials in the tellurite-based network leads to variation in the physical, thermal, optical and structural properties of the glasses and more importantly to a decrease of the OH content. It is clearly shown that the variation of these properties depends on the nature of the alkaline and alkaline earth introduced.

The glass' molar volume and thus the associated free volume dictate the open space within a glass network where OH can reside, either as "bound" (interstitial) water or molecular water. Bound water can be physically bonded (as an anion to a cation in the network) whereas molecular water can sit in a network void which when dry is vacant. The addition of Li_2O to the reference glass creates non-bridging oxygen [NBO] in the glass network which results in a decrease in T_g [De,09]. However, the small Li^+ radius causes the surrounding matrix to collapse around it, slightly reducing the V_m in the lithia containing glasses. The role of the potassium oxide is similar in its formation of NBO, however due to its larger ionic radius, K^+ addition increases V_m, while also slightly reducing the glass T_g from that of the alkali free glass. BaO also serves as a modifier, creating NBOs and hence free volume in the glass network, as indicated by the decrease in V_m [De,09]. Here the larger Ba^{2+} not only opens the network, but partially fills the increase in space (free volume) that results. This filling of interstitial volume prevents OH species from occupying this void.

As seen in Figure IV.28a, the reduction of the OH content increases in the order of $Li^+<K^+<Ba^{2+}$ where the baria-containing glass shows the lowest OH content. As seen

in Figure IV.29a, the introduction of these alkalines and alkaline earth in the tellurite network also leads to variation of the glass network. The addition of Li_2O and K_2O to the tellurite network leads to more significant variations of the glass structure than the addition of BaO. The shift to higher wavenumber of the band at 740 cm^{-1} and the decrease of the band at 660 and 400 cm^{-1} compared to that at 740 cm^{-1} may suggest that the addition of Li_2O and K_2O results in the conversion of the TeO_4 units into TeO_3/TeO_{3+1} with NBO and a decrease of the Te-O-Te linkages. The larger variations in the Raman spectrum of the K-containing glass compared to those observed in the spectrum of the Li-containing glass may indicate that the introduction of K^+ depolymerizes the tellurite network to a greater extent than the addition of Li^+ by promoting a larger conversion of TeO_4 into TeO_{3+1} and TeO_3 with an increase of non-bridging oxygen (NBO). This is in agreement with the variation discussed in Table IV.10. Due to its small ionic radii, Li^+ is believed to enter into the network without altering it dramatically, in agreement with the slight decrease in the molar volume; we believe that K^+ replacement may introduce further distortion of the tellurite network which leads to a more pronounced increase of the molar volume and consequently to a decrease of the OH content. The absence of variation in the Raman spectra with the introduction of Ba^{2+} into the tellurite network suggests that Ba^{2+} enters in the tellurite network without creating a significant change in both TeO_4 and Te-O-Te units. This is interpreted to be due to the lower number of NBO's formed by BaO versus alkali oxides. The larger decrease of the OH content with the introduction of BaO may be related to less numerous NBOs forming in the glass network and to the dramatic decrease of the molar volume. This may be related to the large bond strength through the Ba^{2+} high field strength in agreement with

[Me,01] and also to the large mass of Ba^{2+} which leads to a large density of the Ba-containing glass in agreement with [De,09]. It is interesting to point out that the glass transition temperature increases in the order of $Li^{+}<K^{+}<Ba^{2+}$ as expected from the stronger bonds through the higher field strength cations in agreement with [Me,01].

As seen in Figure IV.28b it is also possible to reduce the OH content of the tellurite-based glasses by changing the raw materials and the environment used during the melting of the glass. When the glass is melted in O_2-rich environment or when the glass is prepared using ZnF_2 instead of ZnO, the density of the glass increases and its molar volume decreases. This is in agreement with Karmarkar et al. who observed the same phenomena in calcium metaphosphate glasses melted in O_2 atmosphere. They demonstrated that a glass attains a denser structure with a large dehydroxylation [Ka,99]. The effect of melting in an O_2-rich environment yields the most pronounced change in properties of all the compositional variations. As compared to the "air-melted" reference (Laboratory has a relative humidity (RH) of ~ 45%) the glass melted in a drier O_2-rich environment (O_2-flow rate=0.4 L/min) has a higher T_g and density, in addition to its much reduced OH content. These suggest that the O_2 molecules present in the melt environment displace OH from the network, reducing both bound R^{+}-OH^{-} units as well as molecular water which occupy the reference glass network. When considering the flow rate and the volume of the furnace used, it is assumed that, when the melting temperature is reached approximately 95% of the original atmosphere (air) is replaced by oxygen coming from the compressed oxygen tank (UN 1072). This increase in the glass' free volume is seen in the decrease of V_m which accompanies the increase in density and T_g.

As no variation could be observed in the Raman spectrum of the glass prepared in O_2-rich atmosphere as compared to that of the glass prepared under air, it is conceivable that a constant flow of O_2 during the glass melting, which leads to a glass with lower OH content, inhibits the bonding of OH to the tellurium network as well as repulses the free OH out of the tellurite network [Pe,06]. This flow of O_2 during the melting is expected to reduce the moisture in the furnace chamber and thus the moisture absorption during the glass melting [Eh,04]. The higher T_g of the glass when melted in O_2 rich atmosphere can be related to the decrease in OH concentration. In agreement with Min'ko et al [Mi,07b], the decrease of the OH groups leads to changing in the strength of the weak hydrogen bond giving rise to an increase in the glass transition temperature as seen in Table IV.10.

Fluorine is a powerful drying agent in glass processing, as it can displace bound OH in the glass network. The hydroxyl and fluorine ions are isoelectronic, have similar ionic size and hydroxyl ions can be easily replaced by fluorine during melting. Therefore, the decrease of both absorption bands in the IR spectra, as seen in Figure IV.28b, can be interpreted on the basis of an introduced fluorine concentration increase. Its larger ionic size and polarizability, as compared to the bridging and non-bridging oxygen it replaces leads to a reduction in V_m and a much lower T_g than its ZnO counterpart. According to [Na,03], the reaction of evaporation of the fluorine compound can be simplified as follows: $OH^- + F^- \rightarrow HF + O^{2-}$. The reaction of the fluorine evaporation allows the dehydroxilation of the melt. Compared to the Raman spectrum of the glass prepared using ZnO, the shift of the band at 740 cm^{-1} to larger wavenumbers reveals an increase of the TeO_3/ TeO_{3+1} units. As fluorine ions are not expected to act as a bridge between two Te atoms [Na,03], the increase of the Te-based units with NBO can be related to the

presence of remaining fluorine, in agreement with the lower T_g of the glass prepared using ZnF_2 compared to that of the glass prepared with ZnO (Table IV.10). Using wavelength-dispersive x-ray fluorescence spectrometry, 1.88wt% of fluorine is found to remain in the glass network as terminal species on what were most likely R-OH^- site that have been eliminated. It is clearly shown in Figure IV.28a and b that the use of the self drying effect of fluorine or the addition of an alkaline earth in the glass network can lead to a tellurite-based glass with a low OH content due to a reduced free volume in the glass and to a lower number of non bridging oxygens in the glass network.

As melting in oxygen-rich environment was found to be an efficient technique to reduce the OH content in the glass, two 30 g batches with the composition $70TeO_2$-$10Bi_2O_3$-20ZnO were melted in air and an oxygen-rich environment and were quenched in a cylindrical mold preheated below the T_g of the glasses in order to process two core preforms with various OH contents. After annealing at 285 ^oC for 15 hours, the preforms were drawn into 125 µm diameter fibers using the drawing technique detailed in §III.6.3. The losses in the fibers were measured as a function of wavelength and the spectra are shown in the Figure IV.30. The spectrum of the "air-melted" fiber exhibits a band at 1,470 nm. As suggested by [Ta,02], the absorption band at ~ 1,470 nm can be related to vibrational resonances of the OH at 2.71 µm and to the harmonic and combination tones of OH with Te. As this band is absent in the spectrum of the fiber drawn from a preform melted in oxygen-rich environment, it is possible to think that the melting of a 30g batch in oxygen-rich atmosphere can lead also to fiber with lower OH content than when the preform is melted in air. From Table IV.10, the OH content in the fiber is expected to be

at least 1.71 10^{19} ions/cm^3 when the preform batch is melted in O_2-rich environment. Such high OH content should produce a significant OH absorption band. The lack of absorption band in the loss spectrum can be related to the high background loss of the fiber induced by extrinsic absorption from impurities, such as Fe, Cu, Co, Ni, Mn, and Cr absorbing strongly in the wavelength range 0.6 - 1.6 μm. These impurities are thought to be present in the raw materials or to be contaminants from the crucible. The high losses in the fiber can also be related to imperfections in the fiber core such as bubbles and micro-cracks. Furthermore, it is important to mention that cleaving the fibers in a repeatable fashion was challenging due to the low mechanical strength of the fiber, and variation in the cleave quality in either fiber end can also affect the measurement of the background loss. Compared to losses in silica fiber, typically 0.15 dB/km at 1.55 μm [Na,02], the losses of the tellurite fiber with low OH content are still too high to use these novel fibers for optical applications. Additional purification, drying of the raw materials and use of higher purity raw materials prior to the glass melting will be necessary to further reduce the losses in the fibers.

V.4.2 Processing and characterization of glasses with reduced OH content.

It is clearly shown in Figures IV.28 a and b that the use of the self drying effect of fluorine and the addition of an alkaline or alkaline earth in the glass network can lead to the processing of a tellurite-based glass with a low OH content due to a reduced free volume in the glass and to a lower number of non bridging oxygen in the glass network. Based on these results, a glass with the composition 4BaO- 96(0.70TeO_2-0.1Bi_2O_3-

0.2ZnF_2) was melted in an O_2-rich environment. As fluorine was found to be a powerful drying agent, the glass batch was pre-mixed with 20 weight% NH_4F-HF prior to the melting to further decrease the OH content in the glass. Figure V.3 presents the infrared spectra of the Ba-containing glasses prepared with ZnO or ZnF_2, melted in air or in oxygen-rich environment with and without a pre-heating step with NH_4F-HF prior to the melting.

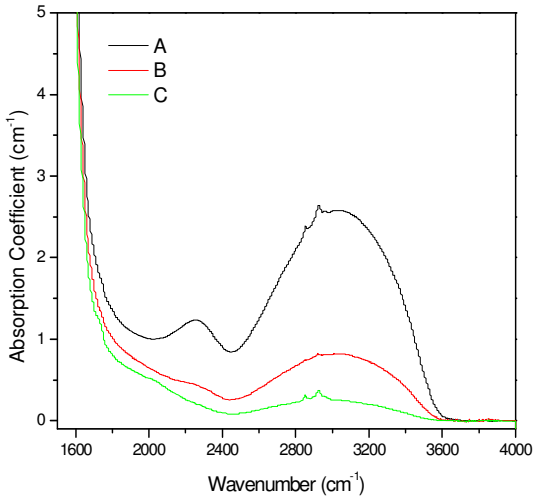

Figure V.3: Near infrared absorption spectra of glasses with low OH content. A = 4BaO-96(0.7TeO_2-0.1Bi_2O_3-0.2ZnO), B= 4BaO-96(0.7TeO_2-0.1Bi_2O_3-0.2ZnF_2) melted in O_2 and C = 4BaO-96(0.7TeO_2-0.1Bi_2O_3-0.2ZnF_2) melted in O_2 after a pre-treatment using 20 weight% of NH_4F-HF.

The amplitude of the absorption band centered at 3,000cm^{-1} dramatically decreases when the glasses are prepared using ZnF_2 and melted in O_2 rich-environment. The decrease of the band amplitude is even more pronounced when the batch is pre-heated with NH_4F-HF prior to the melting confirming that NH_4F-HF compound can react with the moisture at the grain interface reducing the OH trapped in the batch as seen in [Pe,06]. It is important to point out that the absorption band at 2,225cm^{-1} almost disappears, confirming the efficient dehydration of the glass batch prior to the melting.

Table V.3 presents the density, molar volume and glass transition temperature of the new investigated glasses.

Table V.3: Density, molar volume and glass transition temperature of low OH containing glasses.

Glass composition	**Density (g/cm^3) ($\pm 0.02 g/cm^3$)**	**Molar Volume (cm^3/mol) ($\pm 0.09 cm^3/mol$)**	**T_g (^oC) ($\pm 5^oC$)**	**OH (10^{19} ions/cm^3) (± 0.01 ions/cm^3)**	**F from XRF (weight%) (± 0.5 %)**
0.96 ($70TeO_2$–$10Bi_2O_3$–$20ZnO$) – $0.04BaO$	6.12	28.02	340	3.15 (144ppm)	NA
0.96 ($70TeO_2$–$10Bi_2O_3$–$20ZnF2$) – $0.04BaO$, melted in O_2-rich-environment					
No pre-heat treatment with NH_4F-HF	6.19	28.07	321	1.00 (44.7ppm)	1.10
With pre-heat treatment with NH_4F-HF	6.20	28.02	311	0.32 (14.6ppm)	1.45

The Ba-containing glasses melted in O_2 with and without pre-treatment with NH_4F-HF have a higher density and lower T_g than the F-free "air-melted" glass. As mentioned in the previous paragraph, the increase in the glass density of the glass melted in O_2-rich environment can be explained by the decrease in structural defects. The decrease in T_g can be related to the presence of remaining fluorine in the tellurite network as confirmed using XRF. As seen in Table V.3, a larger wt% of fluorine remains in the glass pre-mixed with NH_4F-HF. This is probably due to the short heat treatment at 500^oC and/or to the low temperature of heat treatment which did not lead to complete evaporation of fluorine prior to the melting. We expect that an appropriate pre-heat treatment duration and temperature prior to the melting could lead to a tellurite glass with only few ppm of fluorine. As seen in Table V.3, we are able to process a tellurite-based

glass with a quantity of OH groups as low as (0.32±0.01) *10^{19} ions/cm^3 (corresponding to a decrease of 93% of the original value) by

i) adding Ba^{2+} which is expected to reduce the free volume in the glass network,

ii) replacing ZnO by ZnF_2,

iii) controlling the atmosphere during the melting (melting in O_2 rich-environment) and

iv) pre-heating the batch prior to melting with NH_4F-HF.

This quantity of OH groups in this new glass is low compared to the quantity of OH reported at 2.44*10^{19} and ~6*10^{19} ions/cm^3, respectively in germano- and Zn-containing tellurite-based glasses [Fe,01] [Da,06].

Figure V.4 presents the Raman spectra of the new glasses.

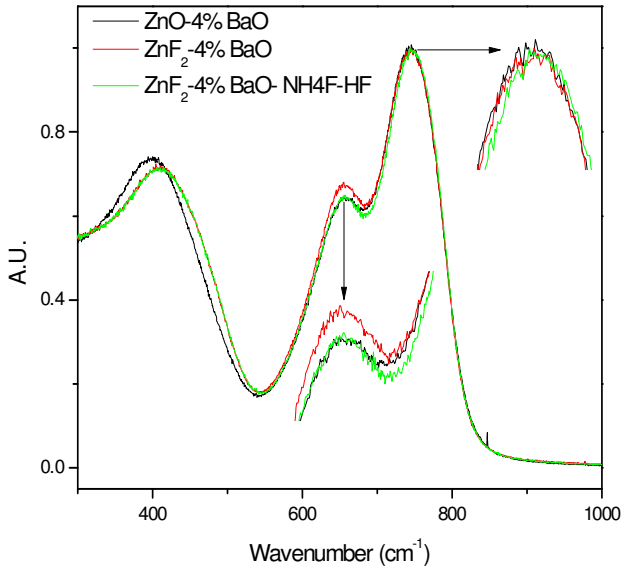

Figure V.4: Raman spectra of glasses with low OH content. A = 4BaO-96(0.7TeO_2-0.1Bi_2O_3-0.2ZnO), B= 4BaO-96(0.7TeO_2-0.1Bi_2O_3-0.2ZnF_2) melted in O_2 and C = 4BaO-96(0.7TeO_2-0.1Bi_2O_3-0.2ZnF_2) melted in O_2 after a pre-treatment using 20 weight% of NH_4F-HF.

As seen in the Raman spectrum of the glass processed using ZnF_2 depicted in Figure IV.29b, the main band at 740 cm^{-1} in the Raman spectra of the new investigated glasses processed using fluorine-based raw materials shifts toward higher wavenumber when the batch is prepared with ZnF_2 and pre-heated with NH_4F-HF prior to the melting. As explained in the previous paragraph and in agreement with the decrease in T_g, this confirms the presence of residual fluorine which leads to an increase of the Te-based units number with non bridging oxygen as suggested by [Na,03]. Moreover, it is interesting to point out that the position of the band at 400 cm^{-1}, the intensity of which decreases strongly as compared to that of at 740 cm^{-1}, shifts to larger wavenumber when the Ba-containing glass is processed using fluorine-based raw materials. These variations reveal a decrease of the Te-O-Te, O-Te-O and Bi-O-Bi bonds in the glass network. It is possible to think that the remaining fluorine in the glass network induces more distortion of the Ba-containing glass network than in the Ba-free glass. This is probably due to the presence of Ba^{2+} in the glass network which leads to the formation of weaker bonds in the tellurite network due to the formation of NBO.

V.4.3 Effect of OH reduction on the nucleation and growth behavior of bulk and fiber

As discussed in the previous paragraph, bulk glass and corresponding fiber with x = 20 were prepared by melting the glass in air and in an O_2-rich environment in order to produce glasses with various levels of OH content. The thermal properties of the bulk glass and fibers were measured and compared as a function of the OH contents. As seen in Figure IV.31a, while the “air-melted” bulk glass processed was found to have only one

exothermic peak, the glasses prepared with reduced OH content possesses 3 exothermic peaks corresponding probably to the 3 different crystal forming in this glass system (Bi_2O_3, $Bi_2Te_4O_{11}$ and $Zn_2Te_3O_8$) reducing the ΔT, the difference between the onset temperature of the first crystallization peak and the glass transition temperature, from (127±2) ^oC to (35±2) ^oC as seen in Table IV.11. This clearly shows that the reduction of OH content in the tellurite glass leads to the formation of a glass less resistant to crystallization. Similar results are seen in the fibers; the fiber processed with reduced OH content exhibits a lower ΔT than the "air-melted" fiber (Table IV.11).

The E_a, the activation energy for T_g, E_{c1}, E_{c2} and E_{c3} the activation energies for T_{p1} T_{p2} and T_{p3} respectively, of the bulk and fibers were measured and compared as a function of OH contents. As seen in Table IV.12, there is no significant effect of OH content on the E_a, E_{c1}, E_{c2} and E_{c3} in the accuracy of the measurement.

The nucleation- and growth-like curves, exhibited in Figures IV.32, were obtained using the methods detailed in §II.2. It can be seen that the maximum of the nucleation-like curve decreases from (390±2) ^oC to (365±2) ^oC for the bulk and from (382±2) ^oC to (378±2) ^oC for the fiber, when the glasses are prepared with reduced OH content. These changes in temperature of maximum nucleation indicate that the low OH containing bulk glass and fiber nucleate at lower temperature than the "air-melted" bulk glass and fiber. This is in agreement with the lower ΔT of the low OH containing materials compared to that of the materials melted in air, seen in Table IV.11.

The growth-like curve exhibits 1 inflection point measured at (372±2) ^{o}C when the glass is processed with reduced OH content whereas no inflection point could be observed in the growth-like curve of the "as-melted" bulk glass. As explained in §V.2.1, the absence of maximum in the growth-like curve can be related to the high growth rate of the crystal as suggested by Ray et al [Ra,01]. The appearance of an inflection point in the growth-like curve indicates that crystals, probably Bi_2O_3, grows, both at the surface and in the volume on the glass but on two distinct temperature range. The growth-like curve of the fiber prepared with low OH content presents no maximum while it exhibits two inflection points when the fiber is processed in air. These changes in the growth-like curve indicate that the crystals formed in the fibers with reduced OH content grow with a faster rate.

As discussed in §V.2.1, an overlap between the nucleation- and growth-like curves of the "air-melted" bulk glass was suspected and crystals were found to grow when the glass with x = 20 was heat treated at its temperature of maximum nucleation. As seen in Figure IV.32a, the nucleation and growth like curves of the bulk glass processed with reduced OH content overlap on a larger temperature range than those of the "air-melted" glass indicating that crystals will nucleate and grow fast when the glass processed with reduced OH content is heat treated at the temperature of maximum nucleation. A smaller overlap can be seen in the nucleation and growth like curves when the fiber is processed with reduced OH content (Figure IV.32b) showing that when heat treated at its temperature of maximum nucleation, crystals with a small size distribution will form into the fiber with reduced OH content, however the size distribution after heat treatment could not be quantify due to the small size of the fiber.

Bulk glasses processed with reduced OH content were treated at 360°C, the temperature of maximum nucleation, for 2 to 40 hours. As observed in the "air-melted" glasses, crystals with a square shape form during the heat treatment. The size of the crystals forming in the bulk (not at the surface) was measured as a function of heat treatment duration to determine the growth rate curve which is presented in Figure IV.33. One can notice that the amplitude of the maximum growth rate slightly decreases and the temperature of maximum growth rate decreases from (476±2) °C to (468±2) °C when the glass is processed with reduced OH content. The decrease in the growth rate can be attributed to an increase of the glass viscosity, which is expected to increase the kinetic barrier (ΔG_d) as suggested by [Go,79] while the decrease in the temperature of maximum growth rate can be related to the decrease in the glass stability to crystallization. Furthermore, the crystal growth in the glass with reduced OH content is found to occur on a narrower temperature range than in the "air-melted" glass. Also shown in Figure IV.33 are the nucleation rate and concentration of nuclei in the as-quenched glass determined using the experiment proposed by Ranasinghe et al [Ra,02]. The maximum nucleation rate as well as the temperature for maximum nucleation rate significantly decreases when the glass is processed with reduced OH content. The decrease in nucleation rate is in agreement with results reported by Davis et al. in silicate melts [Da,97]. The number of quenched-in nuclei in the glass processed with reduced OH content was found i) to be 10 times greater than in the high OH containing glass and ii) to vary from 1.98 10^{10} m^{-3} to 3.65 10^{11} m^{-3} over the entire nucleation temperature range. This increase in number of quenched-in nuclei is in agreement with the decrease in the

glass stability to crystallization when the glass is prepared with reduced OH content. The complete nucleation-like and the growth rate curves in Figures IV.32a and IV.33 clearly show that crystals in the glasses with reduced OH content form and grow at a lower temperature, at a lower rate and over a smaller temperature range than in the "air-melted" glass. Of great interest would be to perform a set of samples with various OH contents to have a better understanding of the OH content effect on the nucleation and growth behavior and impact on the viscosity of the glasses.

The JMA exponent of the glasses and fibers were measured and compared. As seen in Table IV.13, there is no significant effect of the OH reduction process on the JMA of the crystallizations in both bulk glass and fiber. Thus, the OH reduction does not induced changes in the crystallization dimensionality. For all the investigated materials, the n of the 3rd crystallization peak remains in the range $1.5<n<2.5$, the n for 1st crystallization is <1.5 and for the 2nd crystallization >2. As explained in §V.2.2, the low value of n for the 1st exothermic peak may indicate that the first crystals form at the surface of the bulk and fiber [Ch,65] while the larger value of n for the 2nd and 3rd exothermic peaks suggest the formation of crystals in the volume of the glass and fiber.

In this section, we reported results on the processing and characterization of new tellurite-based glasses in the TeO_2-Bi_2O_3-ZnO glass family to engineer a tellurite-based glass with a significantly reduced OH content. We demonstrated the successful processing of tellurite-based glass in the TeO_2-Bi_2O_3-ZnO system with an amount of OH as low as $(0.32\pm0.01)*10^{19}$ ions/cm^3 (corresponding to a decrease of 93%) by drying the batch prior to the melting using F-based raw materials (ZnF_2 and/or NH_4F-HF),

controlling the atmosphere during the melting (O_2-rich environment) and finally by modifying the glass network with the addition of BaO. The effect of OH reduction on the optical loss of a fiber was assessed. It was found that a decrease in OH content decreases the background loss of the fiber. However the losses of the fiber with low OH content are still too high to use these novel fibers for optical applications due to the presence in the fiber of micro-crack, small bubbles and/or from impurities, such as Fe, Cu, Co, Ni, Mn, and Cr which absorb strongly in the wavelength range 0.6~1.6um. Lastly the effect of OH reduction on the nucleation and growth behavior of bulk and fibers was studied. We showed that the OH reduction in bulk and fiber has no effect on the E_a, the activation energy for T_g, nor on E_{c1}, E_{c2} and E_{c3} the activation energies for T_{p1} T_{p2} and T_{p3} , respectively, and on the JMA parameter. However, the low OH containing bulk glass and fiber with x = 20 have a higher tendency to crystallize. They are expected to crystallize at a lower temperature with a slower the nucleation and growth rates than the bulk glass and fiber processed with larger OH content.

CHAPTER VI: CONCLUSIONS

This dissertation summarizes findings on tellurite-based glasses with the composition (90-x)TeO_2-10Bi_2O_3-xZnO with x = 15, 17.5, 20 and 25 that have been processed and characterized for their potential application as novel optical fibers.

The physical, thermal and optical properties as well as the viscosity properties of the glasses in the (90-x)TeO_2-10Bi_2O_3-xZnO (TBZ) glass composition have been discussed in regard to structural variation with increasing ZnO content. As the ZnO content increases, density decreases and viscosity as a function of temperature as well as the thermal properties such as glass transition temperature all shift to higher temperature probably due to ZnO which is believed to cross-link the tellurite network. The decrease of the glasses' refractive index and increase in the fragility parameter with an increase of ZnO content can be related to the cross-linking effect of Zn in the glass structure, decreasing the polarizability, and the increase of the [TeO_3]/[TeO_{3+1}] units which leads to a structure more floppy, respectively.

Complete nucleation- and growth-like curves as well as the quantitative nucleation and growth rates have been measured and found to be dependent on glass composition. Based on the study of the nucleation and growth behavior of the glasses, the glasses with x=15 and 25 are probably not appropriate materials for applications which require controlled nucleation and growth: the glass with x =15 is expected to crystallize with a large distribution of crystal size when heat treated at the temperature of maximum nucleation and the glass with x = 25 fully crystallizes over a short temperature range. These different behaviors of nucleation and growth were related to the domain of glass

formation in the TeO_2-Bi_2O_3-ZnO ternary glass system. The glasses with x = 15 and 25 are expected to be at the limit of the glass formation while the glasses with 17.5 and 20 are in the middle of the glass formation domain. We showed that the predominant crystallization occurs in 3 dimensions. Bi_2O_3 was found to be the first crystal growing via diffusion control in all the investigated glasses when heat treated at their respective temperature of maximum nucleation. These crystals completely disappear and $Zn_2Te_3O_8$ and $Bi_2Te_4O_{11}$ crystals appear in the glass when heat treated at a higher temperature. The formation of these crystals in the glasses leads to a decrease in T_g, and T_p and an increase in the thermal expansion coefficient and density. Lastly, we showed that the 68 μm crystals do not lead to variation in the optical band gap. However when the size of the crystals increases to 263 μm and due to the more numerous amount of crystal, the band gap shifts to larger wavelength and a visible tail can be seen due to light scattering.

Additionally, we report the successful drawing of core-clad fiber with the composition 72.5TeO_2-10Bi_2O_3-17.5ZnO and 70TeO_2-10Bi_2O_3-20ZnO, respectively for the core and clad glasses, with a core radius of (57±1) μm. We showed that fiber drawing leads to structure variations due to molecular unit re-orientation during the drawing process: Micro-Raman spectroscopy confirmed the presence of an increased number of TeO_4 units and of Te-O-Te bridges in the resulting fiber compared to the structure of the preform. The propagation losses in the fiber have been measured at (3.2±0.1) dB/m at 632 nm and (2.1±0.1) dB/m at 1.5 μm and have been related to defects and impurities. We showed that the fiber drawing of the glass with the composition 70TeO_2-10Bi_2O_3-20ZnO increases the tendency of the glass to crystallize at lower temperature. Three crystalline phases are expected to form at 3 distinct temperatures in the fiber, first at the

surface, and when heat treated at higher temperature, in the volume of the fiber. Crystals forming in the fiber were found to be difficult to analyze due to the overlap between nucleation and growth as well as overlap between the growth of the various crystals impeding the acquisition of valuable SEM and optical micrographs.

Lastly, we demonstrated the successful processing of tellurite-based glass in the $TeO_2Bi_2O_3$-ZnO system with an amount of OH as low as (0.32±0.01) $*10^{19}$ ions/cm^3 (corresponding to a decrease of 93%) by drying the batch prior to the melting using F-based raw materials (ZnF_2 and/or NH_4F-HF), controlling the atmosphere during the melting (O_2-rich atmosphere) and finally by modifying the glass network with the addition of BaO. The OH reduction in the glass with the composition $70TeO_2$-$10Bi_2O_3$-20ZnO was found to increase the tendency of the glass to crystallize at lower temperature. Three crystalline phases at 3 distinct temperatures and over distinct temperature ranges are expected to form in the low OH containing glass. We finally showed that the melting of a glass in oxygen rich atmosphere can lead to a fiber with decreased losses in the visible and near-infrared.

As a conclusion, this study provided numerous and detailed answers to each and every questions that initiated this work, through careful measurements and methodical analysis of the physical, thermal, optical and structural properties as well as the nucleation and growth behavior of tellurite-based glasses and fibers:

- *What is the compositional effect on the variation of physical properties within the TeO_2-Bi_2O_3-ZnO system?*

- *What are the nucleation and growth behaviors of glasses within the TeO_2-Bi_2O_3-ZnO system?*
- *What significant differences if any, exist between bulk glass and the corresponding fiber?*
- *How can the water be reduced in the glasses and in the resulting fiber?*

As it is often the case in science, these questions lead the path to new ones and invite to a further understanding in a number of domains. In particular, our study calls for a deeper analysis of the nucleation and growth phenomena taking place in optical fibers during drawing.

CHAPTER VII: FUTURE WORK

The next step in this project should involve (1) the processing of monomode fibers using higher purity raw material and dehydroxylation to reduce the loss to its minimum. Additional techniques such TEM would provide even more intimate details on the nature of the crystals growing in the fiber. (2) A complete study of the effect of water on the nucleation and growth behavior should be carried out. For this last point, a humidification system should be developed to obtain glasses with a wide range of water content. (3) In addition, new glasses in the TeO_2-Bi_2O_3-ZnO with a nucleating agent such as Ag should be processed to define a tellurite glass composition which will be stable upon crystallization, will exhibit a predominant bulk 3D crystallization and well separated nucleation and growth domains. To carry out this work, it is suggested to start from binary tellurite glasses, to reduce the number of crystalline phases and assess the effect of modifier addition, successively. (4) Finally, even though it was not the aim of this study to study diffusion modeling, one should consider defining the diffusion mechanism of each element in the tellurite glass network to model the crystallization behavior via molecular modeling.

The knowledge accumulated through the processing and understanding of the glasses and fibers are vital for the necessary long term stability of envisioned device applications.

REFERENCES

[Al,93]: A. Omar, “Elementary Solid State Physics”, Addison Wesley, (1993).

[An,91]: C. A. Angell, "Relaxation in liquids, polymers and plastic crystals -- strong/fragile patterns and problems", Journal of Non-Crystalline Solids, 131-133 (1991) 13.

[Ar,99]: E.B. Araujo, J.A. Eiras, A.C. Hernandes, “Studies on tellurite glasses using differential thermal analysis”, 18 (1999) 793.

[ASTM,03]: "Standard Test Method for Annealing Point and Strain Point of Glass by Beam Bending," ASTM, C 598-93 (2003).

[Au,78]: J.A. Augis, J.E. Benett, “Calculation of the Avrami parameters for heterogeneous solid state reactions using a modification of the Kissinger method”, Journal of Thermal Analysis and Calorimetry, 13 (1978) 283.

[Av,39]: M.J. Avrami, “Grand partition functions and so-called thermodynamic probability”, Journal of Chemical Physics, 7 (1939) 103.

[Av,40]: M.J. Avrami, “Kinetics of phase change. II transformation-time relations for random distribution of nuclei”, Journal of Chemical Physics, 8 (1940) 212.

[Av,41]: M.J. Avrami, “Granulation, phase change and microstructure kinetics of phase change III”, Journal of Chemical Physics, 9 (1941) 177.

[Ba,01]: R.J. B*ates,* “Optical Switching and Networking Handbook*”, New York: McGraw-Hill. (2001)* ISBN 007137356X.

[Ba,05]: R.W. Balluffi, S.M. Allen, W.C. Carter, “Kinetics of Materials”, Wiley (2005).

[Bl,99]: S. Blanchandin, P. Marchet, P. Thomas, J. C. Champarnaud-Mesjard, B. Frit, “Equilibrium and non-equilibrium phase diagram within the TeO_2-rich part of the TeO_2-Nb_2O_5 system”, Journal of Materials Chemistry, 9 (1999) 1785.

[Bo,91]: J.S. Bowder, S.S. Ballard, P. Kloceck, “Handbook of Infrared Optical Materials”, Chapter 4, P. Kloceck, M. Decker inc., New York, (1991).

[Bo,93]: R. Bohmer, K. L. Ngai, C. A. Angell, D. J. Plazek, "Non-exponential relaxations in strong and fragile glass formers", Journal of Chemistry and Physics, 99 (1993) 4201.

[Br,07]: M. Brown, P. Kent Gallagher, R. Kemp, “Handbook of Thermal Analysis and Calorimetry: Recent Advances”, Techniques and Applications, Elsevier (2007)

[Bü,92]: H. Bürger, K. Kneipp, H. Hobert, W. Vogel, V. Kozhukharov, S. Neov, "Glass formation, properties and structure of glasses in the TeO_2-ZnO system", Journal of Non-Crystalline Solids, 151 (1992) 134.

[Bu,00]: R. Busch, “The thermophysical properties of bulk metallic glass-forming liquids”, Journal of the Minerals, Metals and Materials Society, 52 (2000) 39.

[Bu,04]: J.A. Buck, “Fundamentals of Optical Fibers”, second edition, Wiley (2004).

[Ca,90]: S.F. Carter, M.W. Moore, D. Szbesta, D. Ramsom, P.W. France, “Low loss fluoride fibre by reduced pressure casting”, Electronics Letters, 26 (1990) 2115.

[Ca,97]: T. Cardinal, E. Fargin, G. Le Flem, S. Leboiteux, "Correlations between structural properties of Nb_2O_5-$NaPO_3$-$Na_2B_4O_7$ glasses and non-linear optical activities", Journal of Non-Crystalline Solids, 222 (1997) 228.

[Ca,07]: C. Barry Carter, M. Grant Norton, “Ceramic Materials”, Springer (2007).

[Ch,65]: J.W. Christian, “The Theory of Metals and Alloys”, Pergamon Press, Oxford (1965).

[Ch,82]: K. Chida, F. Hanawa, M. Nakahara, “Fabrication of OH-free multimode fiber by vapor phase axial deposition”, IEEE Journal of Quantum Electronics, QE-18 (1982) 1883.

[Ch,04]: P. Charton, P. Armand, "X-ray absorption and Raman characterizations of TeO_2–Ga_2O_3 glasses", Journal of Non-Crystalline Solids, 333 (2004) 307.

[Ch,07]: C.A. Charitidis, T.E. Karakasidis, P. Kavouras, T. Karakostas, "The size effect of crystalline inclusions on the fracture modes in glass-ceramic materials", Journal of Physics: Condensed Matter, 19 (2007) 266209.

[Ch,07b]: A. Chagraoui, A. Chakib, A. Mandil, A. Tairi, Z. Ramzi, S. Benmokhtar, "New investigation within ZnO–TeO_2–Bi_2O_3 system in air", Scripta Materialia, 56 (2007) 93.

[Ch,09]: W.J. Chung, B.J. Park, H.S. Seo, J.T. Ahn, US Patent: 7,551,348 B2 (2009).

[Cl,93]: N. Clavaguera, "Non-equilibrium crystallization critical cooling rates and transformation diagrams", Journal of Non-Crystalline Solids, 162 (1993) 40.

[Da,76]: H.A. Davies, "The formation of metallic glasses", Physics and Chemistry of Glasses, 17 (1976) 159.

[Da,95]: K.M. Davis, M. Tomozawa, "Water diffusion into silica glass: Structural changes in silica glass and their effect on water solubility and diffusivity", Journal of Non-Crystalline Solids, 185 (1995) 203.

[Da,97]: M.J. Davis, P.D. Ihinger, A.C. Lasaga, "Influence of water on nucleation kinetics in silicate melt", Journal of Non-Crystalline Solids, 219 (1997) 62.

[Da,03]: M.J. Davis, "Crystallization measurements using DTA methods: applications to Zerodur®", Journal of the American Ceramic Society, 86 (2003) 1540.

[Da,06]: S. Dai, C. Yu, G. Zhou, J. Zhang, G. Wang, L. Hu, "Concentration quenching in erbium-doped tellurite glasses" Journal of Luminescence, 117 (2006) 39.

[De,09]: H. Desirena, A. Schulzgen, S. Sabet, G. Ramos-Ortiz, E. De la Rosa, N. Peyghambarian, "Effect of alkali metal oxides R_2O (R=Li, Na, K, Rb and Cs) and network intermediate MO (M=Zn, Mg, Ba and Pb) in tellurite glasses", Optical Materials, 31 (2009) 784.

[Di,07]: S.J. Dillon, M.P. Harmer, "Diffusion controlled abnormal grain growth in ceramics", Materials Science Forums, 558&559 (2007) 1227.

[Du,92]: J.F. Ducel, J.J. Videau, “Physical and chemical characterization of sodium borophosphate glasses”, Materials Letters, 13 (1992) 271.

[Du,06]: M. Dussauze, E. Fargin, A. Malakho, V. Rodriguez, T. Buffeteau, F. Adamietz, "Correlation of large SHG responses with structural characterization in borophosphate niobium glasses", Optical Materials, 28 (2006) 1417.

[Eb,05]: H. Ebbendorff-Heidepriem, T. Monro, “Progress in soft glass microstructured fibres”, IEEE, TuQ1 (invited), (2005) 308.

[Eh,04]: P.R. Ehrmann, K. Carlson, J.H. Campbell, C.A. Click, R.K. Brow, “Neodymium fluorescence quenching by hydroxyl groups in phosphate laser glasses”, Journal of Non-Crystalline Solids, 349 (2004) 105.

[El,92]: R. El-Mallawany, “The optical properties of tellurite glasses”, Journal of Applied Physics, 72 (1992) 1774.

[El,00]: R.A.H. El-Mallawany, Tellurite Glasses Handbook, CRC Press, 2000, pp. 113.

[Fa,91]: W.G. Fateley, F.F. Bentley, *“Encyclopaedia of Physics”*, 2nd edition, 1034, VCH Pub Inc., (1991).

[Fa,98]: E. Fargin, A. Berthereau, T. Cardinal, J.J. Videau, A. Villesuzzanne, G. Le Flem, “Contribution of theoretical chemistry to the investigation of optical non linearities in glasses”, Annales de Chimie Science des Matériaux, 23 (1998) 27.

[Fa,08]: E. P. Favvas, A. Ch. Mitropoulos, “What is spinodal decomposition?”, Journal of Engineering Science and Technology Review, 1 (2008) 25.

[Fe,01]: X. Feng, S. Tanabe, T. Hanada, ”Hydroxyl groups in erbium-doped germanotellurite glasses”, Journal of Non-Crystalline Solids, 281 (2001) 48.

[Fo,05]: V. M. Fokin, M.L.F. Nascimento, E.D. Zanotto, “Correlation between maximum crystal growth rate and glass transition temperature of silicate glasses”, Journal of Non-Crystalline Solids, 351 (2005) 789.

[Fr,87]: P.W. France, S.F. Carter, M.W. Moore, C.R. Day, “Progress in fluoride fibres for optical communications”, British Telecom Tech., 5 (1987) 28.

[Ga,97]: P.H. Gaskell, "Structure and properties of glasses. How far do we need to go?" Journal of Non-Crystalline Solids, 222 (1997) 1.

[Ga,03]: D.R Gaskell, "Introduction to the Thermodynamics of Materials", fourth edition, Taylord & Francis, London, (2003).

[Ga,09]: G. Gao, L. Hu, H. Fan, G. Wang, K. Li, S. Feng, S. Fan, H. Chen, J. Pan, J. Zhang, "Investigation of 2.0 μm emission in Tm^{3+} and Ho^{3+} co-doped TeO_2–ZnO–Bi_2O_3 glasses", Optical Materials, (2009) DOI: 10.1016/j.optmat.2009.07.003.

[Gl,79]: D. Gloge, "The optical fiber as a transmission media", Reports in Progress in Physics, 42 (1979) 119.

[Go,79]: C.J.R. Gonzales-Olivier, P.S. Johnson, P.F. James, "Influence of water content on the rates of crystal nucleation and growth in Lithia-silica and soda-lime-silica glasses" Journal of materials Science, 14 (1979) 1159.

[Go, 80]: C.J.R. Gonzales-Olivier, P.F. James, "Crystal nucleation and growth in a Na_2O 2CaO 3SiO_2 glass", Journal of Non-Crystalline solids, 39&39 (1980) 699.

[Go,05]: N.K. Goel, "Development of core suction technique for fabrication of highly doped fibers for optical amplification and characterization of optical fibers for Raman amplification", PhD dissertation, Virginia polytechnic Institute (2005).

[Gr,98]: K.T.V. Grattan, B.T. Meggit, "Optical Fiber Sensor Technology: Fundamentals", Kluwer Academic Publishers Group, (1998).

[Gu,05]: W. Guo-Nian, S-X. Dai, J-J. Zhang, S-Q Xu, L-L Hi, Z-H. Jiang, "Fluorescence lifetime increasing with F^- ions into ytterbium-doped germanium–lead–tellurite glasses" Chinese Physics Letters, 22 (2005) 457.

[Ha,97]: S. Hazra, S. Mandal, A. Ghosh, "Properties of unconventional lithium bismuthate glasses" Physical Review B, 56 (1997) 8021.

[Ha,99]: D. Harris, "Materials for Infrared Windows and Domes", SPIE press, (1999).

[Ha,00]: N. Hadj Youssef, M.S. Belkhiria, J.J. Videau, M. Ben Amara, "Investigation of the physico-chemical properties of calcium borophosphate glasses. Effect of the substitution of sodium for calcium", Materials Letter, 44 (2000) 269.

[Ha,02]: M. Hafid, T Jermouni, N. Toreis, T. Ghailassi, "Structure of $(45-x)Na_2O-xBaO-5ZnO-50P_2O_5$ glasses studied by DSC and infrared spectroscopy", Materials Letters, 56 (2002) 486.

[He,93]: M.R. Heslin, "Effect of Hydroxyl Ion Concentration on the Nucleation and Crystallization of Glasses", PhD Thesis Alfred University, (1993).

[He,98]: L.L. Hench, T. Kobubo, "Properties of Bioactive Glasses and Glass-Ceramics, Hanbook of Biomaterials Properties", Chapman & Hall, London (1998).

[He,99]: J. Hecht, "City of Light: The Story of Fiber Optics", Oxford University Press (1999) ISBN 0195108183.

[Hi,07]: C.J. Hill, A. Jha, "Development of novel ternary tellurite glasses for high temperature fiber optic mid-IR chemical sensing", Journal of Non-Crystalline Solids, 353 (2007) 1372.

[Ho,02]: W. Holland, G. Beal, "Glass-Ceramic Technology", published by The American Ceramic Society (2002).

[In,88]: J. D. Ingle and S. R. Crouch, "Spectrochemical Analysis", Prentice Hall, New Jersey (1988)

[It,91]: K. Itoh, K. Miura, M. Masuda, M. Iwakura, T. Yamagishi, "Low-loss fluorozirco-aluminate glass fiber," in Proceedings of 7th International Symposium on Halide Glass, Center for Advanced Materials Technology, Monash University, Lorne, Victoria, Australia, (1991) 2.7.

[Ja,82]: P.F. James, "Nucleation in Glass-Forming System: In Advences in Ceramics", edited by J.H. Simmons, D.R. Uhlmann and G.H. Beal, Colombus, OH, American Ceramic Society, 1-48.

[Je,88]: J.M. Jewell, J.E. Shelby, "Effect of water content and alumina additions on the transformation range properties of Na_2O-$3SiO_2$ glasses", Journal of Non-Crystalline Solids, 102 (1988) 24.

[Jh,07]: A. Jha, P. Joshi, S. Shen, L. Huang, “Spectroscopic characterization of signal gain and pump ESA in short-lengths of rare earth-doped tellurite fibers”, Journal of Non-Crystalline Solids, 353 (2007) 1407.

[Ji,00]: S. Jiang, T. Luo, B.-C. Hwang, F. Smekatala, K. Seneschal, J. Lucas, N. Peyghambarian “Er^{3+}-doped phosphate glasses for fiber amplifiers with high gain per unit length”, Journal of Non-Crystalline Solids, 263&264 (2000) 364.

[Jo,97]: P. Joshi, A. Jha, “An investigation on the crystal growth studies and emission line in Er^{3+}-doped sodium tellurite glasses”The Korean Ceramic Society, 6 (1997) 67.

[Ka,48]: W. Kauzmann, “The nature of the glassy state and the behavior of liquids at low temperatures.”, Chemical Reviews, 43 (1948) 219.

[Ka,65]: N.S. Kapany, R.J. Simms, "Recent developments of infrared fiber optics," Infrared Physics, 5 (1965) 69.

[Ka,78]: I. P. Kaminow and L. W. Stulz, “Loss in cleaved Ti-diffused $LiNbO_3$ waveguides”, Applied Physics Letters, 33 (1978) 62.

[Ka,84]: Y. Kanamori, Y. Terunuma, T. Miyashita, "Preparation of chalcogenide optical fiber," Review. Electrical Communication Laboratory, 32 (1984) 469.

[Ka,99]: B. Karmakar, P. Kundu, A.K. Chaudhuri, K. Annapurna, A. Kumar, R.N. Dwivedi, “Effect of Hydroxyl content on the physical properties of calcium metaphosphate glasses”, Bulletin Materials, 22 (1999) 115.

[Ka,00]: S.V. Kartalopoulos, “Introduction to DWDM Technology: Data in a Rainbow”, IEEE Press, 2000.

[Ke,70]: F. Kerkhof, „Bruchvorgange in glasern“, Dtsch. Glastechnische Gesellschaft, Francfurt, Mainz, (1970).

[Ke,95]: K.F. Kelton, “Transient nucleation in glasses”, Materials Science and Engineering B, 32 (1995) 145.

[Ki,57]: H.E. Kissinger,” Reaction kinetics in differential thermal analysis” Analytical Chemistry, 29 (1957) 1702.

[Ki,75]: W.D. Kingery, H.K. Bowen, D.R. Hulmann, ”Introduction to Ceramics“, 2nd edition, Wiley, NY, (1975)

[Ki,81]: R.J. Kirkpatrick, “Kinetics of Crystallization of Igneous Rocks. In: Lasaga”, A.C., Kirkpatrick, R.J. (eds), Kinetics of geological processes. Reviews in mineralogy, 8. Mineral. Soc. Am., Washington, D.C (1981) 321.

[Ki,93]: S.H. Kim, T. Yoko, S. Sakka, “Linear and Nonlinear Optical Properties of TeO_2 Glass**”,** Journal of the American Ceramic Society, 76, (1993), 2486.

[Ki,95]: S.-H Kim, T. Yoko, “Nonlinear optical properties of TeO_2-based glasses: MO_x-TeO_2 (M = Sc, Ti, V, Nb, Mo, Ta, and W) binary glasses”, Journal of the American Ceramic Society, 78 (1995) 1061.

[Ki,07]: N. Kikuchi, T. Shinzawa, T. Negishi, K. Ogura, C. Nielsen, “Observation of crystalline contrast with using low energy electrons in SEM”, Microscopy and Microanalysis, 13 (2007) 972.

[Kn,39]: F. Knoop, C.G. Peters and W.B. Emerson, “A sensitive pyramidal-diamond tool for indentation measurements”, Journal of Research of the National Bureau of Standards, 23 (1939) 39.

[Ko,78]: S. Kobayashi, N. Shibata, S. Shibata, T. Izawa, T., "Characteristics of optical fibers in infrared wavelength region," Review Electrical Communication Lab, 26 (1978) 453.

[Ko,86]: V. Kozhukharov, H. Bürger, S. Neov, B. Sidzhimov, "Atomic arrangement of a zinc-tellurite glass", Polyhedron, 5 (1986) 771.

[Ko,95]: T. Komatsu, R. Ike, R. Sato, K. Matusita, “Mixed alkari effect in tellurite glasses and change in fragility”, Physics and Chemistry of Glasses, 36 (1995) 216.

[Kr,05]: B. Krause (Eds.) “Low Thermal Expansion Glass-Ceramic” Second edition, Springer (2005).

[Ku,95]: A. Kutub, “Optical, infrared and DSC studies of sodium tetraborate glasses containing copper oxide”, Journal of Materials Science, 30 (1995) 724.

[Le,98]: L. Le Neindre, F. Smektala, K. Le Foulgoc, X. H. Zhang, J. Lucas, "Tellurium halide optical fibers", Journal of Non-Crystalline Solids, 242 (1998) 99.

[Le,07]: E.T.Y. Lee, E.R.M. Taylor, "Two-die assembly for the extrusion of glasses with dissimilar thermal properties for fibre optic preforms", Journal of Materials Processing Technology, 184 (2007) 325.

[Ll,75]: J.M. Lloyd, "Thermal Imaging Systems", Plenum Press, New York, 1975.

[Lu,08]: T. Luo, A. Khursheed, "Elemental identification using transmitted and backscattered electrons in an SEM", Physics Procedia, 1 (2008) 155.

[Ma,77]: K. Matusita, S. Sakka, "Kinetic study of the crystallization of glass by differential scanning calorimetry" Physics and Chemistry of Glasses, 20 (1979) 77.

[Ma,81]: A. Marotta, A. Bure, F. Branda, "Nucleation in glass and differential thermal analysis", Journal of Materials Science, 16 (1981) 341.

[Ma,97]: H.L. Ma, M. Matecki, X.H. Zhang, S. Rogard, "Determination of the nucleation and crystal growth rate curves of a chalcohalide glass from DSC experiment", Journal of Materials Science Letters, 16 (1997) 21.

[Ma,03]: S. Marjanovic, J. Toulouse, H. Jain, C. Sandmann, V. Dierolf, A. R. Kortan, N. Kopylov, R. G. Ahrens, "Characterization of new erbium-doped tellurite glasses and fibers", Journal of Non-Crystalline Solids, 322 (2003) 311.

[Ma,04]: M. O'Donnell, "Tellurite and Fluorotellurite Glasses for Active and Passive Fibreoptics Waveguides", PhD Thesis University of Nottingham, (2004).

[Ma,06]: J. Malek, D. Svadlak,T. Mitsuhashi, H. Haneda, " Kinetics of crystal growth of Sb_2S_3 in $(GeS_2)_{0.3}(Sb_2O_3)_{0.7}$ glass". Journal of non-crystalline solids, 352 (2006) 2243.

[Ma,06b]: O. Madelung, U. Rössler and M. Schulz, "Numerical Data and Functional Relationships in Science and Technology: Non-Tetrahedrally Bonded Elements and Binary Compounds I", Springer-Verlag, (2006).

[Mc,00]: D. A. McKeown, I. S. Muller, A. C. Buechele, I. L. Pegg, C. A. Kendziora, "Structural characterization of high-zirconia borosilicate glasses using Raman spectroscopy", Journal of Non-Crystalline Solids, 262 (2000) 126.

[Me,98]: D. Mercurio, J.C. Champarnaud-Mesjard, I. Gouby, B. Frit, "On the crystal structure of $Bi_2Te_2O_7$", European Journal of Solid State and Inorganic chemistry, 35 (1998) 49.

[Me,01]: E. Metwalli, R.K. Brow, "Modifier effects on the properties and structures of aluminophosphate glasses", Journal of Non-Crystalline Solids, 289 (2001) 113.

[Mi,83]: S. Mitachi, Y. Ohishi, T. Miyashita, "A fluoride glass optical fiber operating in the mid-infrared wavelength range", Journal of Lightwave Technology, LT-1 (1983) 67.

[Mi,07]: M.K Miller, P.J. Liaw, "Bulk Metallic Glasses", Springer, (2007).

[Mi,07b]: N.I. Min'ko, V.V. Varavin, "Effect of water on the structure and properties of glass (Review)", Glass and Ceramics, 64, (2007), 71-74

[Mo,93]: C.T Moynihan, "Correlation between the width of the glass transition region and the temperature dependence of the viscosity of high-Tg glasses" Journal of the American Ceramic Society, 76 (1993) 1081.

[Mo,96]: R. Morrell, "Materials Science and Technology Series" Vol 17A, Weinheim, VCH, (1996).

[Mo,97]: A. Mori, Y. Ohishi, M. Yamada, H. Ono, S. Sudo, in: "Optical Fiber Conference", Washington, USA, 1997, PD-1.

[Mo,97b]: A. Mogus-Milankovic; K. Furic; C. S. Ray; W. Huang; D. E. Day, "Raman studies of PbO-Bi_2O_3-Ga_2O_3 glasses and crystallized compositions", Physics and Chemistry of Glasses, 38 (1997) 148.

[Na,85]: T. Nakamura, T. Yamamuro, S. Higashi, Y. Kakutani, T. Kokubo, " A new glass-ceramic for bone replacement: Evaluation of its bonding to bone tissue", Journal of Biomedical Materials Research, 19 (1985) 685.

[Na,02]: K. Nagayama, T. Saitoh, M. Kakui, K. Kawasaki, M. Matsui, H. Takamizawa, H. Miyaki, Y. Ooga, O. Tsuchiya, Y. Chigusa, "Ultra-Low Loss (0.151 dB/km) Fiber and its Impact on Submarine Transmission Systems", Optical Fiber Communication Conference and Exhibit, 2002. OFC 2002.

[Na,03]: V. Nazabal, S. Todoroki, A. Nukui, T. Matsumoto, S. Suehara, T. Hondo, T. Araki, S. Inoue, C. Rivero, T. Cardinal, "Oxyfluoride tellurite glasses doped by erbium: thermal analysis, structural organization and spectral properties", Journal of Non-Crystalline Solids, 325 (2003) 85-102.

[Na,07]: M. L. F. Nascimento, C. Aparicio, "Viscosity of strong and fragile glass-forming liquids investigated by means of principal component analysis", Journal of Physics and Chemistry of Solids, 68 (2007) 104.

[Ni,81]: N. Niizeki, "Recent progress in glass fibers for optical communications", Japanese Journal of Applied Physics, 20 (1981) 1347.

[Ni,92]: J. Nishii, S. Morimoto, I. Inagawa, R. Iizuka, T. Yamashita, T. Yamagishi, "Recent advances and trends in chalcogenide glass fiber technology: a review," Journal of Non-Crystalline Solids, 140 (1992) 199.

[Ni,92b]: J. Nishii, T. Yamashita, T. Tamagishi, C. Tanaka, H. Sone, "As_2S_3 fibre for infrared image bundle," International Journal of Optoelectronics, 7 (1992) 209.

[O'Do,04]: M. O'Donnell, Tellurite and Fluorotellurite Glasses for Active and Passive Fibreoptics Waveguides, PhD Thesis University of Nottingham, (2004).

[O'Do,07]: M.D. O'Donnell, K. Richardson, R. Stolen, A.B. Seddon, D. Furniss, V.K. Tikhomirov, C. Rivero, M. Ramme, R. Stegeman, G. Stegeman, M. Couzi, T. Cardinal, "Tellurite and fluorotellurite glasses for fiberoptic Raman amplifiers: glass characterization, optical properties, Raman gain, preliminary fiberization, and fiber characterization", Journal of American Ceramic Society, 90 (2007) 1448.

[Oh,02]: Y. Ohishi, A. Mori, M. Yamada, H. Ono, T. Kanamori, T. Shimada, "Tellurite Glass, Optical Amplifier, and Light Source", US Patent #6356387, (2002).

[OR,BBV]: Orton Model BBV-1000 Beam-Bending Viscometer. 2003, Westerville, OH: Edward Orton Jr. Ceramics Foundation.

[OR,PPV]: Orton Model PPV-1000 Parallel-Plate Viscometer. 2007, Westerville, OH: Edward Orton Jr. Ceramics Foundation.

[Oz,71]: T. Ozawa, "Kinetics of non-isothermal crystallization", Polymer, 12 (1971) 150.

[Oz,07]: B. Oz, M.L. Ovecoglu, I. Kabalc, G. O Zen, "Microstructural characterization and crystallization kinetics of $(1-x)TeO_2-xK_2O$ (x=0.05, 0.10, 0.15, 0.20 mol) glasses", Journal of the European Ceramic Society 27 (2007) 3239.

[Oz,07b]: J. Ozdanova, H. Ticha, L. Tichy, "Remark on the optical gap in $ZnO-Bi_2O_3-TeO_2$ glasses", Journal of Non-Crystalline Solids, 353 (2007) 2799.

[Pa,02]: M.J. Pascual, A. Duran, L. Pascual, "Sintering behaviour of composite materials borosilicate glass-ZrO_2 fibre composite materials", Journal of the European Ceramic Society 22 (2002) 1513.

[Pe,06]: L. Petit, T. Cardinal, J.J. Videau, E. Durand, L. Canioni, M. Martines, Y. Guyot, G. Boulon, "Effect of niobium oxide introduction on erbium luminescence in borophosphate glasses", Optical Materials, 28 (2006) 172.

[Pi,08]: F.Pietrucci, S.Caravati, M. Bernasconi, "TeO_2 glass properties from first principles", Physical Review B, 78 (2008) 064203.

[Po,77]: M. Poulain, M. Chanthanasinh, J. Lucas, "New fluoride glasses," Materials Research Bulletin, 12 (1977) 151.

[Po,96]: M. Poulain, "Crystallization in fluoride glasses" Thermochimica acta, 280&281 (1996) 343-351.

[Py,70]: L.D. Pye, H.J. Stevens, W.C. Lacourse, "Introduction to Glass Science", Proceedings of a tutorial symposium held at the State University of New York, College of Ceramics at Alfred University, Alfred, NY June 8-19 (1970).

[Ra,97]: C.S. Ray, D.E. Day, " An Analysis of nucleation rate-type of curves in glass as determined by differential thermal analysis", Journal of the American Ceramic Society, 80 (1997) 3100.

[Ra,00]: C.S. Ray, X. Fang, D.E. Day, “New Method for Determining the Nucleation and Crystal-Growth Rates in Glasses”, Journal of the American Ceramic Society, 83 (2000) 865.

[Ra,01]: C. S. Ray, K. S. Ranasinghe, D. E. Day, “Determining crystal growth rate-type of curves in glasses by differential thermal analysis”, Solid State Sciences, 3, (2001) 727.

[Ra,02]: K.S. Ranasinghe, “Differential Analysis of Nucleation and Crystal Growth Rates in Glasses”, PhD Thesis University of Missouri-Rolla, (2002).

[Ro,19]: H.M. Rockwell & S.P. Rockwell, "Hardness-Tester," US Patent 1 294 171, Feb 1919.

[Ro,22]: S.P. Rockwell, “The Testing of Metals for Hardness”, Transactions of the American Society for Steel Treating, II (1922) 1013.

[Ro,24]: S.P. Rockwell, "Hardness-Testing Machine," US Patent 1 516 207, Nov. 1924.

[Ro,02]: V. Rodriguez, C. Sourisseau, “General maker-fringe ellipsometric analyses in multilayer nonlinear and linear anisotropic optical media”, Journal of the Optical Society of America B, 19 (2002) 2650.

[Ru,92]: J. A. Ruller, J. E. Shelby, “Properties of heavy metal oxide glasses”, Physics and Chemistry of Glasses, 33 (1992) 177.

[Sa,00]: N. S Saxena, M.A. Imran, Mousa, D. Bhandari, “Determination of the avrami exponent from non-isothermal differential scanning calorimetry of $Se_{70}Te_{24}Cd_6$ chalcogenide glass”, Physica Scripta, 61 (2000) 502.

[Sc,88]: H. Scholze, “Glas. Natur, Struktur und Eigenschaften”, 3rd edition, Springer, (Berlin, Heidelber), (1988).

[Sc,08]: S. Gaylord, “Thermal and Structural Properties of Candidate Moldable Glass Types” MSc Thesis, Clemson University, South Carolina, 2008.

[Se,92]: T. Sekiya, N. Mochida, A. Ohtsuka, M. Tonokawa, “Raman spectra of $MO_{1/2}$-TeO_2 (M = Li, Na, K, Rb, Cs and Tl) glasses”, Journal of Non-Crystalline solids, 144 (1992) 128.

[Se,94]: T. Sekiya, N. Mochida, A. Ohtsuka, "Raman spectra of MO-TeO_2 (M = Mg, Sr, Ba and Zn) glasses", Journal of Non-Crystalline Solids, 168 (1994) 106.

[Se,04]: G. Senthil-Murugan, E. Fargin, V. Rodriguez, F. Adamietz, M. Couzi, T. Buffeteau, P. Le Coustumer, "Temperature-assisted electrical poling of TeO_2–Bi_2O_3–ZnO glasses for non-linear optical applications", Journal of Non-Crystalline Solids, 344 (2004) 158.

[Sh,76]: J.E. Shelby, G.L. McWay, "Influence of water on the viscosity and thermal expansion of sodium trisilicate glasses", Journal of Non-Crystalline Solids, 20 (1976) 439.

[Sh,97]: Y. Shimizugawa, T. Maesto, S. Inoue, A. Nukui, "Sturcture of TeO_2.ZnO glasses by RDF and Te, Zn K EXAFS", Physics and Chemistry of Glasses, 38 (1997) 201.

[Sh,00]: J. Shelby, Journal of Non-Crystalline Solids, "Properties of alkali–alkaline earth metaphosphate glasses" 263&264, (2000), 271-276.

[Sh,05]: J.E. Shelby, "Introduction to Glass Science", 2nd Edition, RS.C (2005).

[Sh,08]: P. Sharma, S.C. Katyal, "Effect of tin addition on the optical parameters of thermally evaporated As–Se–Ge thin films", Materials Chemistry and Physics, 112 (2008) 892.

[Sm,22]: R.L. Smith, G.E. Sandland, "An Accurate Method of Determining the Hardness of Metals, with Particular Reference to Those of a High Degree of Hardness", Proceedings of the Institution of Mechanical Engineers, I (1922) 623.

[Sm,95]; F. Smektala, M. Matecki, "Determination of ZBLAN glass nucleation and crystallization curves from DSC experiment", European Journal of Solid State and Inorganic Chemistry, 32 (1995) 245.

[St,59]: S. D. Stookey, "Catalyzed crystallization of glass in theory and practice," Industrial and Engineering Chemistry Research, 45 (1959) 805.

[St,82]: J. Stone, P.J. Lemaire, "Reduction of loss due to OH in optical fibres by a two-step OH→OD exchange process" Electronics Letters, 18, (1982), 78-80.

[St,86]: Z. Strnad, “Glass-Ceramic Materials”, Elsevier Science, New York, (1986).

[So,93]: A. Soufiane; M. Poulain, “New fluorogallate glasses”, Journal of Non-Crystalline Solids, 161 (1993) 206.

[Su,92]: S. Surinach, M.D. Baro, J.A. Diego, N. Clavaguera, M.T. Clavaguera-Mora, “A new temperature versus heating rate transformation (T-HR-T) diagram: Application to study the crystallization behaviour of $Fe_{67.5}Co_{15}Nb_{1.5}B_{16}$ metallic glass”, Acta Metallurgica et Materialia,, 40 (1992) 37.

[Su,98]: C. Suryanarayana, Norton M.G., “X-Ray Diffraction a Practical Approach”, Plenum Press, New York, (1998).

[Su,05]: X. Sun, J.G. Lu, S. Guo, Z. Xiu, K. Duan, X. Hu, “Intragranular Particle Residual Stress Strengthening of Al_2O_3–SiC Nanocomposites“, Journal of the American Ceramic Society, 88 (2005) 1536.

[Sy,06]: N. Syam Prasad , J. Wang , R.K. Pattnaik, H. Jain, J. Toulouse, “Preform fabrication and drawing of $KNbO_3$ modified tellurite glass fibers”, Journal of Non-Crystalline Solids, 352 (2006) 519.

[Sz,96]: Z. Szaller, L. Pöppl, Gy. Lovas and I. Dódony, “Study of the Formation of $Bi_2Te_4O_{11}$”, Journal of Solid State Chemistry, 121 (1996) 251.

[Ta,94]: M. Tatsumisago, S-K. Lee, T. Minami, Y. Kowada, “Raman spectra of TeO_2-based glasses and glassy liquids: local structure change with temperature in relation to fragility of liquid”, Journal of Non-Crystalline Solids, 177 (1994) 154.

[Ta,00]: T. David, “The Hardness of Metals”, Oxford University Press (2000).

[Ta,02]: E.R. Taylor, L. Na Ng, N.P. Sessions, H. Buerger, “Spectroscopy of Tm^{3+}-doped tellurite glasses for 1470nm fiber amplifier” Journal of Applied Physics, 92, (2002), 112-117

[Ta,06]: H. Takebe, T. Murakami, M. Kuwabara, D.W. Hewak, “Preparation and properties of La_2O_3-Ga_2S_3 glass-ceramics for IR materials”, Journal of Non-Crystalline Solids, 352 (2006) 2425.

[Th,98]. I.D. Thompson, L.L. Hench, “Mechanical properties of bioactive glasses, glass-ceramics and composites”, Proceedings of the Institution of Mechanical Engineers. Part H, Journal of engineering in medicine, 212 (1998) 101.

[Ti,06]: R.S. Tiwari, N. Mehta, A. Kumar, “Effect of Bi on the crystallization kinetics of a glassy $(Se_{80}Ge_{20})_{100-x}$ Bi_x system”, Chinese Journal of Physics, 44 (2006) 467.

[Tr,82]: D.C. Tran, C.F. Fischer, G.H. Sigel, " Fluoride glass preforms prepared by a rotational casting process”, Electronics Letters, 18 (1982) 657.

[Tr,93]: D. Tran, "Heavy Metal-Oxide Glass Optical Fibers For Use In Laser Medical Surgery," U.S Patent no. 5,274, 728 issued Dec. 28 (1993).

[To,99]: H. G. Tompkins and W. A. McGahan, “Spectroscopic Ellipsometry and Reflectometry”, Wiley, (1999).

[To,00]: E.L. Tobolski, A. Fee, "Macroindentation Hardness Testing," ASM Handbook, Volume 8: Mechanical Testing and Evaluation, ASM International, (2000), p 203-211.

[Ts,03]: K. Tsujikawa, M. Ohashi, K. Tajima, “Optical properties of multicomponent oxide glasses and glass fibers”. Electronics and Communications in Japan (Part I: Communications), 86 (2003) 21.

[Tu,56]: D. Turnbull, “Phase changes”, Solid State Physics, 3 (1956) 225.

[Tu,69]: D. Turnbull, “Under what conditions can a glass be formed”, Contemporary Physics, 10 (1969) 473.

[Tz,01]: M. Tzolov, N. Tzenov, D. Dimova-Malinovska, M. Kalitzova, C. Pizzuto, G. Vitali, G. Zollo, I. Ivanov, "Modification of the structure of ZnO:Al films by control of the plasma parameters", Thin Solid Films, 396 (2001) 276.

[Uh,72]: D.R. Uhlmann, “A kinetic treatment of glass formation”, Journal of Non-Crystalline Solids, 7 (1972) 337.

[Wa,94]: J. Wang, E. Vogel, E. Snitzer, “Tellurite glass: a new candidate for fiber devices”, Optical Materials, 3 (1994) 187.

[Wa,94b]: J.S. Wang, D. Machewirth, F. Wu, E. Snitzer, E.M. Vogel, “Neodymium-doped tellurite single-mode fiber laser”, Optics Letters, 19 (1994) 1448.

[Wa,02]: R.W. Waynant, “Lasers in Medicine”, CRC Press, (2002)

[Wa,06]: J. Wang, S. Prasad, K. Kiang, R.K. Pattnaik, J. Toulouse, H. Jain, “Source of optical loss in tellurite glass fibers”, Journal of Non-Crystalline Solids, 352 (2006) 510.

[We,89]: M.C. Weinberg, D.R. Uhlmann, E.D. Zanotto, “Nose method of calculating critical cooling rates for glasses formation”, Journal of the American Ceramic Society, 72 (1989) 2054

[Wi,98]: M. M. Wierzbicki, J. E. Shelby, "Thermal Stability of Heavy Metal Oxide Glasses," 18th Int'l Congress on Glass, San Francisco, CA, July (1998)

[Ya,05]: M. Yashima, D. Ishimura, K. Ohoyama, “Temperature-dependence of lattice parameters and anisotropic thermal expansion of bismuth oxide”, Journal of the American Ceramic Society, 88 (2005) 2332.

[Yo,07]: E. Youssef, M. Hotzel, C. Russel, “Effect of ZnO and Bi_2O_3 addition on linear and non-linear optical properties of tellurite glasses”, Journal of Non-Crystalline Solids, 353 (2007) 333

[Za,02]: E.D. Zanotto, V.M. Fokin, “Recent studies of internal and surface nucleation in silicate glasses”, Philosophical Transactions: Mathematical, Physical and Engineering Sciences, 361 (1992) 591.

[Zh,03]: Z-Y Deng Y. Zhou, M.E. Brito, J.F. Yang, T. Ohji, “Fracture-mode change in alumina-silicon carbide composites doped with rare-earth impurities”, Journal of the American Ceramic Society, 86 (2003) 1789.